

Chemo-mineralogical and petrophysical alterations on lithotypes due to thermal treatment before stone consolidation

submitted in satisfaction of the requirements for the degree of
Doctor of Natural Sciences in Civil Engineering
of the Vienna University of Technology, Faculty of Civil Engineering

Dissertation

Chemo-mineralogische und petrophysikalische Veränderungen an Gesteinen durch thermische Einwirkung vor einer Gesteinsfestigung

ausgeführt zum Zwecke der Erlangung des akademischen Grades eines
Doktors der Naturwissenschaften
eingereicht an der Technischen Universität Wien Fakultät für Bauingenieurwesen
von

Mag. **Matea Ban** B.Arch.
Registration number: 00474143
Karlsplatz 13/220-1, 1040 Wien

Auditor: Univ.-Prof. **Katja Sterflinger**
Institute of Natural Sciences and Technology in Arts – Academy
of Fine Arts Vienna, Augasse 2-6, 1090 Vienna, Austria

Auditor: Univ.-Prof. **Andreas Kolbitsch**
Institute of Construction, Structural Dynamics and Building
Technology – Building Construction and Maintenance
TU Wien, Karlsplatz 13/208-02, 1040 Vienna, Austria

Supervisor: a.o. Univ.-Prof. **Andreas Rohatsch**
Institute of Geotechnics – Engineering Geology
TU Wien, Karlsplatz 13/220-1, 1040 Vienna, Austria

Vienna, Mai 2021

This work was supported by the project 'Nano-Cathedral' short for 'Nanomaterials for conservation of European architectural heritage developed by research on characteristic lithotypes', funded by the European program Horizon 2020 Call NMP21-AC (GA 646178) and by the Marietta Blau Grant financed by the Austrian Federal Ministry of Education, Science and Research (BMBWF) and coordinated by the Austrian Agency for International Cooperation in Education and Research (OeAD).

Affidavit

I declare in lieu of oath, that this thesis and the work presented in it are my own and have been generated by me as the result of my own research, using only literature cited in this work. Where I have quoted text passages from the work of others, the source is always given and clearly attributed.

I confirm that this work is original and has not been submitted elsewhere for any examination, nor is it currently under consideration for a thesis elsewhere.

Matea Ban _____

Acknowledgements

I owe a great debt to my supervisor Andreas Rohatsch, who never restricted my scientific curiosity and visions. I can tell for sure that without him I would have never become the scientist I am today. Without his support and open-mindedness, this dissertation may have never happened. He believed in me, protected me and gave me the absolute freedom to grow.

A formative force during my entire career was my friend and supervisor Johannes Weber. I shared many moments with him including countless discussions, fights, beliefs, fears and moments of happiness. I am grateful for the established lifelong friendship between us.

Valter Castelvetro might not know it, but he was a constant source of inspiration to me and I could have never wished for a better supervisor. I cannot thank him enough for everything he has done for me. I hope that my future holds many research questions that I can answer with him.

I would like to thank Alberto Viani who shared so much knowledge and wisdom with me while I was growing into the scientist I am now. I want to thank him for the many laughs and the opportunity to be a part of his team. You and your team made Telč feel like home to me. I hope I see you soon Alberto.

I am grateful for knowing Thomas Luxbacher, who introduced me to the world of electrokinetics. I am lucky and honoured that I had the opportunity to work with and learn from him.

I owe so much to Johannes Lützenkirchen, who provided me with a lot of knowledge, support and guidance. I admire his passion for work and the environment. A big thank you goes out to my INE angles, Teba Gil-Diaz, Sanduni Ratnayake and Yasmine Kouhail. I enjoyed the research stay in Karlsruhe so much and do not want to miss this experience. Kudos to all the great people I met there and who supported me in so many ways: Andrej Skerencak and Frank Heberling, you guys are great.

Great thanks to my friend Simona Raneri. I will never forget the countless shifts at the beam line and so many moments we shared. I am sure this collaboration and friendship will hold forever. At this point, I also want to thank Tim De Kock for sharing his knowledge and experience with me. I also want to thank Jose Teixeira for not only correcting all the stuff I wrote about neutrons but for his extensive answers to my questions with specific learning aims. Jose is a great teacher.

I want to thank my lab partner Luca Panariello for the great fun, for teaching me how to synthesise and modify nanoparticle with love, blood and some secret ingredients. Thank you for teaching me how to toughen HDPE and thank you for the many coffees we shared. I also would like to thank Andrea Lazzeri for hosting and supporting me during my research stay in Italy. He is truly one of a kind and he made me go out of my comfort zone. He is the reason why I worked with analytical models, synthesised nanoparticle or why I was toughening HDPE. Besides, without Andrea, I would have never had the opportunity to work with Laura Aliotta and Vito Gigante.

I profited from the extensive knowledge of José Delgado Rodrigues and I am truly thankful I had the opportunity to work with him. I dare to say that he is one of the leading personalities in the field of stone consolidation. I hope I can come close to contributing to the field as much as he did.

I hope that everyone has a friend and colleague like Farkas Pinter it is. I am so thankful for his invaluable support.

Sabrina Bianchi thank you for being who you are. Your nature has made you so much loved and appreciated.

I want to thank my friends Silas Dean and Amanda Clarke for the lovely evenings in Pisa. Amanda, I do not know how I will ever be able to repay your kindness and support. Herewith, I also want to thank my lovely friends from the Opera Della Primaziale Pisana, who welcomed me every time like it was my first time in Pisa. Thank you, Anton Sutter and Roberto Cela.

The colleagues from my research group have been important from my personal and professional development. I want to thank Alexander Preh for his endless support and friendship. Thank you Victor Navas-Basantes for all the advice you gave me like I was your daughter. I truly appreciate this. I am thankful to Christine Cerny for being an inspiration in so many ways to all of us. Every day I was impressed with the strength of her will and how she fought the obstacles that are in her way.

I want to thank Michael Höflinger and Michael Jamek for the collaboration and their advice and experiences on rock mechanics they shared with me.

A huge thanks to my colleagues Tony Baragona and Elisabeth Mascha. Tony was responsible for me choosing this exact PhD topic. Lisi, I am so happy I had you during my entire studies also as a colleague but primarily as my friend. I hope that the future will bring us many discussions and projects. I also want to thank Francesca Gherardi for all her support.

Thank you to my colleagues from the X-Ray centre, Klaudia Hradil and Werner Artner, for their support and hearty hospitality. The same goes for Karin Wriessnig and Franz Ottner. Every time I was at the BOKU I felt like I was part of the institute.

I particularly want to thank Paul Linhardt for teaching me the basics of corrosion science and for a work place in his lab during the pandemic. Paul, I owe you a lot, thank you for being amazing.

Thank you, Giancarlo Sidoti, for showing me Rome and teaching me chemistry. I truly enjoyed the time in your lab and I learned so much from you.

A special thanks go out to Lukas Achleitner, who first became my bachelor's student, then my co-worker and soon one of my best friends. I can say with confidence that people like Lukas teach me more than I could ever teach them. I also want to thank my lovely Verena Hammerschmidt for all her support. Sofia Zamfirescu is gratefully acknowledged for all her help and the work she has done. I was lucky to have such great students.

At this point, I would like to acknowledge Paul Sonnleitner for being the best tutor in physics in the whole world. Thank you, Paul, for being a true friend.

My beautiful sisters, I do not know what I would do without you girls. You mean the world to me. And, thanks to the best parents in the world, I am so lucky to call you mine. And then there is Coco, my little French prince charming, a Bichon Frisé that stumbled into my life and filled it with so much love.

This is dedicated to the love of my life, Peter Urbanek, to whom I owe absolutely everything.

Abstract

A stone consolidation treatment helps restore a degraded substrate's physical and mechanical properties. The treatment efficiency of newly engineered consolidants needs to be assessed on specimens in the laboratory before being applied on-site. Therefore, the substrate is prepared by inducing certain deterioration phenomena in them. Microcracks in the fabric are decay patterns that are frequently found on-site. They can be induced through thermal treatment as heat generates stresses in minerals as they undergo volumetric changes. Therefore, the focus of this study is on two topics, (i) thermal treatment of natural stones to artificially age the substrate, and (ii) the quality and compatibility of newly engineered stone consolidants. Four natural stones, from the European heritage, three carbonates and one silicate, as well as four newly consolidants were used in this study. The consolidants are made up of two nano-TiO₂ modified alkoxysilanes and two colloidal suspensions, nanosilica and nanozirconia.

Thermal treatment causes chemo-mineralogical and petro-physical changes. In-situ X-ray diffraction (XRD) and ζ -potential as determined from streaming current and streaming potential measurements were used to characterise the chemo-mineralogical changes on the surface of flat solid stones. Phase evolution with temperature was analysed using in-situ XRD, while modifications of ζ were used to investigate variations in materials surface and condition. Optical light and scanning electron microscopy, porometric data, ultrasonic pulse velocity and colour measurements were used to examine the physical changes.

Various test methods were used to determine the efficiency and compatibility of stone consolidants. This topic was further subdivided into three topics: (i) standardised or commonly used techniques to examine a treatment's performance, (ii) neutron imaging for evaluating laboratory ageing and treatment application with stone consolidants, and (iii) analysis of the distribution depth of stone consolidants applied on-site. The treatment efficiency was evaluated by scanning electron microscopy, mercury intrusion porosimetry, colour impact and their effect on dynamic modulus of elasticity, splitting tensile- and flexural strengths, capillary water absorption and water vapour permeability. Capillary water absorption and ultrasonic pulse velocity was used to cross-validate neutron imaging. Scanning electron microscopy and image analysis were used to determine the distribution depth, which was combined with an analytical model that is based on a one-dimensional version of Fick's second law. Drilling resistance measurements were also performed on-site, as well as Young's modulus and splitting tensile strength tests on laboratory-treated specimens.

The findings show that the onset and degree of thermal decomposition of dense and porous carbonates vary as shown by in-situ XRD. This work shows that nonequilibrium and time-dependent changes in ζ are associated with the reactivity of porous calcite surfaces. Specifically, in nonequilibrium ζ can be positive and negative and surface roughness influences ζ because it contributes to the dissolution. Thermal treatment changes ζ from negative to positive and when calcium hydroxide on calcite surfaces is present, calcium hydroxide governs ζ . To properly determine ζ when assessed by streaming potential, corrections are needed to account for the effect of pore conductivity. And, when ζ of mixed materials is analysed, their contribution to the overall determined ζ can be singled out.

The effectiveness and compatibility of newly engineered stone consolidants were determined by the textural and microstructural characteristics of the stone, such as the presence of

homogeneously distributed kaolinite that was preferentially penetrated. Furthermore, the kinetics of the gel-forming reaction took longer than expected, which explains why certain material properties change over time. This leads to falsified treatment evaluations. Furthermore, when the stone comes in contact with water during an incomplete polymerisation, water trapping, and pore-clogging are possible as shown by neutron imaging. Wide-ranging adsorption of water and anomalous water distributions and kinetics can result from the use of certain application techniques such as brushing and poultice. Finally, the distribution depth of cured consolidants on-site was successfully described by the analytical model and verified about image analysis. Additionally, drilling resistance performed on-site agreed with the depth distribution of cured consolidants as analysed by image analysis and the applied model. Because of this study, the consolidant could be better interpreted as a function of the sample's depth, which was always a gradient. The exponential decline from the stones' surface to its inner core was shown to be more pronounced for the nano-particle-based consolidants than for reactive alkoxy silane.

Many aspects of stone conservation research are still poorly understood, and extensive research in specific areas of this conservation action is needed. Overall, this thesis aided research in the area of analysis of distribution depths of consolidations applied on-site, evaluation of treatment performances of newly engineered consolidants, and the effects of treatment application and curing durations when (reactive) consolidants are applied. The thesis also showed how streaming potential techniques can be used to investigate the reactivity of natural stone surfaces in both pristine and thermally treated conditions.

Kurzfassung

Natürlich gealterte Baugesteine weisen ein entfestigtes Gefüge auf, weswegen oftmals Festigungsmaßnahmen zur Wiederherstellung der physikalischen und mechanischen Materialeigenschaften erforderlich sind. Neu entwickelte Steinfestiger müssen vor der Anwendung am Original im Labor auf ihre Wirksamkeit überprüft werden. Dafür ist zunächst eine künstliche Alterung der Laborprüfkörper notwendig, um gängige, im natürlichen Gesteinsgefüge beobachtbare Schadensphänomene nachzuahmen. Als besonders geeignet für die künstliche Alterung erwiesen sich thermisch induzierte Gefügeveränderungen, wobei Mikrorisse auf Grund thermischer Beanspruchungen entstehen.

Die vorliegende Arbeit beschäftigt sich mit zwei Themengebieten: (i) mit thermisch induzierten Gefügeveränderungen an Baugesteinen zum Zweck der künstlichen Alterung und (ii) mit der Wirksamkeit neu entwickelter Steinfestiger. Als Substrate dienten ein Quarzsandstein und drei karbonatische Baugesteine. Die Wirksamkeit von Steinfestigern wurde anhand von zwei Nano-TiO₂-modifizierten Alkoxysilanen sowie zwei kolloidalen Nano-SiO₂ und Nano-ZrO₂ Suspensionen evaluiert.

Thermisch induzierte Gefügeveränderungen können in chemo-mineralogische und petro-physikalische Veränderungen unterschieden werden. Die chemo-mineralogischen Veränderungen wurden an Gesteinsoberflächen mittels in-situ Hochtemperatur-Röntgendiffraktometrie (XRD) und dem ζ -Potential (sowohl durch Messungen des Strömungsstroms als auch des Strömungspotentials bestimmt) analysiert. Durch in-situ XRD konnten temperaturabhängige Phasenentwicklungen beobachtet werden, während unterschiedliche Materialzustände mit Hilfe des ζ -Potentials untersucht wurden. Physikalische Veränderungen wurden durch optische und Rasterelektronenmikroskopie, Quecksilberporosimetrie, Ultraschallgeschwindigkeiten und Farbmessungen bestimmt.

Im Themenbereich der Effizienz von Steinfestigern und deren Kompatibilität mit dem Substrat wurden drei Schwerpunkte gesetzt: (i) die Anwendung von etablierten und standardisierten Untersuchungsmethoden zur Bestimmung der Wirksamkeit von neu entwickelten Produkten, (ii) Neutronenbildgebungsverfahren zur Bewertung der künstlichen Alterung und der Applikationsmethoden sowie (iii) die Tiefenverteilung von vor Ort applizierten Festigern im Gesteinsgefüge.

Für die Bestimmung der Wirksamkeit von Steinfestigern wurden Rasterelektronenmikroskopie, Quecksilberporosimetrie, Farbmessungen, dynamisches Elastizitätsmodul, Spaltzug- und Biegefestigkeit, kapillare Wasseraufnahme und Wasserdampfdiffusion gemessen. Zusätzlich zum Neutronenbildgebungsverfahren wurden Wasseraufnahme und Ultraschallgeschwindigkeit an den gleichen Proben gemessen. Die Tiefenverteilung der Festiger wurde mittels Falschfarbenanalyse und mittels Rasterelektronenmikroskopie untersuchten Bohrkernen evaluiert. Um die Tiefenverteilung der Festiger besser zu verstehen, wurde ein analytisches Model, das auf einer Version des ein-dimensionalen Frick'schen zweiten Gesetzes beruht, angewandt. Darüber hinaus wurden Bohrwiderstandsmessungen vor Ort durchgeführt und Spaltzugfestigkeit und E-Modul an Laborprüfkörpern ermittelt.

Die mit Hilfe von in-situ XRD gemessene, temperaturabhängige Strukturumwandlung hat gezeigt, dass sich das Einsetzen und das Ausmaß des thermischen Zerfalls von dichten und porösen

Karbonaten unterscheidet. Zeitabhängige Modifikationen des ζ -Potentials stehen in Verbindung mit dem Nichtgleichgewicht und der Reaktivität von porösen kalzitischen Oberflächen. Demnach kann ζ sowohl positiv als auch negativ im Nichtgleichgewicht sein und die Oberflächenrauigkeit beeinflusst ζ durch das Dissoziieren des Materials. Durch die thermische Zersetzung ändert sich ζ von negativ zu positiv. Wenn Calciumhydroxid an der kalzitischen Oberfläche vorhanden ist, bestimmt es das ζ -Potential. Um das durch Messungen des Strömungspotentials ermittelte ζ korrekt zu interpretieren, muss der Effekt der Porenleitfähigkeit berücksichtigt werden. Im Falle von asymmetrischen Mikrokanälen kann der Beitrag von einzelnen Oberflächen zum gemittelten ζ bestimmt werden.

Im Bezug auf die Effizienz und Kompatibilität von Steinfestigern zeigten die Ergebnisse, dass die Wirksamkeit auch von der Mikrostruktur des Gesteinsgefüges abhängen kann. Dies konnte durch das Festigen von homogen im Gefüge verteilten Kaolinit gezeigt werden. Darüber hinaus ist das Abbinden zur endgültigen Gelbindung auch nach längerer Zeit nicht abgeschlossen, wodurch Materialkennwerten verfälscht werden. Wenn das Baugestein während einer nicht abgeschlossenen Gelbindung mit Wasser in Kontakt kommt, kann ein Porenverschluss zustande kommen oder Wasser im Gefüge eingeschlossen werden, wie mittels Neutronenbildgebung gezeigt wurde. Zudem wurde gezeigt, dass Applikationsmethoden, bei denen Pinsel und Zellulosekompressen benutzt werden, zu anomaler Wasserkinetik und -verteilung führen können.

Die Tiefenverteilung von Festigern im Gesteinsgefüge wurde mit Hilfe des analytischen Modells beschrieben und durch Bildanalysen verifiziert. Darüber hinaus stimmt die Tiefenverteilung auch mit dem vor Ort durchgeführten Bohrwiderstandsmessungen überein. Diese Evaluierungsstrategie ermöglichte eine verbesserte Interpretation der Tiefenverteilung von Festigern, die Gradienten zeigten. Es wurde dargestellt, dass der exponentielle Abfall bei kolloidalen Suspensionen stärker ausgeprägt ist als bei reaktiven Systemen (wie den Alkoxysilanen).

Obwohl viele Aspekte der Gesteinsfestigung noch weiterer Forschung bedürfen, konnte die vorliegende Arbeit in den Bereichen von Tiefenverteilung von vor Ort angewandten Festigern, der Wirksamkeit neu entwickelter Produkte sowie Unterschiede von Applikationsmethoden und Gelbindungsreaktionen das Forschungsfeld der Steinkonservierung ein Stück weit voranbringen. Die Arbeit zeigt auch, dass Strömungsstrom- und Strömungspotentialmessungen angewandt werden können, um die Reaktivität von Natursteinoberflächen in bruchfrischen und thermisch gealterten Zuständen zu analysieren.

Table of Contents

Acknowledgements	3
Abstract	5
Kurzfassung	7
Table of Contents	9
List of appended manuscripts	10
Related conference contributions	11
1. Introduction	12
1.1 Statement of the problem.....	12
1.2 The objective of the study	15
2. Materials and methods	18
2.1 Materials	18
2.1.1 Petrographic characterisation of the lithotypes.....	18
2.1.2 Calcination	19
2.1.3 Consolidants	20
2.2 Methods	21
2.2.1 ζ derived from Helmholtz-Smoluchowski using an asymmetric cell configuration .	22
2.2.2 Analytical, microscopic and physical techniques	31
2.2.3 Neutron imaging	35
2.2.4 An analytical model to evaluate the distribution depth of stone consolidants	37
3. Summary of the scientific articles	40
4. Conclusions and outlook	46
The scientific contribution of the work.....	46
Outlook on open research agenda	51
References	53
Curriculum vitae	61
Appendices	64

List of appended manuscripts

- A. **Ban, M.**, Luxbacher, T., Lützenkirchen, J., Viani, A., Bianchi, S., Hradil, K., Rohatsch, A. & Valter Castelvetro, V. (2021). Evolution of calcite surfaces upon thermal decomposition, characterized by electrokinetics, in-situ XRD, and SEM. *Colloids and Surfaces A: Physicochemical and Engineering Aspects*, 126761.
With corresponding Supporting Data

Credit Authorship Contribution Statement: M.B. and V.C. Conceptualization, M.B. Investigation, Methodology, Data curation, Formal analysis, Funding acquisition, Validation, Visualization, Writing - original draft, J.L. A.V. S.B. K.H. and V.C. Supervision, Resources, Writing - review & editing, A.R. Investigation (petrographic description), T.L. Validation, Formal analysis, Writing - review & editing, V.C. Funding acquisition, Project administration.

- B. **Ban, M.**, Mascha, E., Weber, J., Rohatsch, A., & Delgado Rodrigues, J. (2019). Efficiency and compatibility of selected alkoxy silanes on porous carbonate and silicate stones. *Materials*, 12(1), 156.

Credit Authorship Contribution Statement: M.B., E.M. and J.W. conceived and designed the experiments; M.B. performed and supervised the physical and mechanical experiments; E.M. performed the SEM- and A.R. the optical microscopy analysis; E.M. interpreted the raw data of SEM studies; M.B. and J.D.R. interpreted the raw data of physical and mechanical experiments; M.B. wrote the original draft; all authors reviewed and edited the paper and evaluated the final data; all authors approved the final manuscript.

- C. **Ban, M.**, De Kock, T., Ott, F., Barone, G., Rohatsch, A., & Raneri, S. (2019). Neutron radiography study of laboratory ageing and treatment applications with stone consolidants. *Nanomaterials*, 9(4), 635.
With corresponding Supporting Data

Credit Authorship Contribution Statement: M.B. and S.R. designed the experiments; A.R. performed the petrographic analysis of thin sections; S.R. carried out the treatments application and monitored the curing procedure; M.B., T.D.K. and S.R. performed the experiments at LLB under the supervision of F.O.; M.B. and S.R. pre- and post-processed the gained radiographs; T.D.K. obtained the calibration, analysed and plotted the post-processed data; M.B. performed the UPV and WAC measurements in the laboratory; M.B. performed the visualization of the obtained results and created the tables; M.B., T.D.K. and S.R. prepared the original draft; all authors reviewed and edited as well as agreed on the last version of the manuscript; G.B. and S.R. were responsible for proposal administration at the LLB facility.

- D. **Ban, M.**, Aliotta, L., Gigante, V., Mascha, E., Sola, A., & Lazzeri, A. (2020). Distribution depth of stone consolidants applied on-site: Analytical modelling with field and lab cross-validation. *Construction and Building Materials*, 259, 120394.
With corresponding Supporting Data

Credit Authorship Contribution Statement: Matea Ban: Conceptualization, Data curation, Formal analysis, Investigation, Methodology (in-situ testing, mechanical tests, analytical model), Validation, Visualization, Writing - original draft. Laura Aliotta: Conceptualization, Data curation, Formal analysis, Investigation, Methodology (analytical model), Validation, Writing - review & editing. Vito Gigante: Conceptualization, Data curation, Formal analysis, Investigation, Methodology (analytical model), Validation, Writing - review & editing. Elisabeth Mascha: Investigation, Methodology (microscopy), Writing - review & editing. Antonella Sola: Investigation, Methodology (image analysis), Writing - review & editing. Andrea Lazzeri: Conceptualization, Funding acquisition, Project administration, Supervision, Writing - review & editing.

Related conference contributions

- A.1 **Ban, M.**, Baragona, A., Ghaffari, E., Weber, J., & Rohatsch, A. (2016). Artificial aging techniques on various lithotypes for testing of stone consolidants. In: J.J. Hughes, T. Howind (Eds.), *Science and Art: A Future for Stone. Proceedings of the 13th International Congress on the Deterioration and Conservation of Stone*, the University of the West of Scotland, Paisley, 1: 253-260.

Credit Authorship Contribution Statement: M.B.: Conceptualization, Formal analysis, Investigation, Methodology, Visualization, Writing - original draft. A.B.: Conceptualization, Investigation, Methodology, Writing - review & editing. E.G.: Investigation, Methodology, Writing - review & editing. J.W.: Conceptualization, Funding acquisition, Project administration, Supervision, Writing - review & editing. A.R.: Funding acquisition, Supervision, Writing - review & editing.

- B.1 Mascha, E., **Ban, M.**, Weber, J., & Rohatsch, A. (2020). Silicates for the consolidation of stone: nano silica vs. ethyl silicate. In: S. Siegesmund, B. Middendorf (Eds.) *Monument Future: Decay and Conservation of Stone. Proceedings of the 14th International Congress on the Deterioration and Conservation of Stone*. Göttingen and Kassel, Mitteldeutscher Verlag GmbH, Halle (Saale), 525-531.

Please note that contribution B.1 is not published in open access.

Credit Authorship Contribution Statement: E.M.: Conceptualization, Formal analysis, Investigation, Methodology, Visualization, Writing - original draft. M.B.: Investigation, Methodology, Writing - review & editing. J.W.: Conceptualization, Funding acquisition, Project administration, Supervision, Writing - review & editing. A.R.: Funding acquisition, Supervision, Writing - review & editing.

- C.1 Raneri, S., De Kock, T., Rohatsch, A., & **Ban, M.** (2020). The potential of neutron imaging in stone conservation. In: S. Siegesmund, B. Middendorf (Eds.) *Monument Future: Decay and Conservation of Stone. Proceedings of the 14th International Congress on the Deterioration and Conservation of Stone*. Göttingen and Kassel, Mitteldeutscher Verlag GmbH, Halle (Saale), 1053-1059.

Please note that contribution C.1 is not published in open access.

Credit Authorship Contribution Statement: S.R.: Conceptualization, Formal analysis, Investigation, Methodology, Writing - original draft. T.D.K.: Formal analysis, Investigation, Methodology, Writing - review & editing. A.R.: Funding acquisition, Supervision. M.B.: Conceptualization, Formal analysis, Investigation, Methodology, Visualization, Writing - original draft.

- D.1 Mascha, E., Weber, J., & **Ban, M.** (2018). Forschung zu Nano-Materialien für die Gesteinsrestaurierung. Auswirkung von Festigungsmaßnahmen in Laborversuchen im Rahmen des EU-Projektes Nano-Cathedral. In: P. Gabriele et al. (Eds.) *Natursteinanierung Stuttgart 2018. Neue Natursteinrestaurierungsergebnisse und messtechnische Erfassungen sowie Sanierungsbeispiele*. Fraunhofer IRB Verlag, 75-88

Please note that contribution D.1 is written in German and is not published in open access.

Credit Authorship Contribution Statement: E.M.: Conceptualization, Formal analysis, Investigation, Methodology, Writing - original draft. J.W.: Conceptualization, Funding acquisition, Project administration, Supervision, Writing - review & editing. M.B.: Conceptualization, Formal analysis, Investigation, Methodology, Visualization, Writing - review & editing.

1. Introduction

1.1 Statement of the problem

Heritage building conservation is a common practise that has a global social and cultural influence. Heritage buildings are made of diverse materials but natural stone is the most important for historically valuable ones. Its decay patterns and consolidation treatment efficacy are primarily explained by standardised or commonly used laboratory test methods [1]. Current research mainly focused on the development of new products and methods for validating the effects of consolidants on treated stones. To test the efficiency and compatibility of newly engineered consolidants, a reproduction of key-deterioration patterns in the stone fabric needs to be conducted. Many artificial ageing techniques are limited, they contaminate the substrate or do not allow a repeatable and homogeneous introduction of decay patterns, all of which hinders a large-scale laboratory application and gaining of statistical values necessary for standardised natural stone testing. A large-scale laboratory application was required as this work was part of an industrially driven research, aiming at developing newly engineered nanomaterials for consolidation and protection of monumental stones, in the frame of the 'Nano-Cathedral' project funded by the European programme Horizon 2020 Call NMP21-AC (GA 646178) [2].

Multiple ageing techniques based on chemo-physical weathering, on the other hand, have the disadvantage of forming or precipitating salts as in the case of acidic attack or salt crystallisation [3,4]. The inability to completely remove these contaminants makes it difficult to study the treatment's sole effect. Furthermore, acid attack creates a deterioration profile as the acid can be neutralised when being absorbed by capillarity, making this ageing process unsuitable for standardised natural stone-testing purposes. Furthermore, salt crystallisation can result in surface spalling or localised damage, obstructing the inducement of homogeneously distributed decay patterns throughout the whole diameter of a testing body. Mechanical stresses, on the other hand, depending on the directions of the load applied and on weak zones in the stone fabric, will result in an inhomogeneous distribution of material fatigue [5]. It might be possible to simulate natural weathering conditions in a climatic chamber with simultaneous processes such as rain fall, thermal and freeze-thaw cycling, but this requires a long period for studying the degradation processes [6]. Furthermore, the number of cycles necessary to cause suitable microdamage over the entire diameter of the testing body is difficult, if not impossible to achieve for each lithotype as some varieties show premature flaking, missing parts or large cracks rendering them unsuitable for further testing [7,8]. Nonetheless, the aforementioned ageing techniques are important for in situ degradation processes and should be investigated further due to their ability to mimic natural stone decay patterns. However, naturally aged dimension stones and their surfaces differ in structure, texture and morphology by formed patinas [9], microbiological colonisation [10] or other interactions with their environment [11]. Such a coherent collection of decay patterns depends on the lithotype itself but also on different processes such as microclimate and the climatic region, local air pollution or age and direction of exposure, to name a few, making it difficult to simulate those same conditions in the laboratory. A thorough analysis (influence of organic and inorganic soiling and microstructural alterations) of a naturally aged stone is a more challenging task that will result in research focused on specific case studies. On a laboratory scale, the induced decay pattern must span the entire diameter of a testing body. Thermal treatment, for example, is promising in many ways, causing not only decohesion of grains by forming a network of microcracks but allows also a time-efficient, sustainable and economic technique to age stone specimens on

a larger scale. Thermal treatment proved to be the most successful method to artificially age stone substrates before consolidation as it reduces the stone soundness by introducing microcracks that are decreasing the mechanical strength of the stone and increase its ability to absorb liquids. Furthermore, this artificial ageing technique preserves the outer shape of the specimen, which allows an investigation with natural stone test methods where a statistical number of specimens are required.

Thermal treatment of stone and mineral materials is a widely researched phenomenon in many areas of research and application. It has been used to determine the effect of fire damage on civil and building structures [12,13], as well as in concrete technology [14], geotechnical engineering [15], ceramic firing [16], or studying the dynamics of the earth's interior [17]. It can be used to study the dating of ancient fires [18], the origin of materials [19], materials mix-design [20], to combat microbiological growth on stone surfaces [21], or as an artificial ageing technique before study conservation treatments in the built cultural heritage [22,23]. Physical changes of building stone (e.g. Young's modulus, flexural strength, porosity, etc.) caused by thermal treatment are well-studied phenomena [24-28], but chemo-mineralogical alterations (e.g. decomposition onset, chemical alterations, enhancement of surface reactivity, etc.) have received little attention, especially regarding transition temperatures and transformation extent and consequent influences on the stone's structural integrity. Stones with similar chemical and mineralogical compositions might differ from the point of genesis and therefore microstructure, which means that their resistance to thermal treatment is also likely to vary. Furthermore, stone as agglomerates of minerals, even though monomineralic, varies from single crystals in their susceptibility to thermal treatment [29]. Often temperatures as high as 600 °C are used in order to induce cracks into the fabric. For example, quartz undergoes a sudden volume change due to the α -to- β phase conversion at 573 °C and only then cracks are induced [30].

Fire-related damage is another reason why the topic of thermal treatment of natural stones seems also important. Specifically, throughout history, heritage structures constructed out of natural stone have suffered fire damage around the world [31]. Following recent events at Notre Dame de Paris, Glasgow School of Arts or the New York's Saint Sava Cathedral [32], the question of how to repair the damage on stone monuments caused by higher temperature remains unanswered. A recent study in Nature Materials [33] investigated challenges that a post-fire restoration poses with a focus on Notre Dame de Paris. The same study further suggested that the interiors stone condition implied maximal temperatures of 500 to 600 °C. Fire-related peak temperatures can vary in range and duration; however, 600 °C is a temperature high enough to reduce stone soundness and is, therefore, a widely studied peak temperature in many heat-related studies. Such temperatures are important for investigations of potential phase changes while higher temperatures have also relevance in industrial use and the understanding of planetary dynamics. Siegesmund [34] describes that for thermal expansion in building stone temperatures of up to 120 °C are relevant, however, elevated temperatures are still resulting in much higher residual strain and therefore more damage. He further notes that with temperatures below 500 °C the pore radii do not change significantly and except for very porous stone (>15 %), the higher the temperature, the higher the residual strain. Changes induced to the stone using thermal treatment are reproducible and systematically induced changes that can be tailored and investigated in real-time. While changes on the macroscopic level bring the desired effect of the reduction of soundness, chemo-mineralogical changes are lacking in research.

There are several different types of decay patterns in real life, and consolidation may range from a structural to a surface treatment. Consolidants are added to stone for them to react within the fabric and reinforced the material. They re-establish grain cohesion at the microscopic level, and

they restore the physical properties and mechanical strength of the building material at the macroscopic level. There are several different types of consolidants available on the market and several non-commercial materials are being developed. This can differ in chemical composition, formulation solvent or dispersing medium, as well as functions and properties, such as improved elastic response [35], water repellence [36], modification to fit particular substrates [37], or additional functional properties such as photocatalytic activity [38]. The chemical nature of consolidants ranges from organic materials, synthetic polymers, inorganic products to hybrids such as alkyl alkoxysilanes. Many consolidating materials have been developed and studied only in the academic environment [35-39]. Research on stone consolidants is crucial as different conditions require different consolidants and specific modes of application. However, the access of experts working on-site to these consolidants is limited as they cannot be found on the market. This represents a general shortcoming that deals with the transfer of results from basic to applied research. Moreover, it causes a larger drift between researcher and experts working on-site. An industrially driven project like 'Nano-Cathedral' aimed to develop a technology that has a high Technology Readiness Level, mostly between 5 and 7. This means, that the newly engineered products were also validated in relevant environments and disseminated to the broader public.

In a process ranging from materials development to scale-up and application onto monuments, many steps can be considered worth investigating and are still lacking in research. Thereby, a crucial step that is unavoidable is laboratory testing with standardised or widely accepted techniques commonly employed in the field of built cultural heritage research. Here the research needs to focus on aspects of efficiency and compatibility. As a stone consolidant is supposed to strengthen the substrate, its primary function will always be the restoration of the lost strength. This means that the decohesion between grains should be re-established by bridging those grains with an appropriate consolidant. As a result, any consequences of consolidation that might have a detrimental impact on the construction material should be avoided. Although the term compatibility has a wide range of applications and is often used in different ways, it refers to the letter, that is, the prevention of adverse side effects caused by a procedure. In this regard, many aspects are important. Validation of the penetration depth and final distribution of the consolidants after curing is one such factor. For such purposes, many techniques have been used like optical- and scanning electron microscopy [40], x-ray radiography and tomography [41], vibrational spectroscopic techniques [42,43] or advanced techniques using neutron and synchrotron sources [44,45]. The effect of the treatment method on the consolidant's strengthening effect is also an important topic [50,51]. The above refers not only to the method of application or the number of repetition periods but also to the treatment's effectiveness. It was recently demonstrated that for a low concentration nano-lime to be successful in terms of mechanical strength gain, a minimal number of application cycles are needed [52]. Furthermore, after curing, consolidants have different solid contents, which contribute to differences in their effectiveness or ability to increase mechanical strength when applied to the same substrate [53]. Such an outcome does not imply that a consolidant that has the lowest strength increase is not suitable and should be disregarded. It merely highlights how complex and multifaceted this area of study is because a consolidant should ideally be tailored for the decay pattern it is intended to remedy. As decay patterns reach varying sizes and depths as well as microstructures, it seems difficult, if not impossible, to determine which is the ideal product for all cases. It is almost intuitive and safe to state that there is no such thing. In the field of architectural preservation, it often seems that the scientific community has expectations to solve every possible aspect before a product gets applied to an original monumental surface. This might be the reason why research in this area focuses on many standardised tests that aim to explain varying aspects by using numerous macroscopic and microscopic techniques. The methods used to describe the effects of product application include the analysis

of mechanical properties (e.g. compression-, splitting-, tensile-, pull-off- and shear strength, drilling resistance, Young's modulus) and of the compatibility with the stone (e.g. water vapour permeability, water absorption coefficient, drying behaviour or mercury intrusion porosimetry). Visual and chemo-mineralogical aspects of the stone in different conditions are normally analysed through XRD, Fourier-Transform Infrared Spectroscopy (FTIR), simultaneous thermal analysis (TG-DSC) and colour measurements. The use of so many techniques leads to a quite descriptive character of the gained data. Basic research in the area of conservation science for stone materials is scarce. While several studies have been conducted on the macroscopic interactions of water with stones, understanding the processes at the molecular level at the solid-liquid interface, that is, the reactive mechanism of a porous stone in its setting, is still a challenge. Another issue that has yet to be addressed is the translation of laboratory-based results into treatment application on-site. A direct translation is not possible as many obstacles and limitation are present. These limitations include but are not limited to the non-uniform conservation state of the surfaces, application procedures, the limited number of readings used to evaluate the performance of a treatment on-site, common protocols to prepare and test the substrate before application, and many more. The above-mentioned topics are just indications of what topics are understudied in the field of architectural preservation. It seems that tackling certain research questions is the only way to obtain more of the overall picture on the topic of treatment performance.

This study aimed to investigate (i) the effect of thermal treatment on natural stones for purposes of artificial ageing and, (ii) the efficiency and compatibility of newly engineered stone consolidants.

Regarding thermal treatment, this work looked for answers concerning chemo-mineralogical and physical transformations of calcite surfaces that occurred when the building stone encountered a cycling isothermal treatment at 600 °C. More specifically, the onset of thermal decomposition and extension of phase transformation of solid macroscopic calcites was analysed. Moreover, the reactivity and time-dependent changes of these surfaces when they came in contact with aqueous electrolytes in comparison to pristine or sound stones were determined.

As regards the efficiency and compatibility of stone consolidants the present work was subdivided into three topics. The first topic concerned the use of standardised or widely accepted techniques to evaluate a treatment's performance on laboratory specimens. It aimed to identify if the different consolidants fulfil their intended purpose. The second topic aimed to investigate the water movement and water distribution through artificially aged and consolidated stones. Here the focus was placed on thermal treatment and different application techniques on laboratory specimens and their influence on the water movement inside the fabric. And finally, the third topic aimed to evaluate the depth distribution of stone consolidants applied and cured on-site. Differences of certain consolidants applied on original surfaces were investigated.

1.2 The objective of the study

The objective of the first part of the study is on artificial ageing of stones, as a key part of a larger research on the effectiveness of stone consolidants, was to exploit the potential of ζ -potential measurements to better understand the effects of artificial ageing, or thermal treatment, on the surface properties of the stone. This allowed bridging the gap between largely descriptive approaches of material testing and analysis (all macro and micro parameters linked to consolidation, by various means) to basic research and establish the role of the ζ -potential in the field of conservation science for monumental stone. As a natural product, stone can be an agglomerate of one or different minerals and vary in origin and formation process and thus in chemo-mineralogy

and its petrophysical properties. The interaction of stone and water is of particular interest for the built cultural heritage. The formation of various decay patterns can be directly related to the action of water. On the other hand, the presence of water is inevitable in the field of the built cultural heritage. Restoration steps like cleaning, desalination or consolidation depend entirely on the presence of water. Some consolidants need the presence of water to react and others are water-based suspensions. This is why a deeper understanding of the interaction between stone and water is of utmost importance. For this purpose, the assessment of the surface properties of the stone when in contact with water through ζ -potential measurements was particularly useful. This electrokinetic property is related to the charge of a solid surface when in contact with an aqueous electrolyte solution and it was evaluated using streaming current and streaming potential measurements. Therefore, changes of the ζ -potential when the stone material and the surrounding aqueous solution changed were exploited. As ζ -potential measurements are extremely sensitive to surface changes, they provided additional and new insights on the modifications induced by the thermal treatment as compared to the pristine stone. To extend the understanding of the ζ -potential analysis and the influence the chemically and physically modified stone surfaces have on it, further characterisations using scanning electron microscopy (SEM) and environmental X-ray diffraction (in-situ XRD) were also done. These auxiliary techniques served to determine chemo-mineralogical changes (as analysed by in-situ XRD) and physical changes like the inducement of microcracks (as analysed by SEM). Supportive techniques to assess further physical alterations of the surfaces included the use of colour change and porometric data.

To study newly engineered stone consolidants one has to know the substrate that needs to be consolidated. For such purposes, a better understanding of the macro- and microscopic properties describing the loss of cohesion between the stone grains and the restoration of the mechanical strength upon application of a consolidant is required. A better understanding of the potential damages following the chemical and physical changes occurring after the consolidation is also crucial. Therefore, the objective was to examine the stones in their pristine, artificially aged (thermally treated) and consolidated condition by various macroscopic and microstructural techniques. The methods used to describe the effects of ageing and product application included the analysis of mechanical properties, the compatibility with the stone, and the interaction with water. Visual aspects of the stone in different conditions were analysed through colour measurements. Such a procedure represented a more or less standardised but necessary approach to analyse the efficiency of new consolidants. In this frame, the efficiency corresponded to the mechanical strength gain. Therefore, standardised tests like flexural- or splitting tensile strength were used because the stone is known to have low tensile or bending strength. Furthermore, water-related tests like water vapour permeability or water absorption helped examine if negative consequences arising due to a treatment application. These harmful effects included the analysis of pore-clogging or hindrance of water diffusion through the stone fabric, among others. Within these tests, a first stepping stone was set to determine the usefulness of a certain treatment.

A stone substrate can have different conservation states, different amounts of consolidants with different application techniques can be applied and therefore, the outcome of the treatment might fluctuate. Such a complex system is not easily understood and only certain aspects can be studied one at a time. Analysis surrounding the water movement inside a stone structure gave first insights into such processes. The objective was to analyse differences in substrates (pristine and artificially aged), application techniques (brushing, poultice, capillary suction) and hence amounts of different consolidants applied (different amounts of nano-silica and tetraethyl-orthosilicates). Neutron imaging was the only technique that allowed time-resolved monitoring of water absorption through laboratory specimens that are in different states and consolidated with different

consolidants using different treatment application techniques. Therethrough, an advancement in the understanding of differences between substrates, consolidants applied and application amount and techniques used were investigated.

Changes induced to the stone using thermal treatment and consolidation are reproducible changes that can be investigated in real-time. On the opposite, changes caused by natural weathering over extended periods are difficult to be investigated. A thorough analysis of a naturally aged stone is a more challenging task, which is why only one part of this thesis dealt with applications on naturally weathered surfaces. Using the façade of Vienna's St. Stephen's cathedral, three consolidants have been applied. The preparation of the surfaces and the application treatment was done according to traditional routines normally followed by the experts on-site. The objective of this work was to model and evaluate the distribution depths of three consolidants applied and cured on-site. This was important as the deposition of cured consolidants inside a stone determines the performance of treatment. Moreover, knowing the assets of consolidants might allow tailoring the application towards specific decay patterns.

2. Materials and methods

2.1 Materials

2.1.1 Petrographic characterisation of the lithotypes

The studied lithotypes are representative of European heritage and are still actively quarried for purposes of restoration and reconstruction work [46,47]. The abundance of the main mineralogical components analysed by XRD is listed in **Table 2.1**, while **Table 2.2** exhibits the chemical analysis of the studied lithotypes assessed using XRF.

Table 2.1: Mineralogical composition as examined by XRD for the stones Apuan Marble (AM), Lumauela de Ajarte (LdA), St. Margarethen (SM) and Schlaitdorf (SQ).

Stone	Cal	Dol	Qtz	Kao	Phy	Goeth	KFSP	Pl
AM	***	*	*		tr			
LdA	***		*					
SM	***		tr			tr		
SQ		*	***	**	*		tr	tr

Cal=calcite; Dol=dolomite; Qtz=quartz; Kao=kaolinite; Phy=phyllosilicates; Goeth= Goethite; KFSP=potash feldspar; Pl=plagioclase: tr=trace; *=scarce; **=abundant; ***=very abundant

Table 2.2: Chemical compositions reported in elemental concentration (%) as determined through XRF for the stones Apuan Marble (AM), Lumauela de Ajarte (LdA), St. Margarethen (SM) and Schlaitdorf (SQ).

Stone	O	Ca	Si	Al	Mg	K	Fe	Traces*
AM	50.3	48.4	0.14	0.05	0.82	0.04	0.02	<0.04
LdA	51.21	45.44	1.37	0.75	0.48	0.34	0.20	<0.22
SM	51.38	47.41	0.14	0.13	0.44	0.03	0.23	<0.25
SQ	53.97	0.11	42.41	2.79	0.09	0.36	0.13	<0.14

*Trace elements Ti, Mn, Zr, S, P.

Figure 2.1a shows an overview of the fabric of one of the most renowned white marbles, the Apuan Marble, quarried from the Apuan Alps in northern Tuscany Italy. This fine-grained metamorphic rock consists mainly of calcite and traces of dolomite and quartz and is also known under the name Carrara Marble. Its granulometry is equi- to in equigranular and the grain contacts are polygonal to interlobate with an approx. size of 0.2 mm. Apuan Marble is dense, which is why its Hg-porosity amounts to approx. 0.7 %.

Ajrate Trevino in Spain is the home of a poorly washed biomicrite to microsparite. This biogeneous sedimentary stone appears creamy greyish. **Figure 2.1b** shows the carbonate matrix that consists of recrystallised fossils and shell fragments, but the stone microstructure makes it difficult to distinguish between components and the binder matrix. Furthermore, this stone is not textured and has a high number of intercrystallite pores and generally pores filled with calcite sparite crystals. The porosity of the calcite variety of Ajarte is approx. 23 %.

The biogeneous sedimentary stone St. Margarethen is a biosparite, calcareous arenite that is quarried from the Leitha Mountains on the border between lower Austria and Burgenland. The colour of this detritic limestone ranges from yellow-brownish to light grey. **Figure 2.1c** displays a fabric that is composed of fossils like small fragments of coralline red algae, foraminifera, serpulides, ostracods and echinoderms, some of which can reach a size of up to a few centimetres. The grain contacts of this fossil-rich clastic arenite are cemented with fine-grained calcite, a

sparitic cement. SM is a pure calcium carbonate stone with traces of quartz and its Hg-porosity is approx. 22 %.

The coarse-grained sandstone named Schlaitdorf is located in Württemberg Germany and is light to reddish in colour. Its detrital fraction consists of quartz, feldspar, other rock fragments and cement that consists of coarse spar dolomite and microcrystalline silica binder with smaller amounts of kaolinite and illite materials (see **Figure 2.1d**). The cement is homogeneously distributed in the fabric. This lithotype can be classified as well-sorted, not layered and with a homogeneous texture. The average grain size is about 0.5 mm and reaches a size of up to 1 mm while the grain shape is subhedral to anhedral. Schlaitdorf's main accessory minerals are apatite, tourmaline, zirconia and opaque minerals with less than 1 % occurrence [48]. The open porosity of the stone, measured by Hg-intrusion is 16 %.

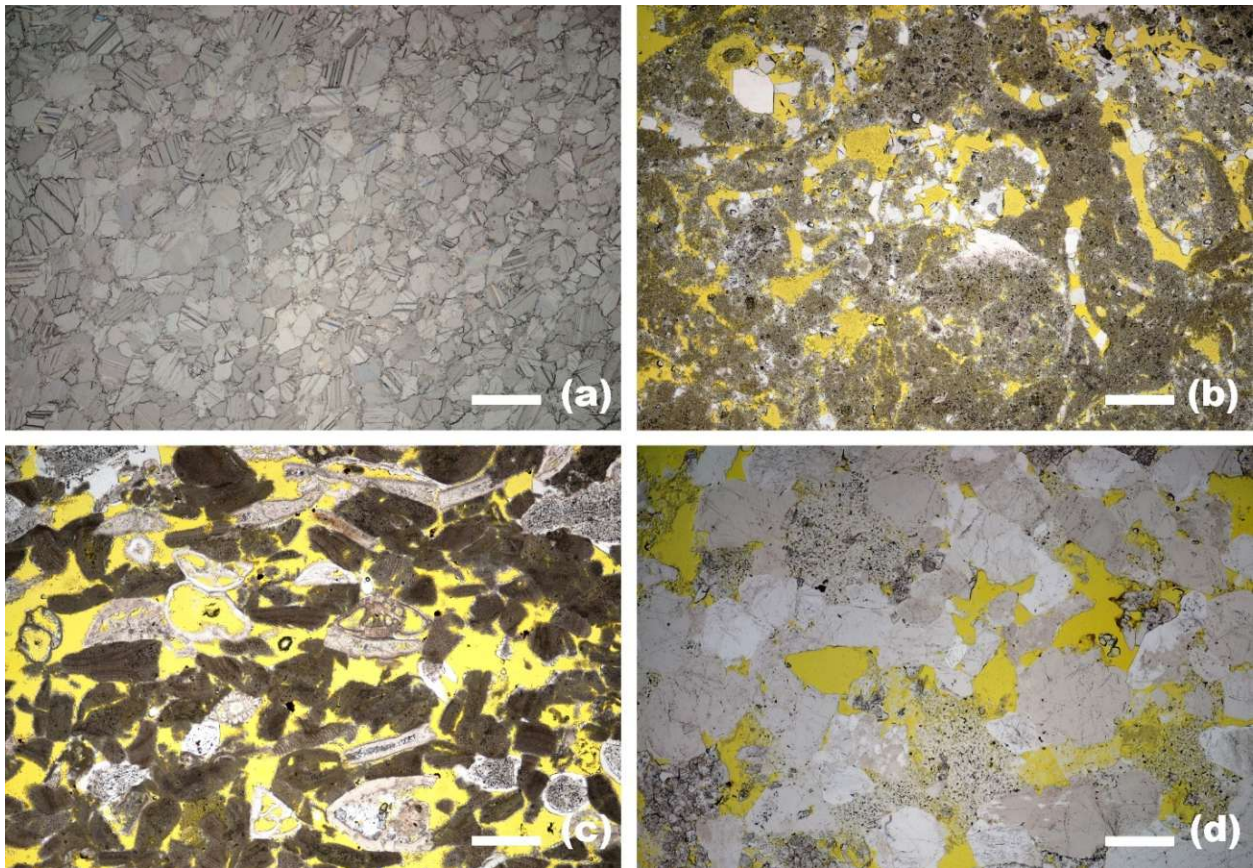


Figure 2.1: Micrographs of the study lithotypes as examined by optical light microscopy: **a)** Apuan Marble, **b)** Lumaquela de Ajarte, **c)** St. Margarethen and, **d)** Schlaitdorf. The yellow resin displays the porosity of the building stones. The scale bar is 500 μm .

2.1.2 Calcination

The quarried stone specimen with dimensions set according to the standardised tests (max. 50 mm in diameter) has been exposed to three thermal cycles at a static peak temperature of 600°C. Therefore, a Thermo Scientific Heraeus K 114 electrically heated furnace with 3.5 L internal volume was used. The heating rate was set to 40 °C min⁻¹ until isothermal conditions were met and subsequently kept for one hour at 600°C. Following a cooling phase to approx. 35 °C with an opened front door to overcome differential stresses caused by rapid cooling, this procedure was repeated three times overall. The residence time was established by experimental pre-screenings for all studied lithotypes [49]. The chosen time showed sufficient strength of the fabrics to

overcome thermal gradients and thus the complete breakdown of the specimens by the formation of larger cracks. Moreover, three cycles displayed the highest threshold for reduction of soundness examined in terms of physical changes using sound speed propagation and water absorption. Even though the stagnation of the reduction of soundness for all lithotypes was not comparable to the same degree, the goal was to reduce the soundness of the fabric to the lowermost degree and study the chemo-mineralogical changes at this transition temperature. However, residence time deviates from the shape of the specimen used and the volume of the oven. This needs to be adapted accordingly to achieve the same degradation effect as in this present study.

2.1.3 Consolidants

Four experimental consolidants, either modified with nanomaterials or consisting of the same and one commercial consolidants were studied (see **Table 2.3**). The newly engineered consolidants are (1) TiO₂ nanoparticles stabilised in tetraethyl-orthosilicate (TEOS) in isopropanol, (2) TiO₂ suspension of alkyl alkoxysilanes and TEOS in isopropanol, (3) a silica suspension in water/ethanol mixed solvent and, (4) a zirconia suspension in water. One commercial consolidants were also used, that is, KSE 300 (Remmers, Germany), a formulation based on TEOS, used as a reference product as a comparison to the TEOS-based consolidants that contain nano TiO₂.

Table 2.3: Characteristics of the studied stone consolidants.

Project labelling	Commercial name (producer, country)	Materials chemistry	Nanoparticles dimension (nm)	Concentration in wt.% (*)
NC-25C	HFES 70 (ChemSpec, IT)	Nano-TiO ₂ (1%) mod. TEOS in Isopropanol	10–20 TiO ₂	43 ± 2
NC-27CP	HFES 90 (ChemSpec, IT)	Nano TiO ₂ (1%) mod. alkyl-trialkoxysilane in Isopropanol	10–20 TiO ₂	59 ± 1
NC-12C	ZG12 (Colorobbia, IT)	SiO ₂ in water/ethanol	~70	20 ± 3
NC-29C	ZR110 (Tecnan, ES)	ZrO ₂ in Water	~119	10 ± 1
Reference	KSE 300 (Remmers, DE)	solvent-free TEOS	n/a	30 ± 1

(*) The solid content after curing was calculated as the difference between the applied weight of consolidants and the residue weight after curing, assessed approx. 2 months after application.

Nanoparticle-based or -modified consolidants are emerging increasingly, as evidenced by recent publishing activities in the field of built cultural heritage. The nanotitania was added to TEOS because of its potential self-cleaning ability and because it have advantageous properties as regards cracking of the cured silica gel (reduced shrinkage of the consolidating gel). Furthermore, nano-TiO₂ has been the subject of several laboratory studies, however, such products are not yet available on the market in large quantities. Nano-silica and nanozirconia suspensions can be tailored in terms of concentration, dimensions, dispersity or, use of solvent, among other properties, all of which determine a treatment performance. While silica sols are commonly used in the field of built heritage and construction sector in general, nanozirconia is used in ceramics- or dentistry research [50] but not in the field of architectural preservation. As nanoparticles can be engineered to have different properties, their exploration in terms of efficiency and compatibility for various decay patterns was the primary goal of their development. Both inorganic particles have good mechanical properties, stability and durability. Furthermore, as the particles are nanometric and possess a high surface area, they are expected to adhere better to the substrates. An

additional advantage of the nanobased consolidants is that the strengthening capacity is achieved as soon as the consolidants dry.

The first product, NC-25C, is a TEOS in isopropanol with 70% active modified with 1% TiO₂ particles. The spherically shaped TiO₂ particles consist of approx. 80% anatase and 20% rutile. Their mean size amounts to 10 to 20 nm. The consolidant has a low viscosity of 3.3 cP and a specific weight of ~1 g/cm³, determined at 25°C. Similarly, NC-27CP is alkyl-trialkoxysilane in isopropanol with 75 % active content containing also 1% TiO₂ particles (same properties of titania as within NC-25C). This product has a higher elasticity due to its modification with organic groups (i.e. Si-O-(CH₂)_n-O-Si) and it should have better adhesion to carbonate substrates. Besides the self-cleaning properties, NC-27CP is consolidant that is hydrophobic. For both products, the reaction time to obtain the silica gel amounts to four weeks and a temperature of ~20 °C with a relative humidity of 45 ± 5%. NC-25C and NC-27CP was developed by the Italian industry Chem Spec S.r.l. while the supplier of the nanoparticle is the Spanish based industry Tecnan (Technologia Navarra de Nanoproductos, S.L., Los Arcos (Navarra) Spain).

NC-12C is a silicon dioxide nanoparticle consolidant in suspension in a neutral water-ethanol mixture (1:1 by volume). The consolidant is a milky liquid with low viscosity and the active ingredient is the suspended silica nanoparticle that makeup 20 ± 3 wt.%. The mean size of the silica is 70 ± 30 nm, as determined using dynamic light scattering, with a polydispersity index of up to 0.6. The density amounts to 1 g/mL and the viscosity to 2 cP (both determined at 25 °C). This product was developed by the Italian based industry Colorobbia S.p.A. (Sovigliana-Vinci (Firenze) Italy).

The water-based nanozirconia suspension, known under the name NC-29C, was developed by the Spanish based industry Tecnan (Technologia Navarra de Nanoproductos, S.L., Los Arcos) in Navarra, Spain. The particle dimension amounts to approx. 120 nm and the zirconia content ranges from 10 to 15 wt.%, which makes the product appear white. The pH of the consolidant is 6, and its density is 1.09 g/mL and the viscosity amount to 7 cP.

The reference product used is known under the name of KSE 300 and it was developed by Remmers, Germany. KSE 300 is a solvent-free TEOS with a gel deposition rate of ~30 % and is frequently used in the field of stone consolidation (e.g. [51]).

2.2 Methods

This section deals with the methods used to evaluate the effects of thermal treatment and the efficiency and compatibility of stone consolidants. A deeper overview will be given on techniques that are not commonly employed in the field of built cultural heritage or are not standardised. Generally, the techniques used can be divided into four major subsections, that is, (i) electrokinetics, (ii) analytical, microscopic and physical tests, (iii) neutron imaging and, (iv) analytical modelling. These subsections are divided according to the manuscripts published. As it is redundant in original articles to cover the theory and a detailed description of the methods, these subsections will be either an addition to the already described procedures or a short repetition of the same to give an overview of the used techniques.

The first subsection focuses on the use of electrokinetics as this is not commonly employed in the characterisation of built materials. In *Manuscript A* two microchannels have been used to assess the reactivity of stone surfaces in their pristine and thermally treated conditions by using the

electrokinetic potential. Therefore, the focus of this subsection lies in a short introduction of ζ and how it is derived from the Helmholtz-Smoluchowski (HS) approach when using an asymmetric cell configuration. Moreover, this subsection also covers corrections of various effects when measuring streaming current and streaming potential measurements.

The second subsection covers all used analytical, microscopic and physical techniques used throughout the published work. The methods described here have been used in the frame of all published manuscripts and conference contributions, either as main evaluation or characterisation tools or, to cross-validate advanced characterisation techniques like neutron imaging.

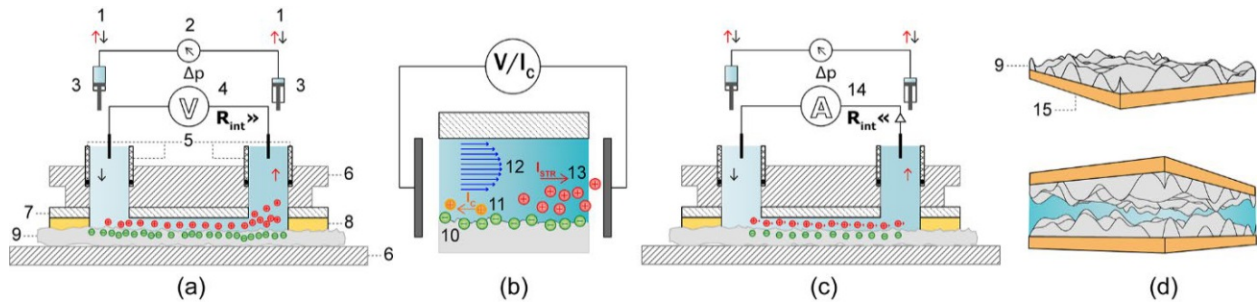
The third subsection gives a short overview of neutron imaging, which is backed up with *Manuscript C* and related *Conference Contribution C1*.

Lastly, the analytical model used in *Manuscript D* to evaluate the distribution depth of stone consolidants will be briefly presented.

2.2.1 ζ derived from Helmholtz-Smoluchowski using an asymmetric cell configuration

The spontaneous development of the surface charge results when a solid comes into contact with an aqueous electrolyte. The surface groups of the solid either react and/or adsorb water ions and ionic species in the solution (e.g. adsorption of counterions, preferential dissolution or adsorption of lattice ions, ionisation of functional groups, etc.). This also occurs on carbonates, where lattice ions adsorb on the carbonate surfaces and are responsible for the partial neutralisation of their intrinsic surface charges. This first layer that adsorbs contains ions tightly bound to the surface; therefore, it is an immobile layer called the Stern layer. The ions that neutralise the residual excess surface charge beyond the Stern layer is mobile. The mobile ions belong to the diffuse layer. The combination of these two layers (the Stern and the diffuse layer) is known under the term electrical double layer (EDL). Further subdivisions of the Stern layer, for example, in the case of calcite [52,53], have also been proposed and concern the interfacial water structure. The electrokinetic potential, i.e. ζ -potential, is an experimentally accessible physical parameter that allows characterisation of the electrokinetic charge. ζ is interpreted as the potential at the slipping plane, or shear plane, located somewhere near the diffuse layer plane (i.e. the outer Helmholtz plane). However, the exact location of the slip- or shear plane is the subject of ongoing research, especially when considering rough and reactive surfaces. By moving the electrolyte in a microchannel over the surface under study, the excess charge of the diffuse layer will be dragged along, increasing the streaming current. Both streaming current and streaming potential can be measured using different microchannels or cell configurations (**Scheme 2.1**). In the case of porous surfaces like a natural carbonate stone, the recorded streaming potential is affected by the presence of additional pathways for the conduction current through the porous carbonate. If present, pore conductance leads to an underestimation of real ζ , which represents a drawback for streaming potential measurement (see **Scheme 2.1 b**) on such materials. To solve the problem the interrelated streaming current should also be measured to validate the results. The ζ -potential corresponds to the charge at the material solution interface and as such, it depends upon both, the surface chemistry of the solid and the surrounding electrolyte. The condition of a solution includes various pH, the concentration of potential determining ions, temperature, ionic strength, etc., to name a few variations.

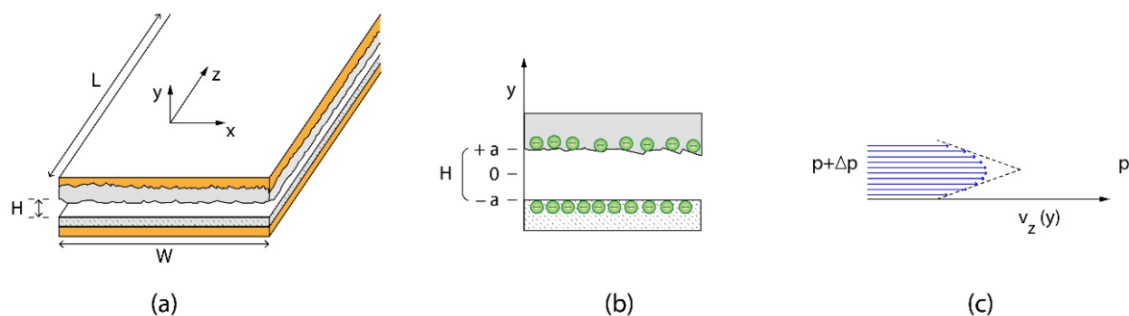
For more details on the theoretical basis of ζ -potential and EDL theory, readers are referred to reviews [54-56] and reference textbooks [57-63]. Electrokinetics and the EDL theory are going beyond materials science applications and frequently employ advanced characterisation techniques and mathematical models [64-66].



Scheme 2.1: Schematics of the clamping cell for ζ analysis of flat macroscopic surfaces and the generation of **a)** streaming potential with a high resistance path, **b)** streaming potential at equilibrium between streaming current and conduction current, **c)** streaming current with a low resistance path, and **d)** the adjustable gap cell configuration. The dimensions are not to scale.

1. Inlet/outlet; 2. differential pressure transducers; 3. syringes for electrolyte transport; 4. voltmeter; 5. electrodes; 6. sample holder; 7. polypropylene reference material; 8. spacer (ethylene propylene diene rubber); 9. calcium carbonate sample; 10. surface charge; 11. back- or conduction current of the counter charge; 12. tangential electrolyte flow; 13. the streaming current of counter charge (direction of liquid flow); 14. ampere metre; and 15. double-sided adhesive tape fixed to the carbonate specimens.

After the short paragraph concerning the theory of ζ , the following text deals with the theoretical analysis of a microchannel that consists of two materials whose net surface charge contributes to the overall ζ (**Scheme 2.2 a**). This is important because in *Manuscript A* two cells, an asymmetric- (i.e. clamping cell) and symmetric (i.e. adjustable gap cell) cell configuration have been used to analyse ζ of natural carbonates in different conditions (see **Scheme 2.1**). The theoretical analysis of ζ derived from HS when using an asymmetric cell configuration is based on the seminal work of Walker et al. [67], who was the first to treat this issue. The authors used polymethyl methacrylate (PMMA), glass, modified glass and polymeric membranes. In their study, PMMA was used as a reference surface for calibrating the asymmetric cell (to determine the fractional contribution of the reference material to the overall measured ζ). In this case, polypropylene (PP) is used as the reference material and Apuan Marble (AM) is the tested surface.



Scheme 2.2: Schematics of the adjustable gap cell for ζ analysis of flat macroscopic surfaces. **a)** A parallel plate microchannel for streaming current and potential measurements where materials can be analysed in a symmetric or asymmetric configuration. **b)** A drawing of the yz plane of a parallel plate microchannel with charged walls of a height $2 \cdot a = h$ where the coordinate y equals zero in the centre of the microchannel. **c)** An illustration showing the fluid flow in the z direction because of a pressure drop Δp over the length of the microchannel L . The velocity profile near the channel walls can be simplified to a linear form. The dimensions are not to scale.

When an electrolyte streams through a microchannel a streaming current arises because the flow carries the ions. This DC is detected at the electrode interface at the outlet of the channel ends. If the flow is laminar, ζ can be calculated after HS, which relates the electrokinetic phenomena of streaming current and/or streaming potential to ζ :

$$\zeta(I_{Str}) = \frac{dI_{Str}}{d\Delta p} \frac{\eta}{\varepsilon_0 \varepsilon_r} \frac{L}{A}; \quad (1)$$

where $\zeta(I_{Str})$ is the ζ -potential derived from streaming current experiments, $(dI_{Str}/d\Delta p)$ is the detected streaming current coupling coefficient obtained from the slope of the streaming current [A] to pressure difference ramp [Pa], (η) is the dynamic viscosity of the electrolyte [Pa s] and $(\varepsilon_r \varepsilon_0)$ the dielectric constant of the electrolyte solution and the permittivity in vacuum [F m⁻¹]. Experimentally, it can be shown that I_{Str} is approximately proportional to Δp ; the streaming current coupling coefficient $dI_{Str}/d\Delta p$ can therefore be assumed to be constant for a specific setup. For laminar conditions in a rectangular channel, where the side walls are neglected and thus an infinitely wide channel is present, the electrolyte velocity profile is given through the Hagen-Poiseuille law:

$$v_z = \frac{\Delta p a^2}{2\eta L} \left(1 - \frac{y^2}{a^2}\right). \quad (2)$$

The pressure gradient (Δp) is applied across the microchannel length (L) where (a) is defined as half the channel height (H) ($a = H/2$) or ($H = 2 \cdot a$) respectively. A further definition includes that the transverse coordinate (y) equals zero in the centre of the microchannel (**Scheme 2.2 b**). **Eq. 2.** provides the fluid velocity profile (v_z) [m s⁻¹] on each point of the cross-section of the channel. Integrating over the entire cross-section ($A = W \cdot H$) [m²], the volumetric flow rate (\dot{V}) [m³ s⁻¹] is obtained as follows:

$$\dot{V} = \int_A v_z dA = \int_0^W dx \int_{-a}^{+a} dy v_z(y) = W \int_{-a}^{+a} dy v_z(y). \quad (3)$$

In **Eq. 3**, it becomes evident that the function depends only on (y). For a sufficiently wide microchannel ($W \gg H$) and by neglecting boundary effects, v_z is independent of the x -coordinate. Therefore, the integral over dx yields just the factor W .

Furthermore, along the (z)-axis, which is the fluid flow direction, the influences of the inlet/outlet are neglected, and the fluid velocity profile does not change. Inserting **Eq. 2** in **Eq. 3** and rearranging the following is obtained:

$$\dot{V} = \frac{W\Delta p a^2}{2\eta L} \int_{-a}^{+a} \left(1 - \frac{y^2}{a^2}\right) dy = \frac{2}{3} \frac{W a^3}{\eta L} \Delta p = \left| a = \frac{H}{2} \right| = \frac{1}{12} \frac{WH^3}{\eta L} \Delta p. \quad (4)$$

Eq. 4 is identical to the general Hagen-Poiseuille relation for a rectangular cross-section [68]:

$$\dot{V} = \frac{dV}{dt} = \frac{H^3 W}{12\eta L} \Delta p [1 - 0.630 HW^{-1}] \approx \frac{1}{12} \frac{H^3 W}{\eta L} \Delta p \text{ if } H \ll W. \quad (5)$$

Rearranging **Eq. 4** and solving for the gap height the following is obtained:

$$H = \left(12\eta \frac{L \dot{V}}{W \Delta p} \right)^{1/3}. \quad (6)$$

Eq. 6 can be used to calculate the channel height. Since laminar flow conditions have been assumed in **Eq. 2**, the volume flow rate is constant for a specific experimental setup. However, **Eq. 6** does not describe the velocity profile at each point in the cross-section like **Eq. 2**, which is necessary for further simplification to solve the HS approach for an asymmetric cell configuration. Specifically, the velocity profile near the channel walls can be simplified to a linear form (**Scheme 2.2 c**):

$$v_z \approx \frac{\Delta p a^2}{\eta L} \left(1 - \frac{|y|}{a} \right). \quad (7)$$

The latter approximation becomes relevant when the streaming current is determined. Subsequently, a physical quantity is considered, that is, the streaming current (I_{Str}), which occurs toward the flow and causes a streaming potential (U_{Str}), which in turn induces a parasite current flowing in the opposite direction, the conduction current (I_{Con}). Therefore, the streaming current and conduction current balance each other under steady-state conditions yielding:

$$(I_{Str}) + (I_{Con}) = 0. \quad (8)$$

As the charge density is not constant when moving along the (y)-axis, the streaming current in the channel is given through the following expression, already identified in **Eq. 3** and modified to obtain the following:

$$I_{Str} = W \int_{-a}^{+a} v_z(y) \rho(y) dy; \quad (9)$$

where (ρ) is the charge density of the electrolyte solution. As already specified above, for a sufficiently wide microchannel, the charge density of the sidewalls of the microchannel is neglected so that the charge density follows a one-dimensional Poisson-Boltzmann equation:

$$\frac{d^2\psi}{dy^2} = -\frac{\rho(y)}{\varepsilon_o \varepsilon_r}; \quad (10)$$

where (ψ) represents the electrical potential of the system. To find a solution between the two planer channel walls, the boundary conditions for **Eq. 10** are:

$$\begin{aligned} \psi &= \zeta_{Reference} \text{ at } y = +a; \\ \psi &= \zeta_{Test} \text{ at } y = -a; \end{aligned} \quad (11)$$

where $\zeta_{Reference}$ (ζ_{PP}) and ζ_{Test} ($\zeta_{Calcite}$) stand for the ζ -Potential of the reference PP surface and the material under study, metamorphic calcite, respectively. Rearranging **Eq. 10** for the charge density and inserting it into **Eq. 9** the following is obtained:

$$I_{Str} = -\varepsilon_o \varepsilon_r W \int_{-a}^{+a} v_z(y) \frac{d^2\psi}{dy^2} dy. \quad (12)$$

The asymmetric clamping cell assures a sufficiently wide separation between the reference surface and the calcite, assuring no presence of an EDL overlap. The addition of the two integrals

(i.e. from each side of the channel wall ($y = \pm a$) to the midplane of the microchannel ($y = 0$)) is possible:

$$I_{Str} = -\varepsilon_o \varepsilon_r W \int_{-a}^0 v_z \frac{d^2 \psi}{dy^2} dy - \varepsilon_o \varepsilon_r W \int_0^{+a} v_z \frac{d^2 \psi}{dy^2} dy. \quad (13)$$

From now on a short mathematical treatment using integration by parts is necessary to simplify the integral:

$$I_{Str} = -\varepsilon_o \varepsilon_r W \left[v_z \frac{d\psi}{dy} \Big|_{-a}^0 - \int_{-a}^0 \frac{d\psi}{dy} \frac{dv_z}{dy} dy + v_z \frac{d\psi}{dy} \Big|_0^{+a} - \int_0^{+a} \frac{d\psi}{dy} \frac{dv_z}{dy} dy \right]. \quad (14)$$

However, the equation is simplified for the following terms on both end sides:

$$\dots - \left[v_z \frac{d\psi}{dy} \Big|_{-a}^0 \right] - \left[v_z \frac{d\psi}{dy} \Big|_0^{+a} \right] \dots; \quad (15)$$

because the potential gradient yields zero at the midplane ($y = 0$) and no EDL overlap occurs. And, when solving **Eq. 2** for the two side walls ($y = \pm a$), the fluid velocity at the surfaces of the channel walls also equal to zero. Therefore, the streaming current assumes the following expression:

$$I_{Str} = \varepsilon_o \varepsilon_r W \left[\int_{\psi(y=-a)}^{\psi(y=0)} \frac{dv_z}{dy} d\psi + \int_{\psi(y=0)}^{\psi(y=+a)} \frac{dv_z}{dy} d\psi \right]. \quad (16)$$

Note how the integration variable changed to $d\psi$. Solving the derivative of the velocity field in **Eq. 7** and inserting the solution for the velocity gradient in **Eq. 16** the result yields:

$$I_{Str} = -\varepsilon_o \varepsilon_r W \frac{\Delta p a}{\eta L} \left[\int_{\psi(y=0)}^{\psi(y=-a)} d\psi + \int_{\psi(y=0)}^{\psi(y=+a)} d\psi \right] \text{ for} \quad (17)$$

$$\frac{dv_z}{dy} = \begin{cases} -\frac{\Delta p a}{\eta L}, & y > 0; \\ \frac{\Delta p a}{\eta L}, & y < 0. \end{cases}$$

Note that the limits of the first integral were reversed. Solving the integral in **Eq. 17** the ζ -potential at the surfaces is obtained:

$$I_{Str} = -\varepsilon_o \varepsilon_r W \frac{\Delta p a}{\eta L} [\zeta_{Referenze} + \zeta_{Test} - 2\psi_0]; \quad (18)$$

And, as the potential at the midplane is zero, the last term in **Eq. 18** can be dropped. Furthermore, to account for contribution surface conductance to the conduction current that flows oppositely to the streaming potential and is thus related to the gradient of the latter (U_{Str}/L), **Eq. 19** derived by Erickson et al. [69] yields:

$$I_{Con} = 2aW \frac{U_{Str}}{L} \kappa_B + (W + 4a) \frac{U_{Str}}{L} \kappa_{S|Reference} + W \frac{U_{Str}}{L} \kappa_{S|Test}. \quad (19)$$

Eq. 19 describes the surface conductivity of the channel walls (κ_S) and the bulk electrolyte conductivity (κ_B), integrated over the entire cross-section of the microchannel. If the surface conductivity is negligible (i.e. in the case of electrolyte concentrations more than 1 mM and larger gap

heights) the last two terms can be cancelled. Combining **Eq. 19**, **18** and **8** the relationship between the analysed ζ and the streaming potential is obtained:

$$\frac{U_{Str}}{\Delta p} = \frac{\varepsilon_0 \varepsilon_r (\zeta_{Reference} + \zeta_{Test})}{\mu \kappa_B} = \frac{\varepsilon_0 \varepsilon_r}{\mu \kappa_B} \zeta_{Average}. \quad (20)$$

Eq. 20 is a modification of the original HS obtained by using the streaming current in **Eq. 1** and substituting streaming potential using Ohm's law:

$$I_{Str} = \frac{U_{Str}}{R} \xrightarrow{\text{yields}} \zeta(U_{Str}) = \frac{dU_{Str}}{d\Delta p} \frac{\eta}{\varepsilon_0 \varepsilon_r} \frac{L}{A} \frac{1}{R}; \quad (21)$$

where R is the electrical resistance inside the streaming channel and $(dU_{Str}/d\Delta p)$ denotes the streaming potential coupling coefficient [VPa^{-1}] obtained from the slope of the streaming potential [V] to the pressure difference ramp [Pa]. Note that the term $(L A^{-1} R^{-1})$ is commonly replaced by the bulk electrolyte solution (κ_B) , as the electrical conductivity inside a streaming channel cannot be measured when the cell constant $(L A^{-1})$ is unknown. The latter is a valid approach and approximation of HS in the case for non-conducting materials. **Eq. 20** makes it obvious that the streaming potential is directly related to the average ζ measured. Therefore, by knowing either the ζ of the reference surface or the ζ of the tested material, the overall ζ is obtained by applying the following relation:

$$\zeta_{Test} = 2\zeta_{Avg} - \zeta_{Ref}. \quad (22)$$

In an earlier study by Elimelech et al. [70], a general expression was derived, characterised as a linear combination of ζ -potential of two mixed materials:

$$\zeta_{Avg} = \lambda \zeta_1 + (1 - \lambda) \zeta_2; \quad (23)$$

where (λ) represents the fraction of the total surface area of a ζ -potential of one material (ζ_1) and $1 - \lambda$ is the fraction of the total surface area belonging to the ζ -potential of the other material (ζ_2). **Eq. 22** can be used only in cases where $\lambda = 0.5$. If all terms of **Eq. 22** are measured, the fraction of the total surface area for both materials can be obtained:

$$\lambda = \frac{\zeta_{Avg} - \zeta_2}{\zeta_1 - \zeta_2}. \quad (24)$$

Additionally, **Eq. 24** is rewritten to account for the analysis of planer samples that have a different roughness:

$$\zeta_{Test} = \frac{1}{\lambda} \zeta_{Avg} - \frac{1 - \lambda}{\lambda} \zeta_{Ref}. \quad (25)$$

After examining what the fractional contribution from an asymmetric sample mounting to the overall ζ is, it might be necessary to consider if surface conductance is influencing ζ readings. Therefore, to ensure that surface conductivity is absent in microchannels with smaller gap heights and in presence of dilute aqueous solutions (electrolyte concentrations < 1 mM), it is recommended to measure both materials separately. For that purpose, **Eq. 19** is written in a slightly modified version where both surfaces consist of the material under study (either PP or calcite):

$$I_{Con} = 2aW \frac{U_{Str}}{L} \kappa_B + 2W \frac{U_{Str}}{L} \kappa_S = \left(\kappa_B + \kappa_S \frac{1}{a} \right) 2aW \frac{U_{Str}}{L}; \quad (26)$$

Where the entire cross-sectional area and wetted perimeter of the microchannel is considered while the contribution of the side walls is neglected. Note that the term tied to (κ_S) correspond to the surface conductivity of the sample under study, in this work either PP or calcite. As $(a = H/2)$

Eq. 26 is further reduced to:

$$I_{Con} = 2aW \left(\kappa_B + \frac{2\kappa_S}{h} \right) \frac{U_{Str}}{L}. \quad (27)$$

To examine if the latter is the case, a modified **Eq. 18** for the case of one material in a symmetric cell configuration is inserted along with **Eq. 27** into **Eq. 8** to obtain the following:

$$\frac{U_{Str}}{\Delta p} = \frac{\varepsilon_0 \varepsilon_r \zeta}{\mu} \frac{1}{(\kappa_B + 2\kappa_S h^{-1})}. \quad (28)$$

Rearranging **Eq. 28** to determine ζ and (κ_S) by measuring (U_{Str}) and (Δp) at different channel height yields:

$$\frac{\varepsilon_0 \varepsilon_r \Delta p}{\mu U_{Str} \kappa_B} = \frac{1}{\zeta} + \left(\frac{2\kappa_S}{\zeta \kappa_B} \right) \frac{1}{h}. \quad (29)$$

Eq. 29 is a linear function ($y = d + k \cdot x$) where the left-hand side of the equation is measured and plotted (y-axis) against the inverse channel height (x-axis). Therefore, the terms on the right-hand side denote ζ , which is the y-intercept and slope is related to the surface conductance of the sample. For a derivation of the HS equations for solid materials with planar surfaces and the analysis of surface conductance, the reader is referred to the work of the group surrounding Werner Carsten (e.g. [71,72]). In the case of this work, it is not the surface conductivity but rather the pore conductivity. The difference between surface conductivity and ionic or pore conductivity needs to be emphasised. Both properties will underestimate ζ obtained through streaming potential measurements, but they refer to different phenomena. To analyse if surface conductivity effects can be neglected in the case of flat surfaces, the channel heights are varied in respect to the liquid bulk conductivity [72,69]. The condition for surface conductivity is similar to particles in dispersion, where the ratio of the particle radius and the extension of the double layer determine the effect of surface conductivity. For solid surfaces, the particle radius is replaced by the distance between adjacent surfaces (here: gap height). Therefore, if there is low ionic strength and smaller gap heights are used the more importance should be given to account for the effects of surface conductivity. As in the CC configuration, the gap height is fixed and the calcite surfaces are rough, the effect of pore conductivity will dominate and is accounted for through measurements of the electric resistance R along the streaming channel by using the ratio of streaming potential and streaming current:

$$\frac{U_{Str}}{I_{Str}} = R. \quad (30)$$

This approach represents a simplified case and neglects the effects of surface conductivity on the determined $\zeta(U_{Str})$, which diminishes at conditions of ≥ 1 mM KCl and gap heights $> 50 \mu\text{m}$. Surface electrical conductivity was accounted for in various experimental settings where the electrolyte flows through porous media [73,74]. To account for the effect of ionic or pore conductivity **Eq. 31** is obtained:

$$\frac{\zeta_{U_{Str}}^{app}}{\zeta_{U_{Str}}^{corr}} = \frac{\kappa_B}{\kappa_B^i} \text{ where } \kappa_B^i = \left(\frac{1}{R} \frac{L}{A} \right). \quad (31)$$

κ_B^i corresponds to the measured electrical conductivity inside the streaming channel as a function of the channel geometry, $\zeta_{U_{Str}}^{app}$ denotes to the measured and underestimated ζ and $\zeta_{U_{Str}}^{corr}$ is the ζ corrected for the effect of pore conductivity. Therefore, by solving for correct ζ values, we obtain **Eq. 32**:

$$\zeta^{corr}(U_{Str}) = \frac{1}{\kappa_B} \kappa_B^i \zeta_{U_{Str}}^{app}. \quad (32)$$

However, Ohm's law ($I = U/R$) is disobeyed through the excess concentration of ions that results in higher electrical conductivity compared to the conductivity of the bulk electrolyte solution. Since the measurements in this work were conducted under nonequilibrium conditions, the ionic conductivity of the sample may be used as an indicator of surface reactivity. The observed changes caused by material contribution (dissolution and ion accumulation) to the overall conductivity can be used to study porosity alterations and reactivity in dynamic environments by:

$$\kappa_B^i - \kappa_B \approx \text{pore conductivity}. \quad (33)$$

Two further corrections are needed, that is, corrections for the channel's geometry and corrections for nonlinear dependency. Namely, custom made cells for flat stone specimens were used and geometry corrections were required to correct the algorithm of the used SurPASS device software developed by Anton Paar, Austria. Furthermore, slight nonlinear dependencies can be accounted for that in the case of highly porous surfaces. For these corrections, **Eq. 6** will be used to account for the actual dimensions of the flow channel:

$$\frac{\zeta_{I_{Str}}^{app}}{\zeta_{I_{Str}}^{corr}} = \frac{\frac{L}{A}}{\frac{L^i}{A^i}}; \quad (34)$$

which uses the apparent or measured values ($\zeta_{I_{Str}}^{app}$), as reported by the instrument software, to obtain the corrected values ($\zeta_{I_{Str}}^{corr}$). By rearranging, the geometrical corrections can be accounted for through **Eq. 35**:

$$\zeta^{corr}(I_{Str}) = \frac{L^i}{L} \frac{W}{W^i} \frac{H}{H^i} \zeta_{I_{Str}}^{app}. \quad (35)$$

The gap height of the channel is calculated from the ratio between volume flow rate on pressure difference, but since a transition from laminar to turbulent flow may be present in the case of highly porous carbonates, a correction for potential nonlinear dependency might be necessary. Taking the corrected term (H^i) over the apparent gap height (H), **Eq. 36** is obtained:

$$H^i = \left(\frac{k^i L^i W}{k L W^i} \right)^{1/3} H; \quad (36)$$

where (k) and (k^i) equal $\left(\frac{\dot{V}}{\Delta p} \right)$ as linear and polynomial fits, respectively. Using a linear regression of nonlinear dependency data would underestimate the gap height. The slope of a second-

order polynomial fit at $\Delta p \rightarrow 0$ Pa describes the permeability of the flow channel more reliably. Therefore, by inserting **Eq. 36** into **Eq. 35**, geometrical correction can be introduced as follows:

$$\zeta^{corr}(I_{Str}) = \left(\frac{k}{k^i}\right)^{1/3} \left(\frac{L' W}{L W^i}\right)^{2/3} \zeta_{I_{Str}}^{app}; \quad (37)$$

where $(\zeta_{I_{Str}}^{corr})$ estimates the corrected ζ -potential of the studied porous carbonate surfaces. Similarly, by using **Eq. 32**, and with the previously introduced corrections for the nonlinear dependency conditions and channel geometry, **Eq. 38** is derived:

$$\zeta^{corr}(U_{Str}) = \left(\frac{1}{\kappa_B}\right) \left(\frac{1 L}{R A}\right) \left(\frac{k}{k^i}\right)^{1/3} \left(\frac{L' W}{L W^i}\right)^{2/3} \zeta_{U_{Str}}^{app}. \quad (38)$$

Fairbrother and Mastin [75] assumed that surface conductivity is suppressed when the conductivity of the electrolyte is high. However, when altering the surface, the conductivity of the contacting electrolyte solution may be modified, particularly so for porous surfaces. This effect of pore conductivity and related changes in the streaming channel may become key for porous carbonates, which ultimately requires the corrections introduced in **Eq. 38**. At this point, note that the terms conductance and conductivity, which describe two properties, are not uniformly used in published literature and therefore also, in this work.

To properly use electrokinetic phenomena of the streaming potential and streaming current, even if only descriptively to analyse different material states, corrections are necessary to account for various effects. In this work, corrections were introduced for: (i) effect of pore conductivity (**Eq. 33**), (ii) geometry corrections due to custom made microchannels (**Eq. 37** and/or **38**), (iii) nonlinear dependency due to rough surfaces (**Eq. 37** and/or **38**) and (iv) calculation of the fractional contribution of the reference surface to the overall measured ζ (**Eq. 24**). It should be noted that when using **Eq. 1** and **Eq. 21** in a microchannel where the walls are made of the same material (i.e. adjustable gap cell) true ζ values are obtained and the latter correction is needless.

2.2.2 Analytical, microscopic and physical techniques

This subsection briefly describes all instruments and standardised tests used for evaluating the effect of thermal treatment and the efficiency and compatibility of consolidants. An overview of the analytical, microscopic and physical techniques is given in **Table 2.4**.

Table 2.4: Overview of tests used to characterise the stones in different conditions (pristine, thermally treated and consolidated)

Type of test	Reference	Main evaluation purposes
In situ and ex situ XRD	Not std.	Qualitative and quantitative mineral and phase identification
XRF	Not std.	Chemical composition
SEM-EDX analysis	Not std.	Physical changes, penetration depth, distribution and morphology of consolidants
Optical light microscopy	Not std.	Petrographic description
Mercury intrusion porosimetry	Not std.	Pore size distribution, no secondary microporosity
Water absorption coefficient	EN 15801:2009	No drastic reduction
Drying behaviour	EN 16322	No drastic reduction
Water vapour permeability	EN 15803:2009	No drastic reduction
Dyn. Elastic modulus (sound speed propagation)	EN 14146 (EN 14579)	Improvement, smooth profile
The contact angle of water	EN 15802:2009	Change $\leq 20\%$ from untreated
Drilling resistance	Not std.	Improvement, smooth profile
Colour measurements	EN 15886:2010	ΔE change < 5
Splitting tensile strength	ASTM D 39967-81	Improvement mechanical strength gain
Flexural strength under a concentrated load	EN 12372:2006	Improvement mechanical strength gain

In-situ XRD spectra were collected using a PANalytical X'Pert MPD Pro powder diffractometer (PANalytical B.V., The Netherlands). A partly focusing mirror was used to select the $\text{CuK}_{\alpha 1/2}$ characteristic lines ($\lambda_{\alpha 1} = 1.54060\text{\AA}$, $\lambda_{\alpha 2} = 1.54443\text{\AA}$) for the experiment. The instrument was set up for Bragg-Brentano reflection geometry in θ/θ -mode. The working distance between the sample and the position-sensitive 1-dim. X'Celerator detector was 240 mm. A high-temperature furnace (Anton Paar HTK 1200 N), operating in air under ambient pressure, was used to track the thermal decomposition of disc-shaped stone specimens, 18 mm in diameter and approx. 2.5 mm thick. Following dedicated temperature steps, the diffraction diagrams were recorded in situ. Therefore, we could observe in situ the phase evolution with temperature. For each temperature step, the data were continuously collected in a range from 15 to 90° diffraction angle 2θ with a speed of $0.01^\circ\Delta 2\theta/\text{s}$. Subsequently, the data were analysed, including also the Rietveld refinement, by the HighScore Plus software package [76] using the Powder Diffraction File (PDF4+ [77,78]; International Centre for Diffraction Data in Philadelphia, USA). The samples were measured at room temperature followed up by heating steps up to 600°C ($40^\circ\text{C min}^{-1}$ heating ramp) simulating the calcination conditions used beforehand in the laboratory. Six subsequent XRD diffraction patterns were collected under isothermal conditions by stopping the heating ramp for 10 min at temperatures 100, 200, 300, 400 and 500 °C, respectively. At 600 °C we used a temperature hold of 60 min, which corresponded to six patterns collected. After heat treatment, the sample was cooled down to room temperature. This heating/cooling cycle was repeated three times to produce the generation of a sufficiently extended surface layer of transition phases. The use of in-situ XRD was particularly useful in the frame of *Manuscript A* as phase transformations on macroscopic solid samples could be tracked.

Before in-situ XRD, on the same sample spot, XRF was measured to obtain information on the chemical composition of the natural stones. The device used for XRF analysis was a Panalytical

AXIOS advanced PW4400/40. Moreover, additionally to in-situ XRD a conventional ex-situ XRD type PANalytical X'Pert Pro was also employed to qualitatively assess the mineralogical content of the analysed stones. For purposes of ex-situ XRD analysis, the samples were grinded.

Scanning electron microscopy equipped with energy-dispersive X-ray spectroscopy (SEM/EDX) was conducted using a QUANTA FEG 450 (FEI). Furthermore, a field-emission scanning electron microscope of the type FEI Quanta 250 FEG was also used. The specimens were mounted on an aluminium stub, coated with an approx. 7 nm thick gold film and observed at 20 kV accelerating voltage in the backscatter and secondary electron mode. OLM was used on polished thin sections using an Olympus BX41 microscope. Besides using cross-polarizes and plain-polarised lights, thin sections have been analysed also under UV light to study crack inducement after thermal treatment. Therefore, samples have been vacuum impregnated with the resin-hardener system XW 396 / XW 397 with a mixing ratio of 10:3 (Huntsman Corporation, Salt Lake City UT, USA) and were cured overnight at 40 °C. Before mixing resin and hardener, 1.3 g Fluorol 008 or EpoDye (Struers Inc., Cleveland OH, USA) was added to 100 g of XW 396. In addition to the thin section analysis, polished cross-section and stone chips (broken pieces of stone) have also been analysed in the frame of this work. The use of microscopy techniques was manifold and ranged from a petrographic description of the building stone to assessments of physical changes caused by either thermal- or consolidation treatments. The main purpose was to evaluate the inducement of microcracks and decay patterns in general, penetration and distribution depths and morphology of cured consolidants.

Porometric properties were determined using the AutoPore IV 9500 (Micro metrics) and the Porosimeter Pascal 140/440 (Porotec) device by a double determination of each sample analysed. Specimen dimension amounted to 1 × 1 × 1 cm. The main properties studied involved pore size distribution, total pore surface, open Hg-porosity and average pore size. Additionally, the use of He-pycnometry (AccuPyc II 1340, Micromeritics) allowed the assessment of changes in obvious skeletal density when the mineral transformation occurred upon thermal treatment. He-pycnometry was used only for Apuan Marble.

The water absorption coefficient (WAC) after one hour was determined according to EN 15801 [79]. After pre-conditioning of the samples, they are placed on water-soaked filter paper (Ahlstrom-Munktell laboratory filter paper, wet-strengthen grades) and the adsorption is monitored gravimetrically. The WAC is reported as $\text{kg}\cdot\text{m}^{-2}\cdot\text{h}^{-0.5}$. This parameter is commonly employed to measure the rate of moisture absorption of building materials or to help analyse the performance of treatment.

The drying behaviour was conducted following the recommendations of EN 16322 [80]. The test allows calculating the water loss of a saturated sample over time. However, in this work, the drying behaviour was monitored for consolidated samples. In the case of reactive consolidants, the drying behaviour can indicate the halt of the reaction, while in the case of colloidal particles it shows when the drying process ends and therefore the strengthening action starts. For these purposes, the drying behaviour was monitored for 30 days and the per cent of adsorbed consolidant was plotted versus the time monitored. Generally, the test includes monitoring of the drying at regular intervals of time by weighting the samples. After each measurement, samples are again placed in a desiccator where they have been stored from the beginning with constant relative humidity and temperature. The side of the samples was not sealed thus drying occurred from the entire sample volume. Moreover, the curves have been plotted as the first derivative of the mass loss to indicate at what time important drying stages are present. To obtain the first derivative at a

given point, the average of the slopes between the point and its two closest neighbours was used and calculated using the software OriginPro2019.

The water vapour permeability was performed according to EN 15803 [81] using the so-called 'wet cup' method with a cup system Type 1 according to the standard. The cups were filled with water and placed in a climatic chamber at ambient conditions of $23 \pm 1^\circ\text{C}$ and $50 \pm 3\%$ RH (Heraeus Vötsch Klimaprüfschrank VC3, model 4034). They were weighed every 24 hours for one week. The results were plotted as the mass change versus time. The slope of the linear section of this curve (G , in $\text{kg}\cdot\text{s}^{-1}$) was determined with the help of OriginPro2019. Subsequently, G was used to calculate the water vapour permeance in $\text{kg}\cdot\text{m}^{-2}\cdot\text{s}^{-1}\cdot\text{Pa}^{-1}$ as shown in **Eq. 39**:

$$W_p = \frac{G}{A\Delta p_v} . \quad (39)$$

A is the test surface area (m^2) while Δp_v represents the water vapour pressure difference (Pa) across the test specimen. The water vapour permeability reported in $\text{kg}\cdot\text{m}^{-1}\cdot\text{s}^{-1}\cdot\text{Pa}^{-1}$ was then determined according to **Eq. 40**:

$$\delta_p = W_p D; \quad (40)$$

where D represents is the average thickness of stone specimens in m. Three specimens per lithotype and treatment with dimensions of $50 \times 50 \times 10$ mm were tested. The water vapour permeability is reported as the ratio of treated to untreated values.

The dynamic modulus of elasticity was determined by the longitudinal resonance frequency of an ultrasound signal in transmission, according to EN 14146 [82]. Therefore, prismatic specimens with dimensions $10 \times 10 \times 40$ mm came to use and a mean value was obtained by the measurement of at least three specimens. The smaller specimen size was selected to ensure the consolidation of the entire test body. The test was performed by an ultrasonic pulse generator (CONOSONIC C2-GS), a pair of transducers (UP-DW) and a notebook preinstalled with the Light House Touch software, developed by Geotron-Elektronik (Pirna, Germany). The dynamic modulus of elasticity (Ed_L), determined through the longitudinal fundamental resonance frequency (F_L) is given by **Eq. 41**:

$$Ed_L = 4 \cdot 10^{-6} \cdot l^2 \cdot F_L^2 \cdot \rho \cdot T . \quad (41)$$

l represents the specimen's length and ρ the stone density. If T needs to be determined, the following relations are used:

$$T = 1 + \frac{\pi^2 \nu^2 i^2}{l^2} . \quad (42)$$

As can be seen from **Eq. 42** T depends on i , which is the radius of gyration of the section of the specimen and on ν , which is the dimensionless material parameter known as the Poisson's ratio.

Furthermore, i is denoted as $\left[i = \sqrt{\frac{I}{A}} \right]$ with (I) being the moment of inertia of the specimen, which

in the case of the given specimen's geometry is $\left[I = \frac{b \cdot h^4}{12} \right]$ and (A) the surface area of the cross-section of the specimen. However, in this case, the width of the specimens is four times the length, so the correction factor T can be assumed to be ≈ 1 in which case **Eq. 41** is simplified to:

$$Ed_L = 4 \cdot 10^{-6} \cdot l^2 \cdot F_L^2 \cdot \rho . \quad (43)$$

The (F_L) was recorded when the deviation of the measured fundamental resonance frequency lay in a range of ± 60 Hz, three times in a row. The dynamic modulus of elasticity is reported in GPa or kN/mm². Furthermore, rapid sound speed propagation tests have been done according to EN 14579 [83] on a minimum of six specimens. The expression of the results is obtained by the following relation:

$$V = \frac{L}{T}; \quad (44)$$

Where V is the pulse velocity reported in km/s, L is the path length in mm and T is the time taken by the pulse to transverse the length, in μ s. These tests have been done to investigate changes in the fabric before and after treatments (either pristine-thermal treatment and thermal treatment-consolidated samples).

The static contact angle of water was determined on the stone surface treated with the water-repellent consolidants. Therefore, the Mobile Surface Analyzer from Krüss GmbH, Germany came to use and the test was done according to EN 15802 [84].

Drilling resistance measurements (DRM) record the penetration force needed for drilling a hole in the material under study. Therefore, the DRMS Cordless device developed by Sint Technology S.r.l. (Calenzano, FI, Italy) was used. The DRM is determined as a function of the speed of rotation, the penetration speed, drill bit diameter and substrate. The speed of rotation and the penetration speed is kept constant and are specific for a type of stone. In the case of St. Margarethen, the speed of rotation was 600 rpm and the penetration speed amounted to 10 mm/min. The drilling depth was set to 15 mm (with mean resistance values ranging from 2 to 13mm) and a custom made 3 mm polycrystalline diamond bit was used. For each surface that was treated with specific consolidants, a separate drill was used to assure no influence on the wear of the drill bit on the recorded results [85].

For measuring the colour difference before and after thermal treatment a Konica Minolta spectrophotometer type CM700d was use with a spot diameter of 8 mm and the test was performed according to EN 15886 [86]. Hereby a standard daylight illuminant D65 with a 10° observer was applied. Following the same standard, a second device was used to assess the colour difference between treated and untreated specimens. Therefore, a ColorLite sph850 spectrophotometer came to use. The results were analysed in the CIE 1976 L*, a*and b* colour space to obtain the overall colour change (ΔE^*). An average of five measurements is reported per sample area and condition. The colour change ΔE^* describes the metric difference between two colours according to the standards of the International Commission on Illumination (CIE) as follows:

$$\Delta E_{t,nt}^* = [(L_t^* - L_{nt}^*)^2 + (a_t^* - a_{nt}^*)^2 + (b_t^* - b_{nt}^*)^2]^{0.5}; \quad (45)$$

where the subscript t stands for treated and nt for untreated specimens and refers to either thermal treatment or treatment with a consolidant.

The determination of the splitting tensile strength was conducted following the recommendations of ASTM D3967-08 [87]. The electro-mechanical tension and compression-testing machine used were a 150 kN Instron Model 4206, developed by Instron GmbH, Germany. The apparatus consisted of a flat bearing block at the bottom and, to reduce the contact stresses, a curved bearing block on the top. Bearing strips with 0.6 mm thickness were used to reduce high-stress concentrations. A minimum of 10 specimens per lithotype and condition was tested, each 60 mm in diameter and 30 mm in thickness. The test was executed in the direction perpendicular to the bedding plane, which was assessed through ultrasound pulse velocity. The splitting tensile strength is calculated by the following equation:

$$\sigma_t = \frac{2P}{\pi LD}; \quad (46)$$

where σ_t is the splitting tensile strength in MPa, P is the maximum-applied load indicated by the testing machine in N, L is the thickness and D diameter of the specimen in mm.

Flexural strength under a concentrated load was determined according to EN 12372 [88]. 10 specimens with a dimension of $25 \times 50 \times 150$ mm were tested. The tests were performed with an electronic spindle-drive testing machine of the type Testomeric Quicktester 100 kN and evaluated by the Test & Motion software developed by DOLI Elektronik GmbH, Germany. The test was conducted in the direction perpendicular to the bedding plane, which was assessed through ultrasound pulse velocity. The flexural strength was calculated according to the following equation:

$$R_{tf} = \frac{3Fl}{2bh^2}. \quad (47)$$

In **Eq. 47** F denotes the breaking load in N, l is the distance between the supporting rollers, b is the width and h the thickness of the specimens in mm. The results are either expressed in MPa or N/mm².

2.2.3 Neutron imaging

Neutron scattering and neutron imaging are techniques commonly employed in the field of cultural heritage [89]. While neutron imaging operates in real space, neutron scattering is described in reciprocal space. What happens in imaging is that a beam of neutrons is passed through the object under study and the neutrons are attenuated by the material studied. Attenuation means that the beam intensity is reduced by a certain amount and this reduction depends on the thickness of the study sample and on the material it is made of. Therefore, we receive information on the composition and inner structure of the samples, as different materials components have different attenuation behaviour. The latter is the reason why with the help of neutron imaging, the structure of a stone, its composition or conservation state is studied in a non-invasive manner. Moreover, larger stone samples relevant for architectural preservation studies can be analysed in situ as neutrons can penetrate most materials. Contrary to X-rays, hydrogen atoms strongly attenuate neutrons, which makes neutron imaging valuable in construction- and geosciences for performing dynamic studies on the movement and retention of water (e.g. [90-93]).

The basic experimental setup for neutron imaging consists of a neutron source, a collimator acting as a beam formatting implement, the object under study and a detector. Since digital processing systems are used, neutron imaging has become a quantitative method (e.g. grey values can be quantified and pixels counted). When neutrons pass through an object, they need to be converted into a radiation form that can be easier detected. For such purposes, scintillator screens are used that convert neutrons into photons. After this conversion, a digital image is recorded by a charge-coupled device (CCD) camera. The spatial resolution depends on the geometrical assembly, that is, the relative distance between the source, sample and detector. In the published literature, this effect is referred to as the ratio of the beams effective length to its diameter, i.e. L/D , and accounts for the divergence of the beam, which has a direct effect on the image resolution (e.g. [94,95]). Noteworthy is that the spatial resolution is not only affected by the magnification, but also by factors as the focal spot size of the source, the pixel size of the detector, some physical phenomena due to radiation-matter interaction, sample thickness and the scintillator material. The

lowest spatial resolution amounts to $\sim 20 \mu\text{m}$, which is limited through the scintillating material employed [96].

The principle of neutron imaging is based on transmission measurements. For a sample with an appropriate thickness θ (cm), the transmission T is given as follows:

$$T = \frac{I}{I_0} = e^{(-\mu\theta)}; \quad (48)$$

where μ represents all attenuation processes. As can be seen in **Eq. 48** neutron transmission can be described with the exponential attenuation law or the universal law of attenuation of radiation for materials (Beer-Lambert law). In detail:

$$I = I_0 e^{-N\sigma\theta}. \quad (49)$$

I is the transmitted intensity and I_0 the incident intensity ($\text{cm}^{-2}\cdot\text{s}^{-1}$). N is the number density of atoms in the sample analysed (cm^{-3}):

$$N = \frac{\rho}{A} N_A; \quad (50)$$

where ρ is the material density ($\text{g}\cdot\text{cm}^{-3}$), A atomic weight ($\text{g}\cdot\text{mol}^{-1}$) and N_A the Avogadro number (mol^{-1}) and σ is the effective interaction area for the neutron with a nucleus, the so-called microscopic cross-section (unit of barns, cm^2) (e.g. [97]). The product of $N\sigma$ gives Σ that represents the macroscopic cross-section (cm^{-1}):

$$\Sigma = N\sigma = \Sigma_a + \Sigma_s; \quad (51)$$

Where Σ_a stands for the cross-section of the absorbed neutrons and Σ_s represents the cross-section of the scattered neutrons. As samples can be made of multiple elements and isotopes a summation is performed:

$$\Sigma_{tot} = \sum_j n_j \sigma_j = \sum_j \Sigma_j; \quad (52)$$

leading to the final expression of the attenuation equation:

$$I = I_0 e^{-\Sigma_{tot}\theta}. \quad (53)$$

To quantitatively interpret the collected data, image analysis is a prerequisite. Pre-processing and image analysis is usually done with the help of Fiji ImageJ (Fiji Is Just ImageJ - Image Processing and Analysis in Java, open-source, public licence) according to in-house protocols in collaboration with the beam scientist [98]. Image pre-processing normally involves corrections with dark-field images, normalisation with open-beam images and noise filtering (including dead camera pixels and spurious gamma events). The raw neutron images of dry and wet stone ($I_{(d)}$ and $I_{(w)}$, respectively) were corrected with dark-field $I_{(df)}$ and open-beam $I_{(ob)}$ images:

$$I_{(d,corr)} = \frac{I_{(d,raw)} - I_{(df)}}{I_{(ob)} - I_{(df)}} C; \quad (54)$$

$$I_{(w,corr)} = \frac{I_{(w,raw)} - I_{(df)}}{I_{(ob)} - I_{(df)}} C. \quad (55)$$

C is a rescaling factor that accounts for beam fluctuations. Dark-field image (beam shutter closed) corrects for the CCD dark-current in the detector while open-beam corrects (flat-field corrections) inhomogeneities in a detector and the source beam [99]. As in this case, the adsorption of water was the aim, the first steps included the normalisation of the water absorption images and normalise them with the steady-state dry images taken before absorption. In that way, the measured transmission can be directly related to the amount of water. For that purpose, the imaging of a vessel filled with water in different volumes with standardised thickness was done, from which a calibration curve of water attenuation and resulting image grey values can be created (e.g. [100,101]) such procedures are necessary to account for deviations from the Beer-Lambert law (i.e. because of the energy dependence of the attenuation coefficient). This step is necessary if samples are thick or a strongly absorbing or -scattering material is present (e.g. water). After this, the images are ready to be used for image analysis and the extraction of physical parameters (e.g. water content distribution). To account for the 2D distribution of water thickness $\theta_w(x, y)$ in a stone specimen [102] Eq. 53 is rewritten for the case at hand:

$$I_{(w,corr)}(x, y) = I_{(d,corr)}(x, y) e^{-(\mu_w \theta_w)}; \quad (56)$$

where $I_{(d,corr)}(x, y)$ represents the contribution of the stone:

$$I_{(d,corr)}(x, y) = I_0(x, y) e^{-(\mu_s \theta_s)}. \quad (57)$$

To repeat shortly, μ_s and μ_w are the stone and water attenuation coefficients respectively while θ_s is the thickness of the stone specimens. Solving Eq. 56 for θ_w the following is obtained:

$$\theta_w(x, y) = -\frac{\ln \left[\frac{I_{(w,corr)}(x, y)}{I_{(d,corr)}(x, y)} \right]}{\mu_w}; \quad (58)$$

where μ_w is obtained from the calibration curve of water attenuation. By expressing the θ_w along the pathlength of the beam (at a specific x,y-position in the image) as a percent of the sample thickness amongst that pathlength (which can physically be measured), a volume percentage of water saturation at that point is obtained. This can be recalculated to weight percent using the known material density and a density of 998 kg/m³ for water. From now on different physical parameters like the water content expressed in e.g. weight per cent can be extracted and used for further analysis in the field of conservation sciences (e.g. [103]).

2.2.4 An analytical model to evaluate the distribution depth of stone consolidants

The analytical model, based on a version of one-dimensional Fick's second law coupled with Darcy's law, Blake–Kozeny and Young–Laplace approximations, was applied to describe the in-depth distribution of cured consolidants inside the stone's fabric. All those approximations are found across the literature in many fields and in the field of stone consolidation (e.g. also Scherer G.W. and Wheeler G.S. [104] used to describe the penetration of consolidants inside a stone by using a similar approach or Peruzzi et al. [105] uses a similar approach to describe the water flow in a porous material). In this case, the analytical model evaluates the quantity of a consolidant as a function of depth. The depth distribution of the consolidant was experimentally assessed on drilled cores, extracted from on-site and investigated using SEM. The SEM micrographs analysis

was then conducted using the software ImageJ [106] (v 1.51r, National Institutes of Health, Bethesda, MD, USA).

The first approximation to model this phenomenon is to view the system (i.e. stone and consolidant) as a filtering system in which the stone acts as a filter against the consolidant that passes through it. In the literature, this approach is usually found in studies concerning oil recovery. The probabilistic sieve model describing microfiltration [107-109], used to analyse pore-blocking processes, allows the determination of physicochemical parameters of nonstationary filtration phenomena of an aqueous suspension. In this case study, the driving forces that carry the consolidant through the stone's fabric are capillary forces. To evaluate the concentration of consolidant as a function of depth, a mass balance is applied in the following form:

$$V \frac{dc}{dx} = D \frac{d^2c}{dx^2}; \quad (59)$$

where D is the diffusivity and V the filtration speed of the study system. As equilibrium conditions are reached (i.e. the curing of the consolidant is complete), time dependence becomes negligible. Therefore, the boundary conditions to solve **Eq. 59** are:

$$B.C. \begin{cases} c(x=0) = c_0; \\ c(x=L) = c_L; \end{cases} \quad (60)$$

where C_0 is the solid content concentration found on the stone's surface at the end of the curing process and C_L is the solid content concentration at the maximum depth reached by the treatment within the analysed sample volume. As the system is described to be a filtration system, where the treated stone is the filter, the expression of velocity follows Darcy's law [110,111]. Therefore, the effective filtering speed V is connected to Darcy's speed V_D according to the following relation:

$$V = \varepsilon \cdot V_D = -\frac{k \Delta P}{\mu L}. \quad (61)$$

In **Eq. 61**, the negative sign of the term on the right-hand side provides positive values of the velocity toward the motion. The suspension viscosity is given by μ , whereas k is the permeability. ε represents the average porosity of the stone, evaluated using image analysis. The permeability indicates the capability of a viscous fluid to penetrate a porous system and can be evaluated through experimental tests or, for well-known systems, found in the literature [112,113]. Otherwise, as a first approximation, the Blake–Kozeny relation can be used to calculate stone porosity k in terms of average pore diameter D_p as follows:

$$k = \frac{D_p^2 \cdot \varepsilon^3}{150 \cdot (1 - \varepsilon)^2}. \quad (62)$$

As capillarity is the driving force of this system, it obeys the Young–Laplace equation:

$$\frac{\Delta P}{L} = \frac{2\sigma \cos\theta}{R_p^2}; \quad (63)$$

where σ is the surface tension, θ the wettability (contact angle) and R_p the pore radii of the system. Inserting **Eqs. 62** and **63** into **Eq. 61**, and the final expression of filtering velocity is obtained. Solving **Eq. 59**, the degree of solid content concentration as a function of sample depth can be described as an analytical solution as follows:

$$\left[-\frac{2D_p \sigma \cos \theta}{75 \mu DL} \cdot \frac{\varepsilon^3}{(1 - \varepsilon)^2} \right] \frac{dc}{dx} = \frac{d^2c}{dx^2}. \quad (64)$$

In **Eq. 64**, it is possible to define the following parameters:

$$A = \frac{\varepsilon^3}{(1 - \varepsilon)^2}; \quad (65)$$

$$B = \frac{2D_p \sigma \cos \theta}{75 \mu DL}; \quad (66)$$

where A is a function of the stone's effective porosity, evaluated by image analysis as the weighted average along with the depth of the stone, and B is an empirical parameter obtained through mathematical iterations, encompassing the wettability, average porous dimensions, permeability and diffusivity of the macroscopic system. Substituting the starting boundary conditions (**Eq. 60**) into **Eq. 64**, we obtain the following solution:

$$c(x) = \frac{(C_L - C_0) \cdot e^{-ABx} - (C_L - C_0) + C_0 \cdot (e^{-ABL} - 1)}{e^{-ABL} - 1}. \quad (67)$$

The analytical solution given through **Eq. 67** indicates that the distribution of the solid content after curing follows an exponential growth or decline. To estimate the adequacy with which they obtained equation describes the depth distribution of the consolidants, it has been verified with the values obtained from image analysis.

3. Summary of the scientific articles

A

Evolution of calcite surfaces upon thermal decomposition, characterized by electrokinetics, in-situ XRD, and SEM

This study systematically modified the surface chemistry of metamorphic and sedimentary calcium carbonates by thermal treatment to induce partial phase and chemical transformations. Subsequently, the electrokinetic potentials of the resulting samples were determined with the aim of improving the understanding of the role of phase transformations and modified (or newly created) porosity and reactivity. Besides streaming current and potential measurements, in-situ XRD and SEM as ancillary techniques were used to explore in more detail the involved surface phenomena.

Physical changes of the samples after thermal treatment were observed using microscopy, porosimetry and sound speed propagation. On the dense sample AM, the formation of new cracks was visible, while the same were difficult to be observed on the inhomogeneous samples of LdA. However, porosimetry and sound speed propagation indicates that there are changes also in the fabric of LdA. Furthermore, visual changes assessed using colour measurements are present on the surfaces of both stones. A silica coating applied on the surfaces after thermal treatment showed embedded rhombohedral crystals on surfaces of AM, while the only discolouration of the nanosilica matrix due to calcium mobilisation was observed on LdA as analysed by SEM/EDX. The latter results displayed that a more pronounced change has happened on the surfaces of AM than on LdA. This difference in the extent of thermal decomposition was also confirmed by in-situ XRD.

The cyclic isothermal treatment at 600 °C caused thermal degradation that differs in extent and onset for the studied stones as examined by in-situ XRD. The dense stone AM decomposed earlier and had more calcium oxide on the surface than the porous stone LdA when exposed to the studied conditions.

In the initial period of testing, positive and negative ζ was observed for the studied carbonates. This is a result of the reactivity of the stones as they were analysed in nonequilibrium conditions. The reactivity was related to surface roughness because the surfaces contributed to dissolution and therefore changes in the background solution.

For highly porous carbonate, a ~90% underestimation of ζ assessed by streaming potential with respect to the streaming current was observed, irrespective of the state of the carbonate surface (i.e. pristine or thermally decomposed), while the underestimation was only ~20% for the pristine dense carbonate ~70% after microcracks generation. Therefore, it was concluded that caution should be taken when assessing solely streaming potential measurements.

Thermal treatment caused a charge reversal from negative (before treatment) to positive (after treatment). The latter was a result of calcium hydroxides solubility and the supply of Ca^{2+} cations, which are known to be the potential determining ions for calcite. If calcium hydroxide is present

at the surface of calcite, it will govern the net electrokinetic potential and isoelectric point (IEP_{pH}), even at low surface coverage.

The pH-dependent electrokinetic measurements exhibited further the difference between the stones. On thermally treated surfaces of AM, ζ was positive due to calcium hydroxide and recovery of ζ was evident due to re-carbonation. No such effect was observed on surfaces of LdA when tested under the same conditions, because this stone is porous and re-carbonates faster and is easily dissoluble already in its pristine state.

Finally, when an asymmetric cell configuration was used, the fractional contribution of the reference surface to the IEP_{pH} was 0.3 and to the overall determined ζ (single-point measurements) it was up to 0.5. Moreover, the use of two cells seemed unsuitable for purposes of quantitative comparison when reactive surfaces are present.

A.1

Artificial aging techniques on various lithotypes for testing of stone consolidants

This contribution was the foundation of this thesis. It concentrated on a series of ageing tests that were performed in the frame of a wider study on the use of innovative consolidants for various architectural stone types. It was a feasibility study on artificial ageing tests that should be used on a large-scale volume of natural stone in the laboratory. This experimental pre-screening proved that thermal treatment was a cost and time-efficient method to artificially age stones for testing stone consolidants. The induced microcracks were compared to natural decay phenomena found in exterior environments of buildings. Furthermore, the thermal treatment allowed to tailor the decrease of mechanical strength and physical changes.

At the beginning of this study, it was necessary to analyse what are the dominant decay patterns that occur on-site on the lithotypes that were studied. The predominant deterioration phenomena were identified to be a loss of grain cohesion and the formation of microcracks. Therefore, the aim was to mimic this key-deterioration effect in the studied fabrics. An additional goal was to mimic a gypsum crust in a porous limestone to achieve a gradient of compactness within a structure, a decay pattern that is often found on-site. The artificial ageing routes to induce these decay patterns were (1) thermal treatment by temperatures up to 600 °C and, (2) artificial ageing with acid attack, freeze-thaw cycles and salt crystallisation alone or along with thermal treatment.

The induced ageing was monitored using changes in ultrasound velocity and WAC by capillarity. At certain stages analysis by optical- and SEM, as well as mercury intrusion porosimetry, was done to evaluate physical changes. With this approach, it was possible to test the sensitivity of each lithotype to predominant decay patterns found on-site.

B

Efficiency and compatibility of selected alkoxy silanes on porous carbonate and silicate stones

This manuscript concerned a complete array of methods to compare the consolidation effect of three alkoxy silanes on two stones and discussed their impact on the compatibility. The main goal of this work was to restore the physical and mechanical properties of the artificially aged specimens where microcracks were induced. For this purpose, two new formulations (1) a TiO_2 modified TEOS in isopropanol with 70% active content and (2) a TiO_2 modified alkyl-trialkoxysilane in isopropanol with 75% active content was compared to a commercial product (3), a solvent-free TEOS with 99% active content. The substrates used in this study were two porous lithotypes, one silicate and one carbonate. The treatments were evaluated by SEM, mercury intrusion porosimetry, colour impact and their effect on dynamic modulus of elasticity, splitting tensile- and flexural strengths, capillary water absorption and water vapour permeability.

The results showed that treatment performance might depend on the textural and microstructural features of a stone. Specifically, the higher increases in deformability modulus and strength in the case of the silicate stone variety were ascribed to its fabric. SEM analysis displayed that the consolidant interpenetration of the kaolinite, which was homogeneously distributed in the fabric. Moreover, mercury intrusion porosimetry analysis showed that the consolidants that increased the mechanical strength more are located in large pores that make up the leading pore ranges in terms of open Hg-porosity. The same increase as the one described for the silicate variety could not be reached within the carbonate. The treatments showed a sufficient increase in strength and deformability, but due to the inhomogeneous nature of the carbonate, the resulting values were always lower. Moreover, the main pore radii, which made up the largest percentage of the open Hg-porosity in the carbonate variety were not filled with the silica gel to the same degree as within the silicate stone.

This study also highlighted that the kinetics of the gel-forming reaction during curing might be dependent or differ between the substrates. The latter was also the reason why water-related properties, as well as visual changes, evolved with time. Unfortunately, no general trend was observed, which might lead to incorrect interpretations of treatment compatibility. This study proved that a wide-ranging treatment performance might be obtained when the same products are applied on different substrates.

B.1

Silicates for the consolidation of stone: nanosilica vs. ethyl silicate

This contribution highlights the advantages and disadvantages of some TEOS and a silica sol as analysed using SEM and selected physicommechanical tests. It was shown that the topographic distribution, shrinkage behaviour and thus bridging capacity as well as adhesion on the substrate differed between these consolidating products. The main advantages of TEOS are a better penetration depth and a more homogeneous distribution inside the fabric, while the advantages of the silica sol are good adhesion to the substrate and a better bridging capacity. Therefore, it was concluded that an application of both consolidants in a two-stage treatment could bring promising results, especially considering decay patterns of varying degrees of severity.

C

Neutron radiography study of laboratory ageing and treatment applications with stone consolidants

This study aimed to use neutron imaging, by monitoring capillary water absorption, to analyse physical changes caused by thermal treatment for purposes of artificially ageing and different treatment applications with stone consolidants. In addition, gravimetrically determining water absorption and ultrasonic pulse velocity were also used and compared to neutron imaging. Therefore, a nanosilica consolidant and nanotitania modified TEOS was applied on two building stones, carbonate and a silicate, by brush, poultice or capillary absorption.

Water absorption as analysed using neutron imaging exhibited negligible changes on samples aged by thermal treatment compared to sound specimens. It was therefore concluded that artificially aged specimens are not a prerequisite when physical changes are studied on porous lithotypes. However, when the mechanical strength increase is studied, artificial ageing should be used to study the efficiency of stone consolidants. The latter was demonstrated with the help of ultrasonic pulse velocity. Namely, when grain contracts are not affected, as is the case in a freshly quarried stone, the consolidation efficiency will yield underestimated values. Ultimately, the capability of a consolidant to strengthen the substrate might be misrepresented.

Similar to *Manuscript B*, in this study, it was also demonstrated that reactive systems like TEOS need an unknown period for polymerisation. When the polymerisation is incomplete, hydrophobic behaviour, water trapping, and pore-clogging was evident with the help of neutron imaging. Moreover, reaction time differences were attributed to different amounts of consolidants applied, which resulted in the chosen application settings. When TEOS was applied using a poultice and

brushing it resulted in wide-ranging amounts of water absorbed and anomalous water distributions and kinetics. An odd behaviour was seen within the carbonate stone, that is, the polymerisation was ongoing within the core of the specimen, while the lateral surfaces were still mostly hydrophobic with the exceptions of small passages.

C.1

The potential of neutron imaging in stone conservation

In support of *Manuscript C*, this contribution intended to give a brief overview of newcomers in the field of architectural preservation that want to use neutrons in their research. Therefore, a short introduction of neutron techniques, major facilities and workshops around Europe is listed to enhance knowledge and support research in this field. This contribution is light in reading and focuses mainly on water transport and retention studies. The experimental data were collected during experiments performed at IMAGINE beamline, located at the Laboratoire Léon Brillouin, at the Orphée Reactor in Saclay, France.

D

Distribution depth of stone consolidants applied on-site: Analytical modelling with field and lab cross-validation.

In this study, an analytical model was applied to understand the distribution depth of cured stone consolidants applied on-site. Therefore, three consolidants, one alkoxysilane and two colloidal suspensions were applied on a historical façade of St. Stephen's Cathedral in Vienna, Austria. Drilled cores were extracted from the façade and analysed by SEM and image analysis after an appropriate curing period. The image analysis was done to map the cured consolidant inside the fabric and showed that all consolidants exhibited an exponential decline, from the surface to the inner part of the fabric to a varying degree. The exponential decline was more pronounced for the colloidal suspensions (i.e. colloidal silica and nanozirconia) than for the reactive alkoxysilane. The reason for the latter behaviour was ascribed to the action of capillary forces, acting upon drying, which was the governing factor for distributing the consolidants for the water-based nano-zirconia and water-alcohol-based colloidal silica. For reactive alkoxysilane, capillary forces acting upon drying were described to be less significant as this consolidant starts to gel faster, which is why such consolidants exhibited a more homogeneous depth distribution.

Furthermore, DRM were performed on-site in the vicinity of the boreholes where the drilled cores have been extracted to confirm the modelled and image-analysed findings. Drilling resistance showed an over-consolidation, which is in agreement with the applied model. Young's modulus

and splitting tensile strength tests performed on laboratory-treated specimens confirmed the mechanical strength gain assessed through DRM. The applied model, based on a version of the one-dimensional Fick's second law, successfully described the depth distribution, allowing improved interpretations and performance indicators for different stone consolidation treatments.

D.1

Forschung zu Nano-Materialien für die Gesteinsrestaurierung. Auswirkung von Festigungsmaßnahmen in Laborversuchen im Rahmen des EU-Projektes Nano-Cathedral.

This contribution, written only in German, gave an overview of the products developed and the testing protocols used in the frame of the EU supported project 'Nano-Cathedral', funded by the European programme Horizon 2020 Call NMP21-AC (GA 646178). Furthermore, it was shown what stones, representative of European heritage, were used and what reference products (i.e. commercially available stone consolidants) were applied and compared in terms of treatment performance to the newly engineered materials. Certain test procedures were presented and advantages and disadvantages of the tested systems were displayed. This work drew upon the results of a large-scale laboratory testing procedure to support practice-oriented solutions and applications on-site.

4. Conclusions and outlook

The scientific contribution of the work

A

Evolution of calcite surfaces upon thermal decomposition, characterized by electrokinetics, in-situ XRD, and SEM

Four important key aspects of this work were identified that are understudied and lack in published literature. These aspects concern (i) the extent and onset of chemo-mineralogical transformations of solid calcite surface upon thermal treatment, (ii) time-dependend changes of ζ for pristine and thermally treated surfaces, (iii) analysis of pore conductivity effects on the determined ζ and, (iv) fractional contribution to the overall calculated ζ when asymmetric microchannel walls are used.

The original aim of this manuscript was to investigate the effects of thermal treatment for purposes of artificial ageing of natural stones to test stone consolidants. While this particular aspect was not discussed here, it was evident that the streaming potential technique is suitable for monitoring surface changes of solid flat natural stones. Moreover, the use of in-situ XRD was well suited to analyse the onset and extent of chemo-mineralogical alterations and exhibit the differences between the used stones.

Studies on nonequilibrium electrokinetic phenomena or time-dependend changes in ζ for pristine and thermally treated samples are rare. Nonequilibrium is often responsible for scattered results in calcite electrokinetics, but few studies are describing the nonequilibrium and long-term tests, which are crucial where surface reactions at mineral-water interfaces occur. ζ of thermally treated surfaces (mixed calcite and calcium-hydroxide surface) is understudied and not well understood, which is what makes this contribution relevant.

As the streaming potential is more commonly measured in published literature, presenting the results of streaming current measurements is beneficial to highlight the difference between , measurements, highlighting thereby the effect of pore conductivity on underestimating the streaming potential readings especially relevant for rougher surfaces. This particular aspect provides evidence of the importance of careful planning and evaluation of the experiments when performing electrokinetic measurements on porous materials.

The determination of the fractional contribution of the microchannel wall surfaces to the overall determined ζ is relevant especially in the case of geomaterials where mixed mineral compositions are commonly present.

Besides the effects of heat treatment for purposes of artificial ageing of natural stones, a better understanding of thermally treated surfaces that come into contact with aqueous electrolytes is also beneficial for investigations surrounding post-fire restoration/conservation actions. Furthermore, in engineering geology, the topic of different pore solutions and their effect on rock

mechanics is becoming increasingly important (e.g. [114]). The data might even contribute to better fitting the experimental data within the DLVO theory (e.g. [115]). Especially, the results concerning the asymmetric cell arrangement might be of interest for example in the development of lab-on-a-chip devices where electrokinetics in networks (i.e. made of different materials) is studied.

The characterisation strategy described here may contribute to a more accurate determination of the electrokinetic potential for porous macroscopic flat surfaces by considering nonequilibrium and time-dependent changes, including the effects of pore conductivity and reactivity.

A.1

Artificial aging techniques on various lithotypes for testing of stone consolidants

This contribution gave an overview of possible ageing methods for testing stone consolidants. The study showed that thermal treatment allows a cost and time-efficient reduction of soundness reflective of one of the most common degradation processes observed in situ, that is, the presence of microcracks. With this artificially ageing method, it was possible to tailor the decay level and adjust it to every lithotype. The most important thing was that it allowed for large-scale production of samples on which the efficiency of consolidants could be assessed. Furthermore, it showed that thermal treatment was an appropriate method to reproducibly age stone samples in the laboratory on a large number of specimens.

This contribution dealt with the physical changes of stones when exposed to cyclic thermal treatment while the corresponding *Manuscript A* represented an in-depth study on the effect of thermal treatment on the surfaces of calcium carbonates concerning chemo-mineralogical and physical changes.

Normally, lower temperatures are used to study artificial ageing of carbonate stones [116] but also the temperature of 600 °C was employed in this regard [117]. The use of higher temperatures is important because generally, the higher the temperature the more severe the damage. And, the degree of degradation is important when studying stone consolidants. In addition, employing higher temperatures is also relevant in many related fields, especially concerning fire resistance studies (e.g. [118]).

B

Efficiency and compatibility of selected alkoxy-silanes on porous carbonate and silicate stones

Testing the properties of a newly engineered consolidant is a prerequisite before the treatment can be applied to pilot areas. Therefore, this work drew upon the results of a large-scale laboratory testing procedure to support practice-oriented solutions and applications on-site. It further contributed to the understanding of reactive consolidants like alkoxy-silanes. Namely, their properties may change with time. Therefore, caution should be taken especially in the first months after application that is often unrepresentative of the outcome of treatment and may yield an over- or underestimation of various physical parameters. Moreover, the dependency of the treatment performed on the substrate was also displayed. Differences in the relative and absolute mechanical strength increase when comparing the same consolidants on different substrates where highlighted. Finally, the study stressed the importance of using several parameters simultaneously to assess the efficiency and compatibility as well as evaluate possible risks.

B.1

Silicates for the consolidation of stone: nano silica vs. ethyl silicate

The scientific contribution of this work was an experimental examination of certain properties of two consolidating systems, alkoxy-silanes and silica sol. Through such a characterisation of the major drawbacks of a consolidant can be considered before application. In this way, possibly, harmful effects can be avoided or at least minimised. Therefore, gathering knowledge about the differing behaviour of stone consolidants is advantageous for on-site applications.

C

Neutron radiography study of laboratory ageing and treatment applications with stone consolidants

As there are no guidelines on how to apply a consolidant on an architectural surface, this study contributed to the topic by analysing the effect of different application techniques and consolidants and their possible consequences. Neutron radiography as a tool to see inside the stone's fabric allowed to follow the inner pathways of adsorbed water in a consolidated substrate. This was invaluable as it allowed to see e.g. that the polymerisation was initiated inside the stone while the outer surfaces were still mostly hydrophobic. Moreover, it was shown that microstructural differences not consolidated to the same degree represent preferential pathways for water ingress. Neutron radiography also exhibited that small passages can transport water into a hydrophobic fabric, which might lead to further damage. One important aspect of this work displayed is that the degree of polymerisation can vary within a stone and in general, application techniques like poultice and brushing are less favourable. Lastly, nanobased consolidants are favourable for follow-up work on-site. However, mechanical strength gain of nanobased consolidants is lower compared to TEOS.

C.1

The potential of neutron imaging in stone conservation

This contribution should serve as an information piece of the possibility's neutron imaging bears in the field of architectural preservation. It gives a brief overview of some application examples and neutron techniques. It is intended for the first stage and recognised researchers in the field of conservation and restoration, who normally do not know the instrumentation and opportunities surrounding large-scale facilities as this is not part of their curricula.

D

Distribution depth of stone consolidants applied on-site: Analytical modelling with field and lab cross-validation.

This contribution combines on-site assessments, laboratory-based research and the use of an analytical model to assess the treatment performance of three consolidants. On-site it is common to find a degradation gradient that is most severe on the surface and it decreases towards the inner bulk fabric. Therefore, describing gradients by any means is advantageous for the field of stone conservation. The latter is especially important as fewer methods are available on-site to describe the outcome of a treatment's performance. As a consolidant is supposed to equalise such a degradation profile by restoring the physical properties to the amount of the bulk fabric, it is important to analyse the distribution depth of stone consolidants applied on-site. The analytical model used within this work represents a tool that provides an advanced description of the distribution depth and allows to draw a comparison between the used consolidants. The evaluation of the distribution depth was also supported by DRM and image analysis performed on drilled cores that were extracted on-site. Furthermore, some mechanical tests were performed in the laboratory to give further indices about a treatment's efficiency.

Most published studies regarding stone consolidation are descriptive. They describe the substrate before and after the treatment, mostly using either well-established techniques or standardised methods. This study will hopefully lay a foundation for systematic activities of modelling in the area of stone consolidation. Only with a combined effort of experimental and numerical work will the complexity of a treatment's outcome be understood in greater precision.

D.1

Forschung zu Nano-Materialien für die Gesteinsrestaurierung. Auswirkung von Festigungsmaßnahmen in Laborversuchen im Rahmen des EU-Projektes Nano-Cathedral.

With this contribution, it was possible to disseminate the laboratory-based testing programme on how to test stone consolidants, which was established in the frame of the Nano-Cathedral project. This German written contribution allowed sharing ideas and coming into a dialogue with colleagues from the German-speaking area. It offered an overview of all testing methods and approaches used to test the newly engineered consolidants as well as the results obtained.

Outlook on open research agenda

If taken seriously, this paragraph can be turned into a manuscript on its own. Instead, it will focus solely on few (most obvious) subject ideas derived from the published manuscripts.

It will take some time until questions related to the position and densities of the ions in the EDL are resolved experimentally in the field of calcite-water interfaces. The effect of surface roughness and porosity on electrokinetics of flat surfaces is still poorly understood. In the case of asymmetric cell configurations, a more quantitative approach is also lacking. Furthermore, time-resolved studies of ζ until equilibrium is reached in various aqueous electrolytes should be analysed with greater precision. A fascinating feature is the presence of different crystallographic faces in a stone. When these faces come into contact with water or different solvents, or when they have a defect-rich structure to varying degrees they can exhibit different behaviours. The latter is important not only for electrokinetics but also for stone consolidation in general.

A thorough understanding of solid-liquid interfaces could aid in more precisely predict the penetration, deposition, and bonding of the consolidants. On a time scale for application to cure, it would be beneficial to calculate related effects regarding the bonding between the substrate and consolidants. However, studying such effects seems ambitious as many molecular-scale phenomena remain difficult to be experimentally retrieved. An easier approach to start dealing with these questions could be to perform batch experiments, that is, sorption studied (adsorption and desorption kinetics) between nanomaterial-based consolidants and stones. Studies using atomic force microscopy that is probing the interaction between minerals and consolidants in different environments are of relevance. Moreover, devices like the surface force apparatus would be suitable to study the hardening of consolidants between single minerals and the breaking force of the same.

The effect of drying or polymerisation of consolidants is understudied in many aspects. A particular aspect of this topic might be which stone parameters influence the reaction rate of TEOS if any. Moreover, if different consolidants are applied, such as silica sols and TEOS, it should be analysed how far do the consolidants influence each other. It would be interesting to know if and how they influence the chemical reaction of each other or the drying stresses. Variation of the amount of consolidant applied, application techniques used, the period after treatment application to analyse the treatment performance, as well as different curing conditions, should be considered for further studies. The influence of substrate contaminants like gypsum, microbiology or salts and their influence on a consolidation treatment is largely unknown. Topics of durability and re-treatment of consolidants are lacking in published literature. In that regard, it would be interesting to compare how a bulk stone age and how does a consolidated stone age. Changes in microclimatic conditions inside a stone, when a treatment is applied, is also an interesting topic.

A building element made out of stone can exhibit varying decay patterns in the vicinity of each other (e.g. disintegration, gypsum crusts, microbiology, efflorescence, intact surfaces, etc.). The aim of a good restoration and concertation action is always to harmonise these conservation states. Therefore, it is likely that degradation profiles will vary in their extent and degree of mechanical strength decrease. It would be advantageous to analyse what consolidants are particularly suitable for specific degradation phenomena and how far-reaching is their mechanical strength gain. All effort is needed to translate the gained laboratory-based research into practise on-site.

Finally, any artificial ageing technique seems appropriate to study the efficiency and compatibility of stone consolidants if it decreases the mechanical strength of the substrate. Studying the starting point of the artificially aged stone and knowing the characteristics of the substrate in detail is a prerequisite to know what modifications were introduced due to the treatment with stone consolidants. Therefore, thermal treatment even up to 600 °C is justified, especially in cases of carbonates, where the surface chemistry recovers due to re-carbonation processes. However, consequences of thermal treatment on permanent modifications of e.g. kaolinite and subsequent consolidation or its reactivity in an aqueous environment were not studied before. Moreover, in-situ XRD and electrokinetics focused on the surface of the stones, therefore, it would be advantageous to study the extent of those chemo-mineralogical changes inside the bulk structure if present. Micromechanical tests of artificially or naturally weathered surfaces with methods like e.g. nanoindentation would be good to measure the hardness of small volumes of surface exposed to the environment and compare them to bulk protected surfaces.

Most above-mentioned topics should be accessed with a combined effort of experimental and numerical work to start resolving the complexity of natural or artificial weathering and a treatment's outcome.

References

1. Delgado Rodrigues J, Grossi A (2007) Indicators and ratings for the compatibility assessment of conservation actions. *J. Cult. Herit.* 8 (1):32-43. doi:10.1016/j.culher.2006.04.007
2. Lazzeri A, Coltelli MB, Castelvetro V, Bianchi S, Chiantore O, Lezzerini M, Gherardi F, Toniolo, L (2016) European Project "NANO-CATHEDRAL: Nanomaterials for conservation of European architectural heritage developed by research on characteristic lithotypes". In 13th International Congress on the Deterioration and Conservation of Stone, University of the West of Scotland, (Vol. 2, pp. 847-854).
3. Alves C, Figueiredo C, Sanjurjo-Sánchez J (2020) Rock Features and Alteration of Stone Materials Used for the Built Environment: A Review of Recent Publications on Ageing Tests. *Geosciences (Basel)* 10 (3). doi:10.3390/geosciences10030091
4. Franzoni E, Sassoni E (2011) Correlation between microstructural characteristics and weight loss of natural stones exposed to simulated acid rain. *Sci. Total Environ.* 412-413:278-285. doi:10.1016/j.scitotenv.2011.09.080
5. Franzoni E, Sassoni E (2012) Comparison between different methodologies for artificial deterioration of stone aimed at consolidants testing. In Proceedings of 12th International Congress on Deterioration and Conservation of Stone, New York City, USA (pp. 22-26).
6. Sitzia F, Lisci C, Mirão J (2021) Accelerate ageing on building stone materials by simulating daily, seasonal thermo-hygrometric conditions and solar radiation of Csa Mediterranean climate. *Constr. Build. Mater.* 266. doi:10.1016/j.conbuildmat.2020.121009
7. Ruedrich J, Kirchner D, Siegesmund S (2011) Physical weathering of building stones induced by freeze-thaw action: a laboratory long-term study. *Environ. Earth Sci.* 63 (7-8):1573-1586. doi:10.1007/s12665-010-0826-6
8. Deprez M, De Kock T, De Schutter G, Cnudde V (2020) A review on freeze-thaw action and weathering of rocks. *Earth Sci. Rev.* 203. doi:10.1016/j.earscirev.2020.103143
9. Rampazzi L, Andreotti A, Bonaduce I, Colombini MP, Colombo C, Toniolo L (2004) Analytical investigation of calcium oxalate films on marble monuments. *Talanta* 63 (4):967-977. doi:10.1016/j.talanta.2004.01.005
10. Sand W, Bock E (1991) Biodeterioration of mineral materials by microorganisms-biogenic sulfuric and nitric acid corrosion of concrete and natural stone. *Geomicrobiol. J.* 9 (2-3):129-138. doi:10.1080/01490459109385994
11. Wilhelm K, Longman J, Orr SA, Viles H (2021) Stone-built heritage as a proxy archive for long-term historical air quality: A study of weathering crusts on three generations of stone sculptures on Broad Street, Oxford. *Sci. Total Environ.* 759:143916. doi:10.1016/j.scitotenv.2020.143916
12. Gomez-Heras M, McCabe S, Smith BJ, Fort R (2009) Impacts of Fire on Stone-Built Heritage. *J. Archit. Conserv.* 15 (2):47-58. doi:10.1080/13556207.2009.10785047
13. Garlock M, Paya-Zaforteza I, Kodur V, Gu L (2012) Fire hazard in bridges: Review, assessment and repair strategies. *Eng. Struct.* 35:89-98. doi:10.1016/j.engstruct.2011.11.002

14. Vazzoler JdS, Vieira GL, Teles CR, Degen MK, Teixeira RA (2018) Investigation of the potential use of waste from ornamental stone processing after heat treatment for the production of cement-based paste. *Constr. Build. Mater.* 177:314-321. doi:10.1016/j.conbuildmat.2018.05.098
15. Tang C-S, Cui Y-J, Tang A-M, Shi B (2010) Experiment evidence on the temperature dependence of desiccation cracking behavior of clayey soils. *Eng. Geol.* 114 (3-4):261-266. doi:10.1016/j.enggeo.2010.05.003
16. Maritan L, Nodari L, Mazzoli C, Milano A, Russo U (2006) Influence of firing conditions on ceramic products: Experimental study on clay rich in organic matter. *Appl. Clay Sci.* 31 (1-2):1-15. doi:10.1016/j.clay.2005.08.007
17. Cerantola V, Bykova E, Kuppenko I, Merlini M, Ismailova L, McCammon C, Bykov M, Chumakov AI, Petitgirard S, Kantor I, Svitlyk V, Jacobs J, Hanfland M, Mezouar M, Prescher C, Ruffer R, Prakapenka VB, Dubrovinsky L (2017) Stability of iron-bearing carbonates in the deep Earth's interior. *Nat. Commun.* 8:15960. doi:10.1038/ncomms15960
18. Sanjurjo-Sánchez J, Gomez-Heras M, Fort R, Alvarez de Buergo M, Izquierdo Benito R, Bru MA (2016) Dating fires and estimating the temperature attained on stone surfaces. The case of Ciudad de Vascos (Spain). *Microchem. J.* 127:247-255. doi:10.1016/j.microc.2016.03.017
19. Gatta T, Gregori E, Marini F, Tomassetti M, Visco G, Campanella L (2014) New approach to the differentiation of marble samples using thermal analysis and chemometrics in order to identify provenance. *Chem. Cent. J.* 8 (1):35
20. Zhao C, Zhang Y, Wang C-C, Hou M, Li A (2019) Recent progress in instrumental techniques for architectural heritage materials. *Herit. Sci.* 7 (1). doi:10.1186/s40494-019-0280-z
21. Tretiach M, Bertuzzi S, Candotto Carniel F (2012) Heat shock treatments: a new safe approach against lichen growth on outdoor stone surfaces. *Environ. Sci. Technol.* 46 (12):6851-6859. doi:10.1021/es3006755
22. Franzoni E, Sassoni E, Scherer GW, Naidu S (2013) Artificial weathering of stone by heating. *J. Cult. Herit.* 14 (3):E85-E93. doi:10.1016/j.culher.2012.11.026
23. Ban M, De Kock T, Ott F, Barone G, Rohatsch A, Raneri S (2019) Neutron Radiography Study of Laboratory Ageing and Treatment Applications with Stone Consolidants. *Nanomaterials (Basel)* 9 (4). doi:10.3390/nano9040635
24. Martinho E, Mendes M, Dionisio A (2017) 3D imaging of P-waves velocity as a tool for evaluation of heat induced limestone decay. *Constr. Build. Mater.* 135:119-128. doi:10.1016/j.conbuildmat.2016.12.192
25. Ozguven A, Ozcelik Y (2014) Effects of high temperature on physico-mechanical properties of Turkish natural building stones. *Eng. Geol.* 183:127-136. doi:10.1016/j.enggeo.2014.10.006
26. Tian H, Kempka T, Xu N-X, Ziegler M (2012) Physical Properties of Sandstones After High Temperature Treatment. *Rock Mech. Rock Eng.* 45 (6):1113-1117. doi:10.1007/s00603-012-0228-z
27. Wang F, Frühwirt T, Konietzky H (2020) Influence of repeated heating on physical-mechanical properties and damage evolution of granite. *Int. J. Rock Mech. Min.* 136. doi:10.1016/j.ijrmms.2020.104514

28. Vagnon F, Colombero C, Colombo F, Comina C, Ferrero AM, Mandrone G, Vinciguerra SC (2019) Effects of thermal treatment on physical and mechanical properties of Valdieri Marble - NW Italy. *Int. J. Rock Mech. Min.* 116:75-86. doi:10.1016/j.ijrmms.2019.03.006
29. Rosenholtz JL, Smith DT (1949) Linear thermal expansion of calcite, var. Iceland spar, and Yule Marble. *Am. Min.* 34 (11-12):846-854
30. Lawn B, Marshall D, Raj R, Hirth G, Page T, Yeomans J (2020) Precipitous weakening of quartz at the $\alpha - \beta$ phase inversion. *J. Am. Ceram. Soc.* 104 (1):23-26. doi:10.1111/jace.17470
31. Kieslinger A (1932) Zerstörungen an Steinbauten: ihre Ursachen und ihre Abwehr. F. Deuticke.
32. Biró A, Hlavička V, Lublőy É (2019) Effect of fire-related temperatures on natural stones. *Constr. Build. Mater.* 212:92-101. doi:10.1016/j.conbuildmat.2019.03.333
33. Praticò Y, Ochsendorf J, Holzer S, Flatt RJ (2020) Post-fire restoration of historic buildings and implications for Notre-Dame de Paris. *Nat. Mater.* 19 (8):817-820
34. Siegesmund S, Snethlage R, eds. (2011) *Stone in architecture: properties, durability.* Springer Science & Business Media.
35. Sena da Fonseca B, Ferreira Pinto AP, Piçarra S, Montemor MF (2020) Alkoxysilane-based sols for consolidation of carbonate stones: Proposal of methodology to support the design and development of new consolidants. *J. Cult. Herit.* 43:51-63. doi:10.1016/j.culher.2019.11.003
36. Ševčík R, Viani A, Machová D, Lanzafame G, Mancini L, Appavou M-S (2019) Synthetic calcium carbonate improves the effectiveness of treatments with nanolime to contrast decay in highly porous limestone. *Sci. Rep.* 9 (1):1-13
37. Costanza Miliani, Melanie L. Velo-Simpson, Scherer GW (2007) Particle-modified consolidants: A study on the effect of particles on solegel properties and consolidation effectiveness. *J. Cult. Herit.* 8:1-6. doi:10.1016/j.culher.2006.10.002
38. Sassoni E, D'Amen E, Roveri N, Scherer GW, Franzoni E (2018) Durable Self-Cleaning Coatings for Architectural Surfaces by Incorporation of TiO₂ Nano-Particles into Hydroxyapatite Films. *Materials (Basel)* 11 (2). doi:10.3390/ma11020177
39. Sierra-Fernandez A, De la Rosa-Garcia SC, Gomez-Villalba LS, Gomez-Cornelio S, Rabanal ME, Fort R, Quintana P (2017) Synthesis, Photocatalytic, and Antifungal Properties of MgO, ZnO and Zn/Mg Oxide Nanoparticles for the Protection of Calcareous Stone Heritage. *ACS Appl. Mater. Interfaces* 9 (29):24873-24886. doi:10.1021/acsami.7b06130
40. Borsoi G, Lubelli B, van Hees R, Veiga R, Silva AS (2016) Understanding the transport of nanolime consolidants within Maastricht limestone. *J. Cult. Herit.* 18:242-249. doi:10.1016/j.culher.2015.07.014
41. Cnudde V, Cnudde JP, Dupuis C, Jacobs PJS (2004) X-ray micro-CT used for the localization of water repellents and consolidants inside natural building stones. *Mater. Charact.* 53 (2-4):259-271. doi:10.1016/j.matchar.2004.08.011
42. Ropret P, Legan L, Retko K, Špec T, Pondelak A, Škrlep L, Sever Škapin A (2017) Evaluation of vibrational spectroscopic techniques for consolidants' penetration depth determination. *J. Cult. Herit.* 23:148-156. doi:10.1016/j.culher.2016.07.004

43. Gil MLA, Luna M, Zarzuela R, García-Moreno MV (2020) Quantitative determination of the penetration of a silica-based consolidant in a limestone by FTIR spectroscopy. *Vib. Spectrosc.* 110. doi:10.1016/j.vibspec.2020.103109
44. Hameed F, Schillinger B, Rohatsch A, Zawisky M, Rauch H (2009) Investigations of stone consolidants by neutron imaging. *Nucl. Instrum. Methods Phys. Res.* 605 (1-2):150-153. doi:10.1016/j.nima.2009.01.139
45. Monico L, Cartechini L, Rosi F, De Nolf W, Cotte M, Vivani R, Maurich C, Miliani C (2020) Synchrotron radiation Ca K-edge 2D-XANES spectroscopy for studying the stratigraphic distribution of calcium-based consolidants applied in limestones. *Sci. Rep.* 10 (1):14337. doi:10.1038/s41598-020-71105-8
46. Rohatsch A (2005) Neogene Bau-und Dekorgesteine Niederösterreichs und des Burgenlandes. In: Schwaighofer, B., Eppensteiner, W. (Eds.), "Junge" Kalke, Sandsteine und Konglomerate - Neogen. Mitteilungen IAG BOKU, pp. 27-31.,
47. Graue B, Siegesmund S, Middendorf B (2011) Quality assessment of replacement stones for the Cologne Cathedral: mineralogical and petrophysical requirements. *Environ. Earth Sci.* 63 (7-8):1799-1822. doi:10.1007/s12665-011-1077-x
48. Graue BJ (2013) Stone deterioration and replacement of natural building stones at the Cologne cathedral - A contribution to the preservation of cultural heritage. Doctoral Thesis. Georg-August-Universität Göttingen,
49. Ban M, Baragona A, Ghaffari E, Weber J, Rohatsch A (2016). Artificial aging techniques on various lithotypes for testing of stone consolidants. In *Science and Art: A Future for Stone: Proceedings of the 13th International Congress on the Deterioration and Conservation of Stone*, University of the West of Scotland, (Vol. 1, pp. 253-260).
50. Denry I, Kelly JR (2008) State of the art of zirconia for dental applications. *Dent. Mater.* 24 (3):299-307. doi:10.1016/j.dental.2007.05.007
51. Berto T, Godts S, De Clercq H (2016) The effects of commercial ethyl silicate based consolidation products on limestone. *Science and art: a future for stone*, 271. In *Science and Art: A Future for Stone: Proceedings of the 13th International Congress on the Deterioration and Conservation of Stone*, University of the West of Scotland.
52. Geissbühler P, Fenter P, DiMasi E, Srajer G, Sorensen LB, Sturchio NC (2004) Three-dimensional structure of the calcite-water interface by surface X-ray scattering. *Surf. Sci.* 573 (2):191-203. doi:10.1016/j.susc.2004.09.036
53. Stipp SLS (1999) Toward a conceptual model of the calcite surface: Hydration, hydrolysis, and surface potential. *Geochim. Cosmochim. Ac.* 63 (19-20):3121-3131. doi:10.1016/S0016-7037(99)00239-2
54. Kirby BJ, Hasselbrink EF, Jr. (2004) Zeta potential of microfluidic substrates: 1. Theory, experimental techniques, and effects on separations. *Electrophoresis* 25 (2):187-202. doi:10.1002/elps.200305754
55. Revil A, Pezard PA, Glover PWJ (1999) Streaming potential in porous media: 1. Theory of the zeta potential. *J. Geophys. Res. Solid Earth* 104 (B9):20021-20031. doi:10.1029/1999jb900089
56. Delgado AV, Gonzalez-Caballero F, Hunter RJ, Koopal LK, Lyklema J, International Union of P, Applied Chemistry P, Biophysical Chemistry Division ITR (2007) Measurement and interpretation of electrokinetic phenomena. *J. Colloid Interface Sci.* 309 (2):194-224. doi:10.1016/j.jcis.2006.12.075

57. Li D. (2004) *Electrokinetics in microfluidics*, vol 2. Elsevier.
58. Delgado ÁV (2001) *Interfacial electrokinetics and electrophoresis*, vol 106. CRC Press.
59. Lyklema J (1995) *Solid-liquid interfaces*. Academic Press.
60. Butt H-J, Graf K, Kappl M (2013) *Physics and chemistry of interfaces*. John Wiley & Sons.
61. Israelachvili JN (2015) *Intermolecular and surface forces*. Academic press,
62. Hunter RJ (2013) *Zeta potential in colloid science: principles and applications*, vol 2. Academic press.
63. Luxbacher T (2014) *The ZETA guide: Principles of the streaming potential technique*. Anton Paar GmbH: Graz, Austria.
64. Brown MA, Abbas Z, Kleibert A, Green RG, Goel A, May S, Squires TM (2016) Determination of Surface Potential and Electrical Double-Layer Structure at the Aqueous Electrolyte-Nanoparticle Interface. *Phys. Rev. X* 6 (1). doi:10.1103/PhysRevX.6.011007
65. Bazant MZ, Kilic MS, Storey BD, Ajdari A (2009) Towards an understanding of induced-charge electrokinetics at large applied voltages in concentrated solutions. *Adv. Colloid Interface Sci.* 152 (1-2):48-88. doi:10.1016/j.cis.2009.10.001
66. Joly L, Ybert C, Trizac E, Bocquet L (2004) Hydrodynamics within the Electric Double Layer on Slipping Surfaces. *Phys. Rev. Lett.* 93 (25). doi:10.1103/PhysRevLett.93.257805
67. Walker SL, Bhattacharjee S, Hoek EM, Elimelech M (2002) A novel asymmetric clamping cell for measuring streaming potential of flat surfaces. *Langmuir* 18 (6):2193-2198
68. Bruus H (2008) *Theoretical microfluidics*, vol 18. Oxford university press Oxford.
69. Erickson D, Li D, Werner C (2000) An Improved Method of Determining the zeta-Potential and Surface Conductance. *J. Colloid Interface Sci.* 232 (1):186-197. doi:10.1006/jcis.2000.7153
70. Elimelech M, Nagai M, Ko C-H, Ryan JN (2000) Relative insignificance of mineral grain zeta potential to colloid transport in geochemically heterogeneous porous media. *Environ. Sci. Technol.* 34 (11):2143-2148
71. Zimmermann R, Osaki T, Schweiß R, Werner C (2006) Electrokinetic microslit experiments to analyse the charge formation at solid/liquid interfaces. *Microfluidics and Nanofluidics* 2 (5):367-379. doi:10.1007/s10404-006-0087-6
72. Werner C, Korber H, Zimmermann R, Dukhin S, Jacobasch HJ (1998) Extended Electrokinetic Characterization of Flat Solid Surfaces. *J. Colloid Interface Sci.* 208 (1):329-346. doi:10.1006/jcis.1998.5787
73. Cherubini A, Garcia B, Cerepi A, Revil A (2018) Streaming Potential Coupling Coefficient and Transport Properties of Unsaturated Carbonate Rocks. *Vadose Zone J.* 17 (1). doi:10.2136/vzj2018.02.0030
74. Li S, Leroy P, Heberling F, Devau N, Jougnot D, Chiaberge C (2016) Influence of surface conductivity on the apparent zeta potential of calcite. *J. Colloid Interface Sci.* 468:262-275. doi:10.1016/j.cis.2016.01.075
75. Fairbrother F, Mastin H (1924) CCCXII. Studies in electro-endosmosis. Part I. *J. Chem. Soc., Dalton Trans.* 125:2319-2330

76. Degen T, Sadki M, Bron E, König U, Nénert G (2014) The HighScore suite. Powder Diffr. 29 (S2):S13-S18. doi:10.1017/s0885715614000840
77. Faber J, Fawcett T (2002) The powder diffraction file: present and future. Acta Crystallogr. Sec. B: Struct. Sci. Cryst. Eng. Mater. 58 (3):325-332
78. Kabekkodu SN, Faber J, Fawcett T (2002) New Powder Diffraction File (PDF-4) in relational database format: advantages and data-mining capabilities. Acta Crystallogr. Sec. B: Struct. Sci. Cryst. Eng. Mater. 58 (3):333-337
79. CEN (2010) Standard EN 15801, Conservation of cultural property. Determination of water absorption by capillarity.
80. CEN (2013) Standard EN 16322, Conservation of cultural heritage. Determination of drying properties.
81. CEN (2010) Standard EN 15803, Conservation of cultural property-test methods-Determination of water vapour permeability.
82. CEN (2004) Standard EN 14146, Determination of dynamic elastic modulus by measuring the fundamental resonant frequency.
83. CEN (2005) Standard EN 14579: Natural stone test methods. Determination of sound speed propagation.
84. CEN (2010) Standard EN 15802 Conservation of cultural property. Determination of static contact angle. UNI, Ente Nazionale Italiano di Unificazione.
85. Rodrigues JD, Costa D (2004) A new method for data correction in drill resistance tests for the effect of drill bit wear. International Journal for Restoration of Buildings and Monuments 10:219-236
86. CEN (2010) Standard EN 15886, Conservation of cultural property. Colour measurement of surfaces.
87. ASTM International WC, USA (2008) ASTM D 3967–08, Standard test method for splitting tensile strength of intact rock core specimens.
88. CEN (2007) Standard EN 12372 Natural stone test methods-Determination of flexural strength under concentrated load.
89. Teixeira J, Magli R, Loupiac C (2015) Neutron scattering and imaging: a tool for archaeological studies. Eur. J. Mineral. 27 (3):289-296. doi:10.1127/ejm/2015/0027-2440
90. Kapral L, Zawisky M, Abele H (2020) Neutron Radiography and Tomography of the Drying Process of Screed Samples. Journal of Imaging (Basel) 6 (11). doi:10.3390/jimaging6110118
91. Perfect E, Cheng CL, Kang M, Bilheux HZ, Lamanna JM, Gragg MJ, Wright DM (2014) Neutron imaging of hydrogen-rich fluids in geomaterials and engineered porous media: A review. Earth-Sci. Rev. 129:120-135. doi:10.1016/j.earscirev.2013.11.012
92. Raneri S, Barone G, Mazzoleni P, Alfieri I, Bergamonti L, De Kock T, Cnudde V, Lottici PP, Lorenzi A, Predieri G, Rabot E, Teixeira J (2018) Efficiency assessment of hybrid coatings for natural building stones: Advanced and multi-scale laboratory investigation. Constr. Build. Mater. 180:412-424. doi:10.1016/j.conbuildmat.2018.05.289

93. Zhang P, Wittmann FH, Lura P, Müller HS, Han S, Zhao T (2018) Application of neutron imaging to investigate fundamental aspects of durability of cement-based materials: A review. *Cem. Concr. Res.* 108:152-166. doi:10.1016/j.cemconres.2018.03.003
94. Schillinger (2019) An Affordable Image Detector and a Low-Cost Evaluation System for Computed Tomography Using Neutrons, X-rays or Visible Light. *Quantum Beam Science* 3 (4). doi:10.3390/qubs3040021
95. Dawson MN (2008) Applications of neutron radiography & tomography. Doctoral Thesis. University of Leeds.
96. Kardjilov N, Manke I, Hilger A, Strobl M, Banhart J (2011) Neutron imaging in materials science. *Mater. Today* 14 (6):248-256. doi:10.1016/s1369-7021(11)70139-0
97. Zambrano M, Hameed F, Anders K, Mancini L, Tondi E (2019) Implementation of Dynamic Neutron Radiography and Integrated X-Ray and Neutron Tomography in Porous Carbonate Reservoir Rocks. *Front. Earth Sci.* 7. doi:10.3389/feart.2019.00329
98. Schindelin J, Arganda-Carreras I, Frise E, Kaynig V, Longair M, Pietzsch T, Preibisch S, Rueden C, Saalfeld S, Schmid B, Tinevez JY, White DJ, Hartenstein V, Eliceiri K, Tomancak P, Cardona A (2012) Fiji: an open-source platform for biological-image analysis. *Nat. Methods* 9 (7):676-682. doi:10.1038/nmeth.2019
99. Hassanein RK (2006) Correction methods for the quantitative evaluation of thermal neutron tomography. Doctoral Thesis. ETH Zurich.
100. Dewanckele J, De Kock T, Fronteau G, Derluyn H, Vontobel P, Dierick M, Van Hoorebeke L, Jacobs P, Cnudde V (2014) Neutron radiography and X-ray computed tomography for quantifying weathering and water uptake processes inside porous limestone used as building material. *Mater. Charact.* 88:86-99. doi:10.1016/j.matchar.2013.12.007
101. Kang M, Bilheux HZ, Voisin S, Cheng CL, Perfect E, Horita J, Warren JM (2013) Water calibration measurements for neutron radiography: Application to water content quantification in porous media. *Nucl. Instrum. Methods Phys. Res.* 708:24-31. doi:10.1016/j.nima.2012.12.112
102. Kim FH, Penumadu D, Hussey DS (2012) Water Distribution Variation in Partially Saturated Granular Materials Using Neutron Imaging. *J. Geotech. Geoenviron.* 138 (2):147-154. doi:10.1061/(asce)gt.1943-5606.0000583
103. Randazzo L, Paladini G, Venuti V, Crupi V, Ott F, Montana G, Ricca M, Rovella N, La Russa MF, Majolino D (2020) Pore Structure and Water Transfer in Pietra d'Aspra Limestone: A Neutronographic Study. *Applied Sciences (Basel)* 10 (19). doi:10.3390/app10196745
104. Scherer GW, Wheeler GS (2009) Silicate consolidants for stone In: *Key Engineering Materials*, Trans Tech Publications Ltd, vol. 391, pp 1-25. doi:10.4028/www.scientific.net/KEM.391.1
105. Peruzzi R, Poli T, Toniolo L (2003) The experimental test for the evaluation of protective treatments: a critical survey of the "capillary absorption index". *J. Cult. Herit.* 4 (3):251-254. doi:10.1016/S1296-2074(03)00050-5
106. Papadopoulos F, Spinelli M, Valente S, Foroni L, Orrico C, Alviano F, Pasquinelli G (2007) Common tasks in microscopic and ultrastructural image analysis using ImageJ. *Ultrastruct. Pathol.* 31 (6):401-407. doi:10.1080/01913120701719189

107. Volfkovich YM, Filippov AN, Bagotsky VS (2014) Structural properties of porous materials and powders used in different fields of science and technology. Springer. doi:10.1007/978-1-4471-6377-0
108. Filippov A, Starov V, Llyod D, Chakravarti S, Glaser S (1994) Sieve mechanism of microfiltration. *Journal of membrane science* 89 (3):199-213. doi:10.1016/0376-7388(94)80102-9
109. Filippov AN, Iksanov RK (2012) Mathematical modeling of microfiltration of polydisperse suspension on heterogeneous membranes. *Pet. Chem.* 52 (7):520-526. doi:10.1134/s0965544112070043
110. Happel J, Brenner H (2012) *Low Reynolds number hydrodynamics: with special applications to particulate media*, vol 1. Springer Science & Business Media.
111. Barenblatt GI, Entov VM, Ryzhik VM (1989) *Theory of fluid flows through natural rocks*.
112. Šperl J, Trčková J (2008) Permeability and porosity of rocks and their relationship based on laboratory testing. *Acta Geodyn. Geomater.* 5 (149):41-47
113. Brace WF (1980) Permeability of crystalline and argillaceous rocks. *Int. J. Rock Mech. Min. Sci. Geomech. Abstr.* doi:10.1016/0148-9062(80)90807-4
114. Pluymakers A, Ougier-Simonin A, Barnhoorn A (2021) Ion-species in pore fluids with opposite effects on limestone fracturing. *Geomech. Energy Envir.* 26. doi:10.1016/j.gete.2021.100233
115. Tetteh JT, Brady PV, Barati Ghahfarokhi R (2020) Review of low salinity waterflooding in carbonate rocks: mechanisms, investigation techniques, and future directions. *Adv. Colloid Interface Sci.* 284:102253. doi:10.1016/j.cis.2020.102253
116. Sena da Fonseca B, Pinto APF, Rodrigues A, Piçarra S, Fonseca D, Montemor MF (2021) On the estimation of marbles weathering by thermal action using drilling resistance. *J. Build. Eng.* doi:10.1016/j.jobbe.2021.102494
117. Aragoni MC, Giacometti L, Arca M, Carcangiu G, Columbu S, Gimeno D, Isaia F, Lippolis V, Meloni P, Ezquerra AN, Podda E, Rius J, Vallcorba O, Pintus A (2021) Ammonium monoethyloxalate (AmEtOx): a new agent for the conservation of carbonate stone substrates. *New J. Chem.* 45 (12):5327-5339. doi:10.1039/d0nj06001a
118. Ersoy H, Atalar C, Sünnetci MO, Kolaylı H, Karahan M, Fırat Ersoy A (2021) Assessment of damage on geo-mechanical and micro-structural properties of weak calcareous rocks exposed to fires using thermal treatment coefficient. *Eng. Geol.* 284. doi:10.1016/j.enggeo.2021.106046

Curriculum vitae

MATEA BAN

ORCID iD: 0000-0002-0169-7327

PERSONAL DETAILS

Date of birth	18/01/1986
Place of birth	Slavonski Brod, Croatia (Croatian nationality)
E-mail	mateaban@yahoo.com
Languages	Croatian (native), German (fluent), English (fluent)

WORK EXPERIENCE (selection)

08/2018 – present

University Assistant, VIENNA UNIVERSITY OF TECHNOLOGY, AT

Faculty of Civil Engineering, Institute of Geotechnics, Research Centre of Engineering Geology.

09/2018 – 03/2020

Research Fellow, MARIETTA BLAU GRANT (BMBWF)

- Institute of Theoretical and Applied Mechanics, Czech Academy of Sciences,
- Department of Civil and Industrial Engineering, University of Pisa, Italy,
- Department of Chemistry and Industrial Chemistry, University of Pisa, Italy,
- Karlsruhe Institute of Technology, Institute for Nuclear Waste Disposal, Germany.

05/2015 – 08/2018

Research Assistant, VIENNA UNIVERSITY OF TECHNOLOGY, AT

Faculty of Civil Engineering, Institute of Geotechnics, Research Centre of Engineering Geology. European Horizon 2020 Project “Nanomaterials for conservation of European architectural heritage developed by research on characteristic lithotypes”, (Nano-Cathedral, GA 646178).

EDUCATION

06/2021 (Defensio planned)

Doctor of Natural Sciences in Civil Engineering, VIENNA UNIVERSITY OF TECHNOLOGY, AT

Title of the thesis: Chemo-mineralogical and petrophysical alterations on lithotypes due to thermal treatment before stone consolidation

Graduation 11/2015

Bachelor in Architecture, ACADEMY OF FINE ARTS VIENNA, AT

Graduation 01/2011

Master in Conservation and Restoration, UNIVERSITY OF APPLIED ARTS VIENNA, AT

Subject area: Stone and mineral materials. Title of the thesis: Aspekte zur Erhaltung von Sichtbetonarchitektur am Beispiel der Wotruba-Kirche.

Journal articles (Peer-Review)

Ban, M., Luxbacher, T., Lützenkirchen, J., Viani, A., Bianchi, S., Hradil, K., Rohatsch, A. & Valter Castelvetro, V. (2021). Evolution of calcite surfaces upon thermal decomposition, characterized by electrokinetics, in-situ XRD, and SEM. *Colloids and Surfaces A: Physicochemical and Engineering Aspects*, 126761.

Ban, M., Aliotta, L., Gigante, V., Mascha, E., Sola, A., & Lazzeri, A. (2020). Distribution depth of stone consolidants applied on-site: Analytical modelling with field and lab cross-validation. *Construction and Building Materials*, 259, 120394.

Ban, M., De Kock, T., Ott, F., Barone, G., Rohatsch, A., & Raneri, S. (2019). Neutron radiography study of laboratory ageing and treatment applications with stone consolidants. *Nanomaterials*, 9(4), 635.

Ban, M., Mascha, E., Weber, J., Rohatsch, A., & Delgado Rodrigues, J. (2019). Efficiency and compatibility of selected alkoxy-silanes on porous carbonate and silicate stones. *Materials*, 12(1), 156.

Contributions to edited volumes (Peer-Review)

Mascha, E., **Ban, M.**, Weber, J., & Rohatsch, A. (2020). Silicates for the consolidation of stone: nano silica vs. ethyl silicate. In: S. Siegesmund, B. Middendorf (Eds.) *Monument Future: Decay and Conservation of Stone. Proceedings of the 14th International Congress on the Deterioration and Conservation of Stone*. Göttingen and Kassel, Mitteldeutscher Verlag GmbH, Halle (Saale), 525-531.

Raneri, S., De Kock, T., Rohatsch, A., & **Ban, M.** (2020). The potential of neutron imaging in stone conservation. In: S. Siegesmund, B. Middendorf (Eds.) *Monument Future: Decay and Conservation of Stone. Proceedings of the 14th International Congress on the Deterioration and Conservation of Stone*. Göttingen and Kassel, Mitteldeutscher Verlag GmbH, Halle (Saale), 1053-1059.

Milchin, M., Pesce, C., Weber, J., Krist, G., **Ban, M.** & Anghelone, M. (2020). An evaluation of shelter coats for the protection of outdoor stones. In: S. Siegesmund, B. Middendorf (Eds.) *Monument Future: Decay and Conservation of Stone. Proceedings of the 14th International Congress on the Deterioration and Conservation of Stone*. Göttingen and Kassel, Mitteldeutscher Verlag GmbH, Halle (Saale), 645-651.

Mascha, E., Weber, J., & **Ban, M.** (2018). Forschung zu Nano-Materialien für die Gesteinsrestaurierung. Auswirkung von Festigungsmaßnahmen in Laborversuchen im Rahmen des EU-Projektes Nano-Cathedral. In: P. Gabriele et al. (Eds.) *Natursteinsanierung Stuttgart 2018. Neue Natursteinrestaurierungsergebnisse und messtechnische Erfassungen sowie Sanierungsbeispiele*. Fraunhofer IRB Verlag, 75-88

Ban M. & Pliessnig M. (2018), The Biedermeier cemetery of St. Marx in Vienna: planning, management and treatment implementation, In: S.M. Sunara, A. Thorn (Eds.), *The Conservation of Sculpture Parks*, London: Archetype Publications Ltd., 59-72.

Ban, M., Baragona, A., Ghaffari, E., Weber, J., & Rohatsch, A. (2016). Artificial aging techniques on various lithotypes for testing of stone consolidants. In: J.J. Hughes, T. Howind (Eds.), *Science and Art: A Future for Stone. Proceedings of the 13th International Congress on the Deterioration and Conservation of Stone*, University of the West of Scotland, Paisley, 1: 253-260.

Ban M. (2015), Pflege und Erhaltung von Sichtbeton. In: G. Krist (Ed.), *Collection Care/Sammlungspflege*, Wien: Böhlau Verlag, 232-335.

Ban M. (2014), Wotruba Church and Cologne Opera: Aspects of concrete aging. In: M. Graham et al. (Eds.), Concrete Solutions, London: Taylor & Francis Group, 619-627.

Ban M. (2014), Aspects of conserving exposed concrete architecture with Wotruba Church as an example. In: D. Bjegovic et al. (Eds.), Proceedings of the RILEM international workshop on performance-based specification and control of concrete durability, Bagneux: RILEM Publications S.A.R.L., 549-557.

Other publications

Ban M., et al. (2018), Leitfaden Schlämmen in Restaurierung und Denkmalpflege, Wien: Bundesdenkmalamt Österreich (<https://bda.gv.at/publikationen/standards-leitfaeden-richtlinien/>).

Appendices

Ban, M., Luxbacher, T., Lützenkirchen, J., Viani, A., Bianchi, S., Hradil, K., Rohatsch, A. & Valter Castelvetro, V. (2021). Evolution of calcite surfaces upon thermal decomposition, characterized by electrokinetics, in-situ XRD, and SEM. *Colloids and Surfaces A: Physicochemical and Engineering Aspects*, 126761.

<https://doi.org/10.1016/j.colsurfa.2021.126761>

<https://www.sciencedirect.com/science/article/pii/S0927775721006300>

Ban, M., Mascha, E., Weber, J., Rohatsch, A., & Delgado Rodrigues, J. (2019). Efficiency and compatibility of selected alkoxy-silanes on porous carbonate and silicate stones. *Materials*, 12(1), 156.

<https://doi.org/10.3390/ma12010156>

<https://www.mdpi.com/1996-1944/12/1/156>

Ban, M., De Kock, T., Ott, F., Barone, G., Rohatsch, A., & Raneri, S. (2019). Neutron radiography study of laboratory ageing and treatment applications with stone consolidants. *Nanomaterials*, 9(4), 635.

<https://doi.org/10.3390/nano9040635>

https://www.mdpi.com/2079-4991/9/4/635?utm_source=TrendMD&utm_medium=cpc&utm_campaign=Nanomaterials_TrendMD_0

Ban, M., Aliotta, L., Gigante, V., Mascha, E., Sola, A., & Lazzeri, A. (2020). Distribution depth of stone consolidants applied on-site: Analytical modelling with field and lab cross-validation. *Construction and Building Materials*, 259, 120394.

<https://doi.org/10.1016/j.conbuildmat.2020.120394>

<https://www.sciencedirect.com/science/article/pii/S0950061820323990>

A

Evolution of calcite surfaces upon thermal decomposition,
characterized by electrokinetics, in-situ XRD, and SEM



Contents lists available at ScienceDirect

Colloids and Surfaces A: Physicochemical and Engineering Aspects

journal homepage: www.elsevier.com/locate/colsurfa

Evolution of calcite surfaces upon thermal decomposition, characterized by electrokinetics, in-situ XRD, and SEM

Matea Ban^{a,b,*}, Thomas Luxbacher^{c,d}, Johannes Lützenkirchen^e, Alberto Viani^f,
Sabrina Bianchi^{b,g}, Klaudia Hradil^h, Andreas Rohatsch^a, Valter Castelvetro^{b,g}

^a Faculty of Civil Engineering, Research Centre of Engineering Geology, TU Wien, 1040 Vienna, Austria

^b Department of Chemistry and Industrial Chemistry, University of Pisa, 56124 Pisa, Italy

^c Anton Paar GmbH, 8054 Graz, Austria

^d Faculty of Chemistry and Chemical Technology, University of Maribor, 2000 Maribor, Slovenia

^e Institute for Nuclear Waste Disposal, Karlsruhe Institute of Technology, 76344 Eggenstein-Leopoldshafen, Germany

^f Institute of Theoretical and Applied Mechanics of the Czech Academy of Sciences, 190 00 Praha, Czech Republic

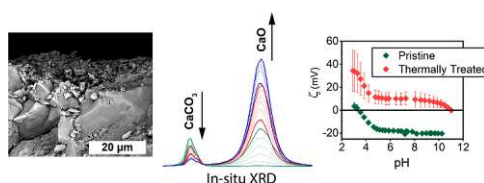
^g National Interuniversity Consortium of Materials Science and Technology (INSTM), 50121 Florence, Italy

^h X-Ray Center, TU Wien, 1060 Vienna, Austria

HIGHLIGHTS

- Thermal decomposition of dense and porous carbonates differs in onset and extent.
- Time-dependend changes of ζ for pristine and thermally treated surfaces were studied.
- Contribution of an asymmetric cell configuration to the overall ζ was determined.
- ζ -potential of mixed calcium hydroxide and calcite surfaces was analyzed.

GRAPHICAL ABSTRACT



ARTICLE INFO

Keywords:

Streaming potential
Streaming current
Zeta potential
Pore conductivity
Calcium carbonate
Non-equilibrium

ABSTRACT

The present study analyses transformation pathways of pristine and thermally treated porous limestone and dense marble surfaces by means of time-resolved streaming current and potential measurements coupled with scanning electron microscopy and in-situ X-ray diffraction. The results reveal that under nonequilibrium conditions the zeta potential (ζ) of natural carbonates may exhibit positive and negative signs and ζ drifts in opposite directions. Sample surface roughness influences ζ because it contributes to dissolution, as observed particularly in the initial period of time-resolved measurements. Thermal treatment causes a temporary charge reversal from negative to positive. The reactivity of calcium hydroxide on calcite surfaces governs the net electrokinetic potential and isoelectric point (IEP_{pH}), even at low surface coverage, as cross-validated by in-situ XRD. It was also found that pore conductivity may lead to $\sim 90\%$ underestimation of ζ when assessed by streaming potential. SEM studies revealed micro cracks inducement on marble after thermal treatment, which can result in underestimation of ζ up to the same extent as for the porous limestone. When an asymmetric cell configuration involving calcite and polypropylene surfaces is used, the fractional contribution of polypropylene to the IEP_{pH} is 0.3 and to the overall determined ζ up to 0.5. Our findings contribute to the understanding of nonequilibrium and time-dependent electrokinetic potential modifications associated with the reactivity of porous surfaces. This study

* Corresponding author at: Faculty of Civil Engineering, Research Centre of Engineering Geology, TU Wien, 1040 Vienna, Austria.

E-mail address: matea.ban@tuwien.ac.at (M. Ban).

<https://doi.org/10.1016/j.colsurfa.2021.126761>

Received 8 December 2020; Received in revised form 13 April 2021; Accepted 27 April 2021

Available online 6 May 2021

0927-7757/© 2021 The Author(s). Published by Elsevier B.V. This is an open access article under the CC BY license (<http://creativecommons.org/licenses/by/4.0/>).

highlights the effectiveness of the streaming potential technique for monitoring such changes further supported by the use of ancillary techniques to analyze the extend of chemo-mineralogical and physical alterations.

1. Introduction

Surface reactions at mineral-water interfaces govern various processes, including sorption, redox processes, weathering, and other phenomena in many environmental and industrial aspects [1,2]. These processes occur under nonequilibrium conditions, and the heterogeneous nature of the surfaces makes their molecular-level origin difficult to study and understand. Accordingly, the dynamic structure of calcite-water interfaces and the role of ions in their hydrodynamic environments are still largely unresolved [3]. As an example, the electrokinetic charge of calcite remains the subject of ongoing debate, and particularly so with reference to the differing zeta-potential (ζ) behaviors observed by different authors, even when adopting comparable experimental conditions [4]. Despite these discrepancies, the electrokinetic potential of a sample is widely accepted to depend on the initial state of its surface and the composition of the contacting aqueous electrolyte [5,6]. When a solid comes into contact with an aqueous electrolyte and its surface groups react and/or exchange with water and ionic species in the solution, spontaneous surface charge development results. This first adsorbed layer, the immobile layer, contains ions that are tightly bound to the surface and is referred to as the Stern layer. The ions that neutralize the residual excess surface charge beyond the Stern layer are mobile ions and are considered to belong to the diffuse layer. The combination of Stern and diffuse layers are commonly referred to as the electrical double layer (EDL). The electrokinetic potential, i.e. ζ , is an experimentally accessible physical parameter that allows characterization of the electrokinetic charge, and it is generally interpreted as the potential at the slipping plane, or shear plane, the exact location of which is the subject of ongoing research, but is expected to be somewhere near the diffuse layer plane (i.e., outer Helmholtz plane) of the standard EDL model.

By moving the electrolyte in a microchannel along the surface under study, the excess charge of the diffuse layer will be dragged along, giving rise to the streaming current. Both electrokinetic phenomena, streaming current and streaming potential, can be measured. According to a recent study [7] in which flat polymer surfaces of differing roughness and textures were investigated, streaming potential data should not be interpreted based solely on absolute ζ readings, but rather on trends and plateaus in pH- and concentration-dependent data. Information regarding the electrokinetic potentials of macroscopic calcites with different roughness is scarce, especially for systems under nonequilibrium, i.e. highly reactive, conditions. In one such study, in a different context, Elimelech et al. [8] demonstrated that, in the initial deposition of colloidal particles in heterogeneous porous media, the controlling factor of the kinetics is the degree of chemical heterogeneity (i.e. spatially variable surface reactivity). The term surface reactivity in the context of calcite refers to reactions at the mineral surface, which determine its stability in a given environment or its resistance towards dissolution, while chemical heterogeneity in natural mineral contexts denotes different chemical compounds, including organic matter, trace elements or different phases, among others.

Even more demanding than the study of the electrokinetic potential of calcites is the investigation of calcite charge alterations or time-dependent transformations, as is expected for mixed calcium hydroxide and calcite interfaces in contact with aqueous solutions. Kosmulski [9] pointed out that, due to the solubility of calcium hydroxide and its reactivity towards carbon dioxide, the results reported in the scientific literature for mixed systems may be largely unreliable. Moreover, the actual degree of hydroxylation/hydroxyl coverage is unknown and changes dynamically. However, such systems are responsible for key phenomena in many areas of research and applications. For instance,

knowledge of in-situ reaction pathways could enhance our mechanistic understanding of the coagulation of cement particles [10], carbon dioxide sequestration, and waste carbonation reactions [11], as well as other industrial applications in which basic calcium oxide surfaces are involved [12]. Furthermore, studies on thermal treatment of stone and mineral materials are relevant in order to understand the effect of fire damage on materials used for civil and building structures [13–15] or in concrete technology [16], among others. Although physical changes of stones caused by thermal treatment are well-studied phenomena [17–19], gaps exist concerning research on chemo-mineralogical alterations, especially regarding transition temperatures and the extents of transformation as well as subsequent influences on the surface when the stones are again exposed to the environment and thus in contact with an aqueous electrolyte. In the aforementioned cases the reactions and interactions at interfaces are difficult to follow experimentally. However, as a recent study demonstrated [20], the observation of electrokinetic phenomena can be employed to track in-situ transformations.

In this study, we systematically modified the surface chemistry of metamorphic and sedimentary calcium carbonates by thermal treatment to induce partial phase and chemical transformations. We then determined the electrokinetic potentials of the resulting samples with the aim of improving our understanding of the role of phase transformations and modified (or newly created) porosity and reactivity. It should be noted that electrokinetic potential is investigated in this study and cannot be supplemented by titrable surface charge, which would yield additional insight in the interfacial charge, because it is difficult, if not impossible, to determine for calcite and calcium-hydroxides. Besides streaming current and potential measurements we used in-situ X-ray diffraction (XRD) and scanning electron microscopy (SEM) as ancillary techniques to explore in more detail the involved surface phenomena.

The results obtained contribute to our understanding of solid calcite and mixed calcite and calcium-hydroxide surface reactivity in dynamic environments and provide knowledge for applications where time-resolved reaction pathways are of concern. Furthermore, given the large variability in the results concerning both the magnitude and even polarity of the electrokinetic potential for calcite previously reported in the literature, the characterization strategy described here may also contribute to a more accurate determination of the electrokinetic potential for porous macroscopic, flat materials by considering nonequilibrium and time-dependent changes, including the effects of pore conductivity and reactivity.

2. Experimental section

2.1. Materials

Two natural carbonate stones, Apuan Marble (AM), often also referred to as Carrara Marble, quarried from the Apuan Alps in Tuscany, Italy, and Lumaquela de Ajarte (LdA), quarried from Ajarte Trevino, Spain, were provided by local quarrying companies. AM has a dense, fine-crystalline metamorphic structure mainly consisting of calcite (~99 wt%), and it is therefore often classified as a monomineralic rock (Fig. 1a). Traces of dolomite and quartz are frequently found in AM, but typically amount to less than 1 wt%. The grains have an average size of 0.1 mm and the grain boundaries make up a large volume fraction of the bulk structure. This lithotype is known for its strength, which is related to its low Hg-open porosity of < 0.7%. LdA is a biogeneous sedimentary lithotype classified as a poorly washed biomicrite (fossil fragments embedded in a matrix derived from calcite mud) to microsparite (sparry calcite cement with readily discernible faces) [21], a so-called wackestone [22], consisting of shell fragments embedded in a carbonate

matrix composed of recrystallized fossil components, mainly foraminifera and echinacea (Fig. 1b). Due to recrystallization, no clear distinction between the inclusion and the cementing minerals is possible, except for some larger biogenic fragments with sizes up to a few millimeters. LdA is both structurally and chemically more heterogeneous than AM. It is composed of ~96 wt% calcite and ~2 wt% quartz with smaller contributions from elements such as aluminum, magnesium, potassium, and iron, among others. A high amount of small intercrystalline pores and larger calcitic sparite crystals can be observed by thin-section optical microscopy. This limestone has a relatively high Hg-open porosity of ~24%. Chemical analysis as determined by XRF and porometric properties are available as [Supplementary Data \(Table S1 and S2\)](#).

2.2. Calcination

Freshly cut $50 \times 50 \times 25 \text{ mm}^3$ specimens of the natural carbonates were studied in their pristine (untreated) and thermally treated conditions. Thermal treatment was performed in an electrically heated Thermo Scientific Heraeus K 114 furnace with a 3.5 L internal volume. The specimens were exposed to three subsequent cycles of thermal treatment consisting of a heating ramp at $40 \text{ }^\circ\text{C min}^{-1}$ followed by a 1 h isothermal step at $600 \text{ }^\circ\text{C}$, and rapid cooling to room temperature before restarting the cycle. The duration of the isothermal step and the heating rate were chosen based on the results of preliminary experiments aimed at avoiding macroscopic failure of the samples (i.e., continuous cracks passing through the specimen). The goal of the cycling treatment was to achieve surface-limited phase transformation, whereby the specimens maintain their outer macroscopic shape and thus allow comparative measurements of ζ . The reversibility of chemical surface modifications under ambient storage conditions (in a desiccator open to atmospheric H_2O and CO_2 at room temperature) allowed time-dependent monitoring of ζ . The samples are labeled according to their preparation (pristine and aged) and storage prior to the zeta potential analysis, i.e., Aged_{1,5}, Aged₂₄ and Aged₃₆₅ corresponding to storage after thermal treatment for 1.5 h, 24 h and 365 days, respectively.

In order to preserve the morphologies of the altered surfaces for the purpose of SEM studies and to obtain well-contrasted grayscale images from the backscattering detector, which highlight chemo-mineralogical changes, the freshly thermally treated specimens were coated with a nanosilica suspension to consolidate the newly generated morphological features. The silica sol (NC-12C, Colorobbia S.p.A., Sovigliana-Vinci, Italy) was applied five days after the thermal treatment. The silica

suspension comprised $15 \pm 2 \text{ wt}\%$ particles approx. 35 nm in size, in a water-ethanol mixture.

2.3. Characterization

2.3.1. Physical and chemo-mineralogical characterizations

SEM with energy dispersive X-ray spectroscopy (EDX) was used to qualitatively assess larger surface areas, corresponding more closely to the dimensions of the streaming channel for ζ -potential analysis. Size and shape of newly formed phases as well as changes in microstructure were investigated with a QUANTA FEG 450 instrument (FEI-Thermo Fisher Scientific, Inc.). The samples were mounted on aluminum stubs, coated with a 5-nm thick gold film prior to analysis, and observed at 20 kV accelerating voltage in backscatter and secondary electron mode.

Observations for thin sections were conducted with a petrographic microscope (Olympus BX41). The samples were embedded with the resin-hardener system XW 396 / XW 397 (Huntsman Corporation, Salt Lake City UT, USA) in a 10:3 wt ratio and cured overnight at $40 \text{ }^\circ\text{C}$. Before mixing resin and hardener, 1.3 g Fluorol 008 or EpoDye (Struers Inc., Cleveland OH, USA) was added to 100 g of XW 396. The thin sections were polished to approx. $30 \text{ }\mu\text{m}$ thickness and analyzed in cross-polarized-, plain polarized- and under UV-light. The characterization under different light helps to detect crystallographic orientations, textural differences or display porosity and cracks.

Additionally, porometric properties, including the total pore surface, average pore size, and open Hg-porosity, were determined using the Porotec Pascal 140/440 porosimeter (Thermo Electron Corporation, former Thermo Fisher Scientific).

Sound speed propagation of longitudinal ultrasonic waves was measured according to EN 14579 [23]. For the test an electrical pulse generator (CONOSONIC C2-GS), a pair of transducers (UP-DW) and an amplifier (VV 41) developed by Geotron-Elektronik (Pirna, Germany) were used. An average of 10 prisms ($1 \times 1 \times 4 \text{ cm}$) were tested on a rubber support and a coupling medium made out of clay was used. The frequency amounted to 80 kHz and the amplitude was adjusted according to sample damping.

Surface color measurements were carried out with a ColorLite sph850 spectrophotometer following the standard EN 15886 [24]. These measurements involve the International Commission on Illumination CIE L^* , a^* , b^* color parameters. A D65 illuminant at 10° standard observer with a reflectance spectrum in the range of 400–700 nm was used. An average of three measurements each of (L^*), (a^*), and (b^*) obtained at the same spot of the calcite surface was used to obtain the

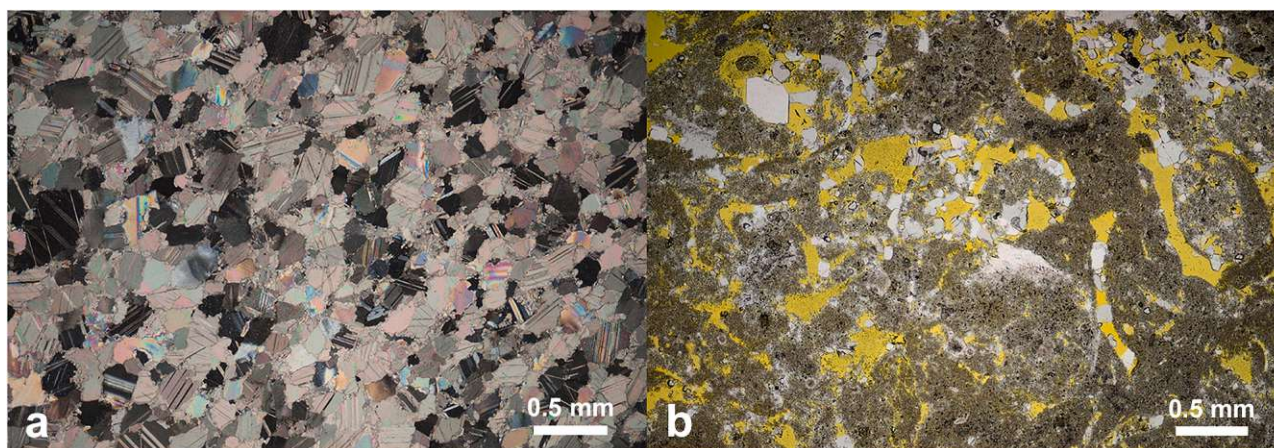


Fig. 1. Micrographs showing the fabric of the studied stones as seen in thin sections under the optical microscope. a) Dense, fine-crystalline structure of Apuan Marble under cross-polarized light. The colors represent different crystal orientations. b) Porous, biocalcarene Lumaquela de Ajarte under plane-polarized light. Shell fragments embedded in a matrix composed of recrystallized fossils are visible. The yellow-resin-impregnated thin section demonstrates the porosity of Lumaquela de Ajarte, which is virtually absent in Apuan Marble. (For interpretation of the references to colour in this figure legend, the reader is referred to the web version of this article.)

total color difference (ΔE^*) between pristine (p) and thermally treated (tt) samples using the following equation:

$$\Delta E_{tt,p}^* = \left[(L_{tt}^* - L_p^*)^2 + (a_{tt}^* - a_p^*)^2 + (b_{tt}^* - b_p^*)^2 \right]^{0.5} \quad (1)$$

Here, ΔL^* ($= L_{tt}^* - L_p^*$) corresponds to the lightness difference, (Δa^*) to the red/green difference, and (Δb^*) to the yellow/blue difference of the tested stone specimens. ΔE^* describes the metric difference or distance between two colors before and after thermal treatment.

Nonambient or in-situ XRD diffractograms were recorded using a PANalytical XPert MPD Pro powder diffractometer (PANalytical B.V., The Netherlands) equipped with a XCelerator detector and working in Bragg-Brentano θ - θ geometry. A partly focusing mirror was used to select the $\text{CuK}\alpha_{1/2}$ characteristic lines ($\lambda_{\alpha 1} = 1.54060 \text{ \AA}$, $\lambda_{\alpha 2} = 1.54443 \text{ \AA}$) for the experiment. A high-temperature furnace (Anton Paar HTK 1200 N), operating in air under ambient pressure, allowed controlled thermal treatment on disk-shaped stone specimens 18 mm in diameter and $\sim 2.5 \text{ mm}$ thick. Diffractograms were recorded in-situ during the programmed temperature steps and allow direct observation of phase evolution with temperature. For each temperature step, data was continuously collected in the 2θ range 15 – 90° at a speed of $0.01^\circ \Delta 2\theta/\text{s}$. Subsequently, the data were analyzed by the HighScore Plus software package [25] using the Powder Diffraction File (PDF4+ [26,27]; International Centre for Diffraction Data, Philadelphia, USA). Rietveld refinement was performed with TOPAS 4.2 [28] (Bruker-AXS) for quantitative analysis of the phases. Essentially, the Rietveld method [29] involves a full-profile fitting procedure, in which the difference between the experimental XRD diffraction profile and the calculated one, according to the information on structure models of each crystalline phase, is minimized through a least-squares procedure. The samples were first studied at room temperature and at selected points during the heating steps up to 600°C ($40^\circ \text{C min}^{-1}$ heating ramp) simulating the calcination conditions used earlier. Six subsequent XRD diffraction patterns were collected under isothermal conditions by pausing the heating ramp for 10 min at 100°C , 200°C , 300°C , 400°C , and 500°C . At 600°C , constant temperature for 60 min was imposed, corresponding to six separate XRD data sets collected at this temperature. After thermal treatment, the samples were let to cool down to 35°C while exposed to room temperature. This heating/cooling cycle was repeated three times to generate sufficient change on the surface layers. All three cycles were recorded by in-situ XRD.

2.3.2. Experimental setup for streaming current and potential measurements

Streaming current and potential measurements were performed with a SurPASS™ Electrokinetic Analyzer (Anton Paar GmbH, Austria) using

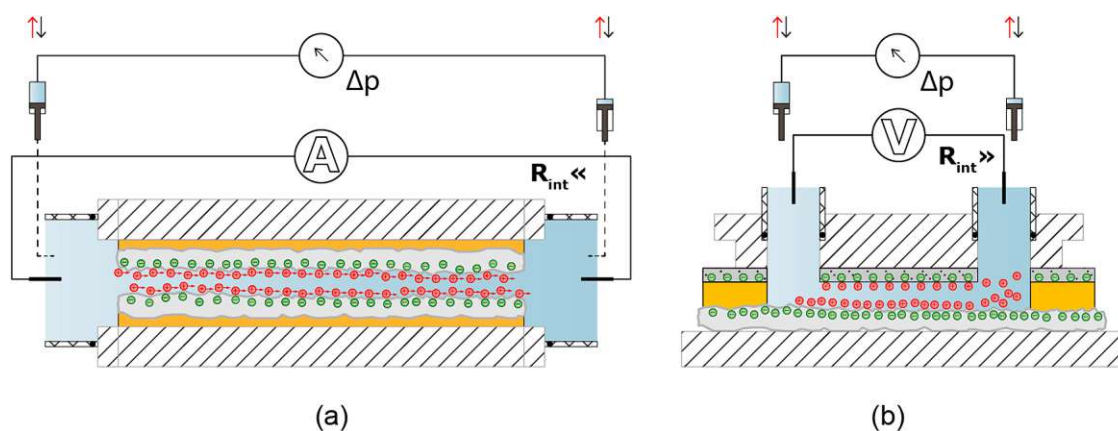
a custom-made clamping cell (CC) with an asymmetric configuration and an adjustable gap cell (AGC) with a symmetric configuration (Scheme 1).

In the CC, the two flat walls of the slit through which the electrolyte solution flows consist of a polypropylene (PP) support serving as a reference surface with holes for liquid inlet/outlet as well as a flat target surface (here a given carbonate sample under investigation). Note that the asymmetric configuration of the streaming channel implies a mixed ζ caused by the carbonate and the reference PP surface. The streaming channel, which is 12.5 mm in length and 6 mm in width, has a gap height of $< 140 \mu\text{m}$ as fixed by a spacer.

The AGC consists of two flat thin slices of the target carbonate specimen placed opposite each other, creating a channel 20 mm in length and 10 mm in width with a gap height that can be adjusted mechanically with a precision screw. By allowing the electrolyte solution to flow through the channel, true ζ of the material forming the channel walls can be determined as $\zeta\text{-True}(I_{\text{str}})$ for streaming current or $\zeta\text{-True}(U_{\text{str}})$ for streaming potential measurements.

Tests performed with the CC configuration comprised pH-dependent electrokinetic measurements performed on pristine, Aged₂₄, and Aged₃₆₅ surfaces using a 10^{-3} M aqueous KCl solution (Carlo Erba Reagents) in milli-Q® water as the background electrolyte. The electrolyte solution was purged with N_2 throughout the measurements to prevent CO_2 dissolution. The pH was adjusted in the pH range from 3 to 11 with either 0.05 M HCl or 0.05 M NaOH (Sigma-Aldrich Chemie GmbH) using the automatic dosing unit of the SurPASS apparatus. Starting pH values were between 5.5 and 6.5. The asymmetric configuration of the CC was generally preferred for studies of surface modification and reactivity because of rapid and precise sample mounting. All measurements were performed at least in duplicate for the pristine and thermally treated calcite. The result reported for each measurement at the given experimental conditions (pH, specimen condition) is the average of four consecutive measurements for which the standard deviation is provided. Before each measurement, the surface of the pristine carbonate was cleaned with pressurized argon to remove any particulate matter. Then the sample was mounted in the measuring cell and rinsed with the probing electrolyte solution for approx. 5 min. This was necessary for proper wetting of the electrodes and to establish laminar flow conditions and contact between the solution and natural carbonate to ensure repeatability of the experimental results.

Continuous time-resolved experiments were also performed using both CC and AGC configurations. AGC experiments comprised long-term, alternating streaming current and streaming potential measurements on pristine calcites. The more accurate AGC setup is difficult to be used for thermally treated calcites owing to (i) the challenging fabrication of the $< 2 \text{ mm}$ thick, precisely cut stone slices required for the



Scheme 1. Schematics of a) the adjustable gap cell (AGC) configuration and b) the clamping cell (CC) with an asymmetric configuration for ζ analysis of flat macroscopic surfaces and the generation of either streaming current with a low resistance path or streaming potential with a high resistance path. The dimensions are not to scale.

AGC, resulting in nearly systematic breakdown of the brittle carbonates; (ii) the macroscopic cracks caused by thermal treatment through differential stresses within the small samples; and (iii) the time-consuming adjustment of gap height and flow rate to ensure suitable conditions for flow in the AGC, which causes inevitable, substantial reactions with the surfaces before reliable data could be collected. Long-term experiments performed with the CC configuration included alternating streaming current and potential measurements on thermally treated calcites, labeled as Aged_{1.5}. With these specimens, long-term monitoring was possible for a more reactive state, i.e., 1.5 h after the thermal treatment. It should be noted that we intentionally omitted the use of samples in such a reactive state for all tests because re-carbonation induced gluing of the specimens to the sample holder. In addition, the AGC configuration allowed to determine the fractional contribution of the reference PP surface to the overall measured ζ .

2.3.3. Calculation of ζ , corrections for permeability and pore conductivity and fractional contribution of the reference surface to the measured ζ

The value of ζ is evaluated from the streaming potential or streaming current that arise due to the electrolyte flow generated by an applied pressure gradient tangential to the surface of the material under study. Evaluation of ζ is usually done via the well-known Helmholtz–Smoluchowski equation for streaming current:

$$\zeta(I_{Str}) = \frac{dI_{Str}}{d\Delta p} \frac{\eta}{\epsilon \epsilon_0} \frac{L}{A}; \quad (2)$$

where $\zeta(I_{Str})$ represents the ζ -potential derived from streaming current measurements, $\left(\frac{dI_{Str}}{d\Delta p}\right)$ is the streaming current coupling coefficient experimentally obtained from the slope of the linear fit of streaming current [A] to pressure difference (Δp) ramp [Pa], η is the dynamic viscosity of the electrolyte [Pa s], and ϵ and ϵ_0 are the dielectric constant of the electrolyte solution and the vacuum permittivity [8.854×10^{-12} F m⁻¹], respectively.

Since Eq. (2) applies under laminar flow conditions, and the flow regime is related to the geometry of the streaming channel and the flow rate, the factors affecting such properties must be accounted for. For a microchannel of length L [m] and rectangular cross-sectional area A [m²] given by channel width W and height H , from the Hagen-Poiseuille relation and according to the approximation of Bruus [30], the volume flow rate \dot{V} [m³s⁻¹] is given by Eq. (3):

$$\dot{V} = \frac{dV}{dt} = \frac{H^3 W}{12\eta L} \Delta p [1 - 0.630 HW^{-1}]. \quad (3)$$

When $H < W$, i.e., $HW^{-1} \rightarrow 0$, the last term $[1 - 0.630 HW^{-1}] \approx 1$ and the gap height is obtained:

$$H = \left(12\eta \frac{L}{W} \frac{\dot{V}}{\Delta p}\right)^{1/3}; \quad (4)$$

where the gap height of the microchannel is determined by the volume flow rate versus pressure difference and the linear dependence of $\dot{V} \propto \Delta p$ assumes laminar flow conditions. To account for the actual dimensions of the flow channel, which becomes necessary when different measuring cells are used, the following relationship applies:

$$\frac{\zeta_{Str}^{app}}{\zeta_{Str}^{corr}} = \frac{L}{A}; \quad (5)$$

which uses the apparent or measured values (ζ_{Str}^{app}), as reported by the instrument software, over the corrected values (ζ_{Str}^{corr}), as given by the custom-made cell. By rearranging, the geometrical corrections can be accounted for through Eq. (6):

$$\zeta_{Str}^{corr}(I_{Str}) = \frac{L^1}{L} \frac{W}{W^1} \frac{H}{H^1} \zeta_{Str}^{app}. \quad (6)$$

The gap height of the channel is calculated from the ratio between volume flow rate and pressure difference, but since a transition from laminar to turbulent flow may occur in the case of highly porous carbonates, a correction for potential nonlinear dependency might be necessary (see Fig. S1). Taking the corrected term (H^1) over the apparent gap height (H), Eq. (7) is obtained:

$$H^1 = \left(\frac{k^1}{k} \frac{L^1}{L} \frac{W}{W^1}\right)^{1/3} H; \quad (7)$$

where (k) and (k^1) equal $\left(\frac{\dot{V}}{\Delta p}\right)$ as linear and polynomial fits, respectively.

Linear regression of nonlinear dependency would underestimate the gap height. The slope of a second-order polynomial fit at $\Delta p \rightarrow 0$ Pa describes the permeability of the flow channel more reliably. Therefore, by inserting Eq. (7) into Eq. (6), the geometrical correction can be introduced as follows:

$$\zeta_{Str}^{corr}(I_{Str}) = \left(\frac{k}{k^1}\right)^{1/3} \left(\frac{L^1}{L} \frac{W}{W^1}\right)^{2/3} \zeta_{Str}^{app}, \quad (8)$$

where (ζ_{Str}^{corr}) estimates the corrected ζ -potential of the studied porous carbonate surfaces.

An additional approximation of Eq. (2) regards the related electrokinetic phenomenon, the streaming potential given by Eq. (9):

$$\zeta(U_{Str}) = \frac{dU_{Str}}{d\Delta p} \frac{\eta}{\epsilon \epsilon_0} \kappa_B; \quad (9)$$

where $\left(\frac{dU_{Str}}{d\Delta p}\right)$ denotes to the streaming potential coupling coefficient [VPa^{-1}] and κ_B the conductivity of the bulk electrolyte solution [$S m^{-1}$]. The latter value is an additional parameter that needs to be measured and as such it introduces additional errors when intrinsic ζ values need to be obtained. This is why Eq. (2) is more convenient for calculating ζ when the channel geometry is known.

Since even sparingly soluble minerals like calcium carbonate dissociate in water, yielding a weak electrolyte solution, dissolution phenomena at the material surface release ions, which contribute to the conductivity inside the streaming channel (and also to the conductivity of the bulk electrolyte solution). As the resulting increased conductivity would lead to an underestimation in the calculation of ζ , corrections are necessary. The farther the material under study is from equilibrium conditions, the larger is the possible deviation from the unperturbed model. At this point, the difference between surface conductivity and the ionic or pore conductivity needs to be emphasized. Both properties will underestimate ζ obtained through streaming potential measurements, but they refer to different phenomena. To analyze if surface conductivity effects can be neglected in the case of flat surfaces, the channel heights are varied in respect to the liquid bulk conductivity [31,32]. As in the CC configuration the gap height is fixed and the calcite surfaces are rough, the effect of pore conductivity will dominate and is accounted for through measurements of the electric resistance R along the streaming channel by using the ratio of streaming potential and streaming current:

$$\frac{U_{Str}}{I_{Str}} = R. \quad (10)$$

This approach represents a simplified case and neglects effects of surface conductivity on the determined ζ -(U_{Str}), which diminish at conditions of ≥ 1 mM KCl and gap heights $> 50 \mu m$ as employed in the present work. Surface conductivity was accounted for in various experimental settings where the electrolyte flows through porous media [33,34]. To account for the effect of ionic or pore conductivity for flat

solid surfaces, Eq. (11) is obtained:

$$\frac{\zeta_{U_{Str}}^{app}}{\zeta_{U_{Str}}^{corr}} = \frac{\kappa_B}{\kappa_B^I} \text{ where } \kappa_B^I = \left(\frac{1}{R} \frac{L}{A} \right). \quad (11)$$

κ_B^I corresponds to the measured electrical conductivity inside the streaming channel as a function of the channel geometry. By solving for correct ζ values, we obtain Eq. (12):

$$\zeta_{U_{Str}}^{corr} = \frac{1}{\kappa_B} \kappa_B^I \zeta_{U_{Str}}^{app}. \quad (12)$$

The use of streaming potential relies on the substitution of the streaming current using Ohm's law ($I = U/R$, where R [Ohm] is the electrical or cell resistance inside the streaming channel). However, Ohm's law is disobeyed because of the local excess concentration of ions that results in a higher electrical conductivity when compared to the conductivity of the bulk electrolyte solution. This difference can be used to analyze the reactivity of different surfaces and thus, by using Eq. (12), and with the previously introduced corrections for the nonlinear dependency conditions and for channel geometry, Eq. (13) is derived:

$$\zeta_{U_{Str}}^{corr} = \left(\frac{1}{\kappa_B} \right) \left(\frac{1}{R} \frac{L}{A} \right) \left(\frac{k}{k^I} \right)^{1/3} \left(\frac{L^I}{L} \frac{W}{W^I} \right)^{2/3} \zeta_{U_{Str}}^{app}. \quad (13)$$

Fairbrother and Mastin [35] assumed that surface conductivity is suppressed when the conductivity of the electrolyte is high. However, when altering the surface, the conductivity of the contacting electrolyte solution may be modified, particularly for porous surfaces. This effect of pore conductivity and related changes in the streaming channel may become a key issue for porous carbonates, which ultimately requires the corrections introduced in Eq. (13). Since the measurements in the present work were carried out under nonequilibrium conditions, the ionic conductivity of the sample may be used as an indicator of surface reactivity. In fact, the observed changes caused by material contribution (dissolution and ion accumulation) to the overall conductivity can be used to study porosity alterations and reactivity in dynamic environments by:

$$\kappa_B^I - \kappa_B \approx \text{poreconductivity}. \quad (14)$$

It should be noted that the absolute values of pore conductivity depend on both cell resistance and bulk conductivity. Therefore, they can only be compared for same cell configurations and sample conditions.

If the CC is used, the fractional contribution of the reference PP surface to the overall determined ζ needs to be considered. Walker et al. [36] assumed equal contributions from their reference surface and different sample surfaces. As streaming potential techniques directly related to the average ζ_{Avg} , knowledge of either ζ_{Ref} of the reference surface or ζ_{Test} of the tested material is required to achieve a complete information on the system according to the following relation:

$$\zeta_{Test} = 2\zeta_{Avg} - \zeta_{Ref}. \quad (15)$$

In an earlier study Elimelech et al. [8] used a linear combination of the ζ values of two mixed materials:

$$\zeta_{Avg} = \lambda\zeta_1 + (1 - \lambda)\zeta_2; \quad (16)$$

where λ and $1 - \lambda$ are the fractional total surface areas of the two materials characterized by different ζ values, ζ_1 and ζ_2 . Eq. (15) can be used only in cases where $\lambda = 0.5$; on the other hand, if all terms of Eq. (15) can be measured, the value of λ can be obtained as:

$$\lambda = \frac{\zeta_{Avg} - \zeta_2}{\zeta_1 - \zeta_2}. \quad (17)$$

3. Results and discussion

3.1. Analysis of textural changes after thermal treatment

The textural (or rock microstructural) evolution after thermal treatment was investigated by quantifying surface color changes, the formation of microcracks, and the development of new phases on the surface of the carbonates, as observed by polarized light- and scanning electron microscopy. Upon thermal treatment, AM samples turn opaque and dull due to phase transformation and changes caused by the induced microcracks. The surface of AM becomes whiter while LdA undergoes a darkening of the bulk fabric after thermal treatment (see Table 1). The change in LdA's color after thermal treatment ranges from reddish to greyish and it is caused by changes of iron-oxy-hydroxide and iron-oxide or similar iron-bearing minerals present in trace amounts in its fabric. Such color change is controlled by mineralogical alterations also affecting the surface chemistry. Moreover, immediately after the thermal treatment a formation of a whitish surface layer on both carbonates was observed, as a result of quick re-carbonation of the CaO surface layer generated by the thermal treatment and the presence of some reactive calcium hydroxide residues (as can be assessed by a 0.1% phenolphthalein indicator solution).

As the studied stones formed under different conditions, their fabric differs (see Fig. 2a-d), which normally implies that their response to thermal treatment will vary. Crack development is the result of thermomechanical stresses caused by several contributions. The most important one is the strong anisotropy of the thermal expansion coefficient of calcite, which is positive along its c-axis and negative perpendicular to it [37]. For AM, the microcracks are more pronounced, owing to its dense structure. The cracks were found to be of both inter- and trans-granular nature, resulting in increased porosity and newly generated exposed surfaces (Fig. 2e). Such severe changes on AM are also displayed by the porometric data (Table 2), showing a noticeable increase in average pore size and total porosity after thermal treatment. Conversely, the porous LdA is more effective in accommodating stresses due to the pore space available for thermal expansion, preventing strain accumulation at interfaces between neighboring minerals, so that the change in porosity remains marginal. A micrographic documentation of both stones before and after treatment, taken at the same magnification, can be seen in Supplementary Data (Fig. S2).

As LdA has an inhomogeneous fabric, microscopic techniques are not reliable in confirming the presence of micro cracks. Therefore, sound speed propagation was measured before and after thermal treatment to confirm the presence of microstructural changes (Table 3). The ultrasound pulse velocity decrease after the thermal treatment, corresponding to longer traveling paths. This indicates widening of existing cracks and generation of new ones. Therefore, a reduction of soundness due to newly generated micro cracks was confirmed.

Phase transformation is likely to be initially limited to surface and subsurface layers as heat transfer proceeds from the outer parts to the inner core of the specimen and also because of the diffusion-limited escape of CO₂ resulting from carbonate decomposition. The mild thermal treatment adopted prevented decomposition or significant phase

Table 1
Color difference measured between pristine and thermally treated Apuan Marble (AM) and Lumaquela de Ajarte (LdA).

Stone	ΔL^*	Δa^*	Δb^*	ΔE^*
AM	9.17 ± 0.12	0.91 ± 0.03	2.31 ± 0.16	9.5 ± 0.11
LdA	- 11.4 ± 0.57	0.58 ± 0.05	- 2.53 ± 0.13	11.69 ± 0.58

ΔL^* the lightness coordinate ranging from 0 (black) to 100 (white), with negative values meaning darkening; Δa^* the red/green coordinate, with +a* indicating redness and -a* indicating greenness; and Δb^* the yellow/blue coordinate, with +b* indicating yellowness and -b* indicating blueness.

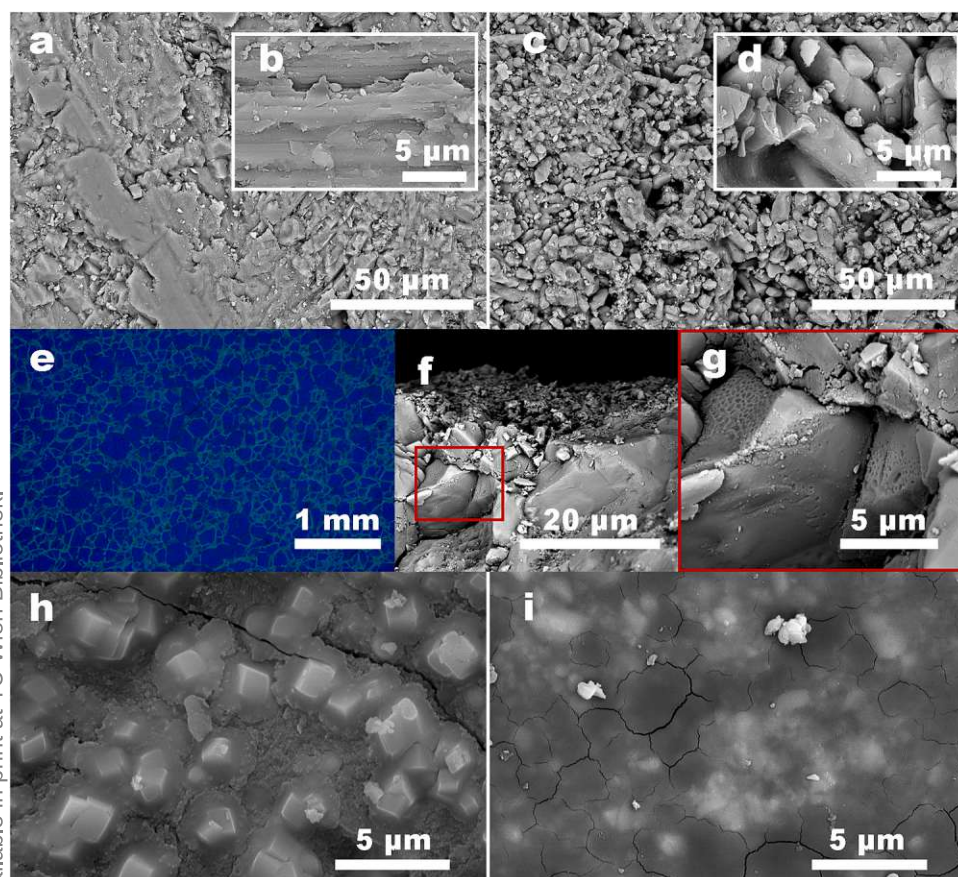


Fig. 2. Surfaces of freshly quarried a-b) Apuan Marble and c-d) Lumaquela de Ajarte displaying differing roughness as observed with a secondary electron detector. e) Inter- and intragranular microcracks in the fabric of Apuan Marble after thermal treatment. The visualization of cracks was performed using UV-light on a thin section embedded in a fluorescence resin. f-g) SEM images of a broken fragment of a thermally treated Apuan Marble sample showing f) precipitates on the surface, and g) a honeycomb-like texture, possibly as a result of beginning thermal degradation, located at an intergranular boundary in the vicinity of the surface. h) Backscatter electron images of embedded rhombohedral crystal in the nanosilica matrix on the surface of thermally treated Apuan Marble and, i) secondary electron images of the discoloration of the nanosilica matrix due to calcium mobilization on surfaces of thermally treated Lumaquela de Ajarte.

Table 2

Porometric data from mercury intrusion tests for specimens in pristine and thermally treated (aged) conditions for Apuan Marble and Lumaquela de Ajarte.

	Apuan marble		Lumaquela de Ajarte	
	Pristine	Aged	Pristine	Aged
Total pore surface [$\text{m}^2 \text{g}^{-1}$]	0.14	0.23	3.03	3.77
Average pore diameter [μm]	0.08	0.24	0.15	0.14
Hg-total porosity [%]	0.72	3.58	23.85	25.12

Table 3

Sound speed propagation before (pristine) and after thermal treatment (aged) on Apuan Marble (AM) and Lumaquela de Ajarte (LdA).

Stone	km s^{-1}		
		Pristine	Aged
AM	Mean	6.17	2.17
	Max/Min	6.28/6.09	2.36/1.85
	Mean	3.22	2.6
LdA	Mean	3.27/3.15	2.65/2.52

transformations of the bulk material. Locally high CO_2 concentration in pores may also have hindered phase transformations in calcite [38]. On the surfaces, changes caused by thermal treatment were mostly observed in the form of small precipitates, as is the case for AM (Fig. 2f). Moreover, a honeycomb-like texture on the mineral is observed in the sub-surface area of the same carbonate, which might be an effect of the thermal treatment (Fig. 2g). Here, the vicinity to the surface and the newly opened cracks offer escape routes for CO_2 , favoring the progress of thermally induced degradation processes.

The SEM analysis clearly indicates products of the thermal decomposition on the surface of AM, showing the presence of rhombohedral crystal bundles of $\sim 1 \mu\text{m}$ cross-section (Fig. 2h). However, the solvent of

the silica sol may be a possible aid in the growth of well-formed crystal nuclei during re-carbonation. Future experiments with solvent and without silica should address this possibility. Moreover, a rim present in the silica matrix around the newly formed calcite crystals shows that calcium is mobilized, since a concentration gradient can be observed around the calcite crystals embedded in the silica matrix (see SEM/EDX spectra in Supporting Data Fig. S3a). Concerning LdA, phase transformation is only indicated by a whitish discoloration of the nanosilica consolidating matrix, which presents a distinguished intensity in Ca-Si ratio, as detected by SEM/EDX (Fig. S3b). Well-formed crystals are not observed for this carbonate under the given conditions. Therefore, changes on surfaces of AM are indicative to be more severe when compared to those present at surfaces of LdA. Overall, the post-treatment with colloidal nanosilica proved useful in preserving newly formed species embedded in the silica matrix.

3.2. Phase evolution with temperature as analyzed by in-situ XRD

In-situ XRD allowed us to follow the phase transformations from the onset a function of temperature. Fig. 3a and b illustrates the quantitative phase evolution with temperature obtained from Rietveld refinement of the XRD patterns (exemplary diffractograms can be seen in Figs. S4 and S5). The two samples follow the same trend of thermal decomposition and re-carbonation, but to different extents and with varying offsets concerning initial decomposition. For AM, the presence of CaO is first detected (approx. 1 wt%) after 10 min isothermal treatment at 600°C in the first heating cycle (see Fig. 3a). At the end of the three subsequent heat/cool cycles, the amount of newly formed CaO is 78.8 wt%, the remaining fraction being CaCO_3 , which has decreased from its initial total amount of 98.8 wt%. The small fraction of dolomite disappears after the first heating cycle during the isothermal stage at 600°C . Accurate quantification of the products of dolomite decomposition into

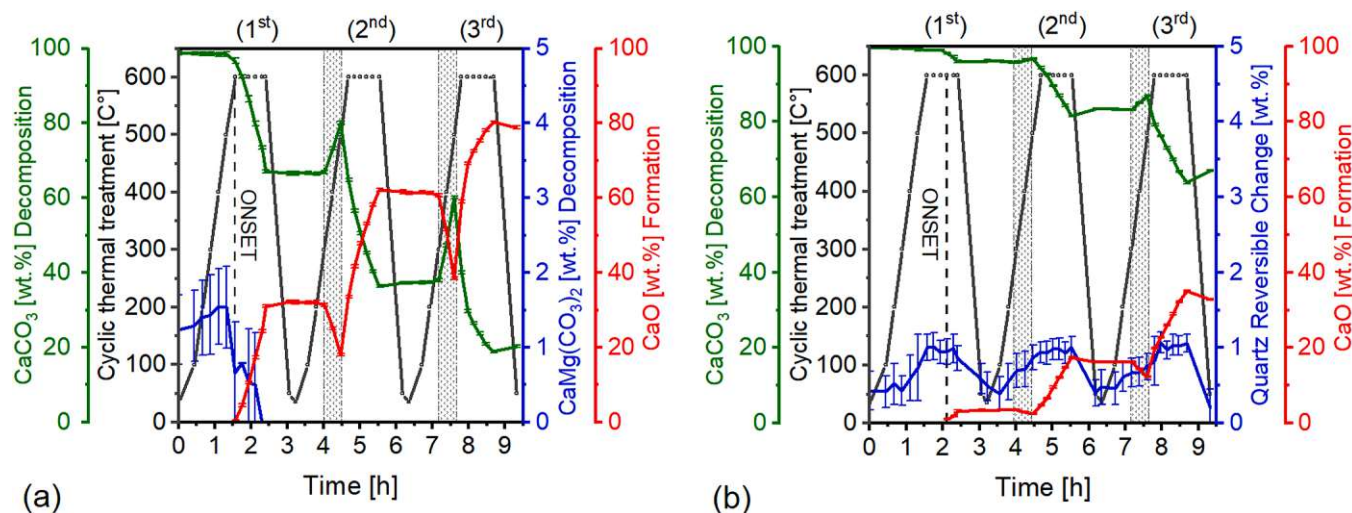


Fig. 3. Phase evolution (wt%) with temperature obtained from Rietveld refinement of in-situ XRD patterns for a) Apuan Marble and b) Lumaquela de Ajarte. Shaded areas highlight the retrograde reaction (in the second and third heating ramp) while the dotted line indicates the onset of thermal decomposition during the isothermal treatment (only reported for the first thermal cycle). (For interpretation of the references to colour in this figure legend, the reader is referred to the web version of this article.)

periclase or brucite was not possible because of their low abundances (< 2 wt%) and texture effects.

The onset of thermal decomposition for LdA is delayed compared to AM and occurs after 40 min of the first isothermal stage at 600 °C. At the end of the three heat/cool cycles, the absolute amount of newly formed CaO is ~32 wt%, and correspondingly the remaining calcium carbonate accounts for ~67 wt%. Quartz transforms reversibly from its room temperature form α -quartz to β -quartz at 573 °C at one atmosphere of pressure. Due to its low amount (< 1 wt%), the fluctuations in phase fraction observed during the thermal cycles (Fig. 3b) are likely caused by the structural changes produced by the phase transition, as explained in Supplementary Data, Fig. S6.

The difference in the onsets of thermal decomposition and the final conversion degrees for the two carbonates can be ascribed to their different microstructural features (i.e., sample surface roughness and porosity) exerting control on thermal transport properties [39]. As the thermal conductivity of air at 600 °C is lower than that of calcite, the former acts as an insulator, slowing down heat transfer more effectively in the porous variety of LdA compared to AM. Overall, the more densely packed AM decomposes earlier because the intergrain thermal resistance is low due to the higher surface area of contact between grains.

An intriguing observation on both carbonates is the retrograde reaction, through which the metastable CaO transforms back to CaCO₃ (Fig. 3, shaded areas). The high-temperature thermal decomposition $\text{CaCO}_{3(s)} \rightarrow \text{CaO}_{(s)} + \text{CO}_{2(g)}$ is typically followed, under normal environmental conditions, by re-carbonation as a two-step reaction. This involves absorption of atmospheric H₂O and results in the formation of a hydrated Ca(OH)₂ intermediate. Subsequent absorption of atmospheric CO₂ with release of H₂O causes the net back reaction $\text{CaO}_{(s)} + \text{CO}_{2(g)} \rightarrow \text{CaCO}_{3(s)}$. While the presence of residual water can be excluded after the first thermal cycle, the highly reactive CaO is metastable also in the presence of CO₂ for the thermally treated specimens during the cooling and re-heating cycles, because some CO₂ is confined within their porous structures. The activation energy for the back reaction is provided by temperatures ranging from ~400 °C to ~500 °C, as shown by the reversal of the phase transformations in the last stage of the second and third heating ramps (shaded areas in Fig. 3). This structural reorganization (i.e., decomposition/re-carbonation reaction) and the cyclic heat-treatments are responsible for a surface limiting transformation, preserving the outer shape of the specimen, and allowing us to carry out streaming current and potential measurements.

3.3. Time-resolved monitoring of ζ and pore conductivity of pristine and thermally treated samples

By using the AGC configuration, the true ζ values, $\zeta\text{-True}(I_{\text{str}})$ and $\zeta\text{-True}(U_{\text{str}})$, are obtained (Fig. 4a–d). A key finding using the AGC is that ζ values resulting solely from the carbonates surface exhibit differing electrokinetic potentials and drift directions for the two studied specimens. The dense variety AM starts at a $\zeta\text{-True}$ of –19 mV and remains negative over 60 h of continuous measurements, reaching a nearly stable value of approximately –10 mV within the first 24 h (Fig. 4a and b). Conversely, LdA exhibits an initially positive ζ -potential that shifts to negative values after ~30 min (Fig. 4c and d). Moreover, AM, the dense crystalline material with a rather smooth surface, under the studied conditions dissolves (or reacts) less and more slowly than LdA, which is an inhomogeneous, rough and brittle conglomerate. Therefore, one distinctive difference between pristine LdA and AM is that the former always causes larger pH shifts in contact with a neutral solution as it has a higher surface roughness. For macroscopic flat surfaces, the surface roughness, which comprises all textural and microstructural features of the stone surface including effects of grain edges and boundaries, is known to contribute to the reactivity of the carbonates as it is related not only to the specific surface area but also to varying crystal faces and defect density [40]. Similarly, for crystal surfaces, surface topography influences the reactivity of calcite [41]. For AM, the pH first increases and then decreases slightly. The decrease corresponds to a proceeding equilibration which is not reached in the given time-frame. ζ becomes less negative with time, which can be attributed to dissolution. This can also be confirmed by a constant increase of the bulk conductivity. The results show that a lack of equilibrium is responsible for the differing ζ -potentials in different carbonates. Besides, the specific surface area and the related reactivity of a given carbonate determines the delay time before a meaningful electrokinetic potential is reached within the initial periods of testing.

As concerns the pore conductivity of the stones in pristine conditions, its contribution affects the recorded streaming potential as a result of the presence of additional pathways for the conduction current through the porous network. By comparing the pore conductivity of pristine AM and LdA it is evident that porosity and pore conductivity correlate, a higher pore conductivity corresponding to a higher surface porosity. Thus, the higher the porosity, the more severe the underestimation of ζ as determined by streaming potential (see the difference between $\zeta\text{-I}_{\text{str}}$ and $\zeta\text{-U}_{\text{str}}$ in Fig. 4). The pore conductivity causes an underestimation of $\zeta\text{-U}_{\text{str}}$

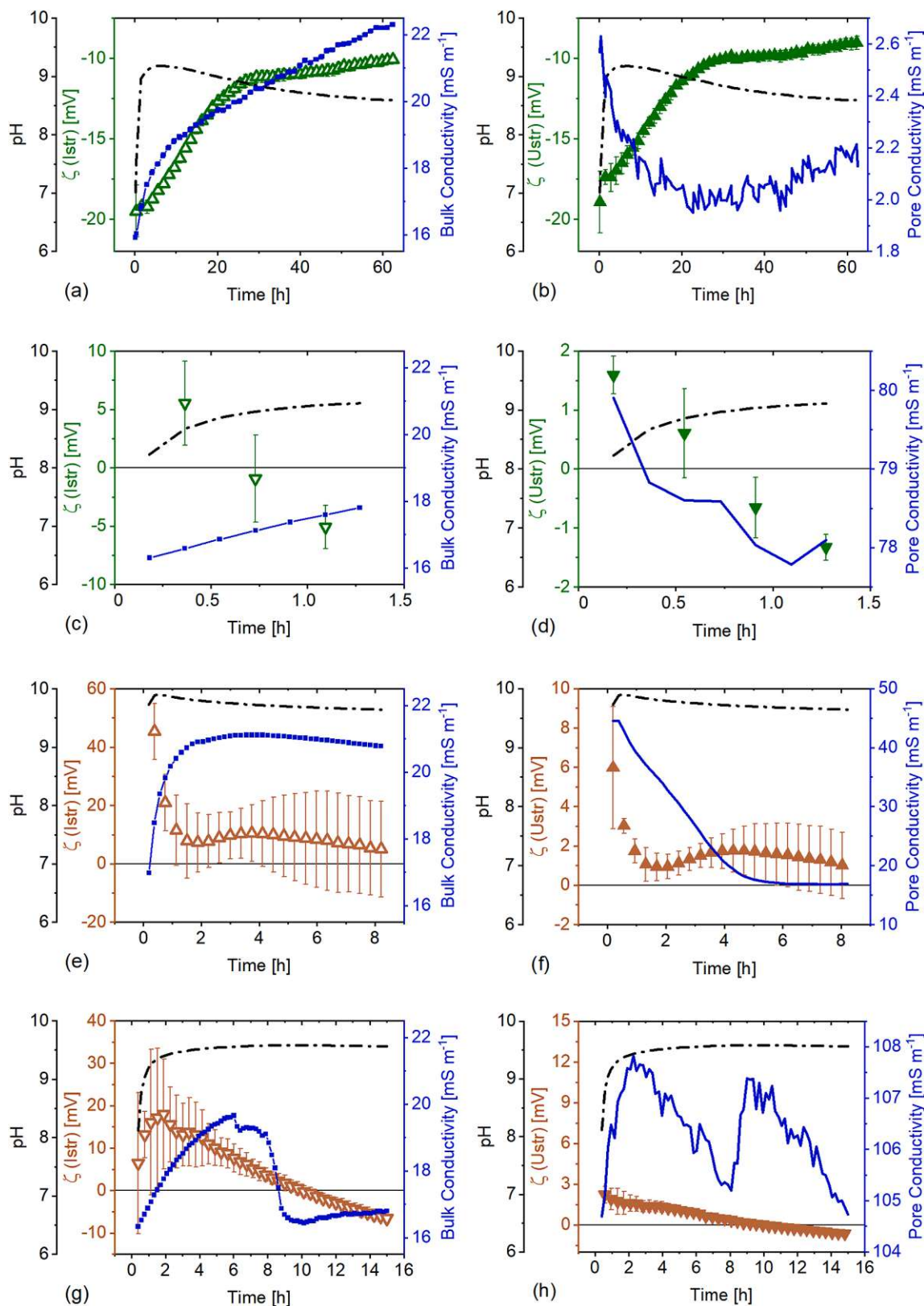


Fig. 4. Time evolution of ζ as obtained from streaming current (I_{str}) and streaming potential (U_{str}) measurements with corresponding pH, bulk- and pore conductivity measurements, on pristine (green) and thermally treated (red) surfaces. Measurements performed with the AGC (pristine) and CC (thermally treated) configurations using an aqueous 10^{-3} M KCl probing electrolyte solution: a-b) pristine Apuan Marble; c-d) pristine Lumaquela de Ajarte; e-f) thermally treated Apuan Marble (ζ -Aged_{1.5}) and g-h) thermally treated Lumaquela de Ajarte (ζ -Aged_{1.5}). Tests were performed until ζ stabilizes or the isoelectric point (IEP_{pH}) was approached/reached. (For interpretation of the references to colour in this figure legend, the reader is referred to the web version of this article.)

values by up to 90% in the case of the highly porous LdA, whereas the underestimation amounts to < 10% for pristine AM. After the thermal treatment, the underestimation of AM increases up to 80% while for LdA it remains the same due to its high porosity even in the pristine state.

The thermally treated samples (ζ -Aged_{1.5}) expose mixed calcite and calcium hydroxide surfaces. The positive ζ measured for thermally treated samples may be explained by a combination of solubilization and re-adsorption processes involving calcium hydroxide, with preferential solubilization of the hydroxide anion along with preferential re-adsorption of solubilized Ca^{2+} cations. The slow decrease of the absolute value of ζ and ultimately sign reversal from positive to negative might be the result of multiple processes that possibly change with time, involving also residual calcium oxide from underneath the hydroxide layer. Kinetic processes including physical and chemical adsorption as well as coupled dissolution-precipitation reactions might explain why ζ is altered [42,43]. By comparing the pH and bulk conductivity evolution over time upon contacting the thermally treated specimens, it is indicative that the electrokinetic potential will depend on the amount of reactive material present at the surface. While neither the exact fractional amount of reactive phases nor the effective surface area are known, the results of the measurements performed with the CC (and thus involving the reference PP surfaces) clearly show that the phases that are more reactive govern the net electrokinetic potential (Fig. 4e–h). Thermally treated AM exhibits a higher pH increase and larger magnitude of ζ during the initial period of the experiments as compared to LdA. This difference in alkalinity between the carbonates corresponds to the in-situ XRD analysis with AM having a higher amount of calcium oxide formed than LdA. This can be further confirmed by the increase of bulk conductivity in the initial period during the experiments and the absolute values (compare the steepness of the bulk conductivity curve between AM and LdA < 2 h and the absolute values reached). Likewise, the isoelectric point (IEP_{pH}) will be influenced by the surface fraction of phase-transformed species (Table 4). After the initial period, the pH remains nearly constant for the thermally treated samples. The reactivity of calcite is indicated by alterations in ζ , bulk- and pore conductivity. For AM-Aged_{1.5} ζ approaches zero after 8 h of testing. Changes in pore conductivity reflect solution changes in the micro-channel. The bulk conductivity decreases only slightly after 3 h of testing. Similarly, ζ of LdA-Aged_{1.5} approaches zero after 8 h. Unfortunately, the pore conductivity alterations on LdA surfaces cannot be tracked with great precision as the readings are suppressed by the presence of high surface porosity. The bulk conductivity of LdA starts decreasing after approx. 6 h of testing. Normally, a decrease on bulk conductivity indicates that ions are removed from the solution but more experiments are needed to confirm these alterations in regard to ζ and to rule out experimental errors.

In general, the time-resolved measurements show that the carbonates are prone to partial dissolution, which is known to cause differences in ζ [44,45]. Such processes are responsible for changes in composition of both the surface and the solution (pH and ionic strength), and therefore of the EDL instantaneous composition. Even if in conditions far-from-equilibrium, the dynamics of these surfaces can be followed through the induced alterations in ζ , pH, bulk- and pore conductivity, which in turn allow to estimate time-dependent changes of these

systems. Thus, nonequilibrium phenomena or time dependent changes in ζ allow to study effects of ageing, temperature or modifications of the composition of contacting solutions that are important for various applications [46–48].

3.4. pH-dependent electrokinetic measurements

When a reactive surface undergoes pH-dependent dissolution and reprecipitation reactions, the associated phenomena cause local perturbations in pH and ionic strength, which may extend to several molecular layers above the surface. In such cases, the possibility that the electrokinetic measurements do not accurately represent the electrokinetic charge and the occurring surface processes, has to be considered. On the other hand, while the absolute ζ values from single-point measurements may be significantly affected by the nonequilibrium interfacial dynamics and the ensuing perturbations of the probing electrolyte solution, IEP_{pH} can be taken as a more reliable parameter; therefore, the electrical properties of the surfaces will be discussed based on this property, taken as a measure of the modifications occurring at the surface. The pH- and salinity dependent behavior of the carbonates was studied by performing a series of electrokinetic measurements over a defined pH range (hereafter referred to as titration), with the goal of analyzing the differences in surface reactivities of the two carbonates according to their different nature and as caused by the effects of thermal treatment and environmental re-carbonation processes.

In Fig. 5 it is evident that the thermal treatment had an effect on ζ and the IEP_{pH} for AM as opposed to LdA. The effect on AM can be discussed in terms of an enhanced alkaline behavior after thermal treatment (ζ -Aged₂₄) and a recovery due to re-carbonation (ζ -Aged₃₆₅), while the measurements on LdA are not significantly affected by the thermal treatment due to its higher porosity promoting solubilization of the carbonate surface already before the thermal treatment. Specifically, the ζ -Aged₂₄ results for AM can be explained by its chemical surface composition consisting of strongly alkaline CaO that quickly hydrates to $\text{Ca}(\text{OH})_2$ upon contact with the electrolyte solution. This causes ζ to remain positive throughout the whole explored pH range as a result of preferential solubilization of the hydroxide anion and/or increased preferential re-adsorption of Ca^{2+} cations (Fig. 5a), as already discussed in Section 3.3. By titrating from neutral towards increasingly alkaline pH, ζ -Aged₂₄ decreases in magnitude and IEP_{pH} is eventually reached at $\text{pH} \approx 11$. Even one year after the thermal treatment, a complete recovery of the surface towards the original carbonate does not occur; this is shown by the shift in IEP_{pH} from pH 3.4 of the pristine stone to pH 4.6 for Aged₃₆₅. The observed slight difference between ζ -Pristine and ζ -Aged₃₆₅ can be at least partially explained by a more effective release of lattice ions after thermal treatment and re-carbonation, ascribed to the increased specific surface area and enhanced solubility of the newly generated carbonate surfaces. Furthermore, the absence of organic matter contamination (completely removed, if initially present, by the thermal treatment) may further contribute to a less negative ζ value in the Aged₃₆₅ sample [49]. In addition, AM Aged₃₆₅ samples displayed a cell resistance of ~ 450 kOhm, much lower than the ~ 1150 kOhm of the pristine sample (Table 5). The decrease in electrical resistance inside the streaming channel gives additional evidence for the thermally altered

Table 4

Summary of relevant properties of pristine and thermally treated (Aged_{1.5}) Apuan Marble (AM) and Lumaquela de Ajarte (LdA) as determined in the asymmetric (CC) and the symmetric (AGC) cell configuration. Note that absolute values of pore conductivity can only be compared for same configurations and sample conditions, as both the cell resistance and the bulk conductivity depend on the amount of the sample tested and therefore, on the type of cell used.

Sample	ζ - _{str} [mV]	Testing pH	IEP_{pH}	Cell Res. [kOhm]	Pore Cond. [mS/m]
AM (AGC) Pristine	-19 ± 1.6 to -10 ± 0.3	7–8.6	n/a	623 ± 53	2.5–2.1
LdA (AGC) Pristine	5.5 ± 3.6 to -5.1 ± 1.9	8.2–9.1	8.9	151 ± 1	78–77
AM (CC) Aged _{1.5}	45 ± 9.5 to -5.0 ± 16	9.6–9.8	~ 9.8	170 ± 28	44–16
LdA (CC) Aged _{1.5}	18 ± 13 to -6.5 ± 1.3	8.1–9.6	~ 9.6	139 ± 2	107–104

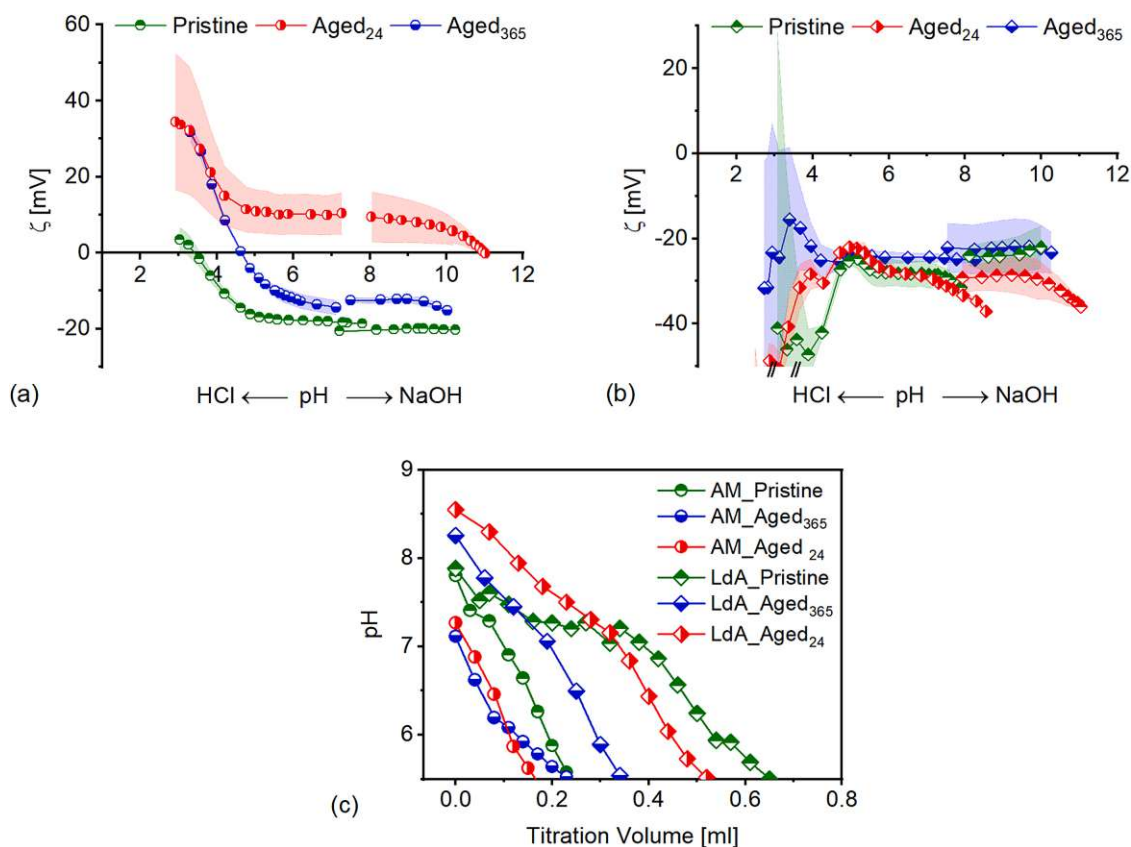


Fig. 5. Streaming current titration in the $3 < \text{pH} < 11$ range performed on pristine and thermally treated (Aged₂₄, Aged₃₆₅) surfaces of a) Apuan Marble, and b) Lumaquela de Ajarte, as analyzed in CC configuration (N_2 -purged 10^{-3} M aqueous KCl probing solution). The shaded areas represent standard deviation ranges. Note that these results involve a combination of pH and salinity variations as the ionic strength changes during titration. Panel c) exhibits the initial pH after rinsing versus titration volume added to reach a pH of 5.5 for both stones and all studied conditions. The auto titrator proceeds by adding given amounts of 0.05 M HCl aqueous solution to the probing electrolyte, thus the small pH shifts recorded in certain pH ranges are indicative of the buffering capacity by the material surface.

Table 5

Summary of relevant properties of pristine and thermally treated (Aged₂₄, Aged₃₆₅) Apuan Marble (AM) and Lumaquela de Ajarte (LdA) measured in the asymmetric cell configuration (CC). pH-dependent electrokinetic measurements are performed for each sample over the $3 < \text{pH} < 11$ range (titration). Note that the pore conductivity refers to the result of single-point measurements in nearly neutral conditions (i.e., before titration; see Fig. S7 in the Supplementary Data).

Sample	ζ -I _{str} [mV]	Testing pH	IEP _{pH}	Cell Res. [kOhm]	Pore Cond. [mS/m]
AM (CC) Pristine	-25.3 ± 4.5	3–11	3.4	1164 ± 44	n/a ^a
AM (CC) Aged ₂₄	5.3 ± 3.6	3–11	11	310 ± 43	32
AM (CC) Aged ₃₆₅	-12.9 ± 0.2	3–11	4.6	453 ± 1	14
LdA (CC) Pristine	-23.4 ± 1.7	3–11	n/a	88 ± 7	228
LdA (CC) Aged ₂₄	-28.1 ± 8.9	3–11	n/a	101 ± 11	181
LdA (CC) Aged ₃₆₅	-23.4 ± 0.9	3–11	n/a	102 ± 0.4	184

^a In the range of experimental error -2 mS m^{-1} (dependent on the correct determination of the cell constant).

surfaces being more prone to dissolution.

Unlike for AM, ζ of LdA does not reach IEP_{pH} in the explored pH range (Fig. 5b) with values ranging between -22 mV and -30 mV for $4 < \text{pH} < 10$ for all specimen conditions. No effect on ζ and the IEP_{pH} are present on surfaces of LdA (Aged₂₄), which can be explained by faster re-carbonation. However, the pristine and Aged₂₄ LdA show

enhanced surface reactivity compared to the Aged₃₆₅ sample. This can be seen through the small pH shifts recorded in certain pH ranges that are indicative of the buffering capacity by the material surface (Fig. 5c). This conclusion is further supported by comparing the results of the initial ζ measurement for each sample (i.e., the first ζ value recorded for each titration scan, towards acid and basic pH, respectively). The smaller dispersion of $\Delta\zeta = 2 \text{ mV}$ for LdA (Aged₃₆₅) as compared with $\Delta\zeta = 5\text{--}8 \text{ mV}$ for pristine and LdA (Aged₂₄) may indicate higher reactivities of the surfaces. The best repeatability in the case of LdA (Aged₃₆₅) occurs, we think, by coincidence rather than by any specific behavior of LdA. Much better correlation between the ζ from the pH scans is observed for AM, independent of its condition.

A peculiar evolution of ζ in the course of titration is observed at $\text{pH} < 5$ where negative ζ increases in magnitude. For pristine and LdA (Aged₂₄), the increase in negative ζ starts below $\text{pH} 4.5$ while the ζ of LdA (Aged₃₆₅) first increases and passes an apparent maximum at $\text{pH} \sim 3.2$ before decreasing again. Other than the reproducibility of ζ for subsequent streaming current measurements at the native pH of the aqueous KCl solution, which we attribute to the varying reactivity of LdA samples, we explain the behavior of ζ at lower pH by the effect of specimen porosity on ζ analysis. Porous materials soaked with aqueous solution become conductive. In the course of the experiment the effect of this ionic conductivity increases with sample porosity and thickness. Both, porosity and thickness are significant for LdA. While pore conductivity suppresses ζ as obtained from streaming potential measurements [50], the contribution of streaming current inside pores, which is enabled by the conductive pathways through interconnected pores [51], to the measured streaming current becomes dominant. The uptake of the aqueous solution into the carbonate by capillary force leads to a partially

soaked cuboid, which prevents quantification of the streaming current through the (wetted) porous network. Changes in the wetting of pore structures between subsequent streaming current measurements may also contribute to the increased standard deviation indicated by the shaded areas in Figs. 5a and b. Overall, the titration results further highlight the influence of surface roughness when assessing the net electrokinetic potentials of macroscopic solid samples. It should be noted that when reactive and rough surfaces are present, the location of the slip plane and the effective surface area that contribute to the recorded streaming current/potential values become inherently more difficult to identify than for well-defined samples. Studies on roughness and corresponding pore solutions and on dynamic solid-liquid interfaces are rare in the literature. Very few studies [52,53] have called attention to this specific and elusive, albeit crucial, issue.

3.5. Asymmetric cell configuration

When electrokinetic measurements are performed using the CC, due to the asymmetric cell wall configuration, corrections are required to obtain true ζ values. This is because the microchannel consists of two different materials, each one contributing with its net surface charge to the overall ζ . In their first description of a similar configuration, Walker et al. [36] assumed equal contributions from the reference poly(methyl methacrylate) and sample surfaces. More recently, the importance of weighing differently the contributions of each surface in a heterogeneous arrangement has been demonstrated [54,55]. This is of particular relevance in the case of reactive and/or porous surfaces that might contribute more significantly to the overall measured electrokinetic parameters. However, differences involving surface roughness and porosity, as affected by actual surface area and pore conductivity, and other factors such as hydrophilicity may significantly affect the results of single-point measurements. Differences in IEP_{pH} are more reliable (i.e. less affected by factors other than the surface chemistry) in providing the fractional contribution of the materials to the overall determined ζ . For this purpose, a nonporous PP was used as the reference material and AM as the tested surface because it is more inert than LdA and its higher compactness allows easier fabrication of the thin rectangular specimens required to fit the AGC. Fig. 6a displays streaming current titration curves to account for the influence of the reference surface.

When using Eq. (17) to analyze the fractional contribution of the studied material through the IEP_{pH} , the influence of the reference PP surface cannot be neglected, as its contribution to the overall ζ amounts to a minimum of $\lambda = 0.3$, and up to $\lambda = 0.5$ for the initial conditions (that is, before starting the titration) based on single point

Table 6

Influence of the reference polypropylene (PP) surface on the overall measured ζ as analyzed with the AGC in titration experiments performed on pristine AM, on PP, and on the combination of PP and AM, respectively, in a 10^{-3} M KCl solution by determining the isoelectric points (IEP_{pH}), single point measurements ($\zeta(I_{str})$) and the initial pH after rinsing for all three setups.

	PP+AM	PP	AM
IEP_{pH}	5.6	4.8	5.9
$\zeta(I_{str})$	-28 to -33	-50 to -55	-16 to -19
Initial pH	7.9	5.8	8.9

measurements (see Table 6). The reactivity of AM can be appreciated through the induced increase of pH, after the standard preliminary rinsing procedure. The pH increase is related to the overall amount of reactive surface present in the microchannel, which results in a drift from the native pH of the probing electrolyte to pH = 7.9 in the case of the mixed PP+AM cell surface, versus pH = 8.9 when both walls of the microchannel are made of AM.

In practice, the simplifying assumption of equal contributions from sample and reference surfaces might be applicable if the surface to be characterized is comparable to that of the reference polymer, i.e., a nonconductive and nonporous material with similar surface roughness and hydrophilicity. However, in the case of large differences between the two surfaces, as it is the case for the rough, porous (i.e., high surface area) and hydrophilic (i.e., with a different and more effective charge formation mechanism compared to a polymer-water interface) carbonate stones, pore conductivity and net release/capture of ionic species make the contribution from the stone surface to the overall ζ dominant. Due to its higher reactivity and brittleness, LdA was not tested to account for the asymmetric cell configuration, but the same considerations about the higher hydrophilicity and surface roughness are expected to apply even more so for this stone.

The use of two different cell configurations involves additional issues when it comes to the interpretation of the measurements of ζ and IEP_{pH} , especially in our case, in which non-equilibrium measurements of reactive surfaces are involved. In previous studies Preočanin et al. [56] found that the measured IEP_{pH} was unaffected by the cell type, while Bukšek et al. [57] found a dependency of the measured ζ on the geometry of microchannels and the size of the tested surface, and Lützenkirchen et al. [58] observed that IEP_{pH} can be affected by the level of roughness. In our measurements the IEP_{pH} value for PP was found to be only slightly affected by the cell type (from pH = 4.6 to pH = 4.8, see Fig. 6b); such slight variation may be ascribed to sample preparation (see Supplementary Data for the preparation method) and experimental

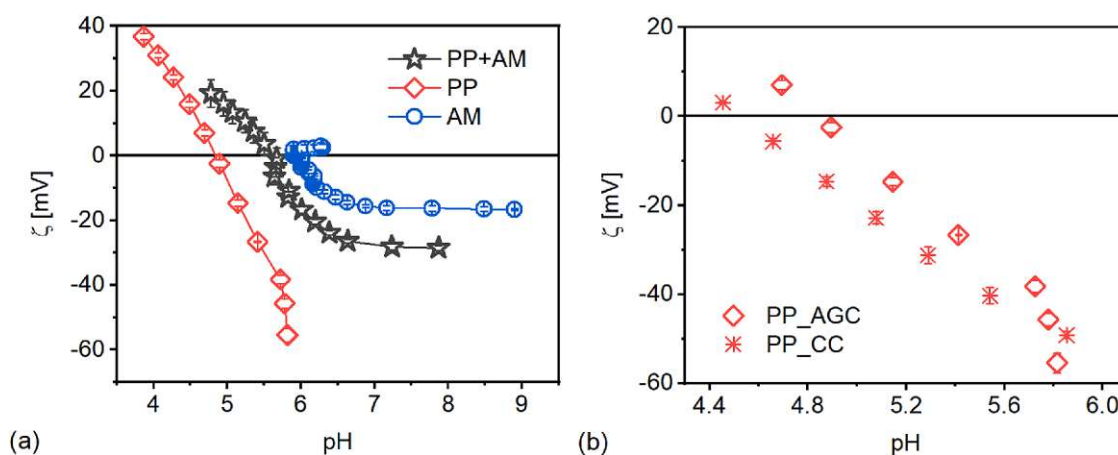


Fig. 6. a) Streaming current titration performed in the AGC on pristine Apuan Marble (AM), polypropylene (PP), and a combination of PP and AM to analyze the influence of the PP reference surface in an asymmetric cell configuration. b) Streaming current titration performed in the AGC and the CC on PP surfaces to analyze the influence of using two cell types. A nitrogen-purged 10^{-3} M aqueous KCl probing solution was used. Note that these results involve a combination of pH and ionic strength variations as a result of both the titration of the probing electrolyte and of the pH-dependent solubility of the tested AM.

errors. However, when reactive materials are present, the surface area analyzed influences the solution chemistry and therefore the readings of ζ and the IEP_{pH}, which is why microchannel geometry takes on a governing role. For a more substantial discussion of the effect of the cell type on the electrokinetic measurements, more experiments are needed (e.g. to account for the possible effects of organic contaminants, instantaneous composition of the probing electrolyte solution, influence of lattice ions on the reference surface if any, etc.). Based on the obtained results, it is apparent that performing electrokinetic measurements with different cells does not lead to directly comparable quantitative data when reactive surfaces are involved. However, the topic of asymmetric cell arrangements, possibly with varying ratios of materials and differing roughness and/or porosities, remains relevant and understudied in light of mixed mineral surfaces that are common in nature. While the AGC is more appropriate for electrokinetic experiments, its limitation is the shaping of specimens to fit a microchannel; the use of the CC is thus justified for the purpose of comparing different surfaces and general trends.

4. Conclusions

Streaming current and potential studies along with physical and chemo-mineralogical characterizations allowed us to follow surface alterations of two natural carbonates in pristine and thermally treated states. Their different reactivities under nonequilibrium conditions in the presence of dilute aqueous electrolytes was investigated. SEM analysis showed newly induced cracks on the thermally treated dense specimens of AM, while the same could not be observed on the inhomogeneous samples of LdA. However, porosimetry and sound speed propagation measurements indicated physical changes also in the fabric of LdA. SEM/EDX analysis showed embedded rhombohedral calcite crystals stabilized by a nanosilica coating applied onto the surface of AM after thermal treatment. For LdA a discoloration of the nanosilica coating occurred due to calcium mobilization. In-situ XRD confirmed that the thermal treatment results in different degradation extent and onset for the two stones. The dense stone AM decomposes earlier and has more calcium oxide on the surface than the porous stone LdA. In the initial period of time-resolved electrokinetic studies, the two analyzed carbonates in their pristine conditions exhibit distinctive electrokinetic potential drifts in opposite directions and differing ζ signs. The initially negative ζ value of AM shifts towards less negative values while the initially positive ζ value of LdA change towards negative ones. Under nonequilibrium conditions, the sample surface roughness influences ζ , as it contributes to dissolution. Thus, the larger effective surface area of LdA caused the strongest increase in solution pH, especially in the initial stages of the experiments. Pore conductivity was found to cause up to 90% underestimation of the absolute value of ζ as assessed by streaming potential. Thermal treatment causes charge reversal from negative to positive for both stones as a result of calcium hydroxide solubility and the supply of Ca²⁺ cations. Therefore, when mixed calcium hydroxide and calcite surfaces are present, the more reactive phases govern the net electrokinetic potential, even when their fractional surface coverage is low. Owing to the ability of these phases to affect conductivity and pH of the probing electrolyte solution, the amount of reactive phases also affect the IEP_{pH}. The pH-dependent electrokinetic measurements further highlight the different behavior of the studied stones. ζ of thermally treated AM is positive due to calcium hydroxide and a recovery of ζ is evident due to re-carbonation. No such effect can be seen on LdA because it is porous and therefore re-carbonates faster and it more easily dissolves already in its pristine state. As a final remark, when due to experimental constraints an asymmetric cell configuration must be employed the fractional contribution of the reference polypropylene on the IEP_{pH} must be considered. In our case the fractional contribution was found to amount to 0.3 and to the overall determined ζ it can reach values of up to 0.5. The obtained data suggest that caution must be taken in the interpretation of results obtained from different cell

configurations in the case of reactive surfaces preventing reliable comparison of quantitative data.

Supplementary data

Permeability of the flow channel; chemical composition as measured by XRF; micrographs; porosimetric and density characteristics of AM; SEM-EDX analysis; exemplary XRD diffractograms and single-point streaming current and potential measurements.

Funding sources

M.B. is a doctoral candidate and acknowledges the support of the Marietta Blau Grant financed by the Austrian Federal Ministry of Education, Science and Research (BMBWF) and coordinated by the Austrian Agency for International Cooperation in Education and Research (OeAD). V.C. and S.B. acknowledge the support by "Nano-Cathedral", funded by the European Program Horizon 2020 Call NMP21-AC (GA 646178). A.V. acknowledges the support from the Czech Academy of Sciences (RVO 68378297). The authors acknowledge TU Wien Bibliothek for financial support through its Open Access Funding Programme.

CRediT authorship contribution statement

Matea Ban: Conceptualization, Investigation, Methodology, Data curation, Formal analysis, Funding acquisition, Validation, Visualization, Writing - original draft. **Thomas Luxbacher:** Validation, Formal analysis, Writing - review & editing. **Johannes Lützenkirchen:** Supervision, Resources, Writing - review & editing. **Alberto Viani:** Supervision, Resources, Writing - review & editing. **Sabrina Bianchi:** Supervision, Resources, Writing - review & editing. **Kludia Hradil:** Supervision, Resources, Writing - review & editing. **Andreas Rohatsch:** Investigation (petrographic description), Writing - review & editing. **Valter Castelvetro:** Conceptualization, Supervision, Resources, Writing - review & editing, Funding acquisition, Project administration.

Declaration of Competing Interest

The authors declare that they have no known competing financial interests or personal relationships that could have appeared to influence the work reported in this paper.

Acknowledgments

Werner Artner is acknowledged for his support in the X-Ray Centre of Vienna University of Technology and Milan Svoboda for the help with mercury intrusion porosimetry and He-pycnometry. Johannes Weber is recognized for his support in obtaining micrographs of thermally treated samples. The authors thank Colorobbia S.p.A for the supplied consolidant NC-12C. Paul Sonnleitner and Peter Urbanek are gratefully acknowledged for proofreading and generally supporting this work.

Appendix A. Supporting information

Supplementary data associated with this article can be found in the online version at [doi:10.1016/j.colsurfa.2021.126761](https://doi.org/10.1016/j.colsurfa.2021.126761).

References

- [1] G.E. Brown, How minerals react with water, *Science* 294 (2001) 67–69.
- [2] C.V. Putnis, E. Ruiz-Agudo, The mineral-water interface: where minerals react with the environment, *Elements* 9 (2013) 177–182.
- [3] P. Fenter, S. Kerisit, P. Raiteri, J.D. Gale, Is the calcite-water interface understood? Direct comparisons of molecular dynamics simulations with specular X-ray reflectivity data, *J. Phys. Chem. C* 117 (2013) 5028–5042.

- [4] D. Al Mahrouqi, J. Vinogradov, M.D. Jackson, Zeta potential of artificial and natural calcite in aqueous solution, *Adv. Colloid Interface Sci.* 240 (2017) 60–76.
- [5] S.L.S. Stipp, Toward a conceptual model of the calcite surface: hydration, hydrolysis, and surface potential, *Geochim. Cosmochim. Acta* 63 (1999) 3121–3131.
- [6] P. Moulin, H. Roques, Zeta potential measurement of calcium carbonate, *J. Colloid Interface Sci.* 261 (2003) 115–126.
- [7] A. Drechsler, A. Caspari, A. Synytska, Influence of roughness and capillary size on the zeta potential values obtained by streaming potential measurements, *Surf. Interface Anal.* 52 (2020) 991–995.
- [8] M. Elimelech, M. Nagai, C.-H. Ko, J.N. Ryan, Relative insignificance of mineral grain zeta potential to colloid transport in geochemically heterogeneous porous media, *Environ. Sci. Technol.* 34 (2000) 2143–2148.
- [9] M. Kosmulski, Isoelectric points and points of zero charge of metal (hydr)oxides: 50 years after Parks' review, *Adv. Colloid Interface Sci.* 238 (2016) 1–61.
- [10] L. Nachbaur, P.C. Nkinamubanzi, A. Nonat, J.C. Mutin, Electrokinetic properties which control the coagulation of silicate cement suspensions during early age hydration, *J. Colloid Interface Sci.* 202 (1998) 261–268.
- [11] A. Sanna, M. Uibu, G. Caramanna, R. Kuusik, M.M. Maroto-Valer, A review of mineral carbonation technologies to sequester CO₂, *Chem. Soc. Rev.* 43 (2014) 8049–8080.
- [12] H. Manzano, R.J. Pellenq, F.J. Ulm, M.J. Buehler, A.C. van Duin, Hydration of calcium oxide surface predicted by reactive force field molecular dynamics, *Langmuir* 28 (2012) 4187–4197.
- [13] M. Gomez-Heras, S. McCabe, B.J. Smith, R. Fort, Impacts of Fire on Stone-Built Heritage, *J. Archit. Conserv.* 15 (2009) 47–58.
- [14] M. Garlock, I. Paya-Zaforteza, V. Kodur, L. Gu, Fire hazard in bridges: review, assessment and repair strategies, *Eng. Struct.* 35 (2012) 89–98.
- [15] Y. Praticò, J. Ochsendorf, S. Holzer, R.J. Flatt, Post-fire restoration of historic buildings and implications for Notre-Dame de Paris, *Nat. Mater.* 19 (2020) 817–820.
- [16] Jd.S. Vazzoler, G.L. Vieira, C.R. Teles, M.K. Degen, R.A. Teixeira, Investigation of the potential use of waste from ornamental stone processing after heat treatment for the production of cement-based paste, *Constr. Build. Mater.* 177 (2018) 314–321.
- [17] E. Martinho, M. Mendes, A. Dionisio, 3D imaging of P-waves velocity as a tool for evaluation of heat induced limestone decay, *Constr. Build. Mater.* 135 (2017) 119–128.
- [18] A. Ozguven, Y. Ozelci, Effects of high temperature on physico-mechanical properties of Turkish natural building stones, *Eng. Geol.* 183 (2014) 127–136.
- [19] F. Vagnon, C. Colombero, F. Colombo, C. Comina, A.M. Ferrero, G. Mandrone, S. C. Vinciguerra, Effects of thermal treatment on physical and mechanical properties of Valderi Marble - NW Italy, *Int. J. Rock. Mech. Min. Sci.* 116 (2019) 75–86.
- [20] M. Prus, K. Szymanek, J. Mills, L.N. Lammers, W. Piasecki, K. Kedra-Krolik, P. Zarzycki, Electrophoretic and potentiometric signatures of multistage CaCO₃ nucleation, *J. Colloid Interface Sci.* 544 (2019) 249–256.
- [21] R.L. Folk, Practical petrographic classification of limestones, *AAPG Bull.* 43 (1959) 1–38.
- [22] R.J. Dunham, Classification of carbonate rocks according to depositional textures, in: W.E. Ham (Ed.), *Classification of Carbonate Rocks*, American Association of Petroleum Geologists Memoir, 1962, pp. 108–121.
- [23] CEN, Standard EN 14579: Natural stone test methods. Determination of Sound Speed Propagation, 2005.
- [24] CEN, Standard EN 15886, Conservation of cultural property. Colour Measurement of Surfaces, 2010.
- [25] T. Degen, M. Sadki, E. Bron, U. König, G. Nénert, The HighScore suite, *Powder Diff.* 29 (2014) S13–S18.
- [26] J. Faber, T. Fawcett, The powder diffraction file: present and future, *Acta Crystallogr. B Struct. Sci. Cryst. Eng. Mater.* 58 (2002) 325–332.
- [27] S.N. Kabekkodu, J. Faber, T. Fawcett, New Powder Diffraction File (PDF-4) in relational database format: advantages and data-mining capabilities, *Acta Crystallogr. B Struct. Sci. Cryst. Eng. Mater.* 58 (2002) 333–337.
- [28] A.A. Coelho, TOPAS and TOPAS-Academic: an optimization program integrating computer algebra and crystallographic objects written in C++, *J. Appl. Crystallogr.* 51 (2018) 210–218.
- [29] H.M. Rietveld, A profile refinement method for nuclear and magnetic structures, *J. Appl. Crystallogr.* 2 (1969) 65–71.
- [30] H. Bruus, *Theoretical Microfluidics*, Oxford University Press, Oxford, 2008.
- [31] C. Werner, H. Korber, R. Zimmermann, S. Dukhin, H.J. Jacobasch, Extended electrokinetic characterization of flat solid surfaces, *J. Colloid Interface Sci.* 208 (1998) 329–346.
- [32] D. Erickson, D. Li, C. Werner, An improved method of determining the zeta-potential and surface conductance, *J. Colloid Interface Sci.* 232 (2000) 186–197.
- [33] A. Cherubini, B. Garcia, A. Cerepi, A. Revil, Streaming potential coupling coefficient and transport properties of unsaturated carbonate rocks, *Vadose Zone J.* 17 (2018), 180030.
- [34] S. Li, P. Leroy, F. Heberling, N. Devau, D. Jougnot, C. Chiaberge, Influence of surface conductivity on the apparent zeta potential of calcite, *J. Colloid Interface Sci.* 468 (2016) 262–275.
- [35] F. Fairbrother, H. Mastin, CCCXII. Studies in electro-endosmosis. Part I, *J. Chem. Soc. Dalton Trans.* 125 (1924) 2319–2330.
- [36] S.L. Walker, S. Bhattacharjee, E.M. Hoek, M. Elimelech, A novel asymmetric clamping cell for measuring streaming potential of flat surfaces, *Langmuir* 18 (2002) 2193–2198.
- [37] S. Siegesmund, K. Ullemeyer, T. Weiss, E.K. Tschegg, Physical weathering of marbles caused by anisotropic thermal expansion, *Int. J. Earth Sci.* 89 (2000) 170–182.
- [38] B.R. Stanmore, P. Pilot, Review-calcination and carbonation of limestone during thermal cycling for CO₂ sequestration, *Fuel Proc. Technol.* 86 (2005) 1707–1743.
- [39] J.D. Merriman, A.M. Hofmeister, D.J. Roy, A.G. Whittington, Temperature-dependent thermal transport properties of carbonate minerals and rocks, *Geosphere* 14 (2018) 1961–1987.
- [40] C. Fischer, R.S. Arvidson, A. Lüttge, How predictable are dissolution rates of crystalline material? *Geochim. Cosmochim. Acta* 98 (2012) 177–185.
- [41] J. Colombani, The alkaline dissolution rate of calcite, *J. Phys. Chem. Lett.* 7 (2016) 2376–2380.
- [42] F. Heberling, T.P. Trainor, J. Lutzenkirchen, P. Eng, M.A. Denecke, D. Bosbach, Structure and reactivity of the calcite-water interface, *J. Colloid Interface Sci.* 354 (2011) 843–857.
- [43] F. Renard, A. Røyne, C.V. Putnis, Timescales of interface-coupled dissolution-precipitation reactions on carbonates, *Geosci. Front.* 10 (2019) 17–27.
- [44] I. Sondi, J. Bišćan, N. Vdović, S.D. Škapin, The electrokinetic properties of carbonates in aqueous media revisited, *Colloids Surf. A Physicochem. Eng. Asp.* 342 (2009) 84–91.
- [45] A. Hiorth, L.M. Cathles, M.V. Madland, The impact of pore water chemistry on carbonate surface charge and oil wettability, *Transp. Porous Med.* 85 (2010) 1–21.
- [46] E. Chibowski, L. Hotysz, A. Szcześ, Time dependent changes in zeta potential of freshly precipitated calcium carbonate, *Colloids Surf. A Physicochem. Eng. Asp.* 222 (2003) 41–54.
- [47] T. Liberto, C. Barentin, J. Colombani, A. Costa, D. Gardini, M. Bellotto, M. Le Merrer, Simple ions control the elasticity of calcite gels via interparticle forces, *J. Colloid Interface Sci.* 553 (2019) 280–288.
- [48] M.D. Jackson, J. Vinogradov, Impact of wettability on laboratory measurements of streaming potential in carbonates, *Colloids Surf. A Physicochem. Eng. Asp.* 393 (2012) 86–95.
- [49] L. Madsen, Calcite: surface charge. *Encyclopedia of Surface and Colloid Science*, CRC Press, 2015, pp. 801–813.
- [50] A. Yaroshchuk, V. Ribitsch, Role of channel wall conductance in the determination of ζ -potential from electrokinetic measurements, *Langmuir* 18 (2002) 2036–2038.
- [51] A. Yaroshchuk, T. Luxbacher, Interpretation of electrokinetic measurements with porous films: role of electric conductance and streaming current within porous structure, *Langmuir* 26 (2010) 10882–10889.
- [52] M. Zembala, Electrokinetics of heterogeneous interfaces, *Adv. Colloid Interface Sci.* 112 (2004) 59–92.
- [53] A.E. Malevich, V.V. Mityushev, P.M. Adler, Electrokinetic phenomena in wavy channels, *J. Colloid Interface Sci.* 345 (2010) 72–87.
- [54] S. Laumann, V. Micic, G.V. Lowry, T. Hofmann, Carbonate minerals in porous media decrease mobility of polyacrylic acid modified zero-valent iron nanoparticles used for groundwater remediation, *Environ. Pollut.* 179 (2013) 53–60.
- [55] I. Petrić, H. Bukšek, T. Luxbacher, T. Pušić, S. Bischof, Influence of the structure of polymer fiber composites on the analysis of the zeta potential, *J. Appl. Polym. Sci.* 135 (2018) 46227.
- [56] T. Preočanin, A. Selmani, P. Lindqvist-Reis, F. Heberling, N. Kallay, J. Lützenkirchen, Surface charge at Teflon/aqueous solution of potassium chloride interfaces, *Colloids Surf. A Physicochem. Eng. Asp.* 412 (2012) 120–128.
- [57] H. Bukšek, T. Luxbacher, I. Petrić, Zeta potential determination of polymeric materials using two differently designed measuring cells of an electrokinetic analyzer, *Acta Chim. Slov.* 57 (2010) 700–706.
- [58] J. Lützenkirchen, G.V. Franks, M. Plaschke, R. Zimmermann, F. Heberling, A. Abdelmonem, G.K. Darbha, D. Schild, A. Filby, P. Eng, J.G. Catalano, J. Rosenqvist, T. Preočanin, T. Aytug, D. Zhang, Y. Gan, B. Braunschweig, The surface chemistry of sapphire-c: a literature review and a study on various factors influencing its IEP, *Adv. Colloid Interface Sci.* 251 (2018) 1–25.

A

Evolution of calcite surfaces upon thermal decomposition,
characterized by electrokinetics, in-situ XRD, and SEM

Supporting Data

Supplementary Data for:

Evolution of calcite surfaces upon thermal decomposition, characterized by electrokinetics, in-situ XRD, and SEM

Matea Ban,^{,a,b} Thomas Luxbacher,^{c,d} Johannes Lützenkirchen,^e Alberto Viani,^f Sabrina Bianchi,^{b,g} Klaudia Hradil,^h Andreas Rohatsch,^a and Valter Castelvetro^{b,g}*

^a Faculty of Civil Engineering, Research Centre of Engineering Geology, TU Wien, 1040 Vienna, Austria

^b Department of Chemistry and Industrial Chemistry, University of Pisa, 56124 Pisa, Italy

^c Anton Paar GmbH, 8054 Graz, Austria

^d Faculty of Chemistry and Chemical Technology, University of Maribor, 2000 Maribor, Slovenia

^e Institute for Nuclear Waste Disposal, Karlsruhe Institute of Technology, 76344 Eggenstein-Leopoldshafen, Germany

^f Institute of Theoretical and Applied Mechanics of the Czech Academy of Sciences, 190 00 Praha, Czech Republic

^g National Interuniversity Consortium of Materials Science and Technology (INSTM), 50121 Florence, Italy

^h X-Ray Center, TU Wien, 1060 Vienna, Austria

CONTENTS

Figure S1 Permeability of the flow channel for the clamping cell	3
Table S1 Chemical composition as determined by XRF	4
Table S2 Mercury intrusion and helium-pycnometry analyses of AM	4
Figure S2a-d Micrographs before and after thermal treatment	5
Figure S3a-b SEM/EDX analysis to determine Ca-Si ratios	7
Figure S4-S5 XRD diffractograms	11
Figure S6 Structural evolution of quartz inversion observed by XRD patterns	14
Figure S7 ζ and pore conductivity of pristine and thermally treated calcite	15
Figure S8 Streaming current and streaming potential titration of LdA	16
Table S3 Summary of relevant properties for all testing conditions	18
Figure S9 Preparation of polypropylene for streaming current titration studies	20

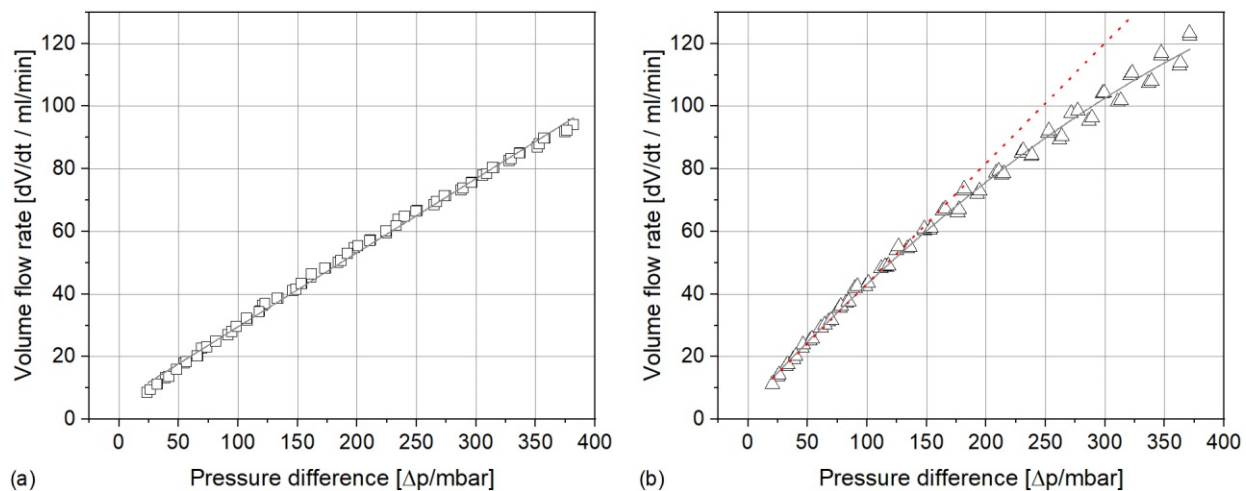


Figure S1. Permeability (volume flow rate vs. pressure difference) for the flow channel in the insert for axial core analysis of the SurPASSTM clamping cell for **(a)** Apuan Marble and **(b)** Lumaquela de Ajarte. The tangent at $\Delta p \rightarrow 0$ mbar shown in (b) shows the slope for calculating the correct gap height. The linear regression of these data underestimates the gap height. The slope of the second-order polynomial fit describes the permeability of the flow channel more reliably. Note that both samples display an acceptable flow rate in both flow directions inside the channel.

Table S1. Chemical compositions determined through XRF and reported as wt.% for Apuan Marble (AM) and Lumaquela de Ajarte (LdA).

Sample	Elemental Concentration [%]								
	O	Ca	Si	Al	Mg	K	Fe	Na	P, Ti
AM	50.3	48.4	0.14	0.05	0.82	<0.05	<0.05	0.2	<0.01
LdA	51.21	45.44	1.37	0.75	0.48	0.34	0.2	<0.05	<0.05

X-ray fluorescence (XRF) was used to obtain information on chemical composition. The instrument used was a Panalytical AXIOS advanced PW4400/40.

Table S2. Mercury intrusion data for specimens in pristine and increasingly thermally treated conditions up to 700 °C for Apuan Marble. Prior to these tests, He-pycnometry (average of four measurements) was carried out on the same samples (1 cm³ in size) to study changes in apparent skeletal density.

Name	Sample Conditioning	Hg-Porosity %	Density g/cm ³
AM Pristine	Sound	0.557	2.718 ± 0.001
AM 200°	200 °C	0.879	2.725 ± 0.011
AM 300°	300 °C	1.027	2.724 ± 0.009
AM 400°	400 °C	1.125	2.712 ± 0.001
AM 500°	500 °C	1.573	2.721 ± 0.001
AM 600° 1 st cycle	600 °C 1 st cycle	2.635	2.715 ± 0.000
AM 600° 3 rd cycle	600 °C 3 rd cycle	3.047	2.717 ± 0.000
*AM 700°	700 °C	10.625	2.699 ± 0.002

*Note that the sample named AM 700° has experienced massive degradation due to transformation processes, which is also indicated by the measured density.

Porometric properties were determined using the AutoPore IV 9500 (Micrometrics) device. The use of He-pycnometry (AccuPyc II 1340, Micromeritics) allowed the assessment of changes in apparent skeletal density when mineral transformation occurred upon thermal treatment.

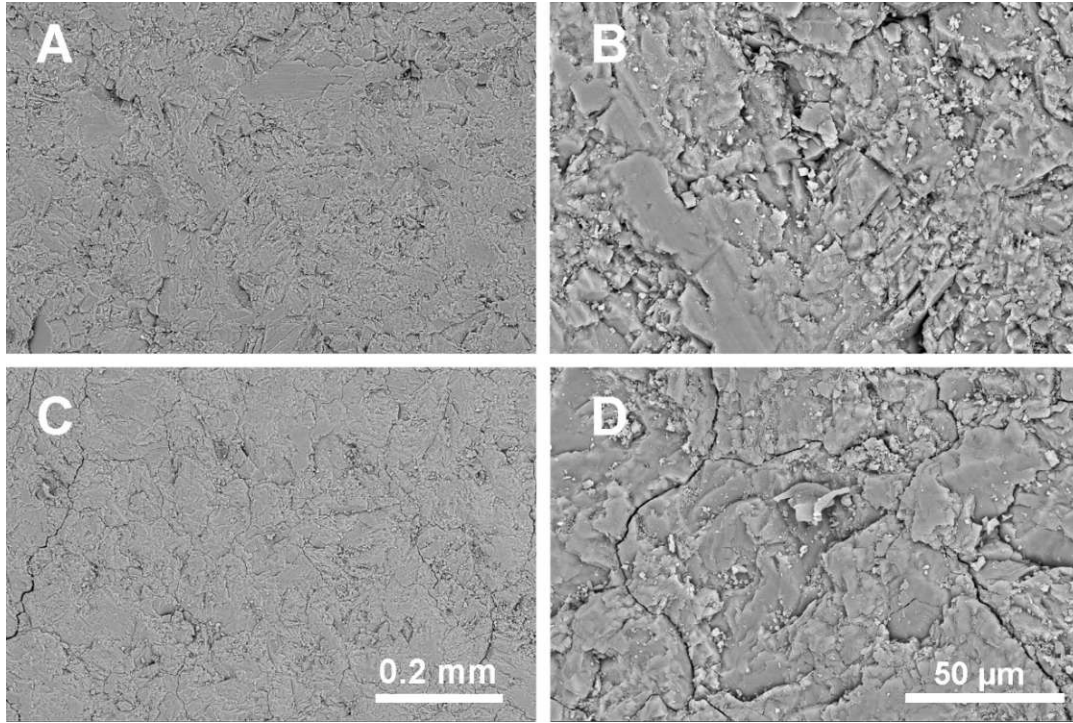


Figure S2a. Scanning electron microscopy micrographs taken with the concentric backscatter detector (CBS) before (a and b) and after thermal treatment (c and d) on surfaces of Apuan Marble.

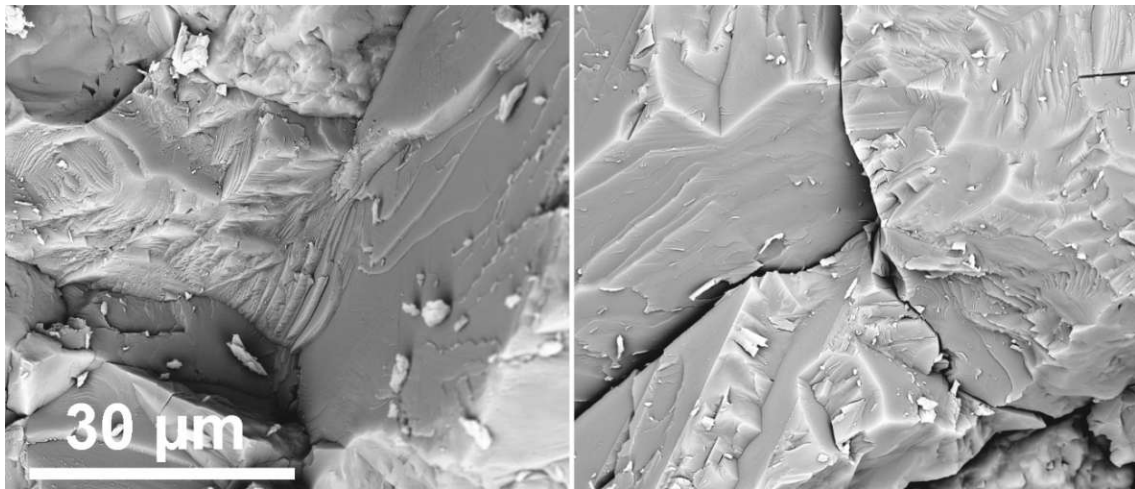


Figure S2b. Scanning electron microscopy micrographs of the BSED signal before (left) and after (right) thermal treatment on a chip (broken piece) of Apuan Marble exhibiting the loss of cohesion on a grain triple junction.



Figure S2c. Polarized microscope micrographs before (**left**) and after (**right**) thermal treatment of Apuan Marble. The fabric after thermal treatment displays mostly microcrack formation along grain boundaries. The scale bar is 200 μm .

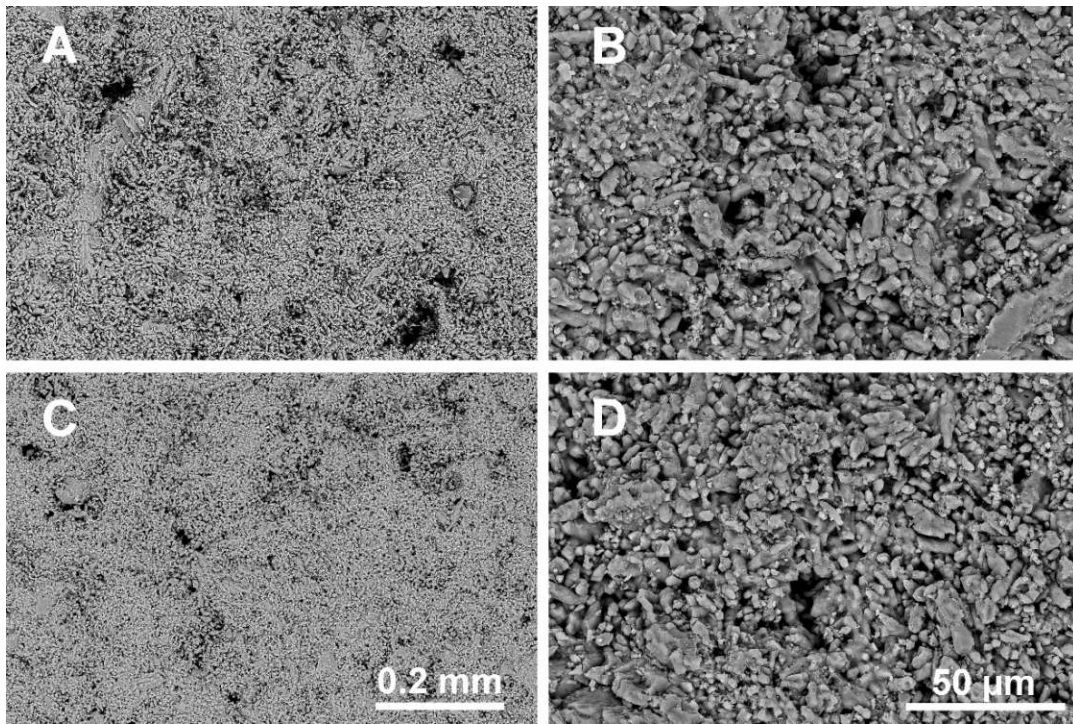
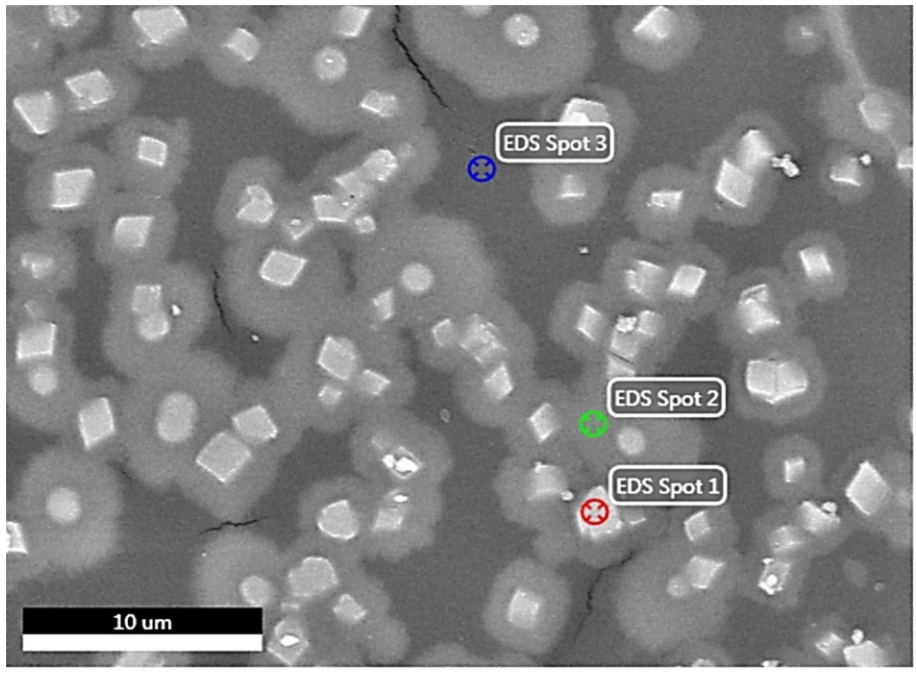
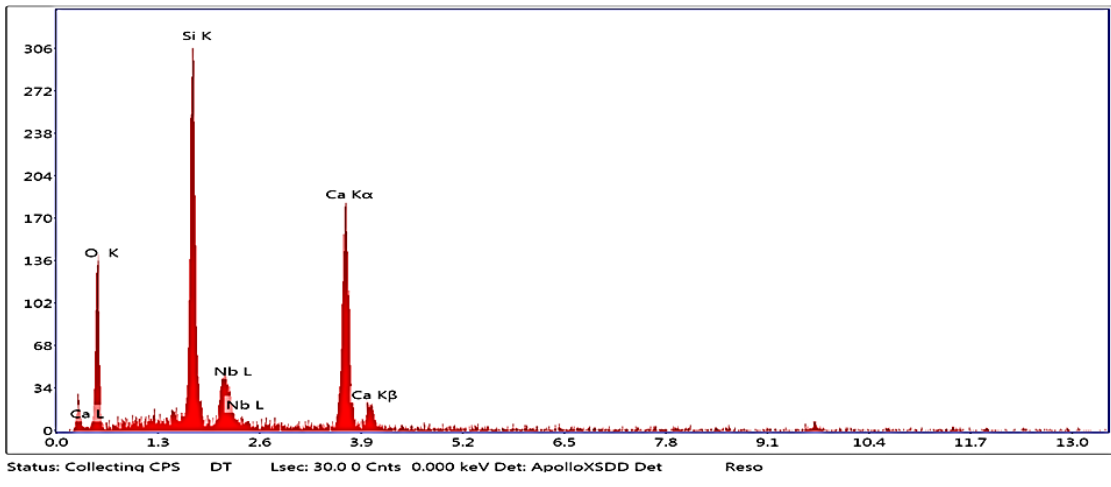


Figure S2d. Scanning electron microscopy micrographs taken with the concentric backscatter detector (CBS) before (**a** and **b**) and after thermal treatment (**c** and **d**) on surfaces of Lumaquela de Ajarte.

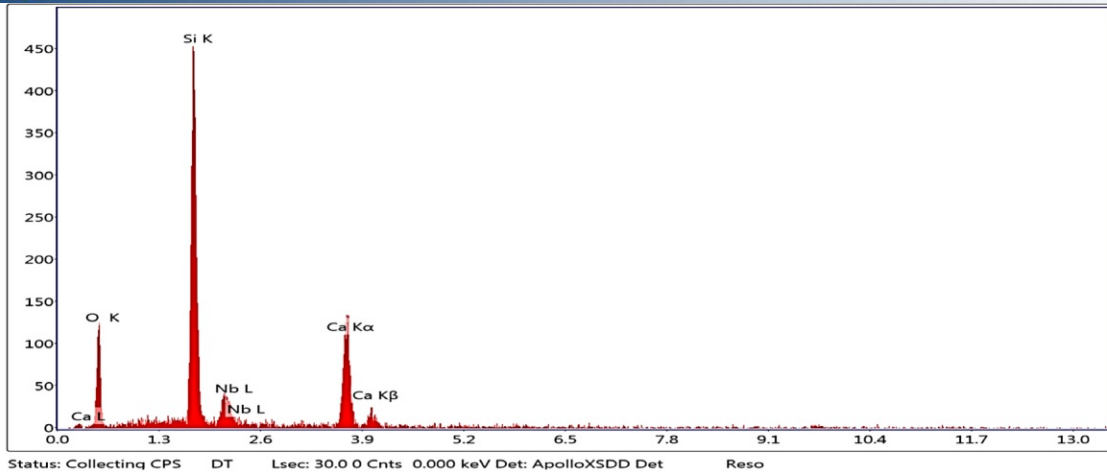


(a)

EDS Spot 1



EDS Spot 2



EDS Spot 3

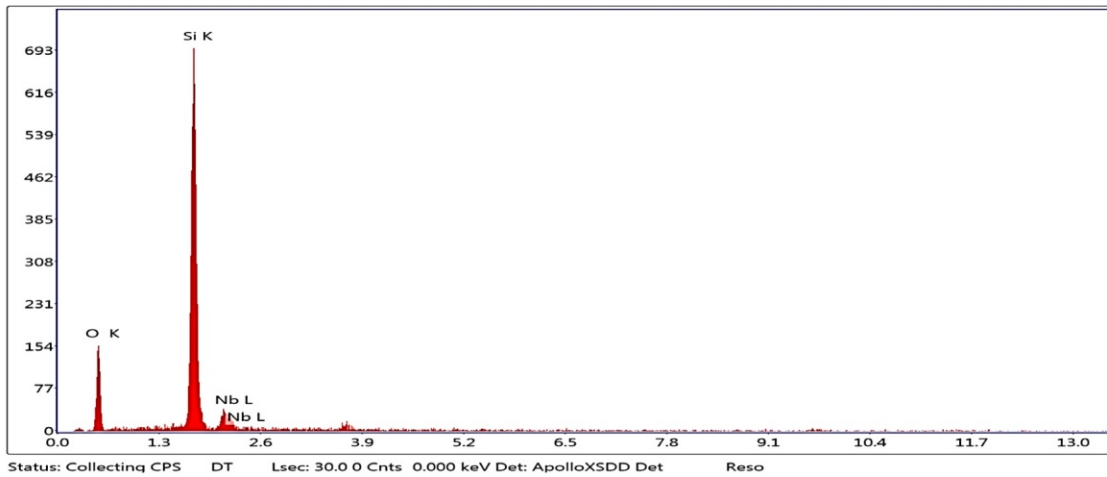
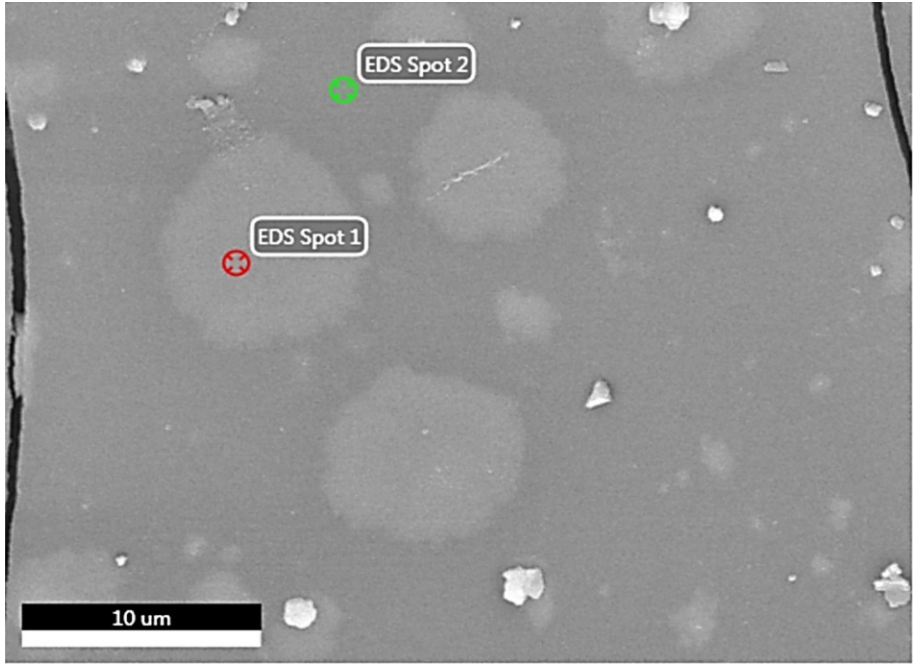
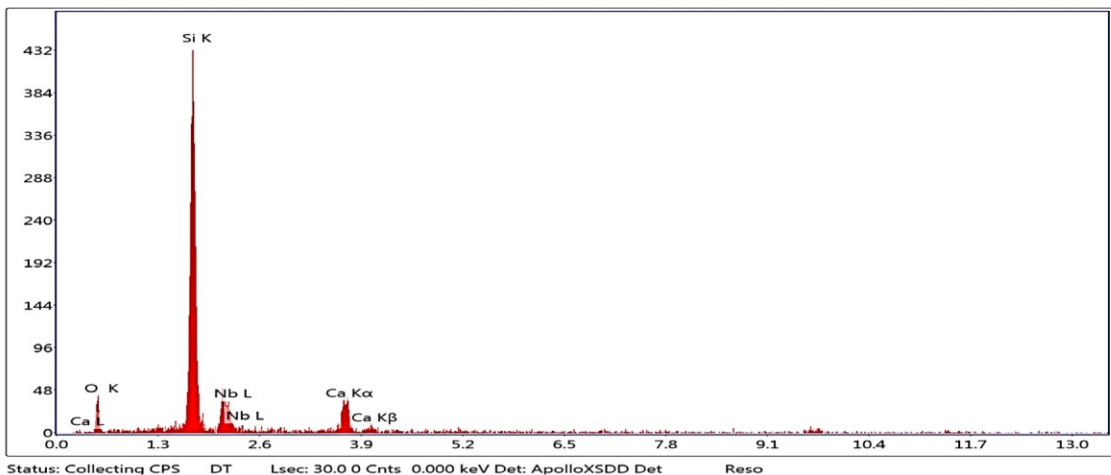


Figure S3a. SEM/EDX analysis of the whitish discoloration in the nanosilica consolidating matrix in Apuan Marble, revealing the distinguished intensities for Ca-Si ratios. The SEM micrograph was obtained in backscatter electron mode, highlighting the concentration gradients around the Ca-rich grains. EDX measurements were focused on the newly formed rhombohedrons (SPOT 1), on the white rim in the silica matrix surrounding the rhombohedrons (SPOT 2), and on the silica matrix surface (SPOT 3) with Apuan Marble as the substrate. The Nb signal is in fact an Au peak (as Au and Nb signals are close together, the software frequently mistakes Nb for Au), so it is present due to the conductive gold coating layer.



(b)

EDS Spot 1



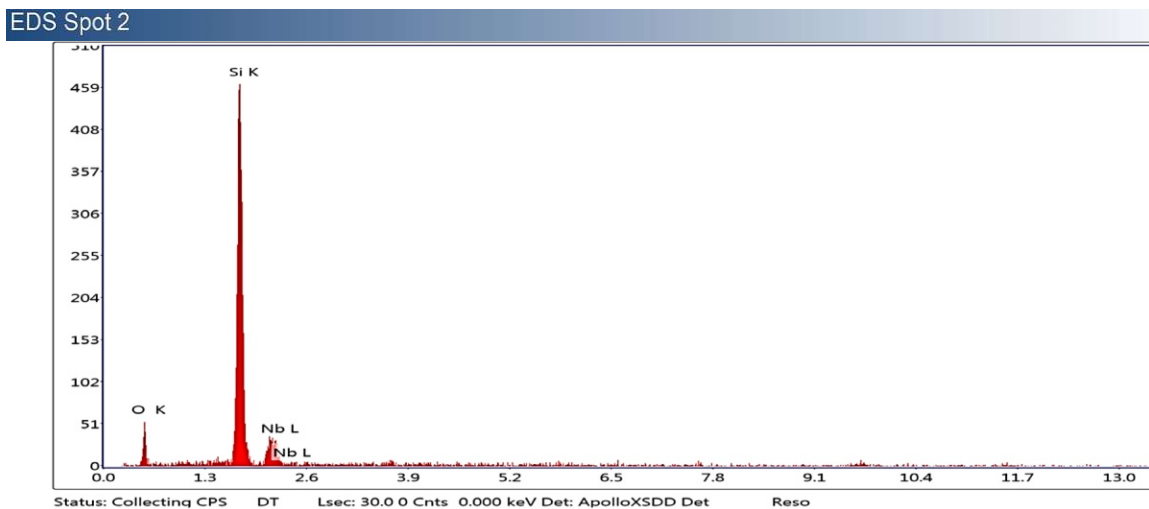
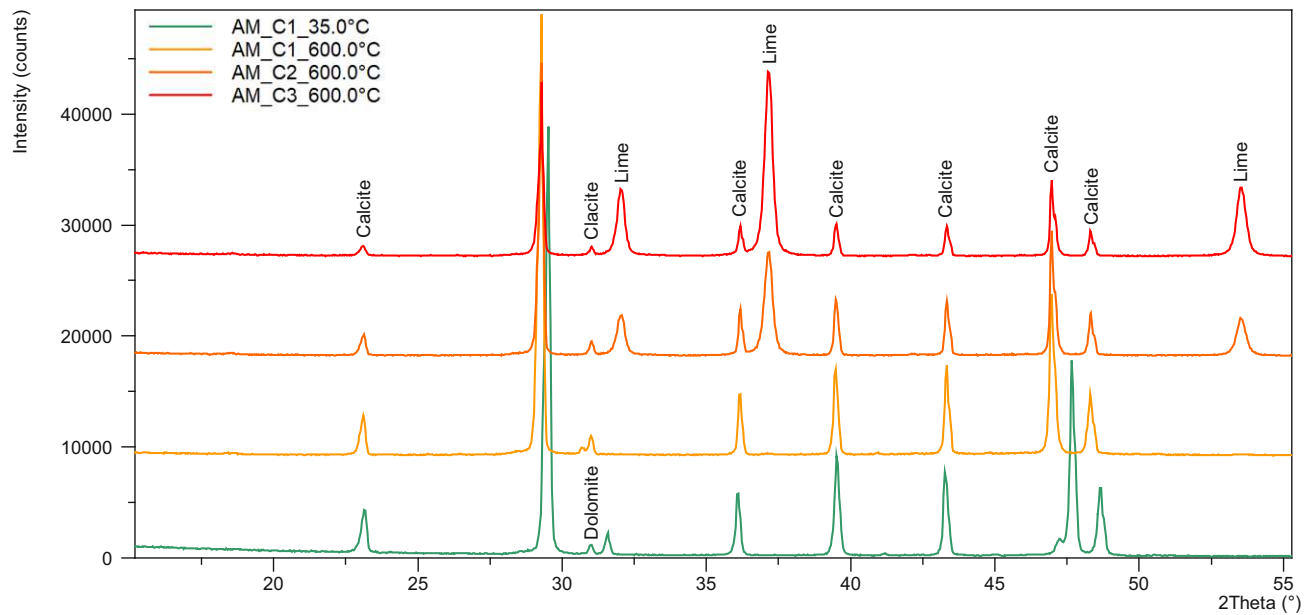


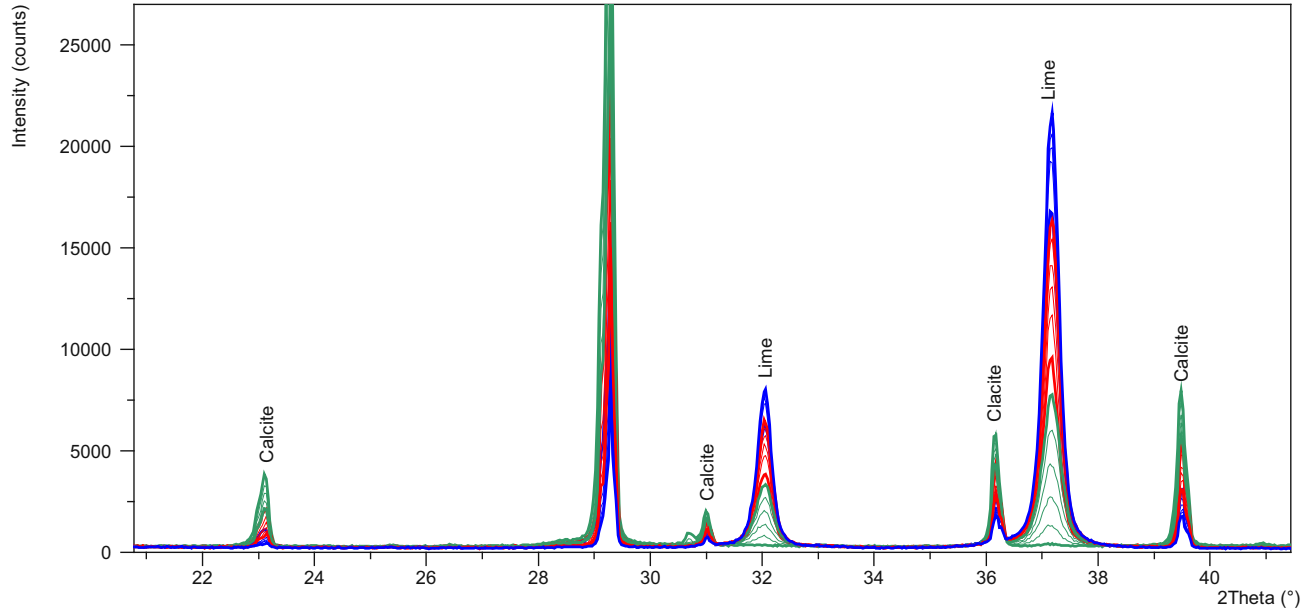
Figure S3b. Details of the SEM/EDX analysis of the whitish discoloration in the nanosilica consolidating matrix in Lumaquela de Ajarte, revealing the distinguished intensities for Ca–Si ratios. The SEM micrograph was obtained in backscatter electron mode. EDX analysis of the white rim present in the silica matrix (SPOT 1) and of the silica matrix (SPOT 2).

Exemplary XRD Diffractograms

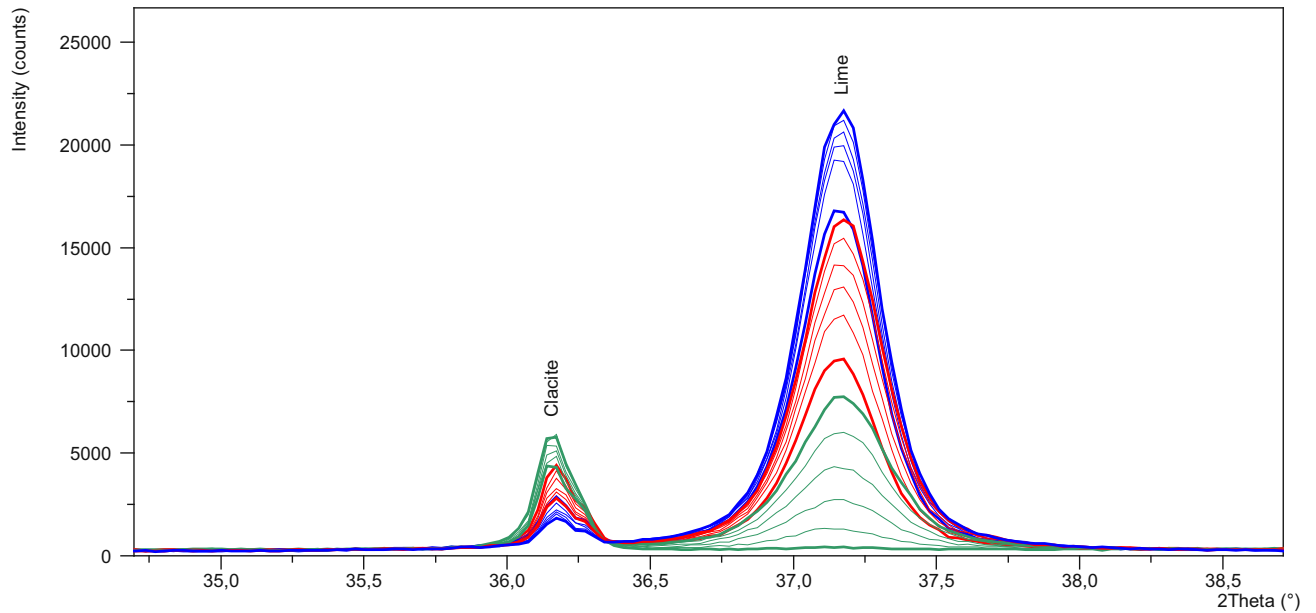
The weight fraction of each of the phases in the samples was obtained adopting the Rietveld method, in which the difference between the experimental XRD diffraction profile and the calculated one is minimized through a least-squares procedure. Typically, during the Rietveld refinement for quantitative phase analysis, the background, some parameters of the peak profile shape, the weight fraction and the parameters of the unit cell of each phase are left free to change, in order to match the experimental diffraction pattern and account for variations, such as those induced by temperature changes (thermal expansion). Few characteristic diffractograms (with measurements performed with constant wavelength) are shown below. Note that the difference in peak position between the spectrum collected at 35 °C and the others is due to the thermal expansion.



(a)

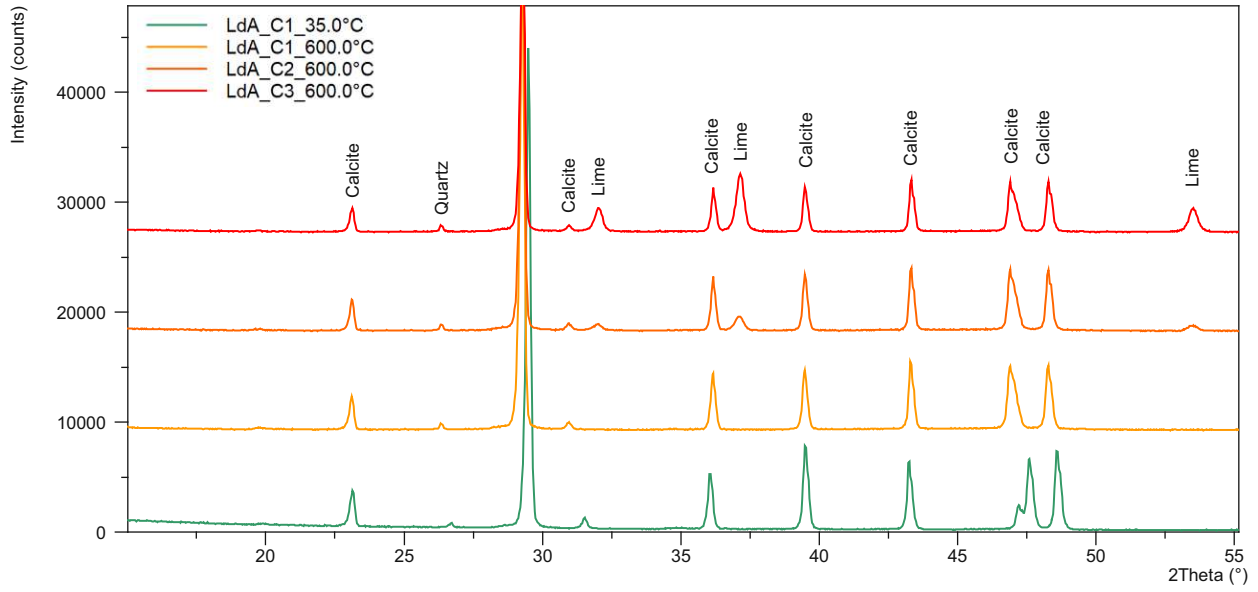


(b)

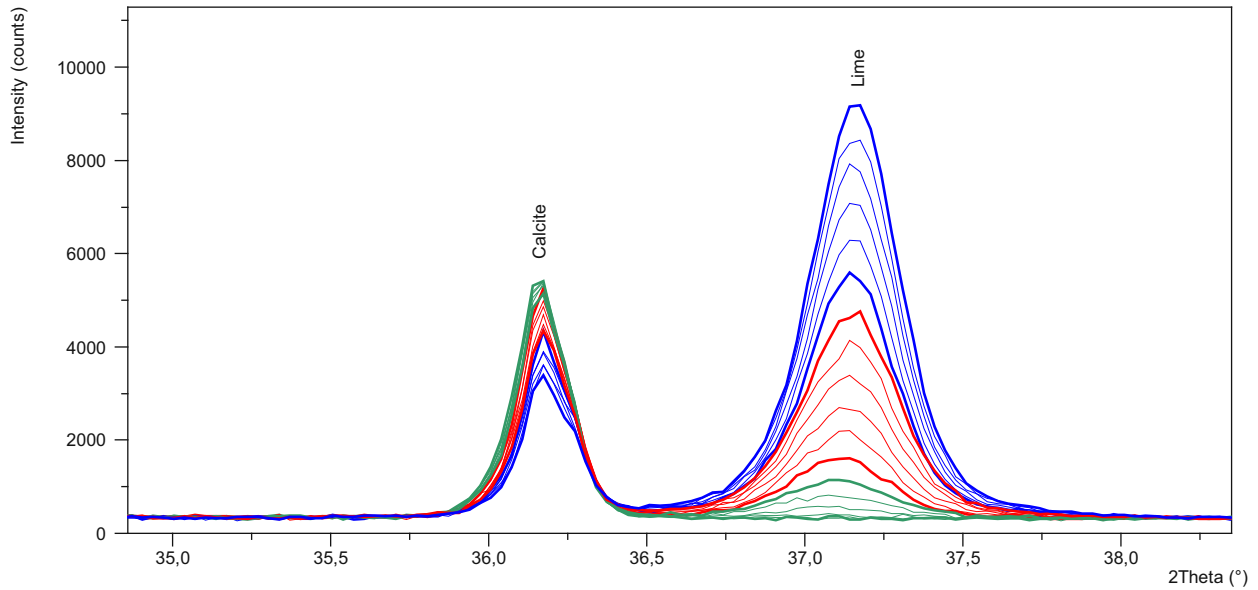


(c)

Figure S4. (a) Apuan Marble diffractograms collected at 35 °C and the first patterns (out of six) collected during the isothermal condition at 600°C per cycle exposed. (b) and (c) Overview and detail of Apuan Marble diffractograms as analyzed by in-situ XRD at isothermal conditions at 600 °C (corresponding to six patterns per cycle). Displayed is the decomposition of calcite and formation of calcium oxide through the cyclic thermal treatments (**green:** 1st isothermal cycle at 600°C, **red:** 2nd isothermal cycle at 600°C and **blue:** 3rd isothermal cycle at 600 °C).



(a)



(b)

Figure S5. (a) Lumaquela de Ajarte diffraction patterns collected at 35 °C and the first patterns (out of six) collected during the isothermal condition at 600°C per cycle exposed. **(b)** Detail of Lumaquela de Ajarte diffractograms as analyzed by in-situ XRD at isothermal conditions at 600 °C (corresponding to six patterns per cycle). Displayed is the decomposition of calcite and formation of calcium oxide through the cyclic thermal treatments (**green:** 1st isothermal cycle at 600°C, **red:** 2nd isothermal cycle at 600°C and **blue:** 3rd isothermal cycle at 600 °C).

Note that the quartz reflections do not disappear but they are shifted slightly towards lower angle in the high temperature regime (**Figure S5a**). To illustrate the changes better we include the difference of low to high quartz in a separate pattern:

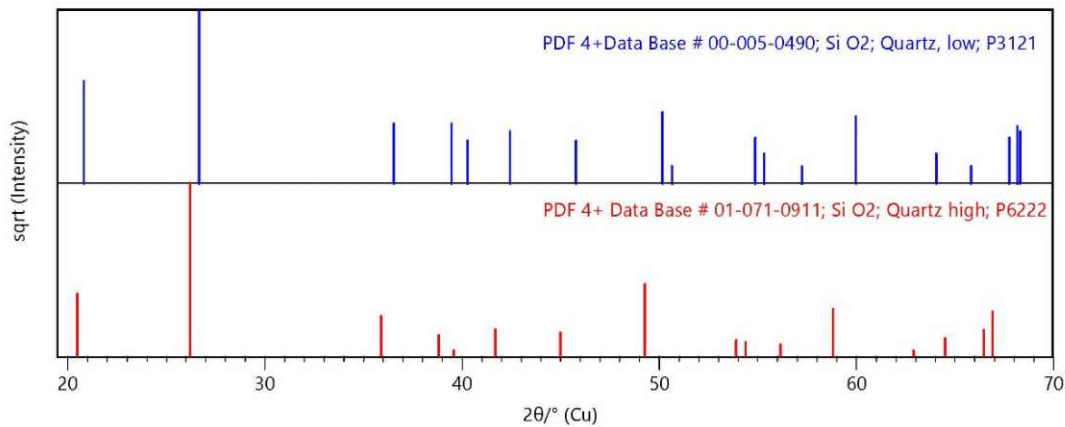


Figure S6. The structural evolution of quartz inversion as observed by XRD patterns

Interatomic distances are correlated with unit cell lattice parameters and employing higher temperatures results in changes of these interatomic distances, which is reflected in the change of the peak position. In the case of quartz two forms are distinct, the alpha- or low quartz that is stable until 573 °C and the beta- or high quartz that is stable above 573 °C [1]. There are no further transformations that occur up to 600 °C. The transition from low- to high quartz is a sudden phase transition (change in crystal structure due to displacement but no bonds are broken [2]) accompanied by a linear expansion. This linear expansion, along with the linear expansion of calcite, is what is responsible for the variations as analyzed by Rietveld refinement (<1 wt.%). The expansion of the minerals causes changes in the penetration depth of the X-rays, which adds to the fluctuation in qualitative analysis. Please note that the specimen displacement was corrected through solving the lattice parameter in each diffractogram.

ζ and Pore Conductivity of Pristine and Thermally Treated Calcite

The electrokinetic properties of the carbonates were studied in their pristine and thermally treated conditions also by employing single-point measurements, as shown in **Figure S7**. A significant difference between the apparent and corrected ζ values obtained from streaming potential measurements, ζ -App(U_{str}) and ζ -Corr(U_{str}), respectively, is prominent in all studied conditions for LdA, while it is significant (i.e., beyond the range of experimental error) only for the thermally treated samples in the case of AM. The resulting differences highlight the necessity of corrections for the effect of pore conductivity. The reason for the difference between ζ -App(U_{str}) and ζ -Corr(U_{str}) for the thermally treated (Aged₂₄ and Aged₃₆₅) AM is the newly formed microcracks. Unlike AM, LdA does not exhibit alterations after thermal treatment, which is in agreement with the limited change in porosity (**Figure S2d** and porometric data from the corresponding manuscript). The higher the porosity, the more severe the underestimation of ζ as determined by streaming potential. The pore conductivity causes an underestimation of ζ -Corr(U_{str}) values by approx. 90% in the case of the highly porous LdA for all studied conditions and up to 20% for the pristine dense AM. After the formation of microcracks, the underestimation of ζ -Corr(U_{str}) for the thermally treated AM increases to ~70%. It should be noted that pH-dependent data exhibit the same underestimation of ζ due to effects of pore conductivity as can be seen in **Figure S8**.

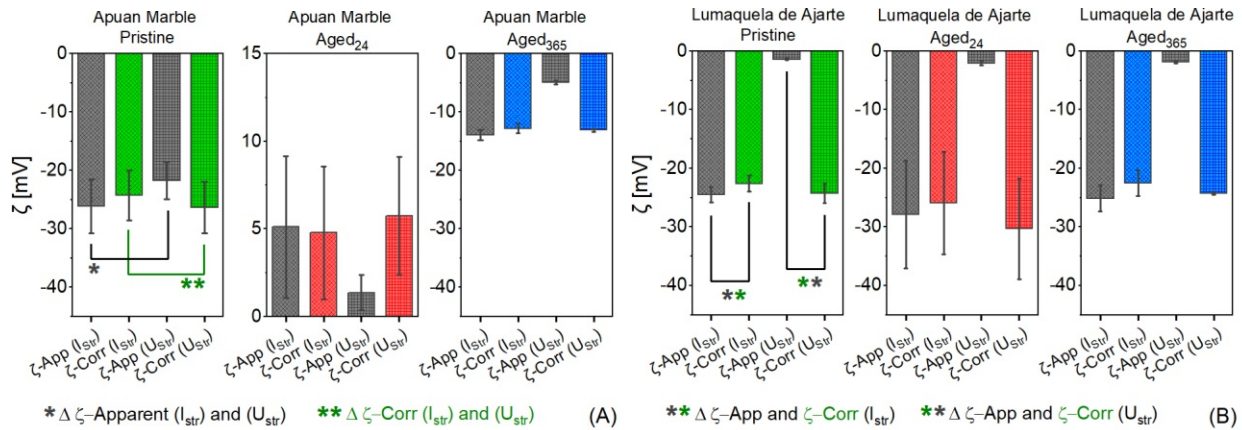


Figure S7. Apparent and corrected (to account for permeability and pore conductivity) ζ -potential values as obtained by streaming current (I_{str}) and streaming potential (U_{str}) measurements under nonequilibrium conditions and neutral pH using a 10^{-3} M KCl probing solution. Measurements performed with a CC cell on pristine and thermally treated (Aged₂₄, Aged₃₆₅) surfaces of **a**) Apuan Marble and **b**) Lumaquela de Ajarte. The pH was varied stepwise from 7.5 to 7.7 for Apuan Marble and from 7.5 to 8.2 for Lumaquela de Ajarte.

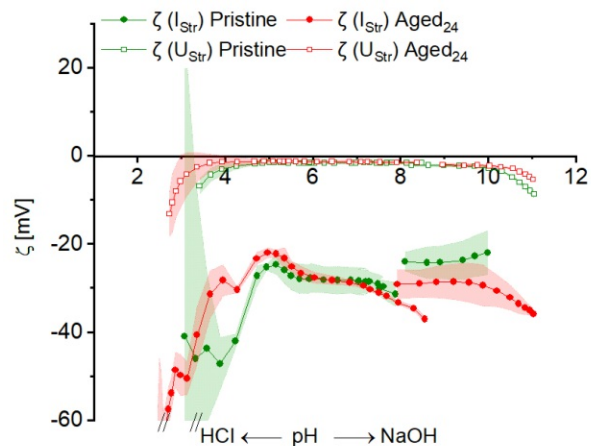


Figure S8. Streaming current (I_{str}) and streaming potential (U_{str}) titration in the $3 < \text{pH} < 11$ range performed on pristine and thermally treated (Aged₂₄) surfaces of Lumaquela de Ajarte, as analyzed in the CC configuration (N_2 -purged 10^{-3} M aqueous KCl probing solution), to assess the influence of pore conductivity on ζ - U_{str} readings. The resulting differences highlight the necessity for corrections of the effect of pore conductivity.

For AM in its pristine state, both $\zeta\text{-Corr}(I_{str})$ and $\zeta\text{-Corr}(U_{str})$ yield values of $-25 \text{ mV} \pm 4 \text{ mV}$. However, upon thermal treatment, they become positive ($5 \text{ mV} \pm 4 \text{ mV}$). The thermally altered surface contains a fraction of highly reactive CaO that quickly hydrates as it comes into contact with the aqueous solution, resulting in positive electrokinetic charge as a consequence of partial hydroxide ionization and the release of hydroxyl ions, leaving a surface excess of calcium cations. These results indicate that reactive phases, when present, may govern electrokinetic charge, even when the surface coverage of the reactive phases is below 50% (note that half of the microchannel inner surface is made of PP and the other half is a mixed system of calcite and calcium (hydr)oxide). Different contributions to electrokinetic charge for mixed systems may involve the combined effects of both higher reactivity and larger effective surface area. Nevertheless, the present measurements were well reproducible, even for these nonequilibrium conditions. A shift in the electrokinetic charge to positive ζ values was detected for the freshly aged AM, as it re-carbonates less rapidly than LdA. Upon re-carbonation, the electrokinetic charge of AM changes sign again, yielding $\zeta\text{-Corr}(I_{str})$ and $\zeta\text{-Corr}(U_{str})$ of -13 mV . The observed difference between the average $\zeta\text{-Corr}$ for AM in its pristine and re-carbonated states can be partially explained by the more effective release of lattice ions after thermal treatment and

re-carbonation (increased adsorption of Ca^{2+} yields more positive ζ values, source of ions is calcite dissolution) and due to the absence of organic matter (organic matter yields more negative ζ values when present). The decrease in the electrical resistance inside the streaming channel gives additional evidence for the thermally altered surfaces being more prone to dissolution (see cell resistance values in **Table S3**), as the interface between the bulk substrate and the phase-transformed/re-precipitated deposits is known to be a weakly bound layer prone to cracking and detachment.

For LdA, ζ -Corr(I_{Str}) and ζ -Corr(U_{Str}) remain comparable in magnitude at around -25 mV for all studied conditions, with the samples Aged24 exhibiting the greatest scattering (± 8.5 mV). Although organic matter may have an influence on the electrokinetic charge of pristine carbonates, making it more negative [3], such influence can be excluded for the surfaces exposed to cyclic heating at 600 °C, which results in the pyrolytic removal of all contaminating organic matter for both freshly thermally treated and re-carbonated samples. Similarly, trace-element incorporation that may affect ζ [4] can be disregarded in the present study, as shown by the substantial invariance of ζ to thermal ageing of the less-pure LdA, i.e., that containing iron oxide-hydroxides which undergo a thermally induced phase transformation [5,6] that is being irrelevant for ζ as it is only present at <1 wt.% (see chemical composition in **Table S1**).

Table S3. Summary of relevant properties for all testing conditions of Apuan Marble (AM) and Lumaquela de Ajarte (LdA) as determined in the asymmetric cell configuration (CC) and the symmetric cell configuration (AGC).

Carbonate (Cell type)	Condition ⁽¹⁾	Testing mode	ζ -I _{str} and ζ -U _{str} [mV] ⁽²⁾	Testing pH	IEP _{pH} ⁽³⁾	Gap Height [μ m] ⁽⁴⁾	κ_B [mS/m]	Cell Res. [kOhm] ⁽⁵⁾
AM (AGC)	Pristine Non-Eq	Time-resolved (62.5 h)	I _{str} -19.5 ± 1.6 to -10.1 ± 0.3 U _{str} -18.9 ± 1.9 to -9 ± 0.4	7 to 8.6	n/a	141	20.3 (± 1.5)	623 (± 53.3)
LdA (AGC)	Pristine Non-Eq	Time-resolved (1.3 h)	I _{str} 5.5 ± 3.6 to -5.1 ± 1.9 U _{str} 1.6 ± 0.3 to -1.3 ± 0.2	8.2 to 9.1	8.9	137	17.1 (± 0.5)	151 (± 1)
AM (CC)	Aged _{1.5} Non-Eq	Time-resolved (8 h)	I _{str} 45.3 ± 9.5 to 5.0 ± 16.4 U _{str} 5.9 ± 3.1 to 1 ± 1.6	9.7 to 9.6	~ 9.8	118	20.7 (± 0.8)	170 (± 27.9)*
LdA (CC)	Aged _{1.5} Non-Eq	Time-resolved (15 h)	I _{str} 18 ± 13 to -6.5 ± 1.3 U _{str} 6.9 ± 6.4 to -0.7 ± 0	6.7 to 9.6	~ 9.6	113	17.7 (± 1.2)	139 (± 1.9)*
AM (CC)	Pristine Non-Eq	Titration and single point	-25.3 ± 4.5	7.5 ± 0.2	3.4	132	19.5	1164 (± 44.5)
AM (CC)	Aged ₂₄ Non-Eq	Titration and single point	5.3 ± 3.6	7.6 ± 0.2	11	128	20.3	310 (± 43)
AM (CC)	Aged ₃₆₅ Non-Eq	Titration and single point	-12.9 ± 0.2	7.7 ± 0.1	4.6	141	17.8	453 (± 1.2)
LdA (CC)	Pristine Non-Eq	Titration and single point	-23.4 ± 1.7	7.8 ± 0.3	n/a	103	21.8	88 (± 7.2)
LdA (CC)	Aged ₂₄ Non-Eq	Titration and single point	-28.1 ± 8.9	8.2 ± 0.2	n/a	110	21.9	101 (± 11.3)
LdA (CC)	Aged ₃₆₅ Non-Eq	Titration and single point	-23.4 ± 0.9	7.6 ± 0.2	n/a	128	22	102 (± 0.4)
AM+PP (AGC)	Pristine Non-Eq	Titration and single point	-28 to -33	7.9	5.6	148	17.1	680 (± 10)
PP (AGC)	Pristine	Titration and single point	-50 to -55	5.8	4.8	115	15.9	785 (± 11)
AM (AGC)	Pristine Non-Eq	Titration and single point	-16 to -19	8.9	5.9	107	17.8	1105 (± 13)
PP (CC)	Pristine	Titration and single point	-49	5.8	4.6	105	16.2	1088 (± 2)

(1) Open system and N₂ purged during experiments. Time passed prior to recording was approx. 5 min, which is necessary to assure a complete wetting of the surface and conditioning for the flow rate measurement. If not stated otherwise, the initial pH of the 1 mM KCl aqueous electrolyte corresponded to approx. 5.5-6.5 due to the use of ultrapure water.

(2) Average ζ -(Corr) values, otherwise time-resolved experiments with first and last recording reported.

(3) Obtained either through titration or time-dependent streaming.

- (4) The channel dimensions were corrected from a width of 5 mm and the length of 25 mm to a width of 6 mm and the length of 12.5 mm due to the use of a custom-made microchannel in the CC configuration.
- (5) The listed cell resistance inside the streaming channel corresponds to the shift from ζ -Istr to ζ -Ustr measurements in single-point mode or to the change from the beginning to the end of the experiments for time-resolved mode. Note that the decrease in cell resistance inside the streaming channel indicates ion accumulation, which can be correlated with porosity (compare AM and LdA or compare AM-Pristine to AM-Aged) and help to account for effects of pore conductivity when streaming potential measurements are obtained. Moreover, changes in cell resistance during the experiments might indicate the reactivity of the sample.

*First recording excluded

Preparation of Polypropylene for Streaming Current Titration Studies

Preparation of the Polypropylene (see **Figure S9**) was done by cutting and grinding the surface with an abrasive paper. To exclude any leaching the surfaces were rinsed with a 0.1 M HCl and 0.1 M NaOH. Subsequently, ethanol was employed to clean the surfaces followed by multiple ultrasonic baths in ultra-pure water.



Figure S9. Preparation of the PP

References

- [1] Britannica, T. Editors of Encyclopaedia (2020). Quartz. Encyclopedia Britannica. <https://www.britannica.com/science/quartz>
- [2] Simmons, W. B. and Stewart, David B. (2018). Silica mineral. Encyclopedia Britannica. <https://www.britannica.com/science/silica-mineral>
- [3] L. Madsen, Calcite: surface charge, Encyclopedia of surface and colloid science, CRC Press 2015, pp. 801-813.
- [4] M. Wolthers, L. Charlet, P. Van Cappellen, The surface chemistry of divalent metal carbonate minerals; a critical assessment of surface charge and potential data using the charge distribution multi-site ion complexation model, Am. J. Sci., 308 (2008) 905-941.
- [5] E. Brendle, J. Dentzer, E. Papirer, Variation of the surface properties of hematite upon heat treatment evidenced by inverse gas chromatography and temperature programmed desorption techniques: Influence of surface impurities and surface reconstruction, J. Colloid Interface Sci., 199 (1998) 63-76.
- [6] A.F. Gualtieri, P. Venturelli, In situ study of the goethite-hematite phase transformation by real time synchrotron powder diffraction, Am. Mineral., 84 (1999) 895-904.

B

Efficiency and compatibility of selected alkoxy silanes on porous carbonate and silicate stones

Article

Efficiency and Compatibility of Selected Alkoxysilanes on Porous Carbonate and Silicate Stones

Matea Ban ^{1,*}, Elisabeth Mascha ², Johannes Weber ², Andreas Rohatsch ¹
and José Delgado Rodrigues ³

¹ Institute of Geotechnics, Research Centre of Engineering Geology, Vienna University of Technology, 1040 Vienna, Austria; andreas.rohatsch@tuwien.ac.at

² Institute of Art and Technology, Conservation Science, University of Applied Arts Vienna, 1010 Vienna, Austria; elisabeth.mascha@uni-ak.ac.at (E.M.); johannes.weber@uni-ak.ac.at (J.W.)

³ National Laboratory for Civil Engineering Lisbon, 1700-066 Lisbon, Portugal; delgado@lnec.pt

* Correspondence: matea.ban@tuwien.ac.at; Tel.: +43-158-801-20318

Received: 1 December 2018; Accepted: 29 December 2018; Published: 6 January 2019



Abstract: This study compares the consolidation efficiency and compatibility of three selected alkoxysilanes on two porous carbonate and silicate substrates. Emphasis was given to artificially induced microstructural defects and subsequent restoration of mechanical and physical properties. Two newly engineered formulations (1) a TiO₂ modified tetraethyl-orthosilicate in isopropanol with 70% active content and (2) a TiO₂ modified alkyl-trialkoxysilane in isopropanol with 75% active content were compared to a commercial product (3), a solvent free tetraethyl-orthosilicate with 99% active content. Treatments were evaluated by scanning electron microscopy, mercury intrusion porosimetry, colour impact and their effect on dynamic modulus of elasticity, splitting tensile- and flexural strengths, capillary water absorption and water vapour permeability. A key outcome was that mechanical strength gain induced by treatments is primarily governed by a stone's texture and microstructure, and secondarily by the gel deposition rate of consolidants. Likewise, the kinetics of the gel-forming reaction during curing is dependent not only on the product but also on the substrate. Therefore, the moisture related properties and the visual impact develop during time. There is no general trend on how it evolves in time, which can lead to incorrect interpretations of treatment compatibility. The results prove that wide-ranging treatment performance is obtained when applying the same products on different substrates.

Keywords: stone consolidants; tetraethyl-orthosilicate; ethyl silicate; TEOS; alkyl-trialkoxysilane; efficiency; compatibility; natural stone; mechanical testing; scanning electron microscopy

1. Introduction

A wide variety of natural stones are used as building materials; they exhibit a correspondingly wide range of chemical, physical and mechanical properties. When exposed to outdoor environments, they undergo changes that range from surface decay and erosion to deep structural disintegration [1]. This decay features often display complex morphological patterns and may necessitate the stone's consolidation to reinstate the lost cohesion. While the assessment of the success of laboratory consolidation treatments of selected test specimens is not simple and depends on a variety of factors, the assessment of on-site treatments of naturally weathered stones under real conditions is even harder and sometimes unpredictable. Every characteristic of the stone as well as the treatment procedures may have a major impact on the efficiency and compatibility of the treatment [2], and by varying one of them, the results might change drastically.

When testing a newly engineered consolidant, the basic conditions of the product application need to be kept simple and reproducible to test the properties of the consolidant in a systematic manner, following a tailored specific protocol. Three main alternatives may be followed in the testing process: (i) to use homogeneous, fresh stone specimens; (ii) to test on naturally aged and (iii) on artificially aged specimens. The first option reduces the number of variables in the process and makes results easier to compare, while the second one tends to increase heterogeneity and dispersion of results. The second alternative is usually supported with the argument that it is more representative of natural conditions. Using samples taken from naturally aged stone would be a good option, but rarely are enough of such samples available for extensive laboratory testing and, therefore, artificially aged samples were used along this study. Most test methods are appropriate for homogeneous specimens of reasonable dimensions; therefore, artificially aged specimens rarely entirely fulfil such requirements and the interpretation of results becomes more difficult. To overcome this important limitation, some authors prefer to use porous stone varieties of similar mineralogical composition in their sound state [3,4].

Artificial aging induces microstructural defects intended to mimic a certain type of natural decay process, thus, it allows the study of the solely properties of a consolidant, and its ability to improve the mechanical and physical properties of a stone. To prepare artificially decayed samples, e.g., thermal treatment of stone specimens [5], and freeze-thaw cycles [6] have been used. Thermal treatment induces micro cracks that correspond to a frequent type of de-cohesion formed by weathering on-site; they reduce the stone soundness by decreasing its mechanical strength and increasing its porosity and rate of capillary absorption [7]. As for freeze-thaw ageing, some stone varieties require many cycles before a microstructural defect is induced and others break prematurely due to the formation of larger cracks, which makes this method not adequate for large-scale testing purposes, especially mechanical testing [8]. Other laboratory ageing methods e.g., with salt crystallization or acid attack produce a pronounced gradient of degradation, which may lead to results difficult to interpret, even when the obtained decay pattern appears to be close to reality. Thermal cycles on the other hand are likely to produce a homogeneous decay pattern through the full diameter of the stone, a prerequisite for testing the macro properties according to most standard natural stone test methods [9].

Whatever aging method is used, the aged samples will never fully mimic reality. Consequently, the option for one or another strategy mostly depends on the available methods and means, and a best fit scenario to test the given hypotheses.

A closer look on the meaning of the terms “efficiency” and “compatibility” of stone consolidants is useful to understand how to assess them. The primary function of a stone consolidant is to re-establish the cohesion between grains thus restoring the mechanical properties of the weathered stone material [10]. Only in this way, the product can be assumed to fulfil its primary function of enhancing a stone’s strength. Therefore, in order to assess its efficiency, the mechanical properties of the specimen before and after the treatment need to be evaluated. The first issue that arises hereby is the definition of the degree to which the mechanical strength needs to be increased in respect to a chosen starting condition, i.e., sound or aged. There are no general rules and only the notion except the general consensus that the treated stone should not be excessively stiffer than the substrate [11,12]. The reasons for the variation in the mechanical strength need to be studied, but insofar as our knowledge of the mechanisms involved in the strength increase due to the treatment is incomplete and vague, validation of test results remains empirical. As an example, it is accepted that increasing the mechanical strength by only a few percent—and this effect was observed in many studies—may be enough when certain decay patterns are in question [13,14].

In the laboratory testing routine, a few techniques including drilling resistance, tensile strength testing, and measurement of ultrasound pulse velocity are employed to evaluate the efficiency of consolidants [15–20]. In addition, various types of tensile test, which include the pull-off adhesive, splitting tensile- or flexural strength tests, are indicators of microstructural defects and thus are apt to describe in the most effective way the action the consolidant exerts on a stone fabric [21]. Even though these methods provide better insights into the effect of a treatment, it must be kept in mind that the

applied stresses do not correspond to the micro- and macro mechanical stresses that a material has to bear on-site where e.g., shear stresses parallel to the surface of exposure may play a major role.

A further technique used to assess the efficiency of a consolidation treatment is the determination of the dynamic modulus of elasticity as described by the fundamental resonance frequency and ultrasound pulse velocity. This is an accurate method capable of describing indirectly the closure of pores and cracks. It can give a bulk indication of the amount of consolidant deposited in the stone. Nevertheless, when a stone accommodates a large amount of a weakly strengthening consolidant, the efficiency may still be poor, which is why a combination of different tests is recommended to assess the treatment's efficiency. Despite the variety of test methods currently available, a systematic protocol to evaluate the efficiency of consolidants—with a multiscale approach—has yet to be defined in the field of architectural conservation science.

The secondary role of a consolidant is its ability to restore the physical properties of the weathered fabric without potential side effects [22]. This is particularly important for the compatibility with the substrate, a broad term comprising issues such as the chemical affinity and the impact on physical parameters relevant to identify and quantify the potential damages caused by the treatment [23,24]. The physical properties frequently used are porosity and moisture related properties, such as water vapour permeability, pore size distribution, and the drying rate of treated vs. untreated stone.

Further means to study compatibility and predict harmfulness may comprise scanning electron microscopy (SEM)-techniques on polished sections of treated specimens. This approach yields information useful to understand both efficiency and compatibility criteria. It can give qualitative insights into the treatment by showing the adhesion to the substrate, bridging capacities, consolidant shrinkage, and the in-depth distribution of the solid consolidant residue in the substrate pore system. Quantitative image analysis may show the depth and degree of pore filling [25–27]. It is of utmost importance to correlate the macro properties of treated specimens with the SEM observations related to the penetration depth and spatial distribution of the consolidant. SEM, for example, is capable of detecting over-consolidation of surface areas, which could explain the results of a drilling resistance measurement.

Compatibility also comprises the visual aspects of a consolidated stone. Well established techniques are used to quantify colour changes and gloss induced by a treatment. It should be kept in mind, however, that these types of changes may regress in time, thus reducing or eliminating their negative impact [28]. Far too seldom have the various techniques employed to assess compatibility been correlated with each other, and still much rarer are the cases where compatibility is comprehensively assessed in a multiparametric approach.

A group of consolidants that has been in use for decades belongs to the family of tetraethyl-orthosilicates (TEOS). Based on the general formula of $\text{Si}(\text{OR})_4$ the products have been modified for different purposes. They were engineered to be water repellent [29,30], have photocatalytic- [31,32] or elastified properties [33] or to have a coupling agent to better adhere e.g., to a carbonate substrate [34]. The gel deposition rate, or the solid content after curing, plays a crucial role in inducing mechanical improvement, and several products are on the market with different gel deposition rates [35]. These modifications are supposed to have impact on the efficiency and compatibility of the consolidation treatment.

This study aims at assessing the effectiveness and compatibility of three different alkoxysilanes applied on one carbonate and one silicate substrates. Strength increase and physical changes induced by the treatments are compared. Two consolidants were newly engineered in the framework of the European project Nano-Cathedral—short for—“Nanomaterials for conservation of European architectural heritage developed by research on characteristic lithotypes” (Grant Agreement No. 646178, Call NMP-21-2014: Materials-based solutions for protection or preservation of European cultural heritage). The products were developed for a large-scale technological applicability by two SME partners. The details of the synthesis route are protected by a non-disclosure agreement. The two novel products are based on nano- TiO_2 particles linked to ethylic esters of silicic acid in isopropanol.

The first product NC-25C is a tetraethyl-orthosilicate in isopropanol, doped with nano-TiO₂ to have photocatalytic activity. It has 70% active content and contains 10⁻² ppm TiO₂ with less than 100 nm in size (generally between 5 and 40 nm, with the highest amount average in size between 10 and 15 nm). The second product NC-27CP is an alkyl-trialkoxysilane in isopropanol with 75% active content and it is containing 10⁻² ppm TiO₂ particles with the same dimensions as described above. The products typical Si–O–C chain was modified with organic groups to obtain higher elasticity by forming Si–O–(CH₂)_n–O–Si. Nano TiO₂ is added to reduce the shrinkage of the consolidating gel and to confer photocatalytic activity to the stone surface. The spherical shaped TiO₂ nano particles occur in two crystal phases, namely anatase (78.8%) and rutile (21.2%). Although the modification of consolidants with nano-TiO₂ has been the subject of several laboratory studies [36,37], such products are not yet available on the market in large quantities. The potential self-cleaning ability conferred by the nano-TiO₂ particles is an added functionality to the consolidants, but it was not integrated in the research work reported here. Both TiO₂ containing products were developed by the Italian company Chem Spec Srl in the framework of the EU-funded *Nano-Cathedral* project. The supplier of the nanoparticle is the Spanish-based industry Tecnan (Technologia Navarra de Nanoproductos, S.L.). These products were selected due to their higher silica gel content when compared to the common commercial products. In principle, higher silica gel contents should result in advanced mechanical consolidation properties. The quantity of the silica gel deposited in the stone fabric after curing can be varied by the mixing ratio of monomer and oligomer molecules in the product, that is to say, the smaller the molecules, the lower the gel deposition rate. Further possible modifications include the addition of catalysts that influence the reactivity of the product, and the addition of solvents. In this way the products can be customized for varying substrates and decay phenomena. The product used as a reference in the present study, traded under the name KSE 300, is produced by Remmers (Löningen, Germany); it is the most widely used stone consolidant in Central Europe. This is a solvent-free tetraethyl-orthosilicate with a gel deposition rate of approximately 30%, which corresponds to 300 g of solid silica content per litre of consolidants.

The results of this study show that treatments' effectiveness is primarily governed by the texture and microstructure of the natural stone and secondarily by the solid content after curing. While in general all studied alkoxysilanes showed to have a certain consolidating effect, the same product gives different results in terms of strength and physical properties when applied on different substrates. Moreover, reaction kinetics is also stone dependent and the time for curing through hydrolysis and condensation differs between the substrates. Because of the curing time, all moisture related properties and colour changes are time-dependent values. In respect to the substrate, the evolution of those values in time follows no general trend and they even have opposing directions varying in absolute and relative magnitude. These results lead to the conclusion that the interpretation of treatments compatibility has to be done with care; especially as the speed of the gel deposit reaction is not only temperature and humidity but also substrate dependent.

2. Materials and Methods

2.1. Petrographic Characterisation

Two porous lithotypes of historic monumental importance, one silicate and one carbonate, were selected as testing substrates:

Schlaitdorf Sandstone, historically quarried in Baden-Württemberg, Germany, is a coarse-grained siliciclastic arenite, classified after R.L. Folk [38,39] as subarkose from the Upper Triassic, with a light to reddish colour and an average grain size of about 0.5 mm (Figure 1b). Quartz, feldspar and rock fragments are roughly equigranular, vary from subangular to rounded and are tightly intergrown. Its texture is mostly homogeneous without any marked layering. The authigenic minerals sum up to 15% and consist of sparitic dolomite, microcrystalline quartz, kaolinite and traces of illite, partly filling the intergranular pores [40] (p. 56). The typical pore size ranges from 0.2 to 1 mm and the effective

open porosity measured by Hg-porosimetry is about 15.4%. *Schlaitdorf Sandstone* has been used as construction material for prominent buildings, such as the cathedrals of Cologne and Münster [41]. The main deterioration phenomena affecting this lithotype are sanding, flaking and scaling [42].

St. Margarethen Limestone is a porous calcareous arenite, quarried in the Rust Hills of Burgenland (Eastern Austria). It is a biogenic detritic sedimentary rock from the Miocene (Langhian) age [43]. It can be classified as a biosparite and grainstone [44,45]. Its colour ranges from yellow-brownish to light grey. This lithotype mainly consists of small fragments of coralline red algae, foraminifers, fragments of bryozoans and echinoids (Figure 1a). Calcite is the dominating mineral, with traces of siliciclastic detritus, mainly quartz and muscovite. The components are cemented with a fine-grained, early diagenetic dogtooth-calcite. Pores and voids range from a few micrometres to millimetre range, and the total open porosity measured by Hg-porosimetry is about 20.7%. *St. Margarethen Limestone* has been used as a construction and sculptural stone from Roman times until today [46]. The main deterioration phenomena affecting this lithotype are granular disintegration, formation of black crusts, scaling, sanding and bursting [47]. This lithotype was used for the restoration of the St. Stephens Cathedral in Vienna since 1845 and in countless monuments in Vienna (e.g., Vienna Town Hall, Palace and Gardens of Schönbrunn, historic St. Marx Cemetery, etc.) and elsewhere in Eastern Austria [48].

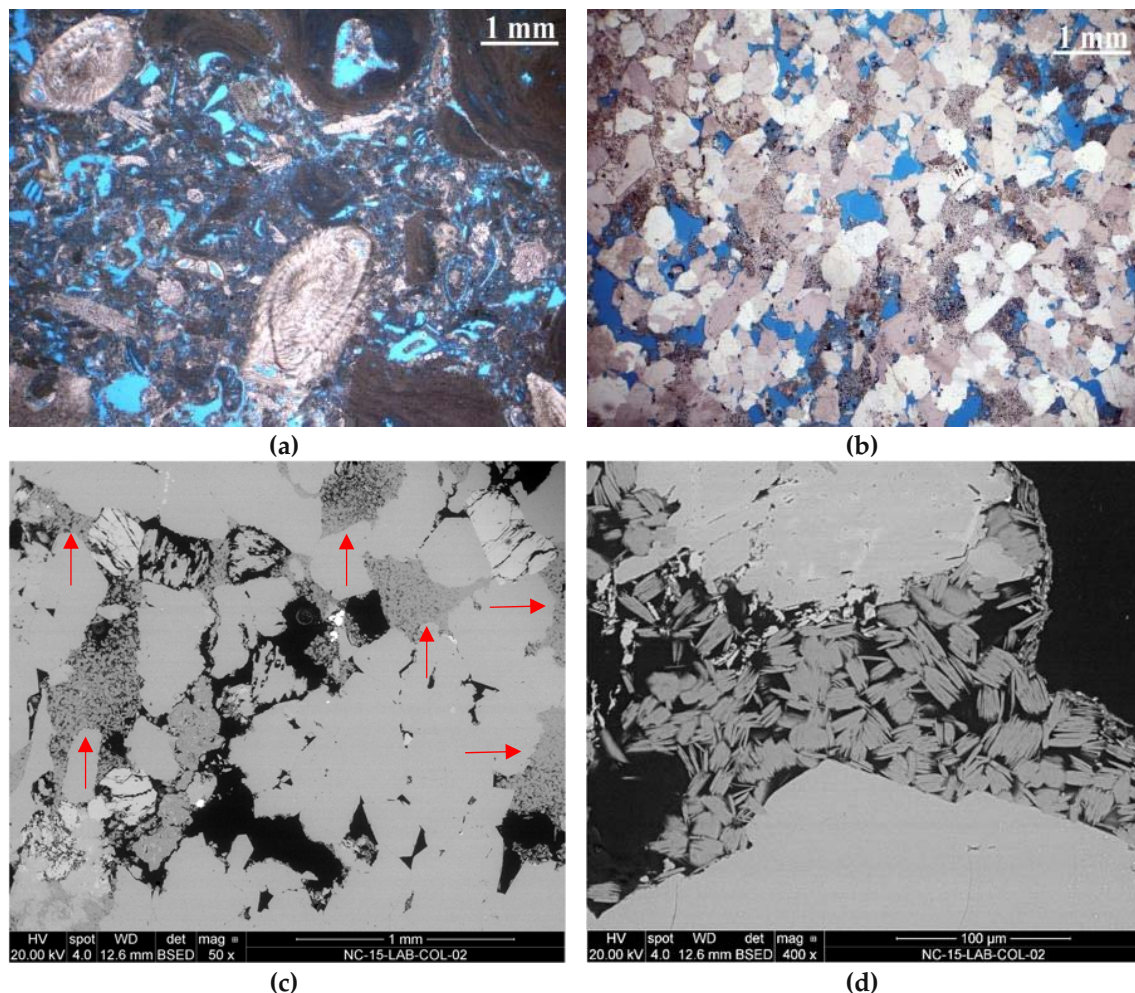


Figure 1. Microphotos of thin sections recorded with a polarised-light microscope (PLM): (a) *St. Margarethen Limestone* with different microfossils such as foraminifers, coralline red algae and debris of echinits; (b) *Schlaitdorf Sandstone*: a coarse-grained quartz arenite with kaolinite and sparitic dolomite; Microphotos of cross sections recorded with a scanning electron microscope (SEM): (c) occurrence of kaolinite (red arrows) up to 15% in *Schlaitdorf Sandstone* indicating its even distribution throughout the fabric; (d) detail of kaolinite in the intergranular pore space between quartz and feldspar.

2.2. Artificial Ageing by Thermal Treatment

Stone specimens of defined geometry and dimensions as required for standardised stone test methods were exposed to a cyclic heat treatment in order to create relevant microtextural defects. The heating gradient was set to a rate of 40 °C/min with a peak temperature of 580 °C for one hour. The cooling phase to room temperature took 24 h before the same procedure was applied. In total three such cycles of heating and cooling were applied. These parameters had been established by a systematic experimental study [9] to ensure the formation of micro fissures throughout the complete sample thickness, which were expected to significantly alter the modulus of elasticity and the water absorption coefficient. In principle, the optimum residence times and peak temperature for each lithotype depend on the dimensions and shape of the specimen and had to be adapted accordingly. To remove all loose dust from the specimens, after the artificial ageing the specimens were washed and dried to constant weight.

2.3. Consolidation Treatment

As pre-conditioning before the application of consolidants, specimens were stored in a container at 70% RH for one week. Then, they were placed on a metal grid with their bottom in contact with the consolidant for one hour, to enable absorption by capillary suction. Within that time, full saturation was achieved in all cases. After the treatment with the consolidants, the specimens were weighed and placed in an airtight container. After 24 h the same treatment procedure was repeated. For the following three days, the consolidated specimens were placed in a sealed container next to cups filled with the consolidation products in order to saturate the atmosphere with the corresponding solvents. To control the backwards migration of the consolidant in the stone specimens by preventing overly rapid evaporation, the box was opened gradually for a period of one week, during which the stone was additionally covered with a plastic foil. In the container the specimens were placed on a grid to assure drying from all surfaces. To observe the reaction and evaporation process, the weight of each consolidated specimen was recorded until constant mass. However, it must be emphasised that mass stability might not necessarily indicate complete reaction of the system, since several products proved still water-repellent beyond the attainment of gravimetric stability, a condition that is typically absent from fully reacted consolidant. Most tested properties of the treated stones are dependent on the consolidant curing state, namely the products' hydrolysis and condensation degree, both implying mass change. The elapsed curing time before testing is indicated in the corresponding tables and diagrams.

2.4. Test Methods for Determining the Efficiency and Compatibility of Consolidants

The artificially aged and subsequently treated specimens were compared to untreated artificially aged and untreated sound specimens. The following test protocol was applied to evaluate those conditions:

1. For the preparation of polished cross sections, laboratory treated specimens with dimensions 50 mm × 50 mm × 50 mm were vacuum impregnated with blue stained epoxy resin and cut perpendicular to the consolidated surface. The section size ensured that treatments which had reached the centre of the treated body could be traced by the analysis. The slices were then polished and examined by SEM. The instrument used was a field-emission scanning electron microscope of the type *FEI Quanta 250 FEG*. The working mode was low vacuum at 20 kV acceleration voltage. Contrast and brightness of the backscattered electron (BSE) images were adjusted to visualize the consolidant in the pores by distinct grey values. For visualisation purpose and image analysis, post processing of the micrographs was done with *Adobe Photoshop* by false-colour-mapping the silica gel inside the stone fabric. Furthermore, when calculations of e.g., the penetration depth to filling degree was to be obtained, the software *ImageJ* proved to be a valuable tool for such purposes.

2. Mercury intrusion porosimetry (MIP) was performed with a Porosimeter *Porotec Pascal 140/440*. Changes in the pore radii distribution and open porosity determined by Hg-intrusion for the different conditions (sound, artificially aged and consolidated) were studied.
3. The dynamic modulus of elasticity was determined with the longitudinal resonance frequency of an ultrasound signal in transmission, according to EN 14146 [49]. Prismatic specimens with dimensions 10 mm × 10 mm × 40 mm were used and mean values of three specimens were computed. The small specimen size was selected to ensure the consolidation of the entire body. The test was performed by an ultrasound pulse generator (*CONOSONIC C2-GS*), a pair of transducers (*UP-DW*), a clamping and pressure device for specimen's assembly as well as and a notebook preinstalled with the *Light House DW* software, developed by *Geotron-Elektronik*, Germany. The UP-DW piezoelectric transducers, operating at a frequency band from 1 to 100 kHz, are specifically manufactured to determine the materials elastic parameter (DW stands for "dehnwelle" and translated from German it means "extensional wave"). This device is equipped with a built-in algorithm that calculates the longitudinal-, transverse-, surface- and extensional waves as well as E- and G Modulus and the Poisson's ratio. However, the principle on how to obtain the dynamic modulus of elasticity (Ed_L) determined through the longitudinal fundamental resonance frequency (F_L) is given by Equation (1):

$$Ed_L = 4 \times 10^{-6} \cdot l^2 \cdot F_L^2 \cdot \rho \cdot T \quad (1)$$

whereby (l) represents the specimens length and (ρ) the stones apparent density. As in our case the width of the specimen is four times its length, the correction factor (T) can be assumed to be 1 in which case the equation is simplified to Equation (2):

$$Ed_L = 4 \times 10^{-6} \cdot l^2 \cdot F_L^2 \cdot \rho \quad (2)$$

(F_L) was recorded when the deviation of the measured fundamental resonance frequency stayed in a range of ± 60 Hz, three times in a row. The dynamic modulus of elasticity is reported in GPa or kN/mm². As for all non-destructive tests, measurements could be performed on the same specimen before and after treatment.

4. Splitting tensile strength was determined following the recommendations of ASTM D 3967-08 [50]. The electro-mechanical tension and compression-testing machine was a 150 kN *Instron Model 4206*, developed by *Instron GmbH*, in Germany. The apparatus consisted of a flat bearing block at the bottom and, to reduce the contact stresses, a curved bearing block on the top. Bearing strips with 0.6 mm thickness were used to reduce high stress concentrations. The loading rate was 100 N/s. 16 specimens per lithotype and condition (sound, aged and consolidated) were tested, each 60 mm in diameter and 30 mm in thickness. For the aged stone specimens and the reference product KSE 300, 10 out of the 16 specimens were tested in the frame of two master theses [51,52]. The test was executed in the direction perpendicular to the bedding plane, which was assessed through ultrasound pulse velocity. For the latter purposes, the frequency for both lithotypes was set to 80 kHz and the amplitude was adjusted according to the samples damping. Specimens were measured without a coupling medium. The splitting tensile strength was calculated with Equation (3) and is here reported in N/mm².

$$\sigma_t = 2 \times \pi^{-1} \cdot P \cdot L^{-1} \cdot D^{-1} \quad (3)$$

(P) is the maximum applied load indicated by the testing machine in newton [N], (L) the thickness, and (D) the diameter of the specimen, in mm.

5. The three-point flexural strength was determined according to EN 12372 [53] with the load increased uniformly at a rate of 0.25 ± 0.05 MPa/s (or 41.67 N/s recalculated for the given dimensions) until the specimen broke. 10 specimens with 25 mm × 50 mm × 150 mm were tested,

whereby the distance between the supporting rollers was 125 mm. The tests were performed with an electronic spindle-drive testing machine of the type *Testomeric Quicktester 100 kN* and evaluated by the *Test & Motion* software developed by *DOLI Elektronik GmbH*, Germany. The test was carried out in the direction perpendicular to the bedding plane, which was assessed through ultrasound pulse velocity. The flexural strength was calculated according to the following Equation (4):

$$R_{ff} = 1.5 \cdot F \cdot l \cdot b^{-1} \cdot h^{-2} \quad (4)$$

where (F) is the breaking load in newton, (l) the distance between the supporting rollers, (b) the width- and (h) the thickness of specimen adjacent to the plane of fracture, all reported in mm. The results are expressed in MPa or here in N/mm^2 ($1 \text{ MPa} = 1 \text{ N}/\text{mm}^2$).

6. Water absorption coefficient after one hour was determined according to standard EN 15801 [54] and is reported as $\text{kg} \cdot \text{m}^{-2} \cdot \text{h}^{-0.5}$. The test was carried out on three $30 \text{ mm} \times 30 \text{ mm} \times 30 \text{ mm}$ specimens per stone and treatment. After a stage of pre-conditioning, samples were placed on water-soaked filter paper (*Ahlstrom-Munktell* laboratory filter paper, wet-strengthen grades) and the absorption of water was monitored gravimetrically. The test was performed on the same specimens before and after treatment.
7. Contact angle of water was determined on the stone surface treated with the water repellent consolidants NC-27CP. Therefore, the *Mobile Surface Analyzer* from *Kriess GmbH*, Germany came to use.
8. Water vapour permeability tests were performed according to EN 15803 [55] using the so-called “wet cup” method with a cup system Type 1 according to the standard. In this case, the cups were filled with water and placed in a climatic chamber at ambient conditions of $23 \pm 1 \text{ }^\circ\text{C}$ and $50 \pm 3\% \text{ RH}$ (*Heraeus Vötsch Klimaprüfschrank VC3, model 4034*). They were weighed every 24 h for one week. The results were plotted as mass change (Δm) against time (t) and the slope of the linear section of the curve (G , $\text{kg} \cdot \text{s}^{-1}$) was determined with the software *OriginPro*. (G) was further used to determine the water vapour permeance (Equation (5), in $\text{kg} \cdot \text{m}^{-2} \cdot \text{s}^{-1} \cdot \text{Pa}^{-1}$):

$$W_p = G \cdot A^{-1} \cdot \Delta p_v^{-1} \quad (5)$$

where (A) represents the specimens surface area in m^2 and Δp_v the water vapour pressure difference reported as Pa across the test specimen. The water vapour permeability reported in $\text{kg} \cdot \text{m}^{-1} \cdot \text{s}^{-1} \cdot \text{Pa}^{-1}$ was then determined with Equation (6):

$$\delta_p = W_p \cdot D \quad (6)$$

where (D) represents the average thickness of the test specimens in m. Three specimens per lithotype and treatment with dimensions of $50 \text{ mm} \times 50 \text{ mm} \times 10 \text{ mm}$ were tested. The water vapour permeability is reported as the ratio of treated to untreated values.

9. Finally, colour parameters were determined with a *ColorLite sph850* spectrophotometer, according to standard EN 15886 [56]. The output of the measurements is reported as CIE (International Commission on Illumination) L^* , a^* , b^* colour parameters, tested with a D65 illuminant at 10° standard observer with a reflectance spectrum in the range of 400 to 700 nm. ΔE^* was reported and describes the metric difference or distance between two colours before and after treatment according to the standards of the International Commission on Illumination. Average (L^*), (a^*) and (b^*) values were used to obtain the total colour difference (ΔE^*) between treated (t) and untreated (nt) measurements with Equation (7).

$$\Delta E_{t,nt}^* = [(L_t^* - L_{nt}^*)^2 + (a_t^* - a_{nt}^*)^2 + (b_t^* - b_{nt}^*)^2]^{0.5} \quad (7)$$

In the latter equation (ΔL^*) corresponds to the lightness difference, (Δa^*) to the red/green difference and (Δb^*) to the yellow/blue difference of the tested stone specimens. Colour values measured for treated and untreated specimens were performed on sound stones, in order to exclude any possible impact induced by heat treatment. The results were calculated from an average of three measurements obtained at the same spot, with the help of stencils, before and after the treatment.

3. Results and Discussion

3.1. Spatial Distribution of Consolidants after Curing Assessed by Scanning Electron Microscopy

The main features studied with SEM were the topographical and morphological appearance of the consolidants and the location of the solid precipitates inside the pore system. This shows the in-depth distribution of the consolidant from the treatment surface inwards and the way it is linked to grains (e.g., coating, or bridging them across pores, the quality of adhesion, and degree of shrinkage). Examples of these features are illustrated in SEM-micrographs shown in Figure 2a–d.

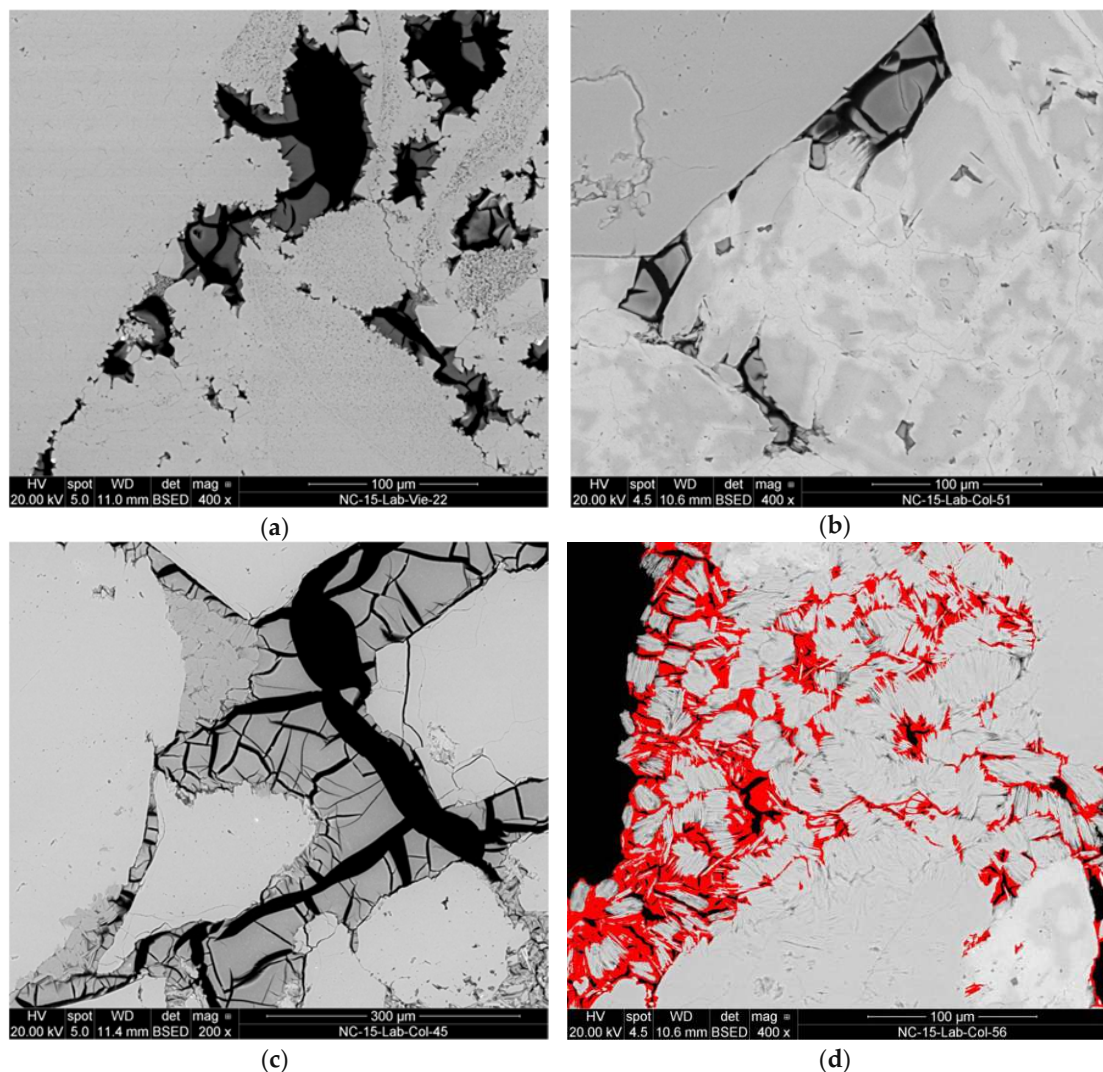


Figure 2. SEM-micrographs displaying some characteristic features of silica gels precipitated from various silicate treatments (gels are clearly visible by their grey value): (a) the adhesion of KSE 300 gel to *St. Margarethen Limestone* due to the advantageous topography of the grain boundary, (b) worse adhesion of KSE 300 gel to *Schlaitdorf sandstone*, (c) the shrinkage of NC-25C gel in intergranular pores of *Schlaitdorf Sandstone*, and (d) the interpenetration of the NC-27CP gel (shown in pseudo-colour-imaging) into the clayey matrix of *Schlaitdorf Sandstone*.

Even if the penetration depth reaches the full depth of the test specimens (50 mm), as observed for all treatments and both stones, differences in the distribution of the solid consolidants are discernible. In the case of *St. Margarethen Limestone* a full and even in-depth-distribution of the solid residues after curing can be observed for treatments NC-25C and NC-27CP, while the solids distributions for KSE 300 can be classified as less homogeneous. In the case of *Schlaitdorf Sandstone* the most homogeneous solids distribution was achieved with NC-27CP while KSE 300 and NC-25C accumulated in the upper parts (approximately 2 cm below the treated surface), as well as on the lateral planes of the samples indicating different rates of back migration upon drying. For both lithotypes, the adhesion of the consolidants to the grains of the substrate is in general not satisfactory, with NC-27CP showing a somewhat better adhesion, followed by KSE 300 and NC-25C treatments. *St. Margarethen Limestone* displays slightly better adhesion because its grain fabric favours the mechanical interlocking (Figure 2a). High shrinkage is visible within all three treatments and for both stones, with KSE 300 and NC-27CP revealing slightly lower shrinkage than NC-25C.

In the case of *St. Margarethen Limestone*, all three products show a high tendency to accumulate in smaller intragranular pores, while only KSE 300 and NC-27CP can be partially observed in the smaller cracks induced by thermal aging. For *Schlaitdorf Sandstone* a slightly better accumulation of all three consolidants within smaller cracks can be determined. A special microtextural feature of *Schlaitdorf Sandstone* was the penetration of the clayey matrix that acts as a filler in the stone while in the consolidated state it might develop properties of a binding medium in the fabric of the sandstone (Figure 2d). Here a better adhesion and a lower shrinkage in the clayey matrix can be observed.

Alkoxysilanes are known to develop cracks inside their gels. Therefore, it is difficult to assess the bridging capacities of these consolidants and report values for their maximal bridging without evaluating this issue in a statistical manner. Due to the drying stresses inside the fabric cracks develop, leaving a plate-like structure of the silica gel as observed in polish cross section. The product manufacturer [57] of classic KSE systems indicates a medium size silica gel plates of approximately 10 μm in size, while Wendler et al. [24] (pp. 47–48, 91) reported bridging capacities to be maximum about 50 μm . In general, the SEM micrographs presented in this study display smaller and larger gel-plates than 50 μm .

It can be concluded that the characteristic properties of the consolidants, namely in-depth distribution, adhesion, shrinkage and bridging capacities, differ for the studied lithotypes. The differences might be explained through the stones texture and topography, while the role played by the stones chemistry cannot be ascertained with these methods and will be the subject of further studies. However, all these properties can be best assessed through SEM of polished cross sections which reveal unambiguous insight into the microstructure, while SEM imaging of fractured surfaces, though more commonly used to visualize consolidants in porous substrates [58–60], is more difficult to interpret.

3.2. Porometric Characteristics Examined by Mercury Intrusion Porosimetry

Mercury intrusion porosimetry (MIP) was used to study the pore space characteristics in sound, aged and consolidated conditions, thus providing insights into the shift of the pore radii distribution, the typical pores size ranges where consolidants were preferentially deposited, and the possible appearance of secondary porosity created within the consolidating gels (Figures 3 and 4). Furthermore, total pore surface, average pore diameter and total porosity by Hg-intrusion are reported in Table 1. The gel deposition rate or solid content of cured consolidants calculated gravimetrically is reported in Table 2.

Due to its inhomogeneity, the effective total porosity of *St. Margarethen Limestone* shows inconsistent values, which could explain why the specimen in aged condition revealed lower porosity as compared to the sound specimen. This indicates the limitation of the used test method for certain types of stone and the caution that needs to be taken when interpreting these results. *St. Margarethen Limestone* has an inhomogeneous structure and the size of the tested specimen is not fully representative since fossils may reach dimensions up to a few centimetres. Therefore, analysis of both the artificially aged and consolidated conditions, leaves some ambiguity in how to interpret the results. As an

example, which can be observed on Table 1, the sample of *St. Margarethen Limestone* treated with KSE 300 shows a porosity higher than the aged one, a treatment that is supposed to leave approximately 30% insoluble residue. Samples heterogeneity may be an explanation, but no definite elucidation has been found. As a consequence of this anomaly, all the values in Figure 4 result mostly uninformative and hard to interpret, especially for the range of pores larger than 10 μm .

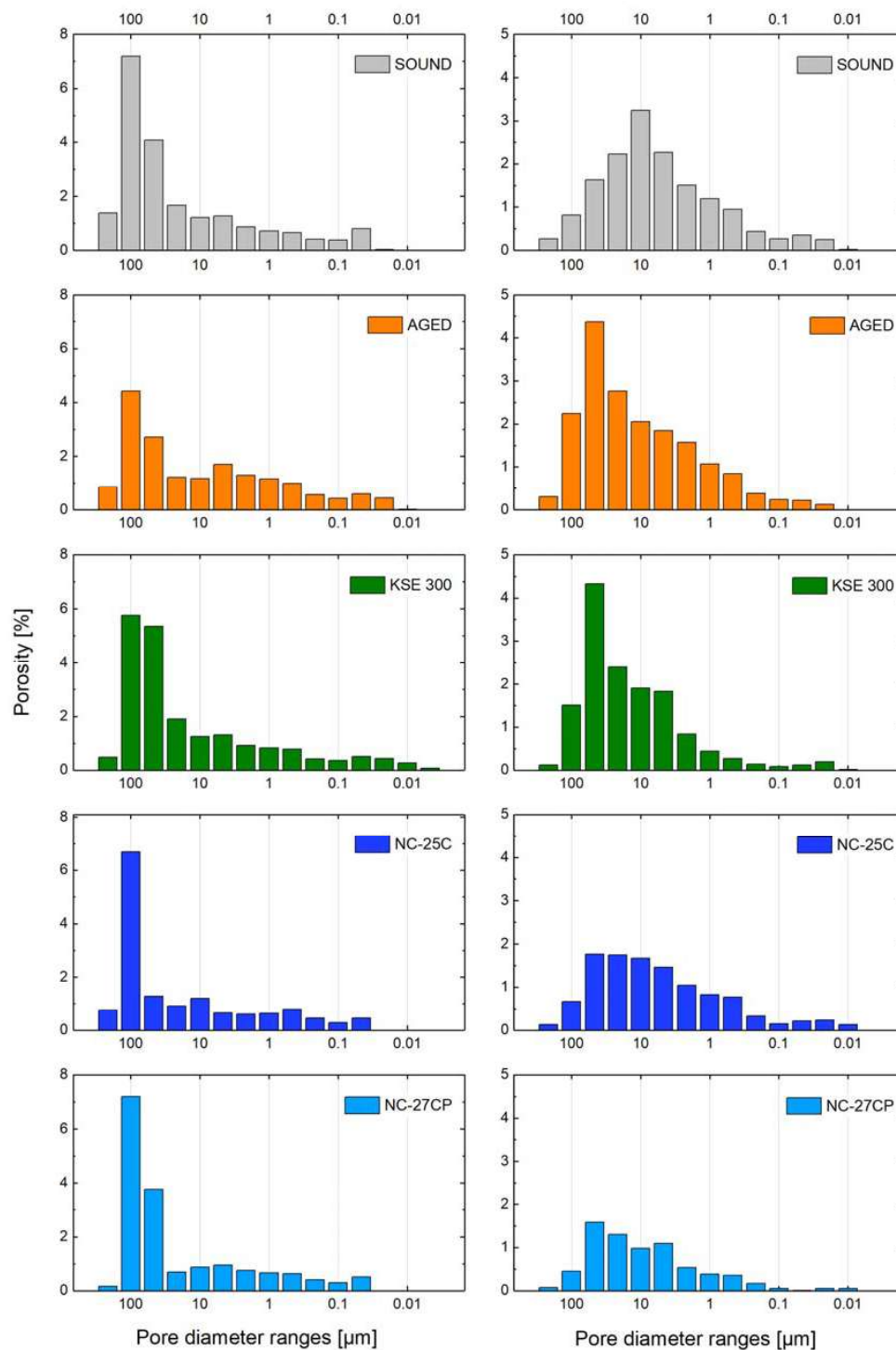


Figure 3. Range of porosimetric parameters (pore radii distribution and open porosity by Hg-intrusion) for the—from top to bottom—sound, aged and consolidated (KSE 300, NC-25C and NC-27CP) conditions determined by mercury intrusion porosimetry; six months after consolidation treatment: values for *St. Margarethen Limestone* (left side) and *Schlaitdorf Sandstone* (right side).

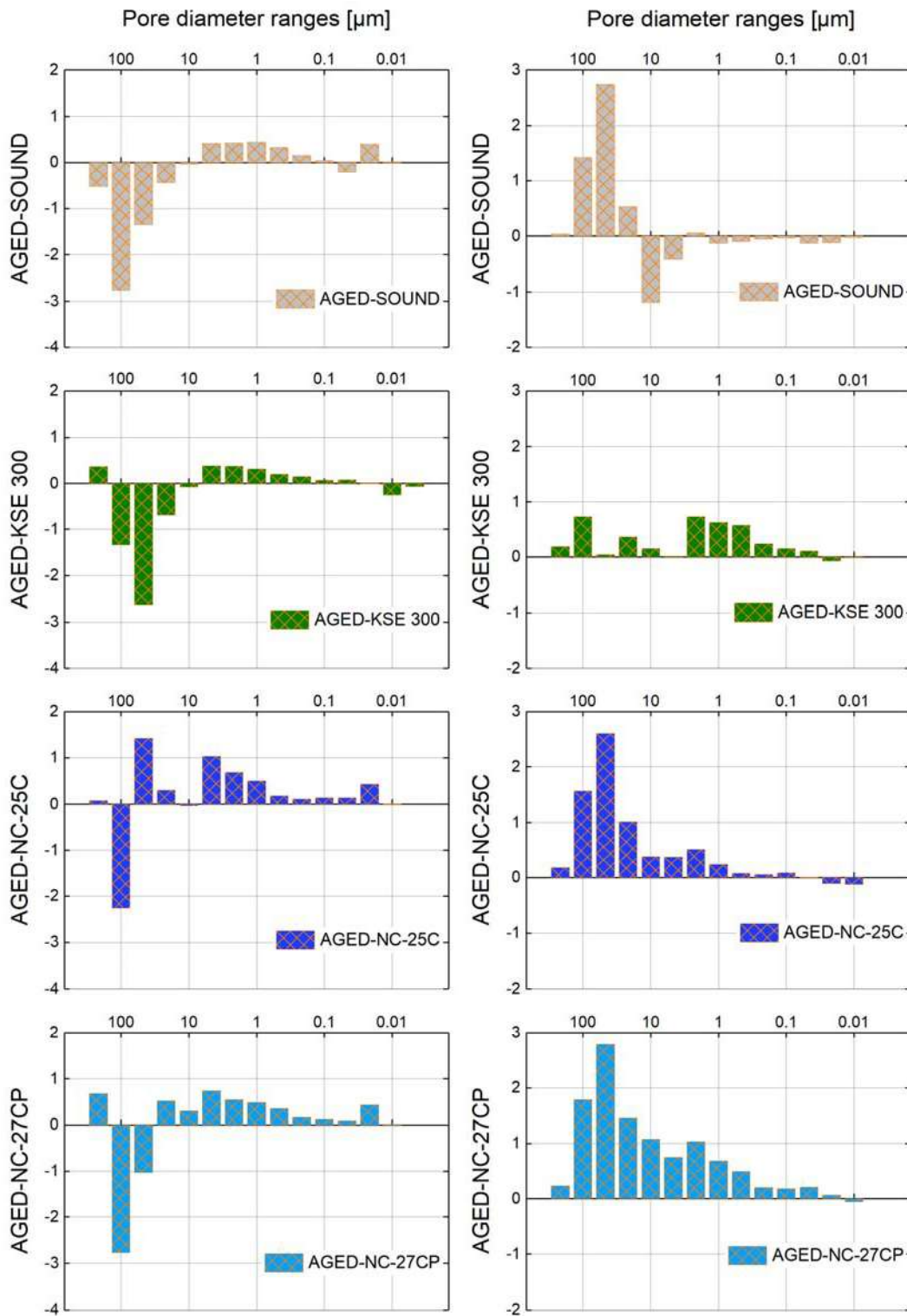


Figure 4. Differences in open porosity for each class of pores determined from the Hg-intrusion porosimetric data. Results for *St. Margarethen Limestone* (left side) and *Schlaitdorf Sandstone* (right side). To read this comparative graph, from aged to sound conditions, the positive values represent the newly created pores in the respective class. When comparing ages to consolidated conditions, the positive values represent the amount of pores that were filled with the consolidant. Negative values for treated *St. Margarethen Limestone* in the range of pores higher than 10 μm would represent an increase in large pores caused by a treatment, which signify a physical impossibility and are due to the inhomogeneous nature of this lithotype.

Table 1. Results from mercury intrusion porosimetry for specimens in sound, aged and consolidated conditions for *St. Margarethen Limestone* and *Schlaitdorf Sandstone*.

Porometric Characteristics of Materials		Conditions				
		Sound	Aged	KSE 300	NC-25C	NC-27CP
<i>St. Margarethen Limestone</i>	Total pore surface [m ² /g]	0.824	1.326	2.168	0.523	0.569
	Average pore diameter [μm]	0.483	0.253	0.183	0.526	0.568
	Total porosity [%]	20.65	17.53	20.63	14.76	16.88
<i>Schlaitdorf Sandstone</i>	Total pore surface [m ² /g]	0.800	0.518	0.477	0.864	0.242
	Average pore diameter [μm]	0.349	0.643	0.533	0.223	0.463
	Total porosity [%]	15.42	18.02	14.20	11.15	7.10

Nevertheless, accepting the limitations of mercury intrusion porosimetry, we can still conclude that the major difference between the reference product KSE 300 and the NC products is the tendency of the NC consolidants to deposit in pores larger than 10 μm, which is especially well seen in *Schlaitdorf Sandstone*. Similar for all three consolidants is the deposition of silica gel in pores smaller than 10 μm. Even after the consolidation, pores in the range of 50–100 μm still represent the largest amount of pores present in the fabric. Treatment KSE 300 most likely indicates cracks in the silica gel, visible through an increase in pores approx. smaller than 0.01 μm, which were not there before. Moreover, treatments NC-25C and NC-27CP cause a disappearance of pores smaller than 0.05 μm, most likely due to the deposition of consolidants in these pores.

Schlaitdorf Sandstone is relatively homogeneous, even in respect to the pore size distribution and geometry of the more or less equi-sized pores, and for this reason MIP values are more informative and easier to interpret. The artificial ageing created an evident shift in the pore radii distribution and an increase of the total open porosity. After ageing, and due to the pore shift, more pores larger than 10 μm and fewer pores smaller than 10 μm are present within the stone fabric when compared to the sound specimen. For both stones, PLM- and SEM studies are more appropriate to explain creations of micro cracks be it due to the artificial ageing or gel shrinkage (see Figure 5).

For *Schlaitdorf Sandstone*, the main modifications in Hg-porosimetry by treatments NC-25C and NC-27CP when compared to KSE 300 are striking (see the comparative graph in Figure 4). The key difference of NC-25C and NC-27CP products is their higher deposition in pores larger than 10 μm. For all three treatments, it can be concluded that the silica gel formed is deposited within a wide range of pores, only in different percentages. Furthermore, all treatments seem to produce a slightly higher amount of pores in the range of 5–10 nm, most probably due to the porosity of the gel shrinkage cracks.

In conclusion, a general tendency that can be extracted from the MIP measurements is that the NC products are able to fill the pores that govern and make up the largest percentage of porosity in the stone fabric and have thus the greatest impact on changes of the pore radii distribution. While all three consolidants are deposited in pores smaller than 10 μm, the capability of NC products to deposit also in larger pores seems to be the main cause for the increase in high mechanical strength, as explained below.

Comparing the values of mercury intrusion porosimetry for the studied stones, it can be concluded that each ageing protocol and the following treatment had their specific impact on the studied substrates. The treatments induce changes of the surface area, average pore size and geometry, pore radii distribution and total open porosity. All those alterations occur to different extents, pointing to the central role of the substrate in governing the effects. Not only are the consolidants different regarding their solid content after curing, but also the substrates capability to accommodate those products differs. However, even though the test results indicate measurable impacts on the physical stone parameters and hence the possible resistance towards weathering [61], potential consequences of those modifications are difficult to evaluate without predictive models and further studies in this area. In addition, the usefulness of this technique for certain types of stone needs to be evaluated with more precision and by statistical means. Until then, tests of mercury intrusion porosimetry will remain empirical and more of an indicative nature.

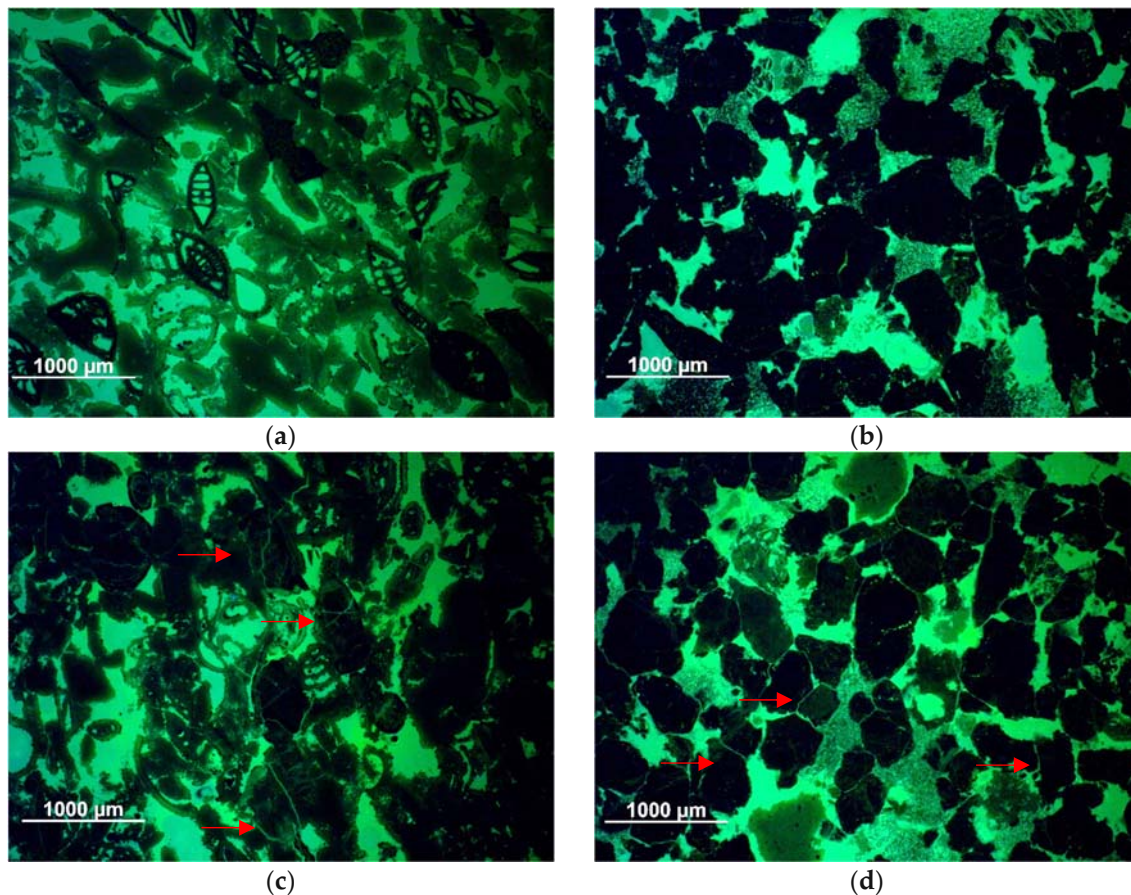


Figure 5. Microscopic views of thin sections made with a polarised-light microscope under UV-light using a fluorescent resin: (a) *St. Margarethen Limestone* in sound condition and (c) *St. Margarethen Limestone* in artificially aged condition displaying micro cracks mostly of an intra-granular nature passing through the microfossils; (b) *Schlaitdorf Sandstone* in sound condition and (d) *Schlaitdorf Sandstone* in artificially aged condition showing micro cracks mostly of an inter-granular nature affecting the grain boundaries.

Table 2. Gel deposition rate or solid content of cured consolidants calculated gravimetrically on three specimens per stone and treatment after 4 weeks of curing. As already mentioned in the text, the values reported may not be definite because of the incomplete reaction at this age.

Product Specification	<i>St. Margarethen Limestone</i>			<i>Schlaitdorf Sandstone</i>		
	KSE 300	NC-25C	NC-27CP	KSE 300	NC-25C	NC-27CP
Solid Content [%]	31.62	47.82	59.73	32.12	46.59	59.98
Standard Deviation	±1.46	±0.57	±0.54	±1.04	±0.67	±0.50

3.3. Evaluation of the Consolidation Efficiency (Mechanical Analysis)

3.3.1. Effects of Thermal Treatment Prior to Consolidation

To assess the efficiency of stone consolidants, changes in strength and deformability (Young's modulus) of sound, aged and consolidated specimens are the key parameters to be studied. The micro cracks induced by thermal ageing have caused a sufficient reduction of soundness in both lithotypes to study the capability of the consolidants to increase the mechanical strength of the samples. The decrease in soundness could be observed by all mechanical properties, namely by means of the dynamic Young's modulus, splitting tensile- and flexural strength. However, the results differ in extent when comparing the lithotypes and test methods (Table 3 and Figure 6).

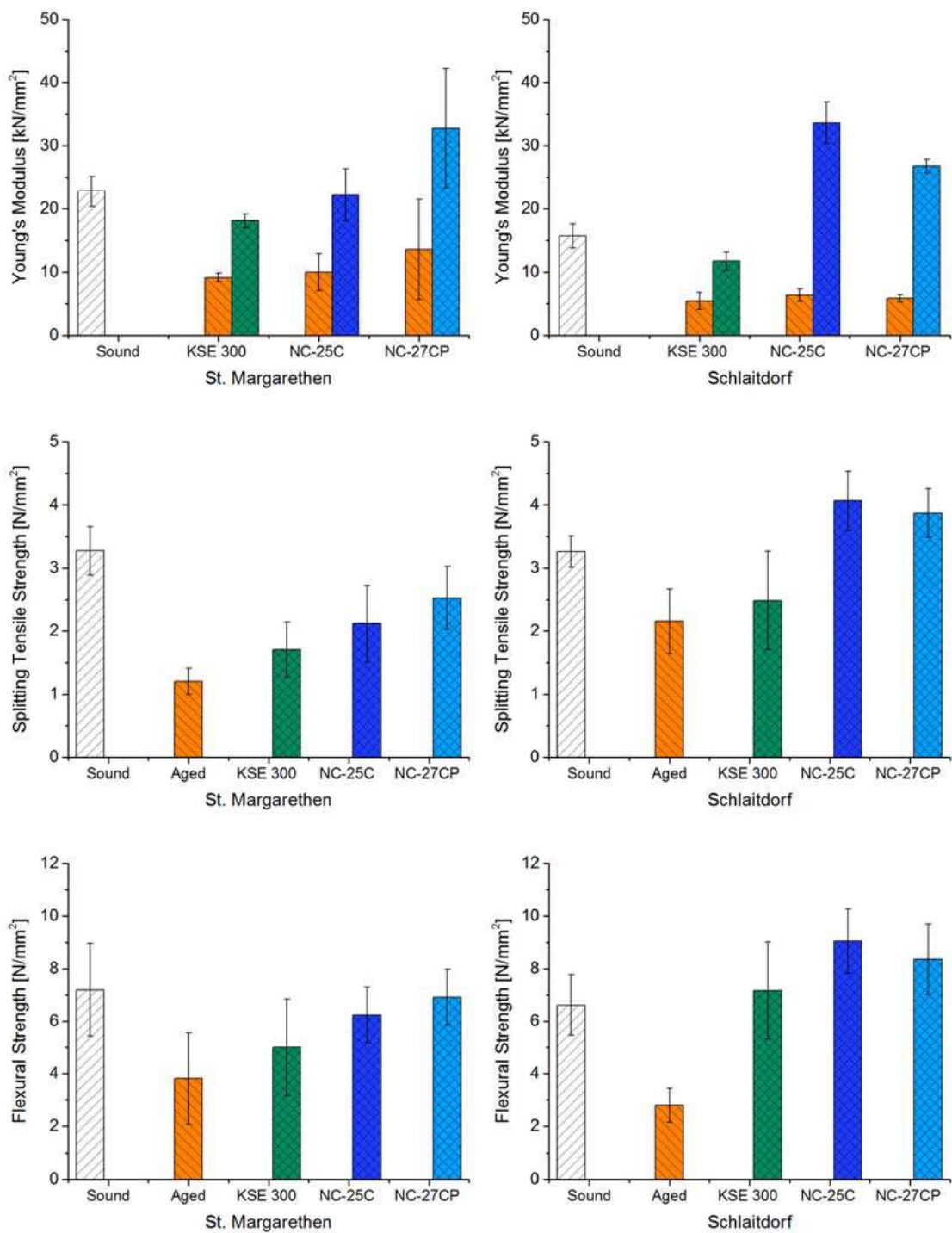


Figure 6. Illustration of Young's modulus [kN/mm²], splitting tensile strength [N/mm²], and flexural strength under concentrated load [N/mm²] for *St. Margarethen Limestone* (left side) and for *Schlaitdorf Sandstone* (right side). All tests performed six months after consolidation. Please note that the dynamic modulus of elasticity was performed on the same specimens before and after treatment. Bars with orange filling represent aged samples before consolidation.

Table 3. Rounded values for relative decrease/increase [%] for sound (S), aged (A) and consolidated (C) samples and absolute average values of Young's modulus [kN/mm²], splitting tensile strength [N/mm²], and flexural strength under concentrated load [N/mm²] for *St. Margarethen Limestone* and *Schlaitdorf Sandstone*. The graphical visualisation of the same values can be found in Figure 6. All tests were performed six months after consolidation.

Consolidant			(S) Sound ± Std.N	(A) Aged ± Std.N	(C) Consolidated ± Std.N	Decrease (S-A, %)	Increase (A-C, %)	Magnitude (S-C, %)
<i>St. Margarethen Limestone</i>	Young's Modulus (kN/mm ²)	KSE 300		9.2 ± 0.7	18.1 ± 1.1	-60	+97	-21
		NC-25C	22.7 ± 2.4	10.0 ± 2.9	22.2 ± 4.1	-56	+123	-2
		NC-27CP		13.6 ± 7.9	32.7 ± 9.5	-40	+141	+44
	Splitting Tensile Strength (N/mm ²)	KSE 300			1.7 ± 0.4		+42	-48
		NC-25C	3.3 ± 0.4	1.2 ± 0.2	2.1 ± 0.6	-63	+76	-35
		NC-27CP			2.5 ± 0.5		+111	-23
	Flexural Strength (N/mm ²)	KSE 300			5.0 ± 1.8		+31	-31
		NC-25C	7.2 ± 1.8	3.8 ± 1.7	6.2 ± 1.1	-47	+64	-13
		NC-27CP			6.9 ± 1.1		+82	-4
<i>Schlaitdorf Sandstone</i>	Young's Modulus (kN/mm ²)	KSE 300		5.5 ± 1.3	11.7 ± 1.4	-65	+114	-26
		NC-25C	15.7 ± 1.9	6.4 ± 1.0	33.6 ± 3.3	-60	+429	+114
		NC-27CP		5.9 ± 0.6	26.8 ± 1.1	-63	+356	+70
	Splitting Tensile Strength (N/mm ²)	KSE 300			2.5 ± 0.8		+16	-24
		NC-25C	3.2 ± 0.2	2.2 ± 0.5	4.1 ± 0.5	-34	+89	+25
		NC-27CP			3.9 ± 0.4		+80	+19
	Flexural Strength (N/mm ²)	KSE 300			7.2 ± 1.9		+156	+8
		NC-25C	6.6 ± 1.2	2.8 ± 0.6	9.0 ± 1.2	-58	+223	+37
		NC-27CP			8.4 ± 1.3		+198	+26

In the case of *St. Margarethen Limestone*, the thermal treatment reduced the soundness on average in terms of the dynamic Young's modulus about 52% and 63% for *Schlaitdorf Sandstone*. Figure 5 displays fissures formed by thermal treatment. In *St. Margarethen Limestone*, the fissures are of a trans-granular type, i.e., crossing the biotitic components, as opposed to *Schlaitdorf Sandstone*, where intergranular fissures affecting grain boundaries are present. Moreover, cracks presented in *Schlaitdorf Sandstone* seem to be more homogeneously distributed through the fabric when compared to *St. Margarethen*. The decrease in soundness determined through the Young's modulus cannot provide direct information about the amount of cracks formed. The distribution of cracks and newly generated pores inside the fabric is also important since sound waves will propagate along the fastest traveling path. However, the Young's modulus did reveal a greater deviation from the mean value in the case of *St. Margarethen Limestone*, which is in general an indication of a more inhomogeneous fabric in respect to the grain size and pore radii distributions as comparison to *Schlaitdorf Sandstone*.

As for the splitting tensile test, strength decreased by $\approx 63\%$ for *St. Margarethen Limestone* and by $\approx 34\%$ for *Schlaitdorf Sandstone*. The flexural strength under concentrated load decreased by $\approx 47\%$ for *St. Margarethen Limestone* and $\approx 58\%$ for *Schlaitdorf Sandstone*. For both lithotypes, the absolute values determined by flexural strength are higher than corresponding properties measured by splitting tensile strength. For brittle materials, the main reason for such a behaviour is explained often with different volumes of material tested and the presence of material defects [62] (pp. 13–14). In other words, in larger samples the probability of defects density and distribution is higher, so the resultant values should be lower. However, Baumgartner [63] pointed out that more effort is necessary to distinguish which features may account for the differences in splitting tensile- and flexural strengths for natural stone. In general, the main factors influencing the indirect tensile strength values depend on the test method, the stone type with its scale and size effects, as well as the loading rate and testing procedure [64]. The actual tensile strength can be derived from indirect tests but only when the moduli ratio in tension and compression is known [65] or other measured properties like e.g., the crack initiation [66]. Moreover, to determine the influence of micro cracks also a closer look on the initial, elastic response of the stress-strain curves is necessary [67]. Such mechanical investigations, including simulations, would go beyond the scope of this study, but are desired in the field of stone conservation due to the microstructural heterogeneity of weathered and consolidated stone. However, even if at the moment closer interpretations are not part of this study, some conclusions can be drawn. Comparing

both test methods, the anisotropy of the absolute average values for aged *Schlaitdorf Sandstone* is 0.76 and 0.31 for *St. Margarethen Limestone*. For *Schlaitdorf Sandstone*, this might be due to a more homogeneous distribution of cracks inside the fabric, while for *St. Margarethen Limestone*, the higher widespread of the absolute values indicate higher inhomogeneity and thus a strong influence of the sample geometry on the obtained values.

In any case, all test methods applied confirm the usefulness of the laboratory ageing prior to testing the efficiency of stone consolidants.

3.3.2. Effects of Consolidation Treatment

All studied consolidation products induced a clear increase in the modulus of deformability (Young's modulus) and strength. This phenomenon can be explained with the porous nature of both stones and the fissures induced through thermal aging, thus thanks to their ability to absorb and accommodate significant amounts of consolidants. Increases in Young's modulus and strength have different impacts on the measured properties for the two lithotypes, with a tendency of *Schlaitdorf Sandstone* to show higher amount of increase (Table 3 and Figure 6). Increases followed a general trend for all three test methods employed with increments of $KSE\ 300 < NC-25C < NC-27CP$ for *St. Margarethen Limestone* and $KSE\ 300 < NC-27CP < NC-25C$ for *Schlaitdorf Sandstone*.

All three treatments had a great impact on the dynamic Young's modulus. While KSE 300 exerts a similar effect for both lithotypes in respect to the relative increase of the modulus, for NC-25C and NC-27CP the modulus increased, respectively, two and three times more for *Schlaitdorf Sandstone* than for *St. Margarethen Limestone* (compare aged to consolidated condition in Table 3 and Figure 6). These latter treatments even raised the modulus to values above those recorded for the sound conditions of *Schlaitdorf Sandstone*—as a consequence of the better distribution of the silica gel in the newly formed fissures, clayey matrix and partly also in the equi-sized voids, thus allowing a faster propagation of the elastic sound wave. The results cannot solely be explained through the solid content after curing since *Schlaitdorf Sandstone* accommodates less consolidant due to its less porous structure when compared to *St. Margarethen Limestone*. Here it becomes clear that the more intense crack network induced by ageing in *Schlaitdorf* and the given microstructure of the fabric have played a role in the treatment performance.

In general, there is no doubt that mineralogical, textural and structural features directly affect the strength of a stone. The same holds for the consolidated stone. Thus, the lithological and mineralogical composition, microstructural and microtextural features as well as petrophysical properties are the keys to understand deterioration processes and mechanical properties of lithotypes in macro scale. In view of this, the most likely reasons for why consolidation is more efficient for *Schlaitdorf Sandstone* than for *St. Margarethen Limestone*, as far as the strength increase is concerned, is the considerable amount of clay minerals and the equi-sized porosity. The non-swelling kaolinite is evenly distributed in the stone fabric, present as a filler component in the intergranular voids of this lithotype. After consolidation, clays seem to have been preferentially strengthened (Figure 2d), which probably helped to increase the mechanical strength above the sound condition. Clay minerals are known to be the governing factor influencing specific stone properties like e.g., sensitivity to weathering [68,69] or the hydro-mechanical behaviour with an extensive loss of strength [70]. In his book about alkoxysilanes and the consolidation of stone, Wheeler [24] (pp. 43–45) dedicated a section to the clay problem and consolidation. Herein he pointed out the contradictory results reported in the literature and the difficulty to draw definitive conclusions about consolidation efficiency of materials containing clays. However, numerous authors report successful treatment of clay bearing materials, for carbonate [24] (pp. 43–45, 54) and silicate varieties [71]. The issue of durability and potentially damaging consequences a consolidated clayey matrix may have is another question and, although not part of this study, it is worth further investigation.

Generally, the silicate substrate *Schlaitdorf* shows the highest consolidation effect and there are two possible reasons for that. The first reason is the often-mentioned concept of chemical affinity of

alkoxysilane to silicate substrates. This means that the consolidation mechanisms in siliceous substrates are of a cohesive nature. It is explained by the formation of Si–O–Si bonds between consolidant and substrate [72]. In the case of the carbonate substrate, the consolidant is often referred to as a mere compacting agent, since it is deposited in the pore space of the fabric. There are two aspects that do not fit well in this concept: (i) in our study, the carbonate variety morphologically shows slightly better adhesion of the consolidant to the substrate, which was explained through the higher microrugosity of the grain interfaces. However, for both stones the adhesion was reported to be poor. In addition, (ii) since the beginning of its use and up to now, successful consolidation performances of alkoxysilanes have been reported for carbonate substrates in numerous studies [4,33,73–79]. Therefore, to explain better consolidation efficiency by solely referring to a chemical concept seems to be insufficient.

Consequently, the second possible reason for the higher effect of consolidation of the silicate substrate is the stone fabric itself. As stated above, the type of stone substrate plays the most significant role in both strength and deformability. Other authors have also pointed out that different fabrics and mineral compositions significantly influence the efficiency of stone consolidants [80,81]. Wheeler addressed the issue of structure by trying to consolidate larger quartz grains, which remained unconsolidated despite their chemical affinity [24] (pp. 46–48). It was pointed out that alkoxysilane gels tend to deposit in pores <50 µm and less on their relative amount. The latter observation suggests that, depending on the deposition of the silica gel in certain pores representative for the studied fabrics, this will lead to efficiency in terms of mechanical strength. As can be extracted from the MIP data in the present study, the highest impact on pore radii can be observed for *Schlaitdorf Sandstone* treated with NC-25C and NC-27CP. Despite their influence on porosity due to the gel deposition rate, the unique property of the NC products is their capability to deposit also in larger pores, which make up the highest percentage in terms of open Hg-porosity (Figure 4). This phenomenon, together with the already described interpenetration of the clayey matrix located between the grains, form the main factors for the increase in mechanical strength.

Further studies are recommended to analyse the main factors (physico-mechanical features) influencing the efficiency of consolidation in terms of strength as well as the actual role of the chemical compatibility (chemi- and physisorption to the surface).

Regarding the practical conservation, the effect of *Schlaitdorfs* drastic increase in strength could result in the overconsolidation of surface layers known to cause harmful effects. In other words, to achieve a high mechanical strength through consolidation is not automatically linked to better performance of a treatment. Given the difficulty to produce a homogeneous in-depth distribution of any consolidant by surface treatment of an object, overconsolidation of certain layers can be hazardous. To avoid this risk, efforts are needed to optimize all controllable parameters related to a product and its mode of application for a lithotype in its given conditions. In stone consolidation, differences in strength and deformability are the most relevant parameters to assess. As thermal behaviour is critical in this respect, it should be included in further studies.

Regarding the mode of mechanical failure in the flexural strength test, it was observed that the sound stone can be categorized as brittle and the aged one rather as ductile (Figure 7). NC-25C has the capability to shift the failure mode from ductile back to quasi-brittle. Moreover, in the case of *Schlaitdorf Sandstone* this treatment restores the mechanical strength by exceeding the level of the sound stone condition. As the silica gel, formed after the curing of the consolidants, is a brittle material, there is no surprise that the stiffness is increased. On the other hand, the silica gel acts as a kind of filler, deposited inside the stone fabric, and reduces the absolute porosity hence the ductile deformability of the stone fabric is decreasing, which is why the failure mode is restored after the consolidation.

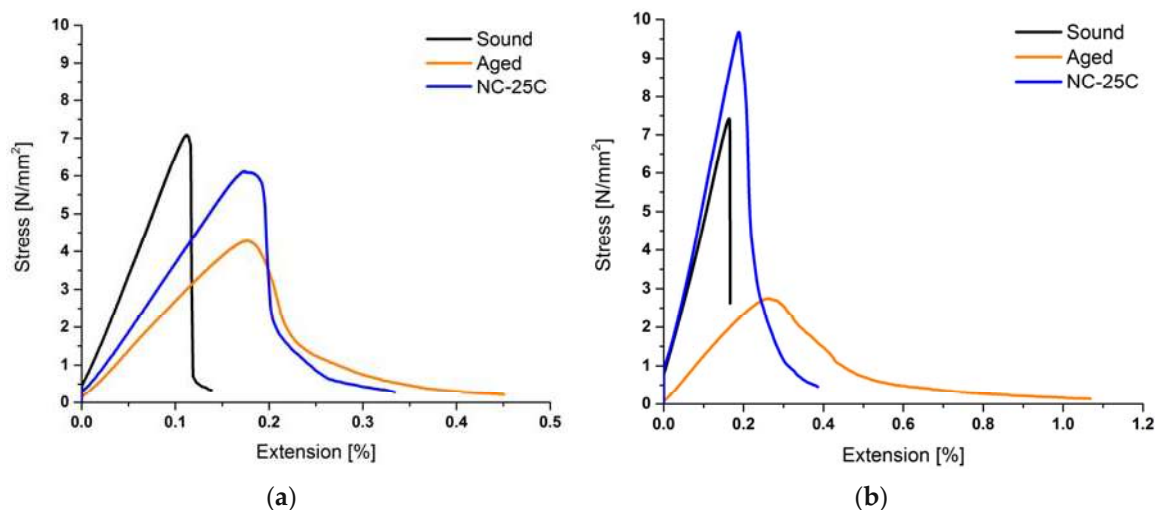


Figure 7. Examples of stress-strain curves exhibiting average values of the flexural strength under concentrated load. Sound, artificially aged, and subsequently consolidated conditions for (a) *St. Margarethen Limestone* specimens; and (b) *Schlaitdorf Sandstone* specimens, both tests performed six months after the consolidation treatment.

3.4. Evaluation of the Compatibility (Moisture Related Properties and Visual Impact)

In laboratory studies of compatibility, the main objective is to identify to what degree the stones' physical properties change after treatment and to assess to which extent those changes may put the stone in jeopardy of an accelerated deterioration. While in the case of hydro-repellent treatments it is well known that some key physical parameters related to water transport get drastically changed. Within certain limits this is also observable for non-hydrophobic consolidation treatments. In this study, the two lithotypes were evaluated in respect to water absorption coefficient (WAC), water vapour permeability (WVP), and colour change. The respective measurements were performed for the lithotype samples in their sound, aged and consolidated conditions. Comparable to tests used to determine the efficiency, all results from the above-mentioned tests show changes of physical properties due to the treatments which, however, utterly differ between the studied lithotypes.

For both lithotypes, the micro cracks induced by ageing have increased the open porosity and correspondingly WAC (Table 4). After consolidation, the WAC is always reduced due to the presence of the consolidant residue in the stone fabric. However, consolidants such as TEOS, need an unknown period of time to fully react by hydrolysis and remain water repellent meanwhile, which results in an overestimation of their effect on WAC. Producers state that reaction times may last to approximately three to four weeks at 20 °C and 50% RH ambient conditions [82], but in laboratory conditions it appears that the system may stay water repellent for much longer time spans. In our study, the first set of tests were made after approximately 6 weeks, but it was considered necessary to repeat the WAC tests 6 months after the application of the consolidants. As evidenced by the results of Table 4 it appeared that for the products KSE 300 and NC-25C the rate of reaction accompanied by the loss of this temporary hydrophobicity not only differs between the products, but also between the substrates. Thus, the treatment KSE 300 does not affect the WAC in the case of *St. Margarethen Limestone* but it does affect *Schlaitdorf Sandstone* resulting in a water repellent surface even after 6 weeks of curing. On contrary, NC-25C does affect the WAC in the same manner within *St. Margarethen Limestone* but does not affect *Schlaitdorf Sandstone*. At the present stage, it is not clear which of the stone parameters influences the reaction rate of TEOS. Measurements taken six months after the application are stabilized and reveal a probable end state of the curing process. This indicates the importance of the timing of the test protocol and points out that even mechanical parameters would evolve within the prolonged periods of curing. These observations are particularly relevant to on-site follow up of restoration and conservation activities.

Table 4. Values of water absorption coefficient after one-hour (WAC) [$\text{kg}\cdot\text{m}^{-2}\cdot\text{h}^{-0.5}$] and ratio of water vapour permeability values (WVP c/a) [$\text{kg}\cdot\text{m}^{-1}\cdot\text{s}^{-1}\cdot\text{Pa}^{-1}$], for sound (s), aged (a) and consolidated (c) specimens of *St. Margarethen Limestone* (SM) and *Schlaitdorf Sandstone* (S) evaluated six weeks (6w) and six months (6 m) after treatment.

Stone	Treatment	WAC(s)	WAC(a)	WAC(c) (6 w)	WAC(c) (6 m)	WVPc/a (6 w)
SM	KSE 300	4.49 ± 0.05	5.23 ± 0.02	4.52 ± 0.06	4.56 ± 0.03	0.89 ± 0.06
	NC-25C	4.50 ± 0.18	5.05 ± 0.11	0.76 ± 0.27	2.99 ± 0.28	0.84 ± 0.03
	NC-27CP	4.51 ± 0.15	5.17 ± 0.18	0.47 ± 0.51	0.54 ± 0.26	0.55 ± 0.02
S	KSE 300	3.29 ± 0.30	3.66 ± 0.28	0.18 ± 0.15	2.14 ± 0.50	1.75 ± 0.45
	NC-25C	2.74 ± 0.72	3.57 ± 0.25	1.65 ± 0.15	1.21 ± 0.28	0.81 ± 0.03
	NC-27CP	2.74 ± 0.59	3.53 ± 0.16	0.08 ± 0.04	0.20 ± 0.04	0.35 ± 0.00

As for the treatment NC-27CP, a consolidant with explicitly hydrophobic components, its lasting water repellence could be proved by the low WAC values even after 6 months of curing. The WAC values can be classified as water repellent and water hindering [83] (p. 215). The slight differences in the 6 months WAC of this product between both lithotypes is also confirmed by the contact angles of water— 96.78° for *Schlaitdorf Sandstone* and 87.26° for *St. Margarethen Limestone*. In the case of *St. Margarethen Limestone* the WAC can be classified as water hindering as it is higher than the referenced threshold ($<0.5 \text{ kg}\cdot\text{m}^{-2}\cdot\text{h}^{-0.5}$). Moreover, it is also slightly below the threshold for the contact angle of water of 90° as reported in some studies [84,85].

The drying properties of consolidated materials are important and are recommended to be analysed further as they can give more insights into potentially damaging consequences.

As regards water vapour permeability (WVP), its drastic reduction is not advantageous for several reasons like, e.g., water trapping and subsequent contour scaling, decreased drying rate and thus mobilization of salts or advancement of bio-growth, etc. Different thresholds (between 5 and 20%) are reported in literature related to an acceptable percentage of decrease in WVP [86,87]. Since in the present study this test was performed only 6 weeks after the treatment of the specimens, the state of progress of the gel forming reaction and hence the temporary water repellency were undefined, possibly under- or overestimating the WVP after consolidation (Table 4). The reason for the behaviour of KSE 300 on *Schlaitdorf Sandstone* is unknown and the increase in WVP after the treatment needs further clarification. On the other hand, increased WVP values following a water repellent treatment have been reported for some cases [88,89]. Generally, it must be assumed that any treatment would have an impact on the polar properties of the mineral surfaces of a porous body and hence influence the wettability in one or the other way. WVP values of KSE 300 in the case of *St. Margarethen Limestone* are reasonably close to the untreated stone and thus a low impact in the overall incompatibility may be anticipated. Changes reported for treatment NC-25C are $<20\%$ and display thus the most promising results for both lithotypes. An interesting phenomenon that can be observed within *St. Margarethen Limestone* is that WAC is drastically affected by the rate of the solid content after curing (differences between 30% and 50%) while the corresponding WVP values remain almost identical.

Nano titania exhibits super hydrophilicity when it absorbs a photon with energy equal or greater than its band-gap (3.0–3.2 eV) [90]. At the moment, this property cannot be distinguished from the hydrophilicity of the silica gel. For such purposes, the same consolidant should have been tested with and without nano titania. The eventual hydrophilic properties of nano titania induced by exposure to UV light will be investigated in subsequent research. The differences in capillary water absorption and water vapour permeability of consolidated stone can at the present stage be attributed to the different amount of solid content after curing, rather than to a hydrophilic behaviour induced by nano TiO_2 .

The hydrophobic treatment NC-27CP shows reductions of WVP ranging from 45% for *St. Margarethen Limestone* to 65% for *Schlaitdorf Sandstone*. This eventually corresponds to a higher impact in respect to incompatibility and related risks, even though no distinct threshold can be stated for all conditions. In addition, numerous authors have reported that the effectiveness and compatibility

of a water repellent treatment depends on the substrate under study [91–93]. What is usually studied in regards to hydrophobic treatments is their durability and subsequent loss of water repellency [94,95] but not the potentially damaging consequences of the treatment. Potential damaging consequences would include studies related to water transport and undesired condensation phenomena, vapour pressure and corresponding temperature differences, comparable to reports obtained elsewhere [96].

For the study of alkoxysilanes, further determination of WVP measurements at different time intervals is desired to better understand the delay due to the chemical reaction. This might be of great importance for on-site conditions where larger penetration depths play a major role and the kinetics of the reaction are often complicated by different contaminants. Moreover, a study of different decay patterns (e.g., biological growth, black crusts, profile of degradation, etc.) in regards to their WVP is also recommended to further analyse the effect of consolidants on-site.

The values regarding colour measurements taken six weeks and one year after consolidation are summarized in Table 5. It was observed that even under laboratory conditions, the colour changes over time due to the chemical reaction and not following the same trends as found in the field. In fact, some values increase while others decrease from 6 weeks to 12 months' time interval. By now, it is clear that the studied substrates affect differently the treatments performance. As a general overview, colours tend to evanesce with time, more systematically in the silicate substrate, coming close to a value of $\Delta E^* < 5$, normally accepted as a threshold of perceptible colour impacts [11,97]. The impact was higher in the carbonate substrate and its evolution in time was less favourable.

Table 5. Colour values measured on sound *St. Margarethen Limestone* (SM) and *Schlaitdorf Sandstone* (S) before and after treatment at different intervals: six weeks (6 w) and twelve months (12 m).

Stone	Treatments	ΔL^* (6 w)	ΔL^* (12 m)	Δa^* (6 w)	Δa^* (12 m)	Δb^* (6 w)	Δb^* (12 m)	ΔE^* (6 w)	ΔE^* (12 m)
SM	KSE 300	4.51	6.62	0.87	0.45	5.30	4.53	7.01	8.03
	NC-25C	0.87	2.71	1.29	0.92	5.15	3.98	5.38	4.90
	NC-27CP	−1.41	0.44	2.10	1.51	7.31	6.15	7.74	6.35
S	KSE 300	−5.49	2.46	1.10	0.81	5.80	3.84	8.06	4.63
	NC-25C	0.30	2.77	0.76	1.39	2.86	5.04	2.97	5.92
	NC-27CP	−2.57	1.63	0.61	0.75	0.76	0.66	2.75	1.91

L^* the lightness coordinate ranging from 0 (black) to 100 (white), with positive values meaning darkening; a^* the red/green coordinate, with $+a^*$ indicating redness and $-a^*$ indicating greenness; and b^* the yellow/blue coordinate, with $+b^*$ indicating yellowness and $-b^*$ indicating blueness.

As usually happens in stone consolidation, the studied products have modified the stone properties, and some modifications signify that they may be responsible for a certain degree of incompatibility, in terms of the methodology proposed by Delgado Rodrigues and Grossi [11]. Given the specific character of this research, a more thoughtful application of that methodology was not considered. However, it needs to be emphasized that the values reported for the compatibility assessment should not be considered as solely entities that must satisfy a rigid requirement. A compatibility assessment, that would include also tests of durability, is a result of multivariate processes that requires the treatment of several parameters simultaneously to end up with an overall risk evaluation. That is to say, not meeting a threshold of one of the above studied parameters cannot result in excluding a consolidation treatment especially after the gained results in this study clearly indicate a wide-ranging evolution of values in time and magnitude.

4. Conclusions

This study addressed the potential efficiency and compatibility of three alkoxysilanes on two substrates of different chemo-mineralogical and petrophysical properties, namely a carbonate and a silicate stone. Results clearly show that treatment performance depends primarily on the textural

and microstructural parameters of the stone fabric. Under the same conditions, the same consolidant applied on different substrates yielded differences in mechanical and physical properties.

For the studied lithotypes, there is a clear trend observed within all three test methods to evaluate the efficiency. The relative percentage of deformability (Young's modulus) and strength increase, and the absolute values achieved, differ between the products applied and the lithotypes studied. The tendencies of *Schlaitdorf Sandstone* to show higher increases in deformability modulus and strength are related to its fabric. SEM studies provided insights into the preferential consolidation and interpenetration of kaolinite that is homogeneously located in intergranular pores inside the fabric. MIP analyses showed that the NC products not only deposit in smaller pores where the clay packs play an important role but also in large pores that actually make up the leading pore ranges in terms of open Hg-porosity. Therefore, it seems likely that the interpenetration of the clayey matrix combined with the deposition of the consolidants in all pore ranges, causing the most pronounced shift in the pore radii distribution, resulted in a mechanical strength above the values of the original stone material.

In what concerns the mechanical strength of the carbonatic lithotype *St. Margarethen Limestone*, the treatments show a sufficient increase in strength and deformability but the fabrics inhomogeneity with large voids and intragranular cracks passing through the microfossils did not allow the increase to be as high as the one described for *Schlaitdorf Sandstone*. Moreover, the main pore radii, which makes up the largest percentage of the open Hg-porosity in *St. Margarethen Limestone* seemed not to be filled to the same degree with the silica gels as observed within *Schlaitdorf Sandstone*.

In regards to the strength parameters, the experimental data also show that the amount of a consolidant deposited after curing has a relevant contribution for the overall consolidation action, even if its incidence is not fully proportional, as seen by the lower increments in deformability and strength caused by NC-27CP in *Schlaitdorf Sandstone* when compared to NC-25C. The reason for such behaviour needs to be further studied.

Despite the differences in strength increase, all consolidants show a strengthening action, therefore fulfilling their intended purpose.

The physical changes induced by treatments showed to be dependent on the time span after application. The necessary duration needed to obtain stable physical properties is difficult to predict and may primarily depend on the amount of consolidant deposited inside the stone's fabric and are therefore substrate dependent. Relating to water absorption by capillarity recorded six weeks after application, the temporary hydrophobicity of KSE 300 lasts for longer time in the silicate substrate but it does not affect the carbonate substrate. On the contrary, treatment NC-25C affects the carbonate substrate in terms of six weeks hydrophobicity but not the silicate substrate. More research is needed to analyse which stone parameters influence the reaction rate of TEOS. In respect to the substrate, the evolution values in time, for WVP and colour, follow no general trend and display opposing directions varying in absolute and relative magnitude.

It can be concluded that even with a system like alkoxy silanes, which have been in the focus of scientific interest for decades, major differences in compatibility are evident. In this study, it was demonstrated that for such reactive systems, an evaluation within the first months is not representative and yields an over- or underestimation of parameters. This study clearly demonstrated how widespread the gained results are when one system is applied on different substrates, both in time and relative and absolute magnitude.

To tailor the performance of a treatment, an experimental study prior to field application seems unavoidable. This is in order to understand the relationship between substrate and treatment, since all evaluated products, the newly engineered and the reference material, react unpredictably and depend primarily on the substrate. Only with the analysis of several parameters simultaneously, is an overall risk evaluation possible.

Author Contributions: M.B., E.M. and J.W. conceived and designed the experiments; M.B. performed and supervised the physical and mechanical experiments; E.M. performed the SEM- and E.M. and A.R. the optical microscopy analysis; E.M. interpreted the raw data of SEM studies; M.B. and J.D.R. interpreted the raw data of

physical and mechanical experiments; M.B. wrote the original draft; all authors reviewed and edited the paper and evaluated the final data; all authors approved the final manuscript.

Funding: This research was conducted in the frame of the European program Horizon 2020 Call NMP21-AC 646,178 “Nanomaterials for conservation of European architectural heritage developed by research on characteristic lithotypes” (*Nano-Cathedral*).

Acknowledgments: The authors wish to express their gratitude towards Lukas Achleitner, Sofia Zamfirescu, Anna-Maria Tupy, Georg Heidfogel and Anja Ziniel. Anthony Baragona, Peter Urbanek and Vanja Ban are gratefully acknowledged for proofreading and generally supporting this paper. The Scientific Laboratory of the Federal Monuments Authority in Austria is acknowledged for supplying the UV microscopy facilities. Karin Fussenegger is acknowledged for collaborations on mercury intrusion porosimetry. The authors thank Opera della Primaziale Pisana for providing the contact angle device, studios of Vienna’s St. Stephen Cathedral (Austria) and Colognes Cathedral Church St. Peter (Germany) for the provided stone specimens and ChemSpec Srl (Italy) and Remmers (Germany) for the supplied consolidants.

Conflicts of Interest: The authors declare no conflict of interest. The founding sponsors had no role in the design of the study; in the collection, analyses, or interpretation of data; in the writing of the manuscript, and in the decision to publish the results.

References

1. Verges-Belmin, V. *Illustrated Glossary on Stone Deterioration Patterns*; ICOMOS-ISCS (International Scientific Committee for Stone): Paris, France, 2008.
2. Ferreira Pinto, A.; Delgado Rodrigues, J. Stone consolidation: The role of treatment procedures. *J. Cult. Herit.* **2008**, *9*, 38–53. [[CrossRef](#)]
3. Ahmed, H.T. Physical and mechanical characteristics of Helwan limestone: For conservation treatment of ancient Egyptian limestone monuments. *J. Am. Sci.* **2015**, *11*, 136–151.
4. Pápay, Z.; Török, Á. Evaluation of the efficiency of consolidants on Hungarian porous limestone by non-destructive test methods. *Cent. Eur. Geol.* **2007**, *50*, 299–312. [[CrossRef](#)]
5. Franzoni, E.; Sassoni, E.; Scherer, G.W.; Naidu, S. Artificial weathering of stone by heating. *J. Cult. Herit.* **2013**, *14*, E85–E93. [[CrossRef](#)]
6. Da Fonseca, B.S.; Ferreira Pinto, A.P.; Picarra, S.; Montemor, M.F. Artificial aging route for assessing the potential efficacy of consolidation treatments applied to porous carbonate stones. *Mater. Des.* **2017**, *120*, 10–21. [[CrossRef](#)]
7. Zhang, L.Y.; Mao, X.B.; Lu, A.H. Experimental study on the mechanical properties of rocks at high temperature. *Sci. China Ser. E Technol.* **2009**, *52*, 641–646. [[CrossRef](#)]
8. Ruedrich, J.; Kirchner, D.; Siegesmund, S. Physical weathering of building stones induced by freeze-thaw action: A laboratory long-term study. *Environ. Earth Sci.* **2011**, *63*, 1573–1586. [[CrossRef](#)]
9. Ban, M.; Baragona, A.; Ghaffari, E.; Weber, J.; Rohatsch, A. Artificial aging techniques on various lithotypes for testing of stone consolidants. In *Science and Art: A Future for Stone, Proceedings of the 13th International Congress on the Deterioration and Conservation of Stone, Volume 1*; Hughes, J., Howind, T., Eds.; University of the West of Scotland: Paisley, UK, 2016; pp. 253–260.
10. Price, C.A. *Stone Conservation: An Overview of Current Research*; The J. Paul Getty Trust: Los Angeles, CA, USA, 1996.
11. Delgado Rodrigues, J.; Grossi, A. Indicators and ratings for the compatibility assessment of conservation actions. *J. Cult. Herit.* **2007**, *8*, 32–43. [[CrossRef](#)]
12. Sasse, H.; Snethlage, R. Evaluation of stone consolidation treatments. *Sci. Technol. Cult. Herit.* **1996**, *5*, 1996.
13. Graziani, G.; Sassoni, E.; Franzoni, E. Consolidation of porous carbonate stones by an innovative phosphate treatment: Mechanical strengthening and physical-microstructural compatibility in comparison with TEOS-based treatments. *Herit. Sci.* **2015**, *3*. [[CrossRef](#)]
14. Persia, F.; D’Amato, R.; Padella, F.; Piloni, L.; Rinaldi, A.; Tati, A. Performance of nanomaterials for the conservation of artistic stones. *EAI Energ. Ambient. Innov.* **2012**, *II-2012*, 77–81.
15. Siegesmund, S.; Snethlage, R. *Stone in Architecture: Properties, Durability*; Springer: Berlin/Heidelberg, Germany, 2011; pp. 415–550, ISBN 3642144756.
16. Auras, M.; Meinhardt, J.; Snethlage, R. (Eds.) *Leitfaden Naturstein-Monitoring, Nachkontrolle und Wartung als Zukunftsweisende Erhaltungsstrategien*; Fraunhofer IRB Verlag: Stuttgart, Germany, 2011; ISBN 978-3-8167-8407-4.

17. Tiano, P.; Filareto, C.; Ponticelli, S.; Ferrari, M.; Valentini, E. Drilling force measurement system, a new standardisable methodology to determine the stone cohesion: Prototype design and validation. *Int. J. Restor. Build. Monum.* **2000**, *6*, 115–132.
18. Costa, D.; Delgado Rodrigues, J. Evaluation of consolidation treatments applied to granitic materials. Experience and critical overview of laboratory testing. In Proceedings of the International Symposium on Stone Consolidation in Cultural Heritage: Research and Practice, Lisbon, Portugal, 6–7 May 2008; Rodrigues, J.D., Mimoso, J.M., Eds.; LNEC: Lisbon, Portugal, 2008; pp. 389–398.
19. Snethlage, R.; Ettl, H.; Sattler, L. Ultrasonic measurements on PMMA-impregnated marble sculptures. *Zeitschrift der Deutschen Geologischen Gesellschaft* **1999**, *150*, 387–396.
20. Snethlage, R. *Leitfaden Steinkonservierung, Planung von Untersuchungen und Maßnahmen zur Erhaltung von Denkmälern aus Naturstein*; Fraunhofer IRB Verlag: Stuttgart, Germany, 2008; ISBN 978-3-8167-8407-4.
21. Drdácý, M. Testing efficiency of stone conservation treatments. In *Advanced Materials for the Conservation of Stone*; Majid, H., Ioannis, K., Eds.; Springer: Cham, Switzerland, 2018; pp. 175–184. ISBN 978-3-319-72259-7.
22. Price, C.A.; Doehne, E. *Stone Conservation: An Overview of Current Research*, 2nd ed.; Getty Publications: Los Angeles, CA, USA, 2011.
23. Clifton, J.R. *Stone Consolidating Materials: A Status Report*; NBS Technical Note 1118:46; U.S. Department of Commerce, National Bureau of Standards: Washington, DC, USA, 1980.
24. George, W.; Goins, E.S. *Alkoxysilanes and the Consolidation of Stone*; Getty Publications: Los Angeles, CA, USA, 2005.
25. Ghaffari, E.; Köberle, T.; Weber, J. Methods of polarising microscopy and SEM to assess the performance of nano-lime consolidants in porous solids. In Proceedings of the 12th International Congress on the Deterioration and Conservation of Stone, Columbia University, New York, NY, USA, 22–26 October 2012; pp. 22–26.
26. Mascha, E.; Weber, J.; Ban, M. Erforschung von Nano-Materialien in der Gesteinsrestaurierung: Auswirkung von Festigungsmaßnahmen anhand von Laborversuchen innerhalb des EU-Projektes Nano-Cathedral. In Proceedings of the Natursteinsanierung Stuttgart 2018: Neue Natursteinrestaurierungsergebnisse und Messtechnische Erfassungen Sowie Sanierungsbeispiele, Stuttgart, Germany, 16 March 2018; Patitz, G., Grassegger-Schön, G., Wölbart, O., Eds.; Fraunhofer IRB Verlag: Stuttgart, Germany, 2018.
27. Pintér, F.; Weber, J.; Bajnóczi, B. Visualisation of solid consolidants in pore space of porous limestone using microscopic method. In Proceedings of the 11th International Congress on Deterioration and Conservation of Stone, Torun, Poland, 15–20 September 2008; pp. 473–480.
28. Zornoza-Indart, A.; Lopez-Arce, P.; Zoghliani, K.; Leal, N.; Simão, J. Marine Aerosol weathering of Mediterranean calcarenite stone: Durability of ethyl silicate, nano Ca(OH)₂, nano SiO₂, and nanostructured consolidating products. *Stud. Conserv.* **2018**, 1–17. [[CrossRef](#)]
29. Wendler, E.; Klemm, D.; Snethlage, R. Consolidation and hydrophobic treatment of natural stone. In Proceedings of the 5th International Conference on Durability of Building Materials and Components, Brighton, UK, 7–9 November 1990; Chapman & Hall: London, UK, 1990; pp. 203–212.
30. Charola, A.E. Water repellents and other “protective” treatments: A critical review. *Restor. Build. Monum.* **2003**, *9*, 3–22. [[CrossRef](#)]
31. Zhang, P.; Tian, J.; Xu, R.F.; Ma, G.J. Hydrophilicity, photocatalytic activity and stability of tetraethyl orthosilicate modified TiO₂ film on glazed ceramic surface. *Appl. Surf. Sci.* **2013**, *266*, 141–147. [[CrossRef](#)]
32. Gherardi, F.; Goidanich, S.; Dal Santo, V.; Toniolo, L. Layered nano-TiO₂ based treatments for the maintenance of natural stones in historical architecture. *Angew. Chem. Int. Ed. Engl.* **2018**, *57*, 7360–7363. [[CrossRef](#)]
33. Maravelaki-Kalaitzaki, P.; Kallithrakas-Kontos, N.; Korakaki, D.; Agioutantis, Z.; Maurigiannakis, S. Evaluation of silicon-based strengthening agents on porous limestones. *Prog. Org. Coat.* **2006**, *57*, 140–148. [[CrossRef](#)]
34. Da Fonseca, B.S.; Picarra, S.; Ferreira Pinto, A.P.; Montemor, M.F. Development of formulations based on TEOS-dicarboxylic acids for consolidation of carbonate stones. *New J. Chem.* **2016**, *40*, 7493–7503. [[CrossRef](#)]
35. Berto, T.; Godts, S.; De Clercq, H. The effects of commercial ethyl silicate based consolidation products on limestone. In *Science and Art: A Future for Stone, Proceedings of the 13th International Congress on the Deterioration and Conservation of Stone, Volume 1*; Hughes, J., Howind, T., Eds.; University of the West of Scotland: Paisley, UK, 2016; pp. 271–280.

36. Sassoni, E.; D'Amen, E.; Roveri, N.; Scherer, G.W.; Franzoni, E. Photocatalytic hydroxyapatite-titania nanocomposites for preventive conservation of marble. *IOP Conf. Ser. Mater. Sci. Eng.* **2018**, *364*, 012073. [[CrossRef](#)]
37. Miliani, C.; Velo-Simpson, M.L.; Scherer, G.W. Particle-modified consolidants: A study on the effect of particles on solegel properties and consolidation effectiveness. *J. Cult. Herit.* **2007**, *8*, 1–6. [[CrossRef](#)]
38. Folk, R.L. *Petrology of Sedimentary Rocks*; Hemphill Publishing Company: Austin, TX, USA, 1980.
39. Pettijohn, F.; Potter, P.; Siever, R. *Sand and Sandstone*, 2nd ed.; Springer: New York, NY, USA, 1987.
40. Graue, B.J. Stone Deterioration and Replacement of Natural Building Stones at the Cologne Cathedral—A Contribution to the Preservation of Cultural Heritage. Ph.D. Thesis, Georg-August-Universität Göttingen, Göttingen, Germany, 2013.
41. Graue, B.; Siegesmund, S.; Middendorf, B.; Oyhantcabal, P. Requirements for replacement stones at the Cologne cathedral—A systematic approach to general criteria of compatibility. In Proceedings of the 12th International Congress on Deterioration Conservation of Stone, Columbia University, New York, NY, USA, 22–26 October 2012.
42. Grimm, W. *Bildatlas wichtiger Denkmalgesteine der Bundesrepublik Deutschland*; Bayerisches Landesamt für Denkmalpflege: München, Germany, 1990; Volume 50.
43. Gradstein, F.M.; Ogg, J.G.; Hilgen, F.J. On The Geologic Time Scale. *Newsl. Stratigr.* **2012**, *45*, 171–188. [[CrossRef](#)]
44. Dunham, R.J. Classification of carbonate rocks according to depositional textures. *Am. Assoc. Pet. Geol.* **1962**, *1*, 108–121.
45. Embry, A.F., III; Klovan, J.E. A late Devonian reef tract on northeastern Banks Island, NWT. *Bull. Can. Pet. Geol.* **1971**, *19*, 730–781.
46. Moshhammer, B.; Uhlir, C.; Rohatsch, A.; Unterwurzacher, M. Adnet 'marble', Untersberg 'marble' and Leitha limestone—Best examples expressing Austria's physical Cultural Heritage. *Eng. Geol. Soc. Territ.* **2015**, *5*, 253–257.
47. Rohatsch, A. *Neogene Bau- und Dekorgesteine Niederösterreichs und des Burgenlandes*; Mitteilungen IAG BOKU: Wien, Austria, 2005.
48. Ban, M.; Pliessnig, M. The Biedermeier cemetery of St Marx in Vienna: Planning, management and treatment implementation. In *Conservation of Sculpture Parks*; Archetype Publications Ltd.: London, UK, 2018; pp. 59–72.
49. CEN. *Standard EN 14146, Determination of Dynamic Elastic Modulus by Measuring the Fundamental Resonant Frequency*; BSI: London, UK, 2004.
50. ASTM International. *ASTM D 3967–08, Standard Test Method for Splitting Tensile Strength of Intact Rock Core Specimens*; ASTM International: West Conshohocken, PA, USA, 2008.
51. Baumgartner, M. Auswirkungen von Steinfestiger auf die Mechanischen Eigenschaften von Natursteinen historischer Bauwerke: Teil 3. Untersuchungen und Prüfungen von Gealterten und Gefestigten Steinproben. Master's Thesis, Vienna University of Technology, Vienna, Austria, 2017.
52. Ziniel, A. Auswirkungen von Steinfestiger auf die mechanischen Eigenschaften von Natursteinen historischer Bauwerke: Teil 2. Brazilian Test, Druck-, Biegezug- und direkter zweiseitiger Scherversuch. Master's Thesis, Vienna University of Technology, Vienna, Austria, 2017.
53. CEN. *Standard EN 12372 Natural Stone Test Methods—Determination of Flexural Strength Under Concentrated Load*; BSI: London, UK, 2007.
54. CEN. *Standard EN 15801, Conservation of Cultural Property—Test Methods—Determination of Water Absorption by Capillarity*; BSI: London, UK, 2010.
55. CEN. *Standard EN 15803, Conservation of Cultural Property—Test Methods—Determination of Water Vapour Permeability*; BSI: London, UK, 2010.
56. CEN. *Standard EN 15886, Conservation of Cultural Property—Test Methods—Colour Measurement of Surfaces*; BSI: London, UK, 2010.
57. Remmers. Technical Guideline, KSE Modular System. Available online: http://www.remmers.co.uk/fileadmin/doc/pz/TL_0571_EN.pdf (accessed on 28 November 2018).
58. Cnudde, V.; Cnudde, J.P.; Dupuis, C.; Jacobs, P.J.S. X-ray micro-CT used for the localization of water repellents and consolidants inside natural building stones. *Mater. Charact.* **2004**, *53*, 259–271. [[CrossRef](#)]
59. Pesce, G.; Morgan, D.; Odgers, D.; Henry, A.; Allen, M.; Ball, R. Consolidation of weathered limestone using nanolime. *Proc. Inst. Civil Eng. Constr. Mater.* **2013**, *166*, 213–228. [[CrossRef](#)]

60. Alvarez De Buergo, M.; Fort, R.; Gomez-Heras, M. Contributions of scanning electron microscopy to the assessment of the effectiveness of stone conservation treatments. *Scanning* **2004**, *26*, 41–47. [[CrossRef](#)]
61. Croveri, P.; Luigi, D.; Joann, C.; Chiantore, O. Porosimetric changes and consequences for damage phenomena induced by organic and inorganic consolidation treatments on highly porous limestone. In *Science and Art: A Future for Stone, Proceedings of the 13th International Congress on the Deterioration and Conservation of Stone, Volume 1*; Hughes, J., Howind, T., Eds.; University of the West of Scotland: Paisley, UK, 2016; pp. 67–74.
62. Vutukuri, V.S.; Lama, R.D.; Saluja, S.S. *Handbook on Mechanical Properties of Rocks: Testing Techniques and Results*, 1st ed.; Trans Tech Publ.: Clausthal, Germany, 1974; Volume 1.
63. Baumgartner, L. Das Festigkeits- und Verformungsverhalten von Postaer Sandstein bei Zugbeanspruchung. In Proceedings of the 19 Tagung für Ingenieurgeologie und des Forums für junge Ingenieurgeologen, Technische Universität, München, Germany, 13–16 March 2013; pp. 407–414.
64. Coviello, A.; Lagioia, R.; Nova, R. On the measurement of the tensile strength of soft rocks. *Rock Mech. Rock Eng.* **2005**, *38*, 251–273. [[CrossRef](#)]
65. Chen, R.; Stimpson, B. Interpretation of indirect tensile-strength tests when moduli of deformation in compression and in tension are different. *Rock Mech. Rock Eng.* **1993**, *26*, 183–189. [[CrossRef](#)]
66. Perras, M.A.; Diederichs, M.S. A review of the tensile strength of rock: Concepts and testing. *Geotechn. Geol. Eng.* **2014**, *32*, 525–546. [[CrossRef](#)]
67. Aydin, A.; Basu, A. The use of Brazilian test as a quantitative measure of rock weathering. *Rock Mech. Rock Eng.* **2006**, *39*, 77–85. [[CrossRef](#)]
68. Delgado Rodrigues, J. Swelling behaviour of stones and its interest in conservation. An appraisal. *Mater. Constr.* **2001**, *51*, 183–195. [[CrossRef](#)]
69. Jimenez-Gonzalez, I.; Rodriguez-Navarro, C.; Scherer, G.W. Role of clay minerals in the physicochemical deterioration of sandstone. *J. Geophys. Res. Earth Sur.* **2008**, *113*. [[CrossRef](#)]
70. Cherblanc, F.; Berthonneau, J.; Bromblet, P.; Huon, V. Influence of Water Content on the Mechanical Behaviour of Limestone: Role of the Clay Minerals Content. *Rock Mech. Rock Eng.* **2016**, *49*, 2033–2042. [[CrossRef](#)]
71. Snethlage, R.; He, L.; Ma, T.; Wendler, E.; Sattler, L.; Simon, S. Der Sandstein von Dafosi—Untersuchungen zu den Ursachen der Schäden und zur Konservierung—The Sandstone of Dafosi Investigation into Causes of Deterioration and Conservation Methods. *ICOMOS—Hefte des Deutschen Nationalkomitees* **1996**, *17*, 220–239.
72. Scherer, G.W.; Wheeler, G.S. Silicate consolidants for stone. *Key Eng. Mater.* **2009**, *391*, 1–25. [[CrossRef](#)]
73. Milchin, M.; Weber, J.; Krist, G.; Ghaffari, E.; Karacsonyi, S. Ethyl-silicate consolidation for porous limestone coated with oil paint—A comparison of application methods. In *Science and Art: A Future for Stone, Proceedings of the 13th International Congress on the Deterioration and Conservation of Stone, Volume 2*; Hughes, J., Howind, T., Eds.; University of the West of Scotland: Paisley, UK, 2016; pp. 889–896.
74. Park, H.D.; Shin, G.H. Geotechnical and geological properties of Mokattam limestones: Implications for conservation strategies for ancient Egyptian stone monuments. *Eng. Geol.* **2009**, *104*, 190–199. [[CrossRef](#)]
75. Sassoni, E.; Graziani, G.; Franzoni, E. An innovative phosphate-based consolidant for limestone. Part 1: Effectiveness and compatibility in comparison with ethyl silicate. *Constr. Build. Mater.* **2016**, *102*, 918–930. [[CrossRef](#)]
76. Martinho, E.; Mendes, M.; Dionisio, A. 3D imaging of P-waves velocity as a tool for evaluation of heat induced limestone decay. *Constr. Build. Mater.* **2017**, *135*, 119–128. [[CrossRef](#)]
77. Jerome, P.S.; Weiss, N.R.; Gilbert, A.S.; Scott, J.A. Ethyl silicate as a treatment for marble: Conservation of St. John's Hall, Fordham University. *APT Bull.* **1998**, *29*, 19–26. [[CrossRef](#)]
78. Ksinopoulou, E.; Bakolas, A.; Moropoulou, A. Consolidation effectiveness of modified Si-based nanocomposites applied to limestones. *Mater. Struct.* **2018**, *51*. [[CrossRef](#)]
79. Rohatsch, A.; Nimmrichter, J.; Chalupar, I. Physical properties of fine grained marble before and after conservation. In Proceedings of the 9th International Congress on Deterioration and Conservation of Stone, Venice, Italy, 19–24 June 2000; pp. 453–458.
80. Stuck, H.; Forgo, L.Z.; Rudrich, J.; Siegesmund, S.; Torok, A. The behaviour of consolidated volcanic tuffs: Weathering mechanisms under simulated laboratory conditions. *Environ. Geol.* **2008**, *56*, 699–713. [[CrossRef](#)]
81. Pápay, Z.; Török, Á. Micro-Fabric, Pore-size distribution and water absorption of consolidated porous limestone. In *Engineering Geology for Society and Territory—Volume 8*; Springer: Cham, Switzerland, 2015; pp. 553–556. [[CrossRef](#)]

82. Remmers. Technical Data Sheet, KSE 300. Available online: http://www.remmers.co.uk/fileadmin/doc/tm/TM1_0720_EN.pdf (accessed on 28 November 2018).
83. Häupl, P.; Homann, M.; Kölzow, C.; Riese, O.; Maas, A.; Höfker, G.; Christian, N. *Lehrbuch der Bauphysik: Schall-Wärme-Feuchte-Licht-Brand-Klima*; Springer: Berlin, Germany, 2017; p. 215. ISBN 3658160748.
84. Ballester, M.A.D.; Gonzalez, R.F. Basic methodology for the assessment and selection of water-repellent treatments applied on carbonatic materials. *Prog. Org. Coat.* **2001**, *43*, 258–266. [[CrossRef](#)]
85. Tsakalof, A.; Manoudis, P.; Karapanagiotis, I.; Chrysosoulakis, I.; Panayiotou, C. Assessment of synthetic polymeric coatings for the protection and preservation of stone monuments. *J. Cult. Herit.* **2007**, *8*, 69–72. [[CrossRef](#)]
86. Charola, A.E. Water-repellent treatments for building stones: A practical overview. *APT Bull.* **1995**, *26*, 10–17. [[CrossRef](#)]
87. Lettieri, M.; Masieri, M. Performances and coating morphology of a siloxane-based hydrophobic product applied in different concentrations on a highly porous stone. *Coatings* **2016**, *6*, 60. [[CrossRef](#)]
88. Kronlund, D.; Bergbreiter, A.; Meierjohann, A.; Kronberg, L.; Lindén, M.; Grosso, D.; Smått, J.-H. Hydrophobization of marble pore surfaces using a total immersion treatment method—product selection and optimization of concentration and treatment time. *Prog. Org. Coat.* **2015**, *85*, 159–167. [[CrossRef](#)]
89. Gherardi, F.; Roveri, M.; Goidanich, S.; Toniolo, L. Photocatalytic nanocomposites for the protection of European architectural heritage. *Materials* **2018**, *11*, 65. [[CrossRef](#)]
90. Fujishima, A.; Zhang, X.; Tryk, D. TiO₂ photocatalysis and related surface phenomena. *Surf. Sci. Rep.* **2008**, *63*, 515–582. [[CrossRef](#)]
91. Moreau, C.; Leroux, L.; Vergès-Belmin, V.; Fronteau, G.; Barbin, V. Which factors influence most the durability of water repellent treatments: Stone properties, climate or atmospheric pollution. In Proceedings of the Hydrophobe V, 5th International Conference on Water Repellent Treatment of Building Materials, Brussels, Belgium, 15–16 April 2008; pp. 129–142.
92. Boutin, F. Comparative study of the efficiency of protective treatments applied to stone. In Proceedings of the Hydrophobe III, Third International Conference on Surface Technology with Water Repellent Agents, Universität Hannover, Hannover, Germany, 25–26 September 2001; pp. 233–244.
93. De Clercq, H.; De Witte, E. Effectiveness of silicon based water repellent agents at different application conditions. II. Commercial water repellents. *Int. J. Restor. Build. Monum.* **2001**, *7*, 641–654.
94. Poli, T.; Toniolo, L.; Sansonetti, A. Durability of protective polymers: The effect of UV and thermal ageing. *Macromol. Symp.* **2006**, *238*, 78–83. [[CrossRef](#)]
95. Wendler, E.; von Plehwe-Leisen, E. Water repellent treatment of porous materials. A new edition of the WTA leaflet. *Hydrophobe V Water Repel. Treat. Build. Mater.* **2008**, 155–168.
96. Hansen, C.M. Water transport and condensation in fluoropolymer films. *Prog. Org. Coat.* **2001**, *42*, 167–178. [[CrossRef](#)]
97. Garcia, O.; Malaga, K. Definition of the procedure to determine the suitability and durability of an anti-graffiti product for application on cultural heritage porous materials. *J. Cult. Herit.* **2012**, *13*, 77–82. [[CrossRef](#)]



© 2019 by the authors. Licensee MDPI, Basel, Switzerland. This article is an open access article distributed under the terms and conditions of the Creative Commons Attribution (CC BY) license (<http://creativecommons.org/licenses/by/4.0/>).

C

Neutron radiography study of laboratory ageing and
treatment applications with stone consolidants



Article

Neutron Radiography Study of Laboratory Ageing and Treatment Applications with Stone Consolidants

Matea Ban ^{1,*}, Tim De Kock ² , Frédéric Ott ³, Germana Barone ⁴, Andreas Rohatsch ¹ and Simona Raneri ⁵

¹ Institute of Geotechnics, Research Centre of Engineering Geology, Vienna University of Technology, 1040 Vienna, Austria; andreas.rohatsch@tuwien.ac.at

² Department of Geology, Ghent University, 9000 Ghent, Belgium; Tim.DeKock@UGent.be

³ Laboratoire Léon Brillouin, Université Paris-Saclay, Centre d'Etudes de Saclay, 91191 Gif sur Yvette CEDEX, France; Frederic.Ott@cea.fr

⁴ Department of Biological, Geological and Environmental Sciences, University of Catania, 95129 Catania, Italy; gbarone@unict.it

⁵ Department of Earth Sciences, University of Pisa, 56126 Pisa, Italy; simona.raneri@unipi.it

* Correspondence: matea.ban@tuwien.ac.at; Tel.: +43-158-801-20318

Received: 11 March 2019; Accepted: 11 April 2019; Published: 19 April 2019



Abstract: A nano-silica consolidant and nano-titania modified tetraethyl-orthosilicate were applied on two building stones, a carbonate and a silicate, by brush, poultice or capillary absorption. Neutron radiography was used to monitor capillary water absorption, and to analyse changes in physical properties caused by heat treatment of specimens for the purposes of artificially ageing and different treatment applications with stone consolidants. Moreover, ultrasonic pulse velocity and gravimetrically determined water absorption were analysed to cross-validate neutron radiography. The results reveal that reactive systems like tetraethyl-orthosilicates need an unknown period for polymerisation, which makes nano-silica consolidants more favourable for construction follow-up work. While polymerisation is incomplete, hydrophobic behaviour, water trapping and pore clogging are evident. Within the tetraethyl-orthosilicate treatment, poultice and brushing are strongly influenced by the applicant, which results in wide ranging amounts of water absorbed and anomalous water distributions and kinetics. The carbonate lithotype displays polymerisation initiated in the core of the specimen, while the lateral surfaces are still mostly hydrophobic. Reaction time differences can be attributed to the different amounts of consolidants applied, which is a result of the chosen application settings. Artificial ageing of stone specimens is a prerequisite when mechanical strength gain is studied, as demonstrated by sound speed propagation.

Keywords: neutron radiography; stone consolidation; treatment application; artificial ageing; water absorption; brushing; poultice; capillary absorption

1. Introduction

In the field of built cultural heritage, the preservation of monumental stone represents a challenging task. Basically, preservation can be divided into the protection and the consolidation of stone materials, which are accomplished by applying materials onto the stone surface. In the case of protection, products are applied to prevent harm from environmental factors, while in the case of consolidation, they are used to restore the mechanical strength of the stone by re-establishing the lost grain cohesion. As natural stones vary, so do their decay patterns. The vast majority of these decay phenomena are summarised in the ICOMOS-ISCS glossary on stone deterioration patterns [1]. A great number of these phenomena exhibit a necessity for consolidation. The most important of such phenomena is disintegration, which

can further be subdivided into crumbling and granular disintegration, where the last includes decay patterns like powdering or chalking, sanding and sugaring. Moreover, deterioration patterns like peeling and flaking might also require consolidation. In certain cases, micro fissures induced through differential stresses may be consolidated in order to compensate for the lost mechanical strength. However, all those phenomena occur to a different extent, complexity and can be accompanied by material loss (e.g., loss of the binding matrix, rounding, roughening, etc.). The cause and development of such phenomena is beyond the scope of the present study, and, in most cases, the decay patterns that are in need of consolidation are additionally overlapped with other decay phenomena, e.g., biological colonisation, cracks or deformation, that are in need of additional restoration actions. For such a diversity in substrates and conditions, new products with multi-functional self-cleaning [2], anti-fouling [3], water repelling [4] or anti-fungal [5,6] properties are continually being developed, with the aim of incorporating functionalised systems in consolidants. With such a range of consolidating materials in terms of chemical, physical and mechanical characteristics, the efficiency and compatibility of these treatments are likely to vary. Therefore, study of the physico-mechanical interactions between the substrate and different consolidating materials seems mandatory, in order to prevent eventual harmful effects caused by the treatment itself. It is known that the efficiency and compatibility of a treatment strongly depends on the interplay of several factors [7,8], including the substrate features and its conservation state, application methods and, as already mentioned above, the consolidating product itself.

Porosity and pore geometry of natural stones modified by weathering processes result in different pathologies. To better understand these decay patterns, artificial ageing of stone materials is frequently employed prior to applying and testing stone consolidants. The emphasis lies in the development of micro-cracks caused by differential stresses, which are induced through heat treatment [9,10]. However, several other laboratory test methods exist that supposedly mimic natural weathering decay phenomena, like salt crystallisation, thermal stresses, freeze–thaw and chemical weathering, to name a few. Specific protocols of accelerated aging are difficult to recommend because of the manifold dependency of different lithotypes, with varying degrees of resistance towards the induced stresses, leading to difficulties in adjusting the ageing protocol [11].

Regarding the protocol of treatment in monumental stone consolidation, three application methods—namely brushing, poultice and partial immersion—are commonly employed [12,13]. Brushing seems to be the preferred application technique in Italy, as reported in the literature [14]. It allows control of the amount of consolidant applied, and thus possibly assures reproducibility of the treatment procedure. However, treatment application varies and every country favours its own technique, mostly based on traditions and common local practice. Other application techniques not often discussed in the literature, but still widely employed in stone consolidation, include methods like run-off with different utensils (such as wash bottles, syringes and pipettes), spraying or pumping with different pressures, capillary absorption, vacuum pumping and injections through boreholes [15–17]. It must be pointed out that the differences in application routines also relate to different conservation problems that need to be managed (i.e., surface treatment or structural consolidation associated with larger penetration depths) [18]. For example, if a stone exhibits decay patterns in the form of sugaring or sanding, brushing will not be the method of choice, as it would remove an unknown amount of original material before consolidating it. On the other hand, if a dense surface is followed by a disintegrated subsurface zone, drilling boreholes to reach the material that needs to be consolidated is a prerequisite to remedying the problem. General rules or guidelines for treatment applications are difficult to assess, because of the manifold dependency of different stone types and their decay patterns.

As natural stone can accommodate different amounts of consolidants, and consolidants are used in different concentrations of solid content, it is necessary to tailor those variables in order to study the possible advantages and disadvantages connected to treatment performance. In addition, treatments implemented with different application techniques will most probably result in different amounts of product being applied, and thus different treatment performances. It has already been confirmed that

treatment performance depends on the amount of product applied [19] or the number of application cycles used [20]. In laboratory studies, treatment application is usually time-controlled, by allowing a building material to absorb the consolidant within a defined time span. On-site, it is common practice to apply the consolidant until refusal or full saturation of the substrate is observable. The latter application practice will result in a higher amount of product absorbed than when a consolidant is applied by, for example, a few brush strokes. The penetration depth might also differ when using different application techniques, as in immersion of all surfaces versus absorption from one surface.

The application of nanotechnology has not bypassed the field of architectural preservation. In fact, nano-particle based products have been emerging in recent years with the aim of tackling problems that have not been solved yet in stone conservation. Due to their nano-metric size, the consolidating materials are said to be more reactive and possibly better able to adhere to the surfaces, able to penetrate deeper and into smaller passages, and chemically more compatible with the host substrate, as well as protecting the building material from atmospheric pollution and further environmental agents. The main inorganic nanomaterials include calcium hydroxide and calcium carbonate systems [21–23], different metal oxides [24,25] and colloidal nanosilica [26], either used solely or incorporated into a matrix to obtain a particle-modified consolidant [27]. As the materials are new, many aspects of their use and durability remain unknown. It is certain that these systems will engage many further conservation scientists to come, especially as the use of such systems is not only limited to mineral materials but also regards materials such as wood [28] or paper [29].

Across the large range of chemically different stone consolidants, tetraethyl-orthosilicates—better known as TEOS—are the most widely used group. Through a step-wise polymerisation, a silica gel is formed by hydrolysis and condensation that, in consequence, consolidates the substrate. TEOS have been modified for different purposes, including with regards to the application procedure. Dilution of the consolidant was a common practice to reduce over-consolidation [30]. For the application method known as the vacuum-circling process [31], used to enhance penetration depths, specially tailored products have been engineered by Remmers (Löningen, Germany) [32]. The main purpose of the modification was to facilitate the process of hydrolysis. Enhancement of hydrolysis was desired because the consolidant could remain liquid in the stone material for an unknown period.

Any consolidation will ultimately change the stones' petrophysical properties (e.g., reduction of capillary water absorption or changes in water vapour permeability, shift in the pore radii distribution, changes in modulus of elasticity, etc.). For building materials in general, modifications of water transport and retention are particularly relevant. Moisture represents the most common cause of damage in monumental stones, therefore, change in water absorption by capillarity is an important property to be studied. To evaluate changes in water absorption before and after a treatment, laboratory and on-site tests are often employed [33,34]. However, a non-invasive method, such as neutron imaging, seems to be an adequate technique to fully investigate aspects related to local distributions of water quantities and kinetics. This method goes beyond simple visual inspections of advancement fronts of water, and the gravimetric quantification of water absorbed [35]. Furthermore, neutron imaging allows assessment of the penetration depth and distribution of products inside the material [36,37], and it provides a direct non-destructive evaluation technique where the same specimens can be used for further analysis.

Different natural stones, their varying decay patterns, numerous consolidating materials and application techniques employed result in many variables that are responsible for the outcome of a treatment performance. Research is lacking on all these variables, and they are thus not fully understood. In view of this, the goal of the present experimental study is to analyse how water absorption by capillarity is influenced when different consolidants are applied by different techniques. Through this, an understanding of the possible advantages and drawbacks of certain application techniques and consolidants can be gained, which is crucial for on-site work on monuments. For this purpose, neutron radiography has been used at the *IMAGINE* beamline, located at the Laboratoire Léon Brillouin (LLB), at the Orphée Reactor in Saclay, France [38]. This imaging technique allowed

monitoring of the water absorption by capillarity in two different porous stones, consolidated with two different products applied by three application techniques. The two newly developed consolidants are a nano-silica suspension in a mixture of water-ethanol, called NC-12C, and a nano-titania particle modified tetraethyl-orthosilicate in isopropanol called NC-25C. Both products were developed as part of the European project named “*Nano-Cathedral*” (Grant Agreement No. 646178) [39]. The consolidants were applied by brush, poultice or capillary absorption. Depending on the mode of application, different amounts of product were applied, allowing us to assess whether possible changes of material properties might be related to the treatment application itself, as well as the effective amount of solid content after curing that is precipitated in the stone material. Furthermore, a specific task of the present study included the analysis of the early stage of consolidant application, as this represents a crucial time step and determines the follow up work on the construction site.

The results demonstrate that the application technique, and therefore the amount of product absorbed, are relevant when reactive systems like TEOS are used. The amount of consolidant applied also governs the speed of polymerisation. The apparent hydrophobicity, present due to incomplete polycondensation even six weeks after application, causes pore clogging and water trapping. Poultice and brushing methods are strongly influenced by the applicant, which results in wide ranging levels of water absorption and anomalous water distribution and absorption kinetics within specimens treated with TEOS. This study reveals that, in the case of the carbonate lithotype, while the lateral surfaces remain mostly hydrophobic, polymerisation initiated in the core of the specimens might be present. Nano-silica-consolidated stone displays homogenous water absorption regardless of the amount of product applied and application technique used, which presents a clear advantage of such systems for on-site use. For studies concerning the mechanical strength gain, artificial ageing of stone specimens should be a prerequisite. While the cross-validation of neutron imaging with ultrasonic pulse velocity and water absorption coefficient was successful, insights into water trapping and local anomalies were only possible through neutron radiography.

2. Materials and Methods

2.1. Characterisation of the Lithotypes

Two porous sedimentary stones, a carbonate and silicate, were characterised by polarised light microscopy (PLM, Zeiss, Italy). The selected stones exhibited different mineralogical compositions, textures and structures, which were important prerequisites for this study in order to distinguish the possible influences a stone material can have on treatment applications. The petrographic differences of both lithotypes can be observed in Figure 1a–d. Results and a discussion concerning the mercury intrusion porosimetry of both lithotypes can be found in a previous study [40].

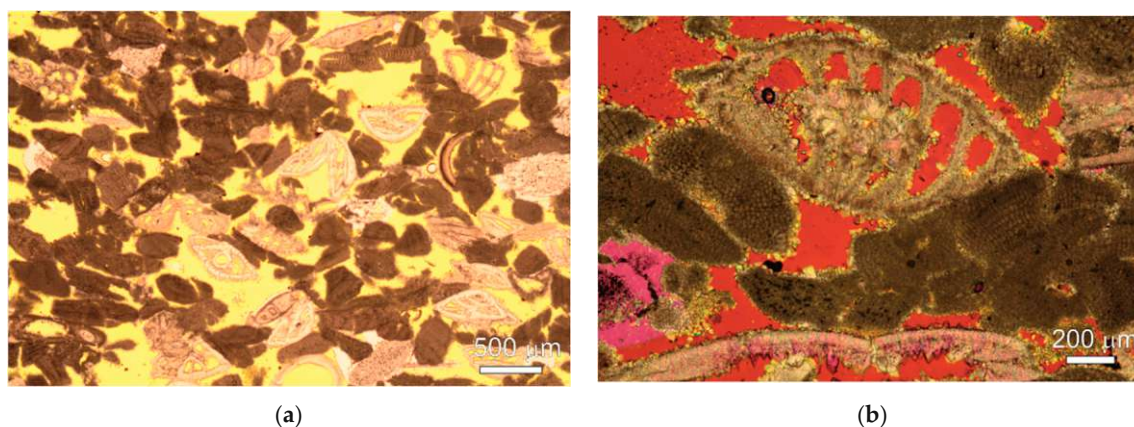


Figure 1. Cont.

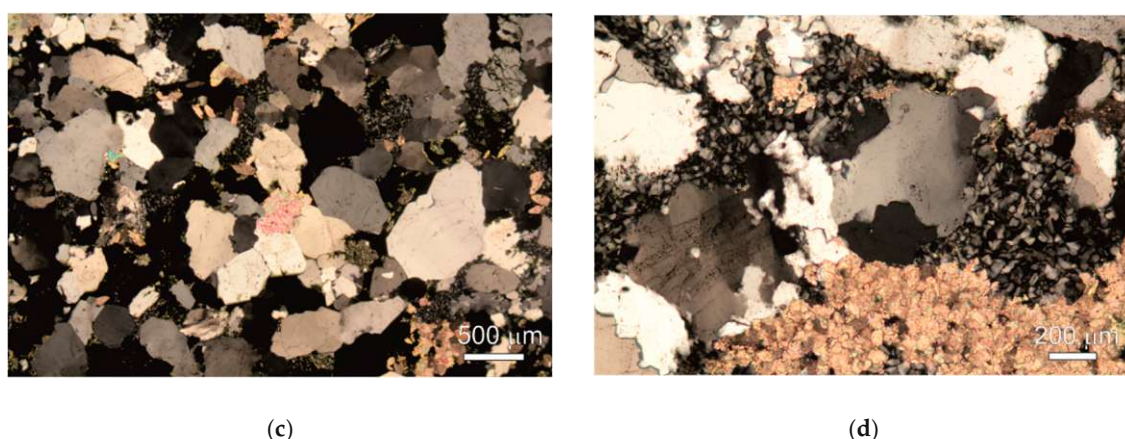


Figure 1. Micrographs of the stone fabric taken with a polarized light microscope: (a) Fabric of St. Margarethen Limestone with nearly equally distributed debris of coralline red algae and rotaliide foraminifers; (b) detail of the so-called dogtooth cement displayed as yellow binder between the microfossils; (c) fabric of Schlaitdorf Sandstone mainly consisting of quartz beneath feldspar and carbonate (pinkish colour), with planar to lobate grain boundaries, and (d) detail of the grain boundaries, the kaolinite matrix and sparitic carbonate.

Miocene (Langhian) calcareous arenite, known as St. Margarethen Limestone, can be classified as a porous grainstone or biosparite [41]. This limestone has been extracted from Roman times through to today in the quarry of St. Margarethen in Burgenland, Austria. It mainly consists of debris from coralline red algae, beneath foraminifers, and debris of echinoids and bryozoans, as well as traces of quartz and muscovite from the metamorphic geological hinterland. The cementation can be classified as early diagenetic fine-grained dogtooth calcite. The grainsize distribution can be described as nearly equigranular and moderate to well sorted. The mean grainsizes range from 0.5 to 1 mm, and the total porosity is between 25 to 30 vol.%. Additionally, larger fossils such as rhodolithes, oyster shells and skeletons of sea urchins up to several centimetres in size can be observed.

The Triassic (Keuper) lithotype, known as Schlaitdorf Sandstone, can be classified as a porous medium-grained siliciclastic arenite, which has been quarried since Roman times through to today in the province of Baden-Württemberg in Germany. This sandstone mainly consists of quartz (~72%), feldspar (~2%) beneath dolomite spar and calcite (~8%) and lithic fragments (~12%), as well as a clayey matrix which mainly consists of kaolinite (~6%) and traces of illite. The grainsize distribution can be described as well sorted, with an average grainsize of about 0.5 mm. The mean pore radius is about 3 μm, with a total effective porosity of approximately 20 vol. % [42].

Both lithotypes have been extensively used in construction of emblematic buildings across Austria and Germany, respectively. While Schlaitdorf Sandstone is still used for construction purposes, St. Margarethen Limestone is, in the present day, primarily used for restoration work. Their decay patterns range from surface deteriorations to structural disintegration, and both varieties are commonly in need of consolidation, since they are prone to weathering.

2.2. Stone Consolidants

The stone consolidants selected for the present study are newly designed products, developed in the frame of the European Horizon 2020 funded *Nano-Cathedral* project, short for “Nanomaterials for conservation of European architectural heritage developed by research on characteristic lithotypes” (Grant Agreement No. 646178). The project’s goal was to develop new, and modify existing, materials for the protection and consolidation of monumental stone. As many developed products never make it to the market, the project call for nanomaterials, advanced materials, and production (NMP-21-2014: materials-based solution for protection or preservation of European cultural heritage) aimed at large-scale production and application of the newly developed materials. Innovative SMEs (small

and medium-sized enterprises) and industries have been partnered to achieve this, as the designed products require a high technological readiness to enter the market after successful completion of the project, which is why the synthesis routes of the materials are protected by a non-disclosure agreement. Two newly developed products were tested in the present study.

The first product, NC-12C, is a silicon dioxide nanoparticle consolidant in suspension in a neutral water–ethanol mixture. The consolidant appears as a milky liquid with a low viscosity. The active ingredient is the suspended silica nanoparticles that make up 17 wt. %, and their average dimensions are 35 nm. The density amounts to 1 kg/L and the viscosity to 2 mPa s (both determined at 25 °C). If the consolidant is stored in a cool, dry place, the shelf life is at least one year. The product was developed by the Italian based industry Colorobbia S.p.A. (Sovigliana-Vinci (Firenze) Italy). Nanoparticle-based products are emerging more and more, as evidenced by recent publishing activities in the field of built cultural heritage [43]. These materials can be beneficially tailored in terms of dimensions, concentration, and use of solvent, to name just a few properties, all of which determine treatment performance. As soon as the solvent evaporates, the deposited nano-particles are structured into a solid material that is supposed to strengthen the stone.

The second product, NC-25C, is a tetraethyl-orthosilicate in isopropanol with 70% active content and TiO₂ dispersed particles. The spherical TiO₂ particles come in two crystal phases, namely anatase (approximately 80%) and rutile (approximately 20%). Approximately 1% added titania has a positive effect on the self-cleaning abilities of the consolidant, which can be considered an additional value when compared to commercial TEOS. The average size of the nano-titania is 10 to 15 nm. The consolidant appears white and has a low viscosity. The specific weight is ~1 g/cm³, while the viscosity is 3,3 cSt (both determined at 25 °C). The reaction takes place after four weeks at room temperature (~20 °C) and with a relative humidity of 45 ± 5%. If the consolidant is stored in a cool, dry place, the stability of the product is at least six months. The consolidant was developed by the Italian industry Chem Spec S.r.l. while the supplier of the nanoparticle is the Spanish based industry Tecnan (Technologia Navarra de Nanoproductos, S.L., Los Arcos (Navarra) Spain). TEOS are favoured for their low viscosity and thus good penetration depths, chemical resistivity and induced mechanical strength. As nano-particle based consolidants, TEOS can also be tailored to obtain different properties. This is achieved through the pre-polymerisation degree, addition of solvents, admixtures of catalysts, ratio of different mono- to oligomers, or the addition of compounds to gain more elasticity, better adhesion to carbonate substrates, and so forth. According to the manufacturers of the products, the ideal condition for polymerisation is four weeks at a temperature of 20 °C and a relative humidity of 50%. During the curing period, the system is known to possess hydro-repellent properties. The silica gel formed in the pores of the substrate undergoes continuous drying accompanied by shrinkage over an unknown time span.

2.3. Artificial Ageing of Stone

Cyclic heat treatment was chosen as an artificial ageing technique, as it showed sufficient ability to cause a reduction of soundness. The aim of the ageing was to cause microstructural defects in the form of micro cracks, and to observe the alterations caused by the cracks to the stone's capillary water absorption. Two main reasons motivated the use of temperatures as high as 600 °C. The first reason is the porosity of the stone, where higher temperatures needed to be employed to assure sufficient microstructural damage. In the case of St. Margarethen Limestone, large pores and microfossils are able to accommodate more stresses during thermal expansion, which is why higher temperatures and cyclic stresses were preferred. The second reason is that, for the silicate variety Schlaitdorf, only temperatures above 573 °C cause sudden volumetric expansion when transforming from α - to β quartz, which results in thermal expansion and subsequent micro cracking.

The stones were heat treated in an electric furnace of 3.5 L volume from Thermo Scientific (Fisher Scientific Austria GmbH Vienna), model Heraeus K 114. The heating rate was 40 °C/min until a static temperature of 600 °C was reached and maintained for one hour. This procedure was repeated three

times, with a cooling of the specimens between the cycles. To guarantee the same starting point, all samples were washed and dried to a constant weight before the consolidation treatment.

2.4. Consolidation of Stone: Treatment Procedure and Curing

In total, 60 specimens with dimensions of 2 cm × 2 cm × 5 cm were washed with deionized water, dried at 50 °C until they reached a constant mass and kept under laboratory conditions for 24 h before the treatment application. The dry mass of the stone specimens was recorded before the treatment procedure. For each studied condition (sound, aged and consolidated), three specimens were used for both lithotypes (see Table 1). The consolidants were applied by capillary absorption, brushing and poultice (see Figure 2).

Table 1. Labelling for the studied conditions: sound and aged stone specimens as reference conditions, consolidated specimens with either NC-12C or NC-25C applied by different application techniques: capillary absorption, brushing and poultice for both lithotypes.

Reference Specimens	Consolidated Specimens		
	Capillary	Brushing	Poultice
Sound	C_NC-12C_P ¹	B_NC-12C_P ¹	P_NC-12C_P ¹
Aged	C_NC-25C	B_NC-12C_wP ³	P_NC-25C
	C_NC-25C_Oc ²	B_NC-25C	

¹ Pre-wetting. ² Overconsolidated. ³ Without pre-wetting.

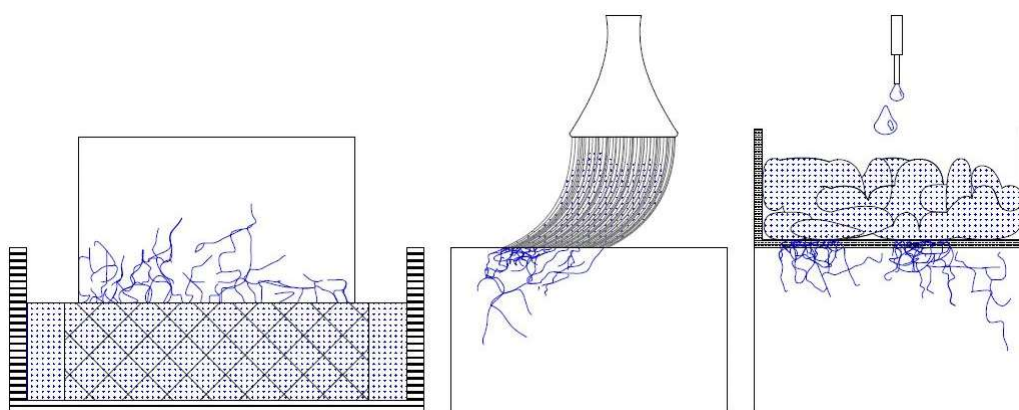


Figure 2. Schematic representation of application techniques used to consolidate stone specimens. Capillary absorption for one hour (**left**), brushing with 10 strokes (**middle**), and poultice, where a cellulose pulp packed in Japanese paper was placed on the stone surface for 1 h (**right**).

Treatment by capillary absorption was performed by placing the samples in contact with the consolidants for one hour. The specimens were placed on a wide meshed plastic grid, allowing the absorption of the products to take place from one side by capillary forces. The consolidant was refilled to assure a constant contact with the treated surface, making sure that no immersion of the specimen occurred through the lateral sides of the specimens. For such purposes, a wider box filled with consolidants was suitable. In the case of capillary absorption treatment with the product NC-12C, pre-wetting with ethanol was conducted. The aim of such pre-treatments was inspired by on-site work. Apparently, a pre-treatment using the corresponding solvent of the product allows a deeper penetration of the consolidants into the stone and avoids glossiness through particle efflorescence at the surface. Moreover, a so-called over-consolidation in the case of the capillary absorption specimens treated with the product NC-25C was mimicked by repeating the procedure three days in a row. In the case of over-consolidation, the sample was left under laboratory conditions between the application cycles (T: 20 °C ± 3 °C and RH: 55% ± 3%), where a chemical reaction might already have started.

The aim of such a procedure was to study the impact of over-consolidation [20]. According to technical guidelines, such an application procedure should be avoided, as pore clogging may occur due to the already-started polymerisation. The right approach when working with reactive consolidants like TEOS is to do the treatment wet-in-wet to avoid such phenomena as pore clogging and accumulation of the consolidant into the sub-surface zone. In the present work, the goal was to study, indirectly, through the absorption of water, if such an over-consolidation would retard the polymerisation.

Treatment application by brushing was done following the recommendations reported in the literature [44], by a continuous application of 10 strokes onto the stone surface. Concerning consolidation with NC-12C, one set of specimens was pre-wetted with ethanol, while a second set was consolidated without pre-wetting. The aim of such a procedure was to compare the possible influences of the pre-treatment on the behaviour of water absorption by capillarity. Pre-wetting with ethanol was completed by brushing the surface 10 times in a row.

For treatment application by poultice, it was applied following procedures reported elsewhere [12]; a cellulose pulp soaked with the consolidating products was stirred for two hours prior to application onto the stone surface. During stirring, evaporation of the solvent was avoided by the use of a sealed container. A weight ratio between cellulose pulp and consolidants of 1 to 8 was mixed. The layer of the consolidant-soaked cellulose pulp which came in contact with the stone surface was approximately 2 cm thick. The poultice was wrapped in a so-called Japanese paper that was subsequently placed in contact with the stone surface for one hour. The Japanese paper was used to avoid direct contact of the stone with the cellulose derivate, to avoid gluing or even soaking of the pulp into the substrate. For the application of NC-12C, specimens were pre-wetted with ethanol by stirring the solvent with the cellulose pulp for two hours, and subsequently placing the mixture for one hour on the surface of the sample.

After treatment, samples were weighed, placed in a sealed box and wrapped for 48 h in a plastic foil to prevent quick evaporation and back-migration of the consolidants. The next step was outdoor curing, which took place in a sheltered area in the courtyard of the Department of Earth Sciences at the University of Pisa in Italy. The consolidated specimens were gravimetrically monitored every day for three weeks, and the environmental conditions were recorded once per day in the early afternoon (see Figure S1 in Supplementary Materials). The daily temperatures ranged from 17 °C to 28 °C, while the relative humidity varied between 30% and 85%. It must be noted that a day to night fluctuation of the temperature and relative humidity during the curing period was not recorded. The values recorded can be viewed as quasi-ideal for curing conditions (according to common technical sheets, 20 °C and 50% RH for three to four weeks), but it must be emphasised that the temperatures dropped during the night.

Prior to neutron radiography studies, the stone specimens were stored under laboratory conditions for three additional weeks, which means that the first scans were determined six weeks after treatment applications.

2.5. Neutron Radiography and Image Processing

Neutron radiographs were acquired at the instrument *IMAGINE* of the Laboratoire Léon Brillouin in Saclay, France. A neutron beam was sent onto the samples. Some of the neutrons were absorbed or scattered. One measures the intensity of the so-called transmitted beam—the part that crosses the sample without interacting with it. The flux of the incident beam was 2×10^7 neutrons $\text{cm}^{-2} \text{s}^{-1}$. It was a so-called white beam that included a large spectrum of cold neutrons, with a wavelength in the range of 3 to 20 Å. The optical setup was defined by the L/D ratio of 400. The L/D ratio (ratio of L being the distance between the entrance aperture of the beam to the image plane over D that is the diameter of the beam aperture) represents a key factor determining the quality of the resolution [45]. The bigger the L/D ratio, the lower the angular resolution of the neutron beam and the better the resolution. Detection was achieved using a sCMOS camera (Andor) coupled with a lithium scintillator of 100 μm thickness. This set-up allowed a spatial resolution of about 250 μm . In our case, the main contrast was due to

hydrogen atoms being more present in water than in the samples. The cross section of a hydrogen nucleus is almost two orders of magnitude larger than those of the majority of nuclei, including those of the stones. For details regarding a closer description of the technique and the use of neutrons in cultural heritage, the reader is referred to References [46,47] for further information.

Dark field and open beam images were first acquired and used for further corrections. Stone specimens were placed on a stack of filter paper and arranged in an aluminium container so that the whole stone specimens, from top to bottom, could be scanned. Reference images in dry state were acquired. To monitor the water absorption by capillarity, water was manually added into the aluminium box, which ensured the saturation of the filter paper pack (with a 10 mm thickness, obtained from Kaltek S.r.l. Padova Italy). After the addition of the water, scans were acquired with an exposure time of 10 s until full saturation, or after a maximum duration of 30 min.

The images were pre-processed according to the in-house protocol at the *IMAGINE* beamline, performing a correction with dark-field images, normalization with open beam images and noise filtering (dead camera pixels and spurious gamma events). Absolute transmission images of the samples were obtained with an absolute precision in the 1% range. Neutrons, being strongly scattered by hydrogen atoms, with equivalent thicknesses of 20 μm of H_2O in a sample, can be detected in favourable cases. To analyse the absolute water content, water absorption images were normalised with the steady-state dry images taken prior to absorption, to obtain images in which the measured transmission was directly related to the amount of water in the sample [48]. A similar approach was performed on a staircase-like sample holder containing twelve different water volumes with standardised thickness. The neutron transmission was plotted over these twelve water thicknesses from 0.09 mm to 5.00 mm and used as a calibration curve for the water content of the water absorption images. This procedure was necessary because for high water contents (>2 mm equivalent thickness), the transmission does not follow a simple Beer–Lambert law. Pre-processing and image analysis were performed using Fiji ImageJ (Fiji Is Just ImageJ - Image Processing and Analysis in Java, open source, general public license) [49].

2.6. Ultrasonic Pulse Velocity and Water Absorption Coefficient

Two additional non-destructive natural stone test methods were carried out in the laboratory to investigate a possible cross-validation for the use of neutron radiography. For this purpose, the determination of the ultrasonic pulse velocity (UPV) and water absorption coefficient (WAC) were used on the same specimens that were studied by means of neutron radiography. Three specimens for each condition were analysed.

The velocity of propagation of pulses of ultrasonic waves was determined according to the standard EN 14579 [50]. The device used consisted of an electrical pulse generator (type Conosonic C2-GS) and a pair of transducers (UP-DW, with a diameter of 24 mm but a coupling surface as a probe tip), all developed by Geotron-Elektronik (Pirna, Germany). UPV is reported in [km/s], and the frequency used for both stones amounted to 80 kHz, while the amplitude was selected according to samples damping; for the studied stones, it was between 200–500 mV.

The water absorption coefficient was determined after 30 min (WAC_{30}). The specimens were in direct contact with the wet filter paper (obtained from Kaltek S.r.l. Padova Italy), and the weight increase was recorded at time intervals of 1, 3, 5, 10, 15, 20, 25 and 30 min. The surface that was in contact with water was the surface that was treated by the consolidants. It is important to note that, for porous stones, the slope of the curve represents the speed of adsorption and the plateau of the curve represents the full saturation of specimens, and these two phenomena are not distinguished in WAC_{30} . In order to differentiate between these two processes, WAC_5 was also introduced, which represents the water absorption coefficient after 5 min. The latter coefficient solely considers the speed of the water absorption, or the initial part of the curve. Both coefficients, WAC_{30} and WAC_5 , are reported as $[\text{kg}/(\text{m}^2 \cdot \text{t}^{0.5})]$.

UPV and WAC were tested eight weeks after the treatment applications. It must be stressed that, in the latter case, the consolidated specimens already came in contact with water during neutron radiography tests and that, therefore, the polymerisation was at an advanced stage.

3. Results and Discussion

3.1. Evaluation of Artificial Ageing

The impact of heat treatment on artificially aged stone substrates prior to consolidation was successfully evaluated by neutron radiography, the water absorption coefficient and the ultrasonic pulse velocity (see Figures 3 and 4).

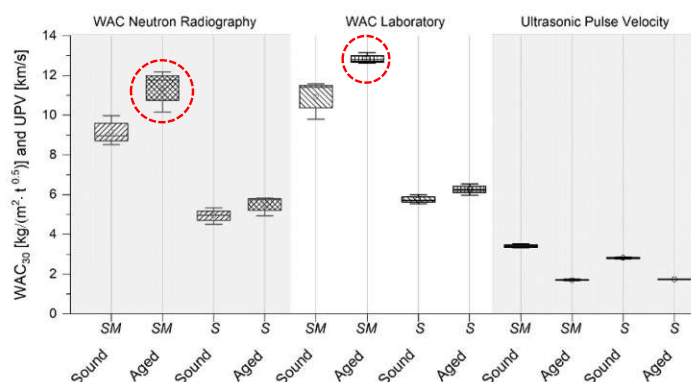


Figure 3. The effect of thermal ageing on St. Margarethen Limestone (SM) and Schlaitdorf Sandstone (S) determined by the water absorption coefficient after 30 min, as well as the ultrasonic pulse velocity before (**sound**) and after artificial ageing (**aged**). WAC was calculated from image analysis obtained from neutron radiographs and gravimetric laboratory analysis. The corresponding values can be extracted from Supplementary Materials, Table S1.

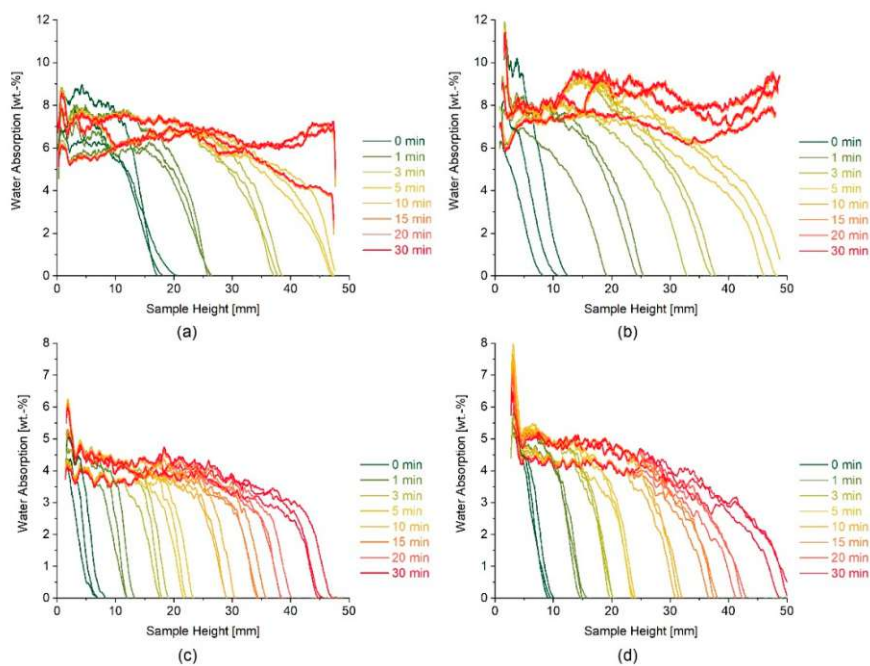


Figure 4. Neutron studies of sound (a) and artificially aged (b) water absorption kinetics (reported as wt. % and as a function of the sample height at intervals of 1, 3, 5, 10, 15, 20, 25 and 30 min) for three stone specimens of St. Margarethen Limestone, as well as sound (c) and artificially aged (d) water absorption curves of three stone specimens of Schlaitdorf Sandstone.

In the case of highly porous materials, the WAC sometimes displays marginal differences between sound and artificially aged substrates, due to the limits of accommodating water. That is, with only a few induced micro cracks, the magnitude of absorbed water might be negligible in terms of weight increase. For such cases, the initial slope of water absorption curves can give more insight into fabric alterations and the speed of absorbed water than the water absorption coefficient itself. Franzoni et al. [9] have already demonstrated that, for some lithotypes, the initial part or the slope of the curve remains unchanged, because this part is associated with the size and amount of coarser pores, while the second part of the curve increases because the latter part is linked to smaller pores, especially those induced by heat treatment. Following these considerations, Table 2 gives the difference between water absorption coefficients calculated after 30 min and 5 min from both neutron radiographs and gravimetric increases. In the case of the more porous lithotype, St. Margarethen Limestone, the difference between these two coefficients is apparent. As for Schlaitdorf Sandstone, the values are significantly close, because this stone does not reach the saturation equilibrium like St. Margarethen. St. Margarethen Limestone is a typical example of a one-dimensional Fickian diffusion process, where the initial part of the curve displays a linear increase of water absorption with the square root of time until it reaches a plateau, which represents the saturation of the specimen. Schlaitdorf's curve also gradually increased with a linear dependency, but no equilibrium plateau can be reached for the given test time.

Table 2. Difference between water absorption coefficients calculated after 30 min (t) and 5 min (t) for sound and aged St. Margarethen Limestone and Schlaitdorf Sandstone, reported as $[\text{kg}/(\text{m}^2 \text{t}^{0.5})]$.

St. Margarethen Limestone								
Calculation	Neutron Radiography				Gravimetric Increase			
Condition	Sound		Aged		Sound		Aged	
WAC [min]	WAC ₃₀	WAC ₅	WAC ₃₀	WAC ₅	WAC ₃₀	WAC ₅	WAC ₃₀	WAC ₅
Coefficient	9.15	19.92	11.36	22.28	10.92	20.94	12.83	23.64
SD.N.	±0.61	±1.41	±0.87	±1.76	±0.80	±1.01	±0.23	±0.94
Schlaitdorf Sandstone								
Calculation	Neutron Radiography				Gravimetric Increase			
Condition	Sound		Aged		Sound		Aged	
WAC [min]	WAC ₃₀	WAC ₅	WAC ₃₀	WAC ₅	WAC ₃₀	WAC ₅	WAC ₃₀	WAC ₅
Coefficient	4.94	5.70	5.51	6.47	6.26	6.81	5.75	6.75
SD.N.	±0.34	±0.56	±0.41	±0.47	±0.22	±0.41	±0.18	±0.24

Figure 3 displays the trend of the WAC₃₀ calculated through neutron radiography, and WAC₃₀ obtained in the laboratory by gravimetric means. The WAC₃₀ values calculated through neutron radiographs are slightly underestimated in magnitude due to different effects, including: (i) averaging during image analysis, which also assumes a mean density and uniform specimen dimensions, (ii) crop of the bottom of the radiographs for reasons of shift corrections and (iii) effects considering the ratio of the signal to noise, timing and setting of the instrument, which might also include evaporation phenomena. Nevertheless, it was demonstrated that the artificially aged stone had an increase in water absorption by capillarity and a decrease in ultrasound pulse velocity, caused by the formation of micro cracks. Furthermore, in the case of St. Margarethen Limestone, a wider spread of the results is visible when the WAC₃₀ was calculated from radiographs, indicating a more inhomogeneous distribution and speed of water absorbed in the artificially aged specimens (see Figure 3, data marked in red). UPV is suitable for the detection of micro cracks, especially when sound reference values are available.

Neutron radiography was able to detect changes in the speed and amount of water absorption in the case of both lithotypes due to the inducement of micro cracks. The speed of capillary suction was slightly higher for aged compared to sound stone specimens (Figure 4a–d). In the case of St. Margarethen Limestone, after ageing there was a wider spread in kinetics of absorbed water, indicating that the induced micro cracks resulted in a more inhomogeneous substrate. On the contrary,

in the case of Schlaitdorf Sandstone, the recorded speed was more uniform after artificial ageing because of the induced cracks (compare Figure 4c,d).

Changes caused by heat treatment had a measurable impact on water absorption kinetics in both lithotypes, but for practical considerations and because the lithotypes are porous enough even in their sound states, the treatments were performed on sound stone specimens. However, neutron radiography proved to be useful when studying different pathologies of the stones' fabrics caused by artificial ageing. Moreover, as will be demonstrated below, the impact of thermal treatment on the mechanical properties of the stone is a requirement for studies regarding mechanical strength gains, and thus treatment efficiency.

3.2. Evaluation of Treatment Application with TiO_2 Modified Tetraethyl-Orthosilicate on St. Margarethen Limestone and Schlaitdorf Sandstone

In the case of St. Margarethen Limestone, the acquired experimental data show that for the consolidant NC-25C, the reaction kinetics are influenced by the amount of product applied, and therefore it is application treatment dependent. Neutron radiographs clearly demonstrate that six weeks after the treatment application, the system was still largely hydrophobic. Derived from residual ethoxy groups, the system remained water repellent for an unknown period of time, depending on numerous factors. This apparent hydrophobicity disappears with continued hydrolysis–condensation reactions, and can even be overcome by a post-treatment with water, as demonstrated by Franzoni et al. [51]. When in contact with liquid water, the surfaces become less water repellent as hydrolysis proceeds. However, a long-lasting partial hydrophobicity might still be present after years, as shown in previous work [52]. It was determined that this effect of temporary hydrophobicity was most pronounced in the set of samples treated by capillary absorption, where the highest amount of product was deposited inside the stone's fabric (see Figure 5a). Stone specimens treated with brushing and poultice accommodated a smaller amount of product due to the given application settings, thus allowing, on average, a faster polymerisation reaction. It is important to note that it is hardly possible to make assumptions about competing processes of hydrolysis and condensation in the period after initial treatment with neutron radiography, as it cannot provide direct evidence of polymerisation (consumption and production of water), but indicates indirectly the chemical process through which the water is absorbed. A couple of phenomena, not able to be distinguished with the present methodologies, might now be relevant in understanding the polymerisation process in a stone fabric in respect to water absorption: i) capillary flow in mixed patterns of hydrophobic–hydrophilic surfaces, where the latter might correspond to unconsolidated surfaces or already polymerised residues, ii) influence of the compositional and micro structural features of the stone fabric, including effects like surface area to volume ratio of the deposited consolidant [30], surface polarities, effects like vapour pressure, steric hindrance and inductive effects, and iii) dynamic changes occurring due to direct contact with liquid water during the tests. Even without further clarification of the above-mentioned phenomena, neutron radiographs acquired for sound and consequently consolidated stone allowed evaluation of what kind of impact a treatment application might have with respect to capillary water absorption (see Figure 6).

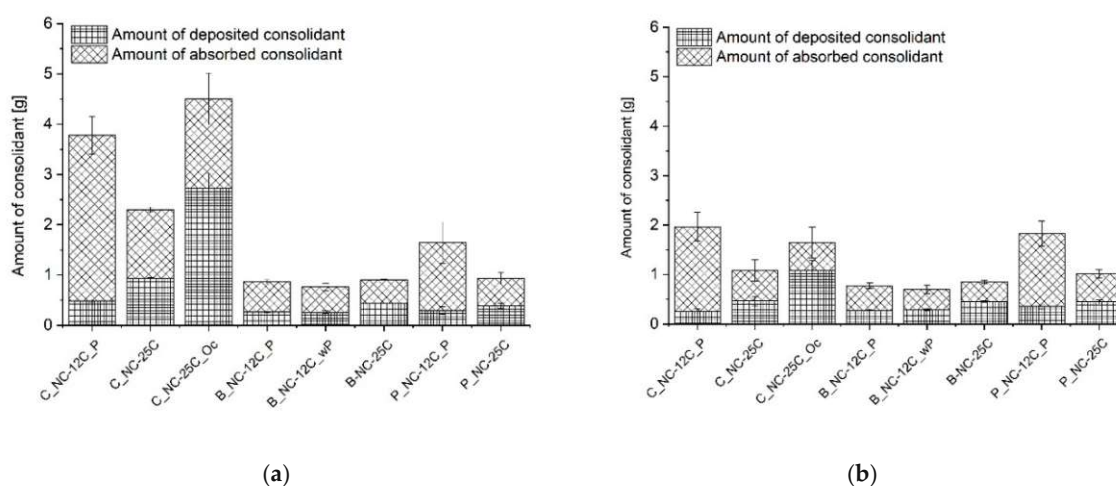


Figure 5. Comparison of the amount absorbed versus amount deposited inside (a) St. Margarethen Limestone and (b) Schlaitdorf Sandstone. For the calculation of the absorbed amount of consolidant, the weight of the stone in the initial dry state was subtracted from the weight after consolidation. To calculate the deposited amount of consolidant, the cured stone was weighed and subtracted by the weight of the initial dry state. The cured state corresponds to the mass recorded at the last day of outdoor curing, three weeks after the treatment application.

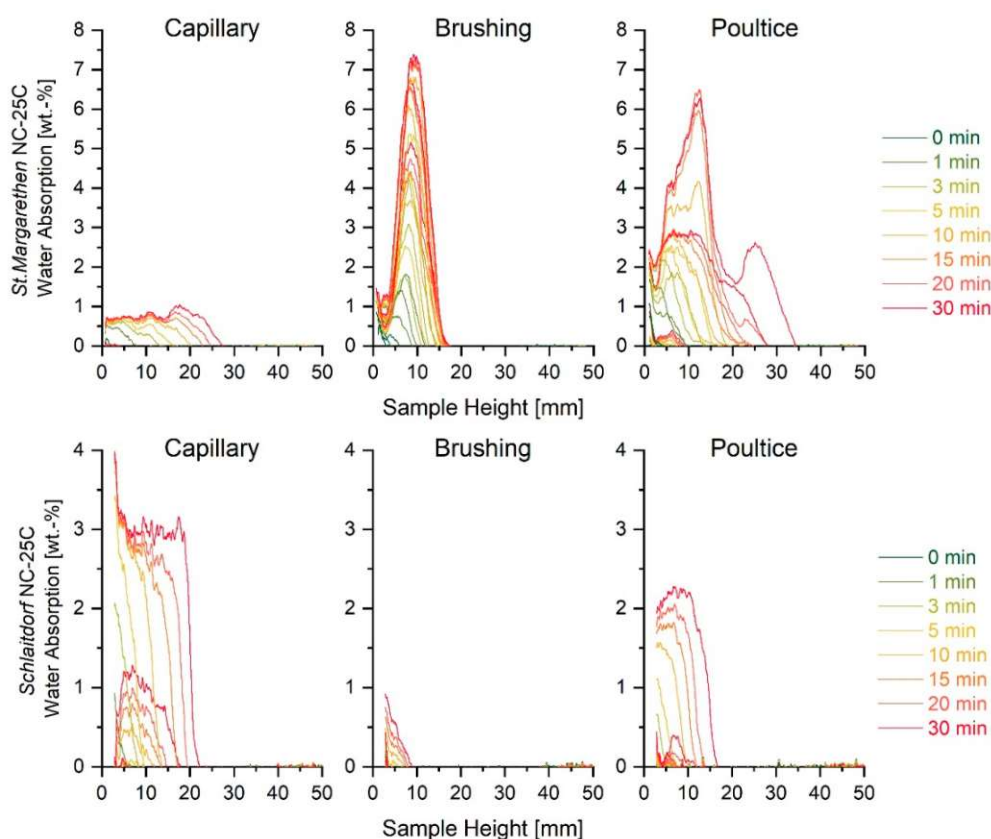


Figure 6. The top graph displays water absorption kinetics reported in weight percentage for three St. Margarethen Limestone specimens treated with NC-25C, while the bottom graph displays the same for Schlaitdorf Sandstone.

It was demonstrated that the specimens consolidated with NC-25C and applied by poulitce and brushing result, due to the apparent hydrophobicity, in so-called ‘water trapping’ (see effects of this phenomenon in Figure 7b,c). This water trapping occurred in the inner core of the stone specimens,

while the lateral surfaces were still mostly hydrophobic with the exception of small passages where capillary forces sucked the water inside the material. This inner core of the stone specimens that was filled with water possibly indicates a polymerisation that was initiated inside the stone or parts of the structure that were not consolidated in the first place. Particularly, Figure 7b suggests that the very bottom of the stone was hydrophobic, and above the water trapping zone the specimen was also hydrophobic, even though it was a highly porous lithotype. The latter radiograph therefore indicates that water was trapped in between the very bottom and first third of the specimen. This represents an unusual phenomenon where hydrophobic and hydrophilic patterns intersect. Trapping of liquid water inside an incompletely polymerised consolidant could jeopardise the silica gel structures, promote the solubility of salts, increase bio-growth or cause spalling of the surface due to differential stresses, all phenomena that potentially lead to harmful effects. Furthermore, neutron imaging was able to show that in the presence of fabric inhomogeneities like the so-called vugs (large pores with calcite crystallization on the pore walls), water uptake was promoted along those structural paths, since these interfaces were most probably not completely covered by the consolidant during the treatment (Figure 7d,e).

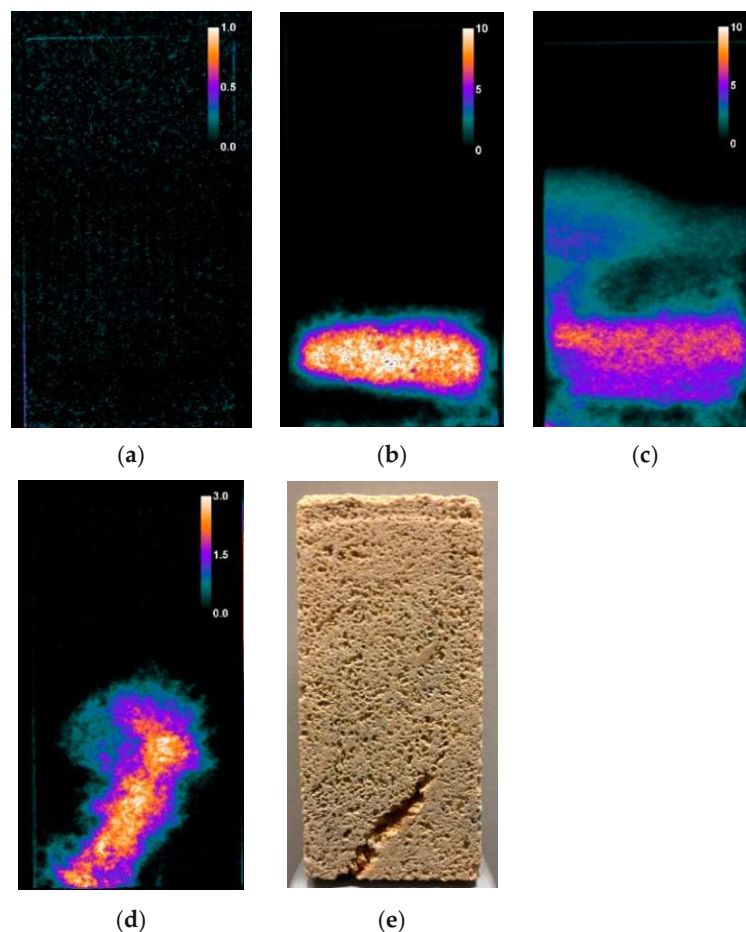


Figure 7. St. Margarethen Limestone radiographs recorded after 30 min of water absorption by capillarity and displaying the water amount in wt. % for specimens treated with NC-25C by (a) capillary absorption, (b) brushing and (c) poultice. A radiograph (d) displays the water absorption by capillarity in the presence of a vugular porosity and (e) the so-called vugs, which are large cavities in a natural stone, usually exhibiting mineral precipitants on the pore walls.

The apparent hydrophobicity present due to an incomplete reaction could also be confirmed by the amount of consolidant absorbed and deposited, which was recorded gravimetrically (Figure 5). The mass percentage of the silica gel that formed after curing could be calculated, but only when

complete hydrolysis and condensation took place, which in the present study was not the case. Incomplete reactions lead to higher values, as can particularly be seen in the case of samples labelled as over-consolidated (C_NC-25C_Oc). It can be supposed that the over-consolidation of specimens retarded the polymerisation. However, at the present moment it is not clear if the delay of the polymerisation was caused solely by the amount of consolidant applied, or possible pore-clogging caused by repetitive treatments—where gelation has already started but a second application cycle was performed onto the already gelled surfaces. In any case, the results indicate that an important factor for reaction kinetics is the amount of product applied. To further enhance our understanding of this, it would be desirable to study the reaction kinetics of consolidated stone exposed to different environmental conditions in terms of temperature and relative humidity, and with respect to varying amounts of consolidants applied on different substrates.

In view of the above observations, it is suggested that the stone fabric plays a decisive role in the polymerisation process, as it can accommodate different amounts of consolidants, which in turn lead to different reaction kinetics. Recent studies by Sena da Fonseca et al. [53] have demonstrated that the silica gel formed in carbonate substrates exhibit poor structural features due to the stone composition, and an in-depth gradient of the polymerisation mechanisms was evident. St. Margarethen Limestone also displays a gradient of polymerisation that is indirectly evident through the amount of water absorbed. Moreover, St. Margarethen Limestone displays anomalous water distributions, evident to a higher degree than can be observed in the more homogeneous silicate variety Schlaitdorf (comparison of the same application techniques on the two studied substrates can be seen in Figure 7b,c and Figure 8b,c). This effect can be ascribed to the different structural features of the studied lithotypes.

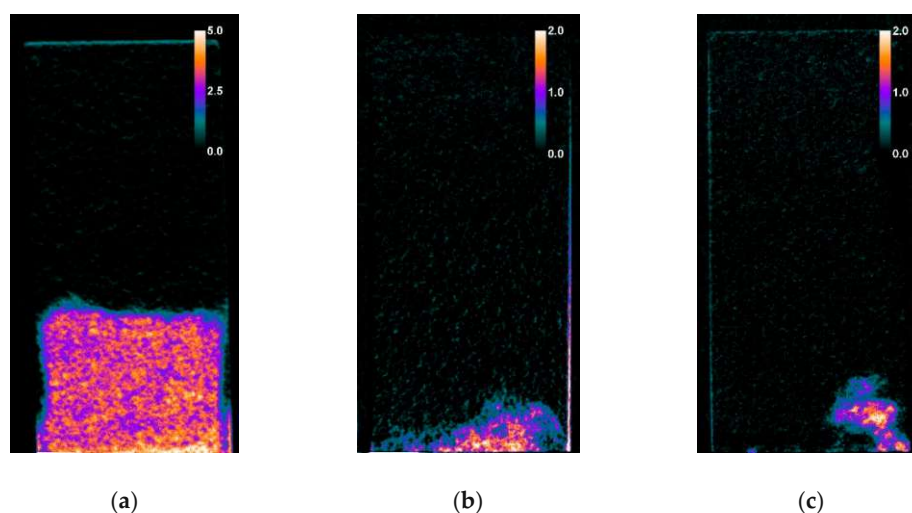


Figure 8. Radiographs of Schlaitdorf Sandstone recorded at 30 min of water absorption by capillarity for specimens treated with NC-25C by (a) capillary absorption, (b) brushing and (c) poultice. The calibration bar displays the water amount in wt. %.

The results concerning the Schlaitdorf Sandstone in many regards overlap with the above-mentioned observations concerning St. Margarethen Limestone. With this stone variety, reaction time differences also resulted from different amounts of applied product. For specimens treated with NC-25C, all three application methods allowed the same amount of product to be absorbed by the stone (see Figure 5b and compare C_NC-25C, B_NC-25C and P_NC-25C). This kind of behaviour cannot be observed with St. Margarethen Limestone, and thus can be viewed as a substrate-dependent characteristic of Schlaitdorf Sandstone. The same behaviour for both lithotypes can be seen within the overconsolidated set of specimens, wherein the amount of deposited consolidant does not represent a complete polymerisation, and thus the values of the deposited amount of consolidant are overestimated. Schlaitdorf Sandstone exhibits a slightly faster polymerisation in

specimens treated by capillary absorption, which was observed in one out of three studied specimens (Figure 8a). Brushing and poultice caused a more pronounced clogging of the pores, so that water penetrated through small, unconsolidated or already polymerised passages in minor amounts.

The water absorption curves obtained from neutron radiography, as shown in Figure 6, are an average of the entire sample width-depth as a function of the height. The same kind of averaging is present within gravimetrically recorded samples. Imaging proves to be a great added value, because, by qualitative, visual analysis of the radiographs, a more profound discussion of the measured values is possible. Locally, increased amounts of water could be found (compare Figure 6, showing the kinetics of three St. Margarethen specimens treated with brushing, and Figure 7b, showing one radiograph where this kinetic was extracted from). Neutron radiography proved to be a valuable tool to examine anomalous water distributions with a strong gradient of water quantities in the stone, which relates to a gradient in polymerisation.

The optimal curing conditions until complete polymerisation, namely 20 °C and 50% relative humidity for four weeks, can rarely be met in time, which is why treatments with alkoxysilanes must be carefully evaluated, as the outcome of treatment performance is multi-dependent and evolves in time as a function of the substrate, temperature, relative humidity, amount of product and the application method employed. Moreover, the role of sample pre-conditioning in the speed of the chemical reaction is unknown and should be further investigated. That is, laboratory storage before the treatment application should be avoided, because the equilibrium humidity inside the stone structure plays a central role in the initiation of the hydrolysis.

3.3. Evaluation of Treatment Application with Nano-SiO₂ Consolidation on St. Margarethen Limestone and Schlaitdorf Sandstone

Radiographs of samples treated with NC-12C are easier to interpret. As this consolidant is non-reactive, the application technique used, and thus the amount of product deposited, in St. Margarethen Limestone leads to marginal changes with respect to water absorption by capillarity (typical radiographs can be seen in Supplementary Materials in Figure S2). This is a clear advantage of such consolidants when compared to reactive systems like TEOS, at least in the initial stage after the treatment application. As soon as the solvent evaporates, the nano-particles aggregate and strengthen the stone, thus follow-up restoration and conservation activities can be implemented immediately afterwards. The latter is not possible with TEOS until the apparent hydrophobicity vanishes.

However, it was observed that the set of samples treated with poultice displayed the highest spread of results and anomalous water kinetics, indicating an inhomogeneous product deposition inside St. Margarethen Limestone when compared to the brushing and capillary absorption techniques (Figure 9). Even with the observed differences in kinetics, all three application methods are relatively comparable and display a negligible impact on the water behaviour of consolidated specimens. The nano-particle based systems can be applied in most environmental conditions if proper aftercare is provided (i.e., sun protection, rain coverage, etc.). Moreover, re-application and cyclic treatments are more likely to succeed within such systems. Finally, pre-wetting with the corresponding solvent prior to consolidation seems to have an insignificant impact on the outcome for the given specimen dimensions. Therefore, such pre-treatments for the product NC-12C are safe to perform, as they might reduce the glossiness on the surface. However, as a consequence of pre-wetting, smaller amounts of nanoparticles could be deposited inside the stone, because it dilutes the active content of the consolidant.

Schlaitdorf Sandstone consolidated with NC-12C exhibits similar properties to the carbonate variety St Margarethen Limestone. A comparable amount of product is deposited despite the three different application techniques. The latter is a characteristic attributed to the structure of Schlaitdorf Sandstone, and differs entirely from St. Margarethen Limestone where the amount of adsorbed consolidant depends upon the application technique used (compare the values in Figure 5). The nano-silica consolidation slows down the capillary water absorption, with comparable trends among application techniques (compare the sound set of specimens in Figure 4c with the Figure 9

bottom graphs). However, based on water absorption profiles extracted from neutron imaging, it can be noticed that the water behaviour was more homogenous in specimens treated by capillary absorption. Brushing and poultice is less favoured, as the widespread nature of the results indicates a more inhomogeneous behaviour of water kinetics caused by the treatment application.

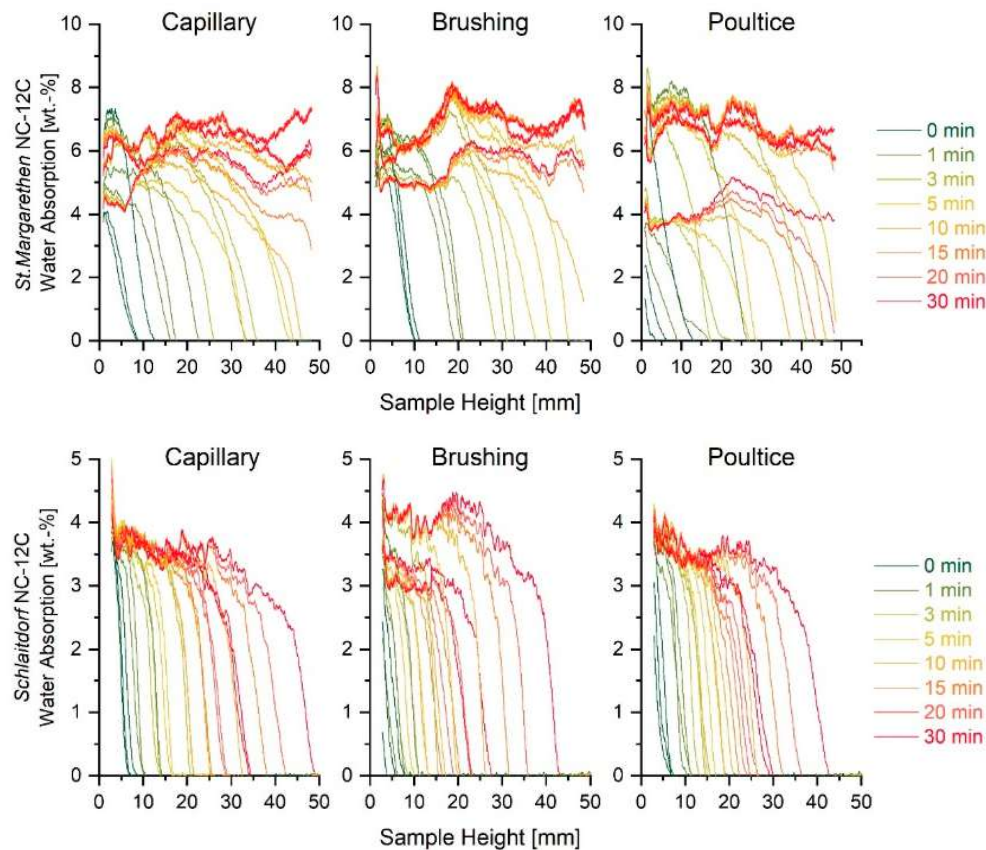


Figure 9. The top graph displays water absorption kinetics reported in weight percentage for St. Margarethen Limestone treated with NC-12C, while the bottom graph displays the kinetics of water absorption by capillarity for Schlaitdorf Sandstone, also treated with NC-12C.

3.4. Cross-Validation of Neutron Radiography with the Water Absorption Coefficient and Ultrasonic Pulse Velocity

To cross validate the water absorption by capillarity, monitored by neutron radiography, the WAC calculated from the laboratory mass increase, as well as UPV, were determined on the same specimens. The comparative values displayed in Figure 10a,b show that there is a clear trend between all tests employed to study alterations caused by the treatment application. When the WAC increased, UPV decreased accordingly. As already mentioned above, the slight difference between absolute values reported for the WAC gained from neutron radiography and laboratory-based gravimetric results can be explained through averaging when image analysis is used. The impact of the advanced polymerisation is visible in the WAC values, based on gravimetrically determined laboratory studies. Those values evolved over time, thus suggesting a more advanced chemical reaction, when compared to the WAC obtained through neutron radiography. The latter effect is evident when comparing calculations from neutrons and laboratory studies of NC-12C with NC-25C values. This comes as no surprise, as these tests were performed eight weeks after consolidation and the specimens had already been in contact with water through previous water absorption tests when the neutron radiographs were acquired.

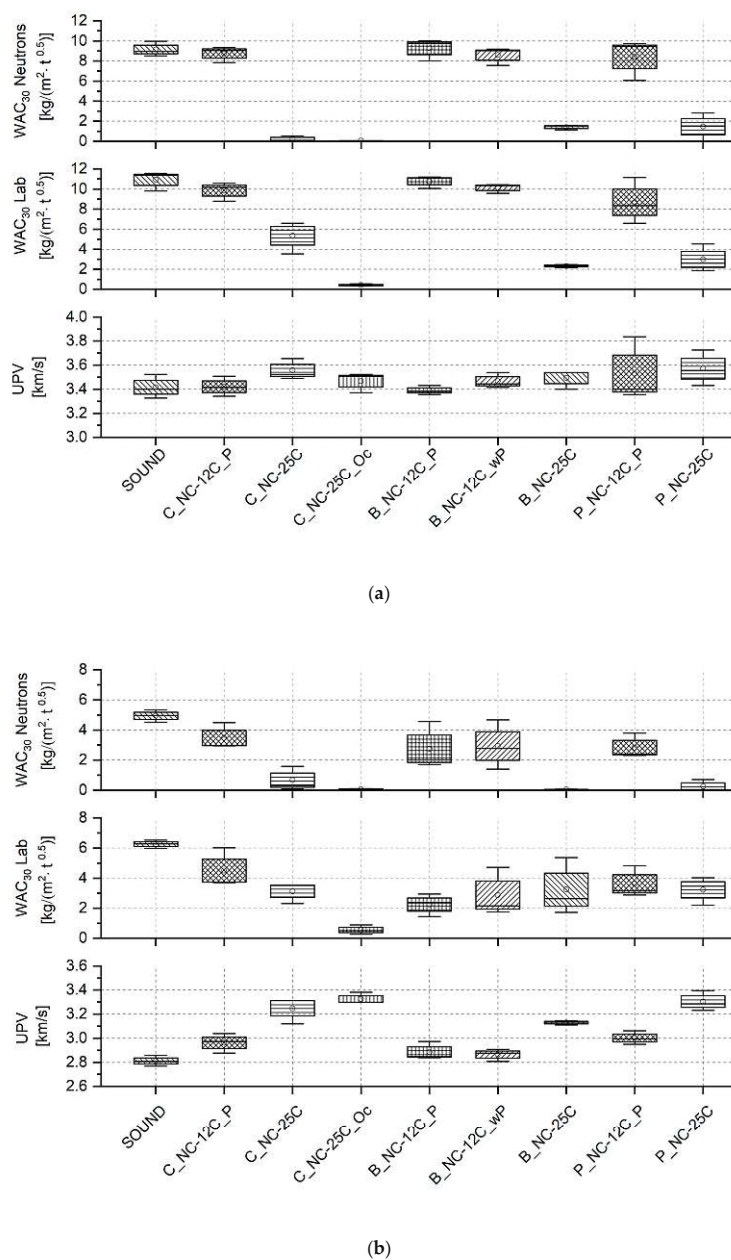


Figure 10. Comparative graph displaying water absorption coefficients reported as $[\text{kg}/(\text{m}^2 \cdot \text{t}^{0.5})]$ after 30 min for (a) St. Margarethen Limestone and (b) Schlaitdorf Sandstone, calculated from (top) neutron radiography and (middle) gravimetrically determined laboratory studies, and compared to values of (bottom) ultrasonic pulse velocity reported in $[\text{km}/\text{s}]$. Corresponding numerical values of the graphical representation can be extracted from Supplementary Materials, Table S2. Moreover, all water absorption curves extracted from neutron radiographs can be seen in Supplementary Materials, Figure S3 (St. Margarethen Limestone) and Figure S4 (Schlaitdorf Sandstone).

One of the main findings is that, in order to study petrophysical changes caused by treatment application by means of neutron radiography, sound samples proved to be convenient. However, the use of sound stone specimens to evaluate the efficacy of a consolidant should be discarded. The reason for this is evident in the comparative graph, because the increase in UPV is minor and can be misinterpreted. Such a slight increase does not rest solely on the treatment's performance, but rather on the conditions of the substrate under study. The hypothesis is that when a sound stone is consolidated, the product will precipitate inside the pores but might not influence the grain contacts, as

these will be intact in a freshly quarried specimen. Thus, the fastest way for a sound wave to propagate through the sample might still be the same as before the consolidation, since the grain contacts were not affected. Therefore, if mechanical strength gain is the subject of study, it is recommended to artificially age and subsequently consolidate specimens and compare those two states with each other. Only in this way can the potential of the consolidant's efficiency, which is defined as the restoration of the mechanical strength of the material, be obtained.

Regarding Schlaitdorf Sandstone, the values of UPV are higher in magnitude when compared to St. Margarethen Limestone. The reason for such a behaviour lies in its micro-texture, which was already reported in a previous study [40]. The consolidation of the clayey matrix, which is homogeneously deposited between the grains of Schlaitdorf Sandstone, lead to a faster propagation of the sound wave, and thus higher values after consolidation. The consolidant NC-25C had a higher impact on the velocity, indicating a higher efficiency than the nano-particle based NC-12C. Moreover, an increase in the amount of applied consolidant resulted in an increase in UPV; thus, higher efficiency is the result. The latter also demonstrates that the efficiency and compatibility of treatments will depend on the amount of applied consolidant.

The water absorption curves are more complicated to interpret when the stone specimens are consolidated, especially when reactive treatments are present. Figure 11b,c displays two curves, depicted as part (i) and (ii) in the graphs, which correspond to changes in slope and thus in water absorption kinetics. For both cases, it can be observed that the water absorption increased steadily, and after five minutes a speed increase of the capillary suction took place. The accelerated water absorption rate, represented as part (ii) where the slope increases, represents a phenomenon where a greater pore volume contributes to the suction and increases the slope. Figure 11d represents a water absorption curve of a hydrophobic specimen, where water is initially absorbed on the surface (measurement at 1 min) and diffuses gradually with time. In the latter case, the magnitude of absorbed water per surface area displays the water repellence or hindrance of the stone specimen. The evolution of water absorption kinetics as the polymerisation proceeds should be investigated more in depth by means of neutron radiography and additional laboratory water-based methods.

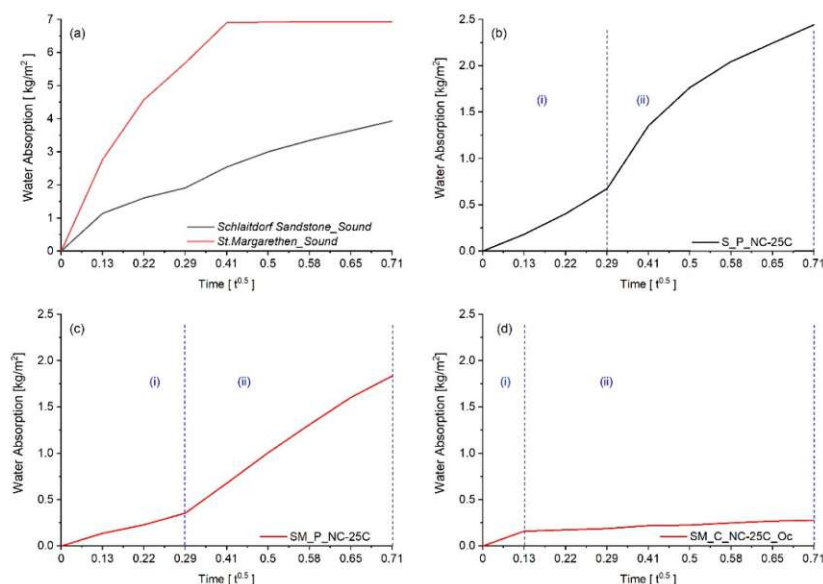


Figure 11. Examples of water absorption curves after 30 min (here reported as the square root of time in hours), extracted from gravimetric monitoring. Graph (a) represents absorption curves from sound stone specimens, (b) Schlaitdorf Sandstone, (c) St. Margarethen Limestone where the consolidant NC-25C was applied by poultice and (d) a specimen of St. Margarethen Limestone representing the over-consolidation attained by a repetitive capillary absorption of NC-25C.

4. Conclusions

Weathering is known to cause a loss of grain cohesion, and thus a reduction of mechanical strength in monumental stone. To regain the lost cohesion, stone consolidants are frequently applied. In the present study, neutron radiography was used to monitor water absorption by capillarity, and to analyse possible alterations caused by artificial ageing of stone and three treatment applications, applied on two different substrates and treated with two consolidants.

The results show that artificially aged or heat-treated stone specimens must not be used when physical changes are studied, as the impact seen by neutron radiography is limited. On the contrary, when studying mechanical strength changes, artificial ageing is a prerequisite in order to study the efficiency of stone consolidants, as findings with UPV demonstrate. When grain contacts are not affected, as is the case in a sound material, the consolidation efficiency will yield underestimated values, which are not representative of the capability of the consolidant to strengthen the substrate.

Concerning the evaluation of treatment applications with stone consolidants by means of neutron radiography, the results reveal that the amount of product applied, and therefore the application technique used, is relevant when using a reactive system like NC-25C—the nano-titania doped tetraethyl-orthosilicate. On the contrary, the nano-silica-based consolidant NC-12C shows comparable results regarding water absorption kinetics regardless of the substrate or treatment application used. For the reactive system NC-25C, different amounts of product applied result in different speeds of chemical reaction, which makes the nano-based consolidant NC-12C more favourable for on-site work. However, the advantage of NC-25C is the higher mechanical strength when compared to NC-12C, as observed by UPV. The differences in the degree of polymerisation are particularly visible on the carbonate variety St. Margarethen Limestone, ranging from water repellence to anomalous water kinetics ascribed to partial polymerisation and initiated in the inner core of the stone specimens. In the latter case, when NC-25C was applied by brushing and poultice, pore clogging in the sub surface area and water trapping, as well as anomalous capillary absorption, were recorded.

Neutron radiography proved to be an excellent tool for dynamic observations of the inner pathways of adsorbed water in a consolidated substrate. It gave insights on the effects of stone texture and structure, the preferential pathways of water being absorbed and distributed throughout the material, which is relevant in determining the final behaviour that cannot be revealed by simple lab-based water absorption tests. While WAC is simply averaging all phenomena and quantities, neutron radiography allowed to see localised quantities, the degree of spreading of the same and the kinetics of those processes. Without neutron imaging, the present study would not be able to observe that the amount of absorbed water in aged samples was higher, but that the speed in some lithotypes and localities slowed down. Furthermore, it would have been impossible to observe that the polymerisation was initiated inside the stone while the outer surfaces were still mostly hydrophobic. Moreover, the vugular porosity that is texturally different from the surrounding structure of the stone indeed represented a preferential pathway for the water in a consolidated stone. Additionally, if the specimens seemed hydrophobic, there was a small passage where the water penetrated into the depth of the stone and did not just stay in the surface zone. All those conclusions would not have been possible without the use of neutron imaging.

The present study focused on two porous lithotypes, but in order to draw wider conclusions relevant to the field and to possibly establish guidelines for treatment applications, the same experimental set-up should be employed on additional lithotypes and with additional consolidating materials. Variation of the amount of consolidant applied, the studied time span after treatment application and different curing conditions should be considered for further studies. Moreover, other application techniques should also be analysed, as well as lithotypes with different natural and artificial decay patterns.

Supplementary Materials: The following are available online at <http://www.mdpi.com/2079-4991/9/4/635/s1>, Figure S1. The upper plot displays the temperature (°C) and relative humidity (%), recorded once per day in the city centre of Pisa, Italy during May 2018. The bottom plot shows the monitored weight of consolidated

St. Margarethen Limestone and Schlaitdorf Sandstone stone specimens. An average of three specimens is shown for each treatment and lithotype. The labelling C_NC-25C stands for treatment application by capillary absorption with nano-titania modified tetraethyl-orthosilicate, while P_NC-12C_P stands for treatment by poultice, pre-wetted by ethanol prior to treatment application. Table S1. Water absorption coefficient [$\text{kg}/(\text{m}^2 \cdot \text{t}^{0.5})$] after 30 min calculated from neutron imaging and gravimetric laboratory analysis as well as ultrasonic pulse velocity [km/s] before (sound) and after artificial ageing (aged) for St. Margarethen Limestone and Schlaitdorf Sandstone. Average data of three stone specimens. Figure S2. Normalised images of sound (top) and consolidated (bottom) St. Margarethen Limestone with the nano-silica consolidant (NC-12C) applied by brushing. Table S2. Comparative graph displaying water absorption coefficients after 30 min [$\text{kg}/(\text{m}^2 \cdot \text{t}^{0.5})$] calculated from neutron radiography and laboratory tests by gravimetric means and compared with ultrasonic pulse velocity [km/s] for St. Margarethen Limestone and Schlaitdorf Sandstone. Figure S3. Water absorption (wt. %) extracted from neutron radiography scans on three specimens per lithotype and condition (sound, aged, consolidated). Figure S4. Water absorption (wt. %) extracted from neutron radiography scans on three specimens per lithotype and condition (sound, aged, consolidated).

Author Contributions: M.B. and S.R. designed the experiments; A.R. performed the petrographic analysis of thin sections; S.R. carried out the treatments application and monitored the curing procedure; M.B., T.D.K. and S.R. performed the experiments at LLB under the supervision of F.O.; M.B. and S.R. pre- and post-processed the gained radiographs; T.D.K. obtained the calibration, analysed and plotted the post-processed data; M.B. performed the UPV and WAC measurements in the laboratory; M.B. performed the visualization of the obtained results and created the tables; M.B., T.D.K. and S.R. prepared the original draft; all authors reviewed and edited as well as agreed on the last version of the manuscript; G.B. and S.R. was responsible for proposal administration at the LLB facility.

Funding: The authors acknowledge the TU Wien University Library for financial support through its Open Access Funding Programme.

Acknowledgments: Sofia Zamfirescu is gratefully acknowledged for helping with ultrasonic pulse velocity and Eleonora Odelli for her help with the micrographs. José Teixeira and Johannes Weber are gratefully acknowledged for proofreading and generally supporting this paper. The authors thank Colorobbia S.P.A., Chem Spec S.R.L and Tecnan for the supplied consolidants. Tim De Kock is a postdoctoral fellow of the FWO (Research Foundation-Flanders) and acknowledges its support.

Conflicts of Interest: The authors declare no conflict of interest.

References

1. Verges-Belmin, V. *Illustrated Glossary on Stone Deterioration Patterns*; International Scientific Committee for Stone (ICOMOS-ISCS): Paris, France, 2008.
2. Sassoni, E.; D'Amen, E.; Roveri, N.; Scherer, G.W.; Franzoni, E. Durable Self-Cleaning Coatings for Architectural Surfaces by Incorporation of TiO_2 Nano-Particles into Hydroxyapatite Films. *Materials* **2018**, *11*, 177. [[CrossRef](#)] [[PubMed](#)]
3. Ruffolo, S.A.; Ricca, M.; Macchia, A.; La Russa, M.F. Antifouling coatings for underwater archaeological stone materials. *Prog. Org. Coat.* **2017**, *104*, 64–71. [[CrossRef](#)]
4. Kapridaki, C.; Maravelaki-Kalaitzaki, P. TiO_2 - SiO_2 -PDMS nano-composite hydrophobic coating with self-cleaning properties for marble protection. *Prog. Org. Coat.* **2013**, *76*, 400–410. [[CrossRef](#)]
5. Vidakovic, A.M.; Ranogajec, J.G.; Markov, S.L.; Loncar, E.S.; Hirszenberger, H.M.; Skapin, A.S. Synergistic effect of the consolidant and the photocatalytic coating on antifungal activity of porous mineral substrates. *J. Cult. Herit.* **2017**, *24*, 1–8. [[CrossRef](#)]
6. van der Werf, I.D.; Ditaranto, N.; Picca, R.A.; Sportelli, M.C.; Sabbatini, L. Development of a novel conservation treatment of stone monuments with bioactive nanocomposites. *Herit. Sci.* **2015**, *3*. [[CrossRef](#)]
7. Delgado Rodrigues, J.; Grossi, A. Indicators and ratings for the compatibility assessment of conservation actions. *J. Cult. Herit.* **2007**, *8*, 32–43. [[CrossRef](#)]
8. Ferreira Pinto, A.; Delgado Rodrigues, J. Stone consolidation: The role of treatment procedures. *J. Cult. Herit.* **2008**, *9*, 38–53. [[CrossRef](#)]
9. Franzoni, E.; Sassoni, E.; Scherer, G.W.; Naidu, S. Artificial weathering of stone by heating. *J. Cult. Herit.* **2013**, *14*, E85–E93. [[CrossRef](#)]
10. Ban, M.; Baragona, A.; Ghaffari, E.; Weber, J.; Rohatsch, A. Artificial aging techniques on various lithotypes for testing of stone consolidants. In *Science and Art: A Future for Stone: Proceedings of the 13th International Congress on the Deterioration and Conservation of Stone, Volume 1*; Hughes, J., Howind, T., Eds.; University of the West of Scotland: Paisley, UK, 2016; pp. 253–260.

11. Lubelli, B.; Cnudde, V.; Diaz-Goncalves, T.; Franzoni, E.; van Hees, R.P.J.; Ioannou, I.; Menendez, B.; Nunes, C.; Siedel, H.; Stefanidou, M.; et al. Towards a more effective and reliable salt crystallization test for porous building materials: State of the art. *Mater. Struct.* **2018**, *51*. [[CrossRef](#)]
12. Franzoni, E.; Sassoni, E.; Graziani, G. Brushing, poultice or immersion? The role of the application technique on the performance of a novel hydroxyapatite-based consolidating treatment for limestone. *J. Cult. Herit.* **2015**, *16*, 173–184. [[CrossRef](#)]
13. Bracci, S.; Sacchi, B.; Ferreira Pinto, A.P.; Delgado Rodrigues, J. Inorganic consolidants on stone artefacts: Optimisation of application procedures for marble and limestones. In *International Symposium on Stone Consolidation in Cultural Heritage—Research and Practice*; Delgado Rodrigues, J., Mimoso, J.M., Eds.; LNEC: Lisbon, Portugal, 2008; pp. 81–90.
14. Ferreira Pinto, A.P.; Delgado Rodrigues, J. Consolidation of carbonate stones: Influence of treatment procedures on the strengthening action of consolidants. *J. Cult. Herit.* **2012**, *13*, 154–166. [[CrossRef](#)]
15. Ban, M.; Pliessnig, M. The Biedermeier cemetery of St Marx in Vienna: Planning, management and treatment implementation. In *Conservation of Sculpture Parks*; Archetype Publications Ltd.: London, UK, 2018; pp. 59–72.
16. Facio, D.S.; Ordonez, J.A.; Gil, M.L.A.; Carrascosa, L.A.M.; Mosquera, M.J. New Consolidant-Hydrophobic Treatment by Combining SiO₂ Composite and Fluorinated Alkoxysilane: Application on Decayed Biocalcareous Stone from an 18th Century Cathedral. *Coatings* **2018**, *8*, 170. [[CrossRef](#)]
17. Ziegenbalg, G.; Drdácák, M.; Dietze, C.; Schuch, D. *Nanomaterials in Architecture and Art Conservation*; Jenny Stanford Publishing Pte. Ltd.: Singapore, 2018.
18. Raneri, S.; Barone, G.; Mazzoleni, P.; Alfieri, I.; Bergamonti, L.; De Kock, T.; Cnudde, V.; Lottici, P.P.; Lorenzi, A.; Predieri, G.; et al. Efficiency assessment of hybrid coatings for natural building stones: Advanced and multi-scale laboratory investigation. *Constr. Build. Mater.* **2018**, *180*, 412–424. [[CrossRef](#)]
19. Braun, F.; Orłowski, J. Effect of Different Silicic Acid Ester on the Properties of Sandstones with Varying Binders. *Restor. Build. Monum.* **2018**, *23*, 1–13. [[CrossRef](#)]
20. De Clercq, H.; De Zanche, S.; Biscontin, G. TEOS and time: The influence of application schedules on the effectiveness of ethyl silicate based Consolidants/Tetraethoxysilan (TEOS) und die Zeit: Der Einfluss unterschiedlicher Anwendungsfolgen auf die Wirksamkeit von Steinfestigern auf der basis von Ethylsilikat. *Restor. Build. Monum.* **2007**, *13*, 305–318. [[CrossRef](#)]
21. Rodriguez-Navarro, C.; Suzuki, A.; Ruiz-Agudo, E. Alcohol dispersions of calcium hydroxide nanoparticles for stone conservation. *Langmuir* **2013**, *29*, 11457–11470. [[CrossRef](#)]
22. Coltelli, M.B.; Paolucci, D.; Castelvetro, V.; Bianchi, S.; Mascha, E.; Panariello, L.; Pesce, C.; Weber, J.; Lazzeri, A. Preparation of Water Suspensions of Nanocalcite for Cultural Heritage Applications. *Nanomaterials* **2018**, *8*, 254. [[CrossRef](#)] [[PubMed](#)]
23. Abbate, M.; D’Orazio, L. Water Diffusion through a Titanium Dioxide/Poly(Carbonate Urethane) Nanocomposite for Protecting Cultural Heritage: Interactions and Viscoelastic Behavior. *Nanomaterials* **2017**, *7*, 271. [[CrossRef](#)]
24. Gherardi, F.; Goidanich, S.; Dal Santo, V.; Toniolo, L. Layered Nano-TiO₂ Based Treatments for the Maintenance of Natural Stones in Historical Architecture. *Angew. Chem.* **2018**, *130*, 7482–7485. [[CrossRef](#)]
25. Sierra-Fernandez, A.; De la Rosa-García, S.C.; Gomez-Villalba, L.S.; Gómez-Cornelio, S.; Rabanal, M.E.; Fort, R.; Quintana, P. Synthesis, photocatalytic, and antifungal properties of MgO, ZnO and Zn/Mg oxide nanoparticles for the protection of calcareous stone heritage. *ACS Appl. Mater. Interfaces* **2017**, *9*, 24873–24886. [[CrossRef](#)] [[PubMed](#)]
26. Zornoza-Indart, A.; Lopez-Arce, P. Silica nanoparticles (SiO₂): Influence of relative humidity in stone consolidation. *J. Cult. Herit.* **2016**, *18*, 258–270. [[CrossRef](#)]
27. Miliani, C.; Velo-Simpson, M.L.; Scherer, G.W. Particle-modified consolidants: A study on the effect of particles on solegel properties and consolidation effectiveness. *J. Cult. Herit.* **2007**, *8*, 1–6. [[CrossRef](#)]
28. Cavallaro, G.; Milioto, S.; Parisi, F.; Lazzara, G. Halloysite nanotubes loaded with calcium hydroxide: Alkaline fillers for the deacidification of waterlogged archeological woods. *ACS Appl. Mater. Interfaces* **2018**, *10*, 27355–27364. [[CrossRef](#)] [[PubMed](#)]
29. Cavallaro, G.; Danilushkina, A.A.; Evtugyn, V.G.; Lazzara, G.; Milioto, S.; Parisi, F.; Rozhina, E.V.; Fakhrullin, R.F. Halloysite Nanotubes: Controlled Access and Release by Smart Gates. *Nanomaterials* **2017**, *7*, 199. [[CrossRef](#)]

30. Wheeler, G.; Goins, E.S. *Alkoxysilanes and the Consolidation of Stone*; Getty Publications: Los Angeles, CA, USA, 2005; pp. 17 and 76.
31. Pummer, E. Vacuum-circulation-process: Innovative stone conservation. In Proceedings of the 11th International Congress on Deterioration and Conservation of Stone, Torun, Poland, 15–20 September 2008; pp. 481–488.
32. Milchin, M.; Weber, J.; Krist, G.; Ghaffari, E.; Karacsonyi, S. Ethyl-silicate consolidation for porous limestone coated with oil paint—A comparison of application methods. In *Science and Art: A Future for Stone, Proceedings of the 13th International Congress on the Deterioration and Conservation of Stone, Volume 2*; Hughes, J., Howind, T., Eds.; University of the West of Scotland: Paisley, UK, 2016; pp. 889–896.
33. Vandevoorde, D.; Cnudde, V.; Dewanckele, J.; Brabant, L.; de Bouw, M.; Meynen, V.; Verhaeven, E. Validation of in situ applicable measuring techniques for analysis of the water adsorption by stone. *Procedia Chem.* **2013**, *8*, 317–327. [[CrossRef](#)]
34. Peruzzi, R.; Poli, T.; Toniolo, L. The experimental test for the evaluation of protective treatments: A critical survey of the “capillary absorption index”. *J. Cult. Herit.* **2003**, *4*, 251–254. [[CrossRef](#)]
35. Perfect, E.; Cheng, C.L.; Kang, M.; Bilheux, H.Z.; Lamanna, J.M.; Gragg, M.J.; Wright, D.M. Neutron imaging of hydrogen-rich fluids in geomaterials and engineered porous media: A review. *Earth-Sci. Rev.* **2014**, *129*, 120–135. [[CrossRef](#)]
36. Graziani, G.; Colombo, C.; Conti, C.; Possenti, E.; Perelli Cippo, E.; Realini, M.; Sassoni, E. Neutron radiography as a tool for assessing penetration depth and distribution of a phosphate consolidant for limestone. *Constr. Build. Mater.* **2018**, *187*, 238–247. [[CrossRef](#)]
37. Hameed, F.; Schillinger, B.; Rohatsch, A.; Zawisky, M.; Rauch, H. Investigations of stone consolidants by neutron imaging. *Nuclear Instrum. Methods Phys. Res. Sect. A* **2009**, *605*, 150–153. [[CrossRef](#)]
38. Alba-Simionesco, C.; Menelle, A.; Visticot, J.P. The Laboratoire Léon Brillouin and the Orphée Reactor: The French National Neutron Facility. *Neutron News* **2011**, *22*, 10–13. [[CrossRef](#)]
39. Lazzeri, A.; Coltelli, M.B.; Castelvetro, V.; Bianchi, S.; Chiantore, O.; Lezzerini, M.; Niccolai, L.; Weber, J.; Rohatsch, A.; Gherardi, F. European Project “NANO-CATHEDRAL: Nanomaterials for conservation of European architectural heritage developed by research on characteristic lithotypes”. In *13th International Congress on the Deterioration and Conservation of Stone, Volume 1*; Hughes, J., Howind, T., Eds.; University of the West of Scotland: Paisley, UK, 2016; pp. 847–854.
40. Ban, M.; Mascha, E.; Weber, J.; Rohatsch, A.; Rodrigues, J.D. Efficiency and Compatibility of Selected Alkoxysilanes on Porous Carbonate and Silicate Stones. *Materials* **2019**, *12*, 156. [[CrossRef](#)]
41. Dunham, R.J. Classification of carbonate rocks according to depositional textures. *Am. Assoc. Pet. Geol.* **1962**, *1*, 108–121.
42. Graue, B.; Siegesmund, S.; Middendorf, B. Quality assessment of replacement stones for the Cologne Cathedral: Mineralogical and petrophysical requirements. *Environ. Earth. Sci.* **2011**, *63*, 1799–1822. [[CrossRef](#)]
43. Sierra-Fernandez, A.; Gomez-Villalba, L.S.; Rabanal, M.E.; Fort, R. New nanomaterials for applications in conservation and restoration of stony materials: A review. *Mater. Constr.* **2017**, *67*. [[CrossRef](#)]
44. Franzoni, E.; Graziani, G.; Sassoni, E.; Bacilieri, G.; Griffa, M.; Lura, P. Solvent-based ethyl silicate for stone consolidation: Influence of the application technique on penetration depth, efficacy and pore occlusion. *Mater. Struct.* **2015**, *48*, 3503–3515. [[CrossRef](#)]
45. Pugliesi, R.; Pereira, M.A.S.; Schoueri, R.M. Method to evaluate the L/D ratio of neutron imaging beams. *Braz. J. Rad. Sci.* **2017**, *5*, 1. [[CrossRef](#)]
46. Bilheux, H.Z.; McGreevy, R.; Anderson, I.S. (Eds.) *Neutron Imaging and Applications: A Reference for the Imaging Community*; Springer: New York, NY, USA, 2009.
47. Anderson, I.S.; Hurd, A.J.; McGreevy, R.L. (Eds.) *Neutron Scattering Applications and Techniques*; Springer: Berlin, Germany, 2008.
48. Dewanckele, J.; De Kock, T.; Fronteau, G.; Derluyn, H.; Vontobel, P.; Dierick, M.; Van Hoorebeke, L.; Jacobs, P.; Cnudde, V. Neutron radiography and X-ray computed tomography for quantifying weathering and water uptake processes inside porous limestone used as building material. *Mater. Charact.* **2014**, *88*, 86–99. [[CrossRef](#)]

49. Schindelin, J.; Arganda-Carreras, I.; Frise, E.; Kaynig, V.; Longair, M.; Pietzsch, T.; Preibisch, S.; Rueden, C.; Saalfeld, S.; Schmid, B.; et al. Fiji: An open-source platform for biological-image analysis. *Nat. Methods* **2012**, *9*, 676. [[CrossRef](#)]
50. CEN. *Standard EN 14579: Natural Stone Test methods. Determination of Sound Speed Propagation*; European Committee for Standardization (CEN): Brussels, Belgium, 2005.
51. Franzoni, E.; Graziani, G.; Sassoni, E. TEOS-based treatments for stone consolidation: Acceleration of hydrolysis–condensation reactions by poulticing. *J. Solgel Sci. Technol.* **2015**, *74*, 398–405. [[CrossRef](#)]
52. Lukaszewics, J.; Kwiatkowski, D.; Klingspor, M. Consolidation of Gotland stone in monuments. In *Proceedings of the Methods of Evaluating Products for the Conservation of Porous Building Materials in Monuments: Preprints of the International Colloquium, Rome, Italy, 19–21 June 1995*; pp. 179–187.
53. Sena da Fonseca, B.; Ferreira, M.J.; Taryba, M.G.; Piçarra, S.; Ferreira Pinto, A.P.; Montemor, M.d.F. Alkoxysilane-based sols for consolidation of carbonate stones: Impact of the carbonate medium in the sol-gel processes. *J. Cult. Herit.* **2018**. [[CrossRef](#)]



© 2019 by the authors. Licensee MDPI, Basel, Switzerland. This article is an open access article distributed under the terms and conditions of the Creative Commons Attribution (CC BY) license (<http://creativecommons.org/licenses/by/4.0/>).

C

Neutron radiography study of laboratory ageing and
treatment applications with stone consolidants

Supporting Data



Supplementary Materials

Neutron Radiography Study of Laboratory Ageing and Treatment Applications with Stone Consolidants

Matea Ban ^{1,*}, Tim De Kock ², Frédéric Ott ³, Germana Barone ⁴, Andreas Rohatsch ¹ and Simona Raneri ⁵¹ Institute of Geotechnics, Research Centre of Engineering Geology, Vienna University of Technology, 1040 Vienna, Austria; andreas.rohatsch@tuwien.ac.at² Department of Geology, Ghent University, 9000 Ghent, Belgium; Tim.DeKock@UGent.be³ Laboratoire Léon Brillouin, Université Paris-Saclay, Centre d'Etudes de Saclay, 91191 Gif sur Yvette CEDEX, France; Frederic.Ott@cea.fr⁴ Department of Biological, Geological and Environmental Sciences, University of Catania, 95129 Catania, Italy; gbarone@unict.it⁵ Department of Earth Sciences, University of Pisa, 56126 Pisa, Italy; simona.raneri@unipi.it

* Correspondence: matea.ban@tuwien.ac.at; Tel.: +43-158-801-20318

Supplementary Graph for the Section 2.4. Consolidation of Stone: Treatment Procedure and Curing

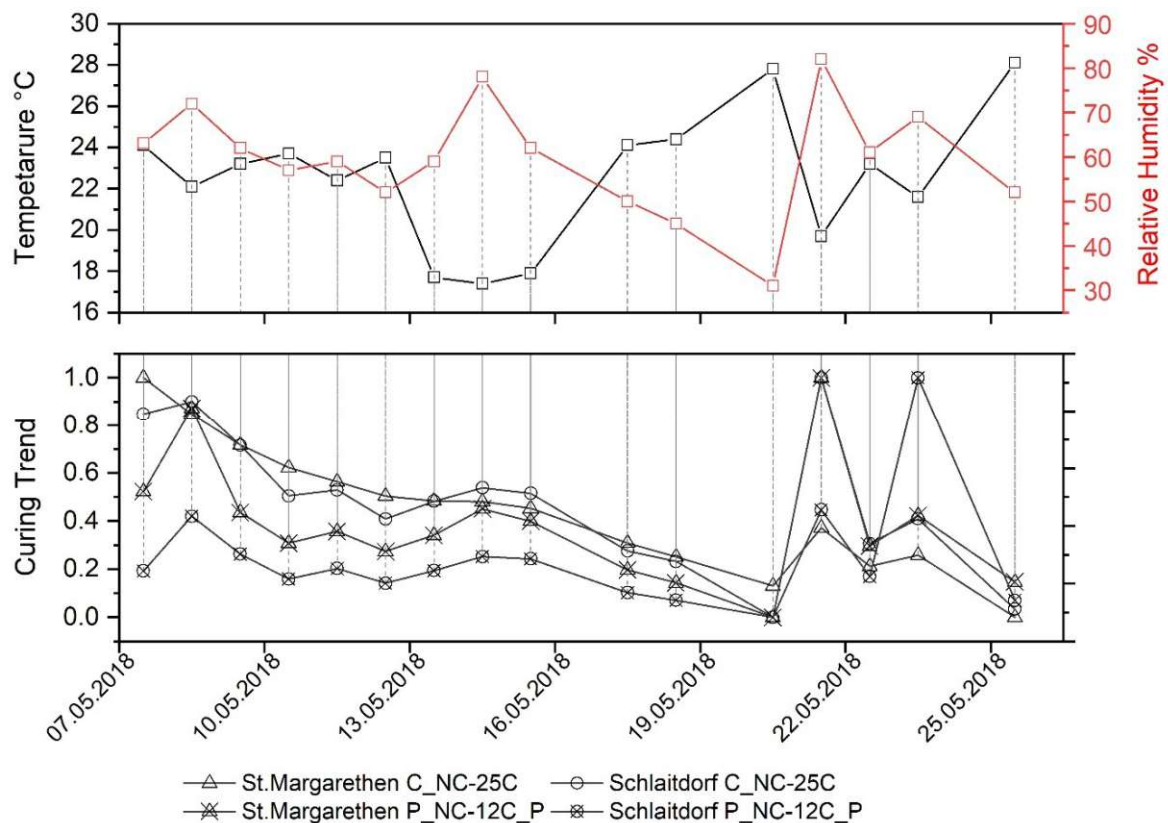


Figure S1. The upper plot displays the temperature (°C) and relative humidity (%), recorded once per day in the city centre of Pisa, Italy during May 2018. The bottom plot shows the monitored weight of consolidated *St. Margarethen Limestone* and *Schlaitdorf Sandstone* stone specimens. An average of three specimens is shown for each treatment and lithotype. The labelling C_NC-25C stands for treatment application by capillary absorption with nano-titania modified tetraethyl-orthosilicate, while P_NC-12C_P stands for treatment by poultice, prewetted by ethanol prior to treatment application.

Supplementary Table for the Section 3.1. Evaluation of the Artificial Ageing

Table S1. Water absorption coefficient [$\text{kg}/(\text{m}^2 \cdot \text{t}^{0.5})$] after 30 minutes calculated from neutron imaging and gravimetrical laboratory analysis as well as ultrasonic pulse velocity [km/s] before (**sound**) and after artificial ageing (**aged**) for *St. Margarethen Limestone* and *Schlaitdorf Sandstone*. Average data of three stone specimens.

<i>St. Margarethen Limestone</i>						
	WAC Neutron Radiography		WAC Laboratory		Ultrasonic Pulse Velocity	
	Sound	Aged	Sound	Aged	Sound	Aged
WAC	9.15	11.36	10.92	12.83	3.42	1.7
SD.N.	± 0.61	± 0.87	± 0.80	± 0.23	± 0.08	± 0.03
<i>Schlaitdorf Sandstone</i>						
	WAC Neutron Radiography		WAC Laboratory		Ultrasonic Pulse Velocity	
	Sound	Aged	Sound	Aged	Sound	Aged
WAC	4.94	5.51	5.75	6.26	2.81	1.74
SD.N.	± 0.34	± 0.41	± 0.18	± 0.22	± 0.04	± 0.01

[1 min] [3 min] [5 min] [10 min] [15 min] [20 min] [25 min] [30 min]

St. Margarethen Limestone Sound



St. Margarethen Limestone B_NC-12C_P

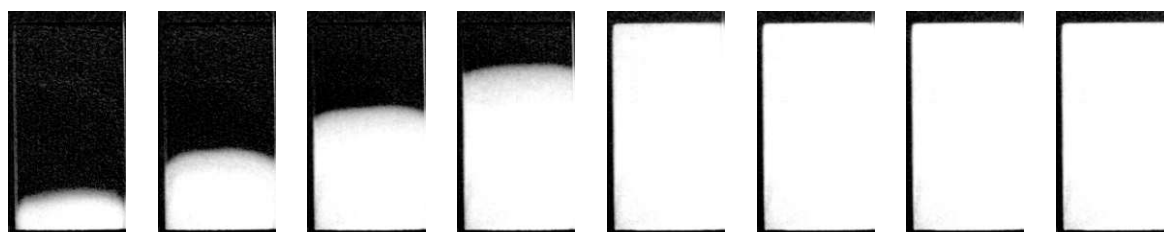


Figure S2. Normalised images of sound (**top**) and consolidated (**bottom**) *St. Margarethen Limestone* with the nano-silica consolidant (NC-12C) applied by brushing.

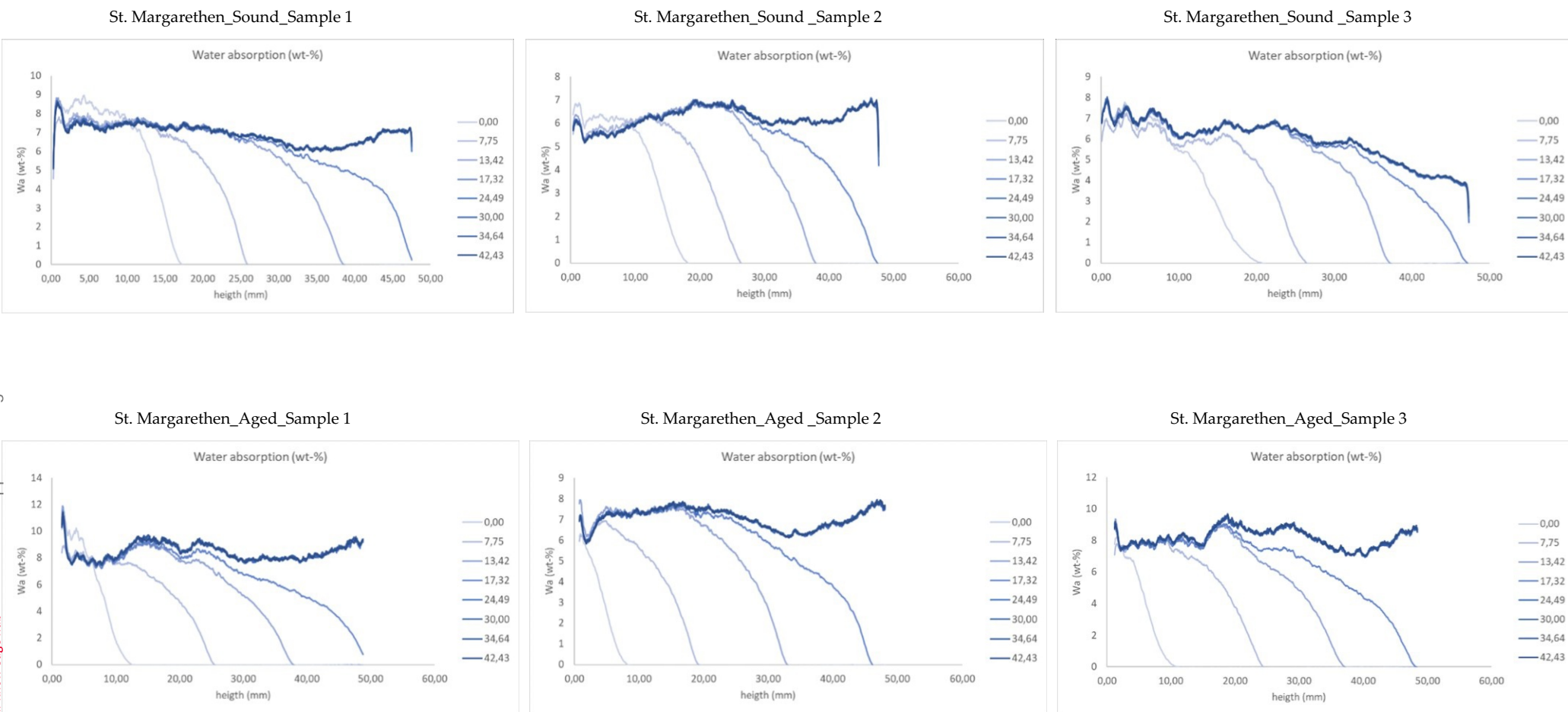
Supplementary Table for the Section 3.4. Cross-Validation of Neutron Radiography with Water Absorption Coefficient and Ultrasonic Pulse Velocity

Table S2. Comparative graph displaying water absorption coefficients after 30 minutes [$\text{kg}/(\text{m}^2 \cdot \text{t}^{0.5})$] calculated from neutron radiography and laboratory tests by gravimetric means and compared with ultrasonic pulse velocity [km/s] for *St. Margarethen Limestone* and *Schlaitdorf Sandstone*.

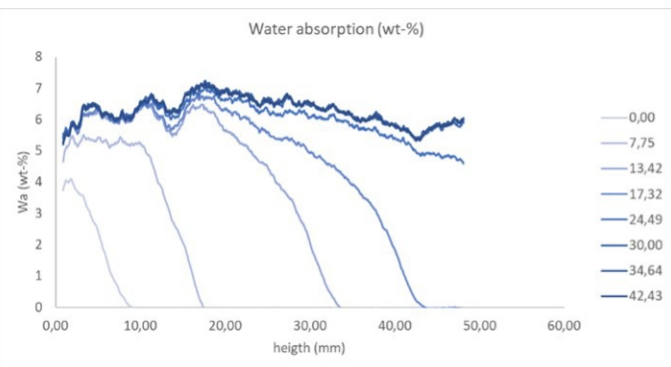
<i>St. Margarethen Limestone</i>									
WAC Neutron Radiography									
		Capillary			Brushing			Poultice	
	SOUND	C_NC-12C_P	C_NC-25C	C_NC-25C_Oc	B_NC-12C_P	B_NC-12C_wP	B_NC-25C	P_NC-12C_P	P_NC-25C
WAC	9.15	8.74	0.23	0.06	9.26	8.59	1.40	8.41	1.45
SD.N.	±0.61	±0.64	±0.21	±0.00	±0.89	±0.72	±0.20	±1.66	±1.14
WAC Laboratory									
		Capillary			Brushing			Poultice	
	SOUND	C_NC-12C_P	C_NC-25C	C_NC-25C_Oc	B_NC-12C_P	B_NC-12C_wP	B_NC-25C	P_NC-12C_P	P_NC-25C
WAC	10.92	9.85	5.34	0.43	10.78	10.12	2.33	8.69	2.99
SD.N.	±0.80	±0.78	±1.31	±0.09	±0.50	±0.38	±0.12	±1.87	±1.12
Ultrasonic Pulse Velocity									
		Capillary			Brushing			Poultice	
	SOUND	C_NC-12C_P	C_NC-25C	C_NC-25C_Oc	B_NC-12C_P	B_NC-12C_wP	B_NC-25C	P_NC-12C_P	P_NC-25C
WAC	3.42	3.42	3.56	3.47	3.39	3.47	3.49	3.53	3.57
SD.N.	±0.08	±0.07	±0.07	±0.07	±0.03	±0.05	±0.07	±0.22	±0.12
<i>Schlaitdorf Sandstone</i>									
WAC Neutron Radiography									
		Capillary			Brushing			Poultice	
	SOUND	C_NC-12C_P	C_NC-25C	C_NC-25C_Oc	B_NC-12C_P	B_NC-12C_wP	B_NC-25C	P_NC-12C_P	P_NC-25C
WAC	4.94	3.47	0.66	0.07	2.76	2.94	0.05	2.83	0.26
SD.N.	±0.34	±0.72	±0.66	±0.03	±1.28	±1.34	±0.03	±0.68	±0.32
WAC Laboratory									
		Capillary			Brushing			Poultice	
	SOUND	C_NC-12C_P	C_NC-25C	C_NC-25C_Oc	B_NC-12C_P	B_NC-12C_wP	B_NC-25C	P_NC-12C_P	P_NC-25C
WAC	5.75	4.49	3.12	0.56	2.24	2.87	3.24	3.63	3.23
SD.N.	±0.18	±1.08	±0.58	±0.25	±0.62	±1.32	±1.55	±0.85	±0.76
Ultrasonic Pulse Velocity									
		Capillary			Brushing			Poultice	
	SOUND	C_NC-12C_P	C_NC-25C	C_NC-25C_Oc	B_NC-12C_P	B_NC-12C_wP	B_NC-25C	P_NC-12C_P	P_NC-25C
WAC	2.81	2.96	3.25	3.33	2.89	2.86	3.13	3.0	3.3
SD.N.	±0.04	±0.07	±0.09	±0.04	±0.06	±0.04	±0.01	±0.05	±0.07

St. Margarethen Limestone

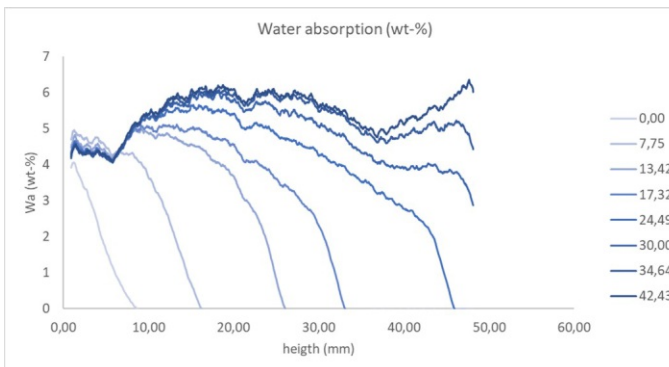
Figure S3. Water absorption (wt-%) extracted from neutron radiography scans on three specimens per lithotype and condition (sound, aged, consolidated).



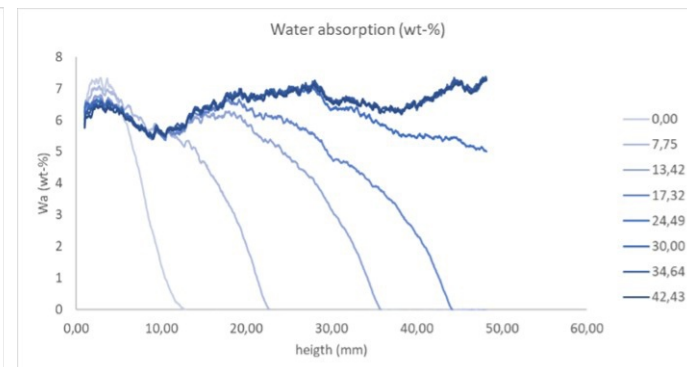
St. Margarethen_C_NC-12C_P_Sample 1



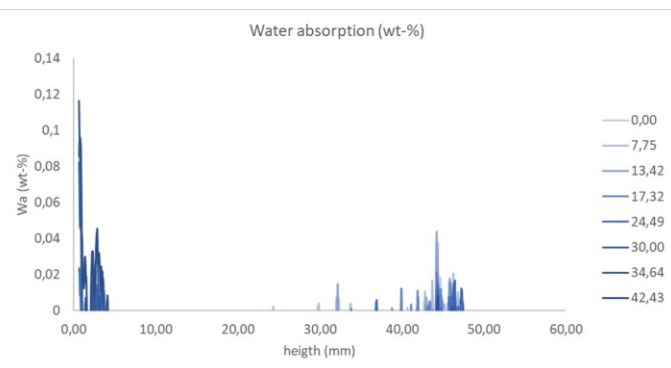
St. Margarethen_C_NC-12C_P_Sample 2



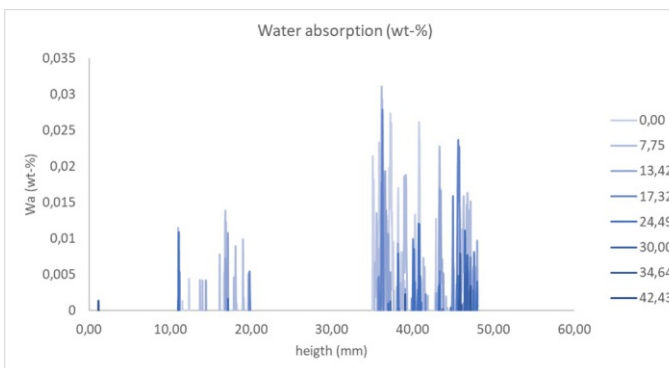
St. Margarethen_C_NC-12C_P_Sample 3



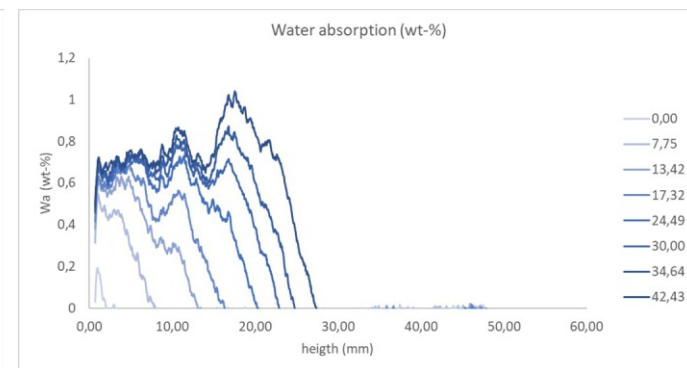
St. Margarethen_C_NC-25C_Sample 1



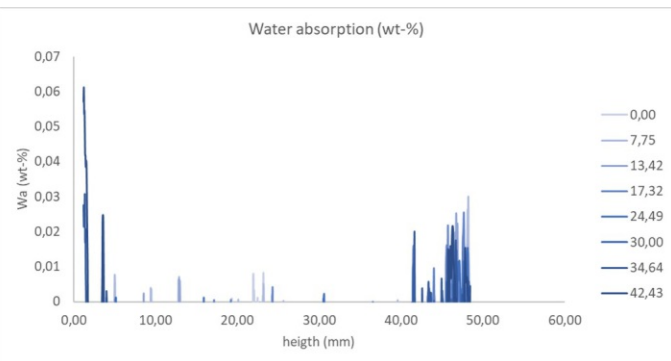
St. Margarethen_C_NC-25C_Sample 2



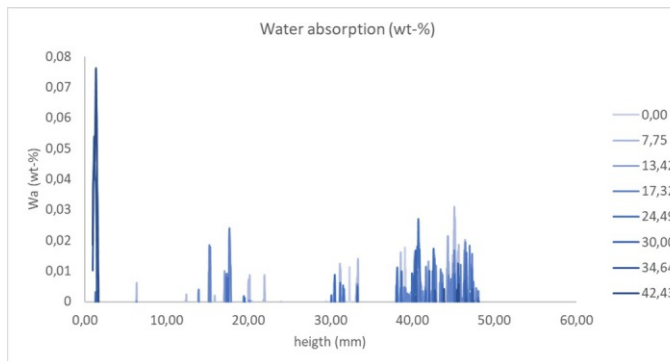
St. Margarethen_C_NC-25C_Sample 3



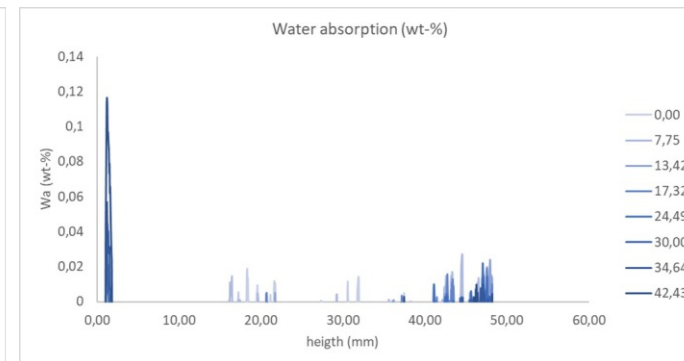
St. Margarethen_C_NC-25C_Oc_Sample 1



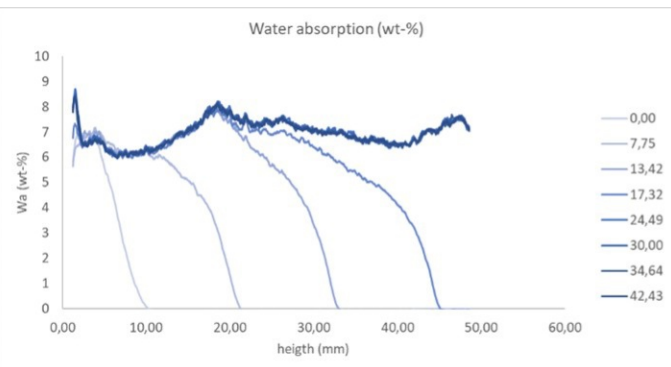
St. Margarethen_C_NC-25C_Oc_Sample 2



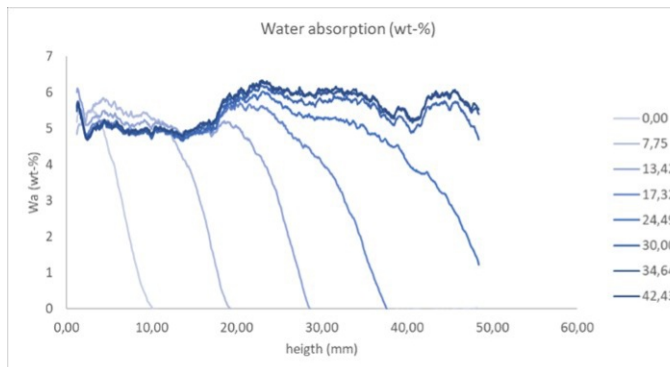
St. Margarethen_C_NC-25C_Oc_Sample 3



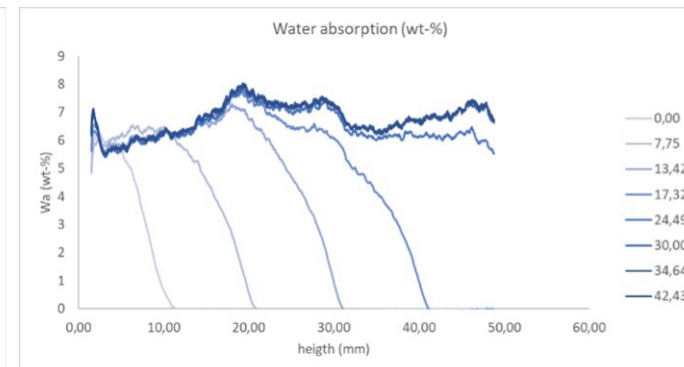
St. Margarethen_B_NC-12C_P_Sample 1



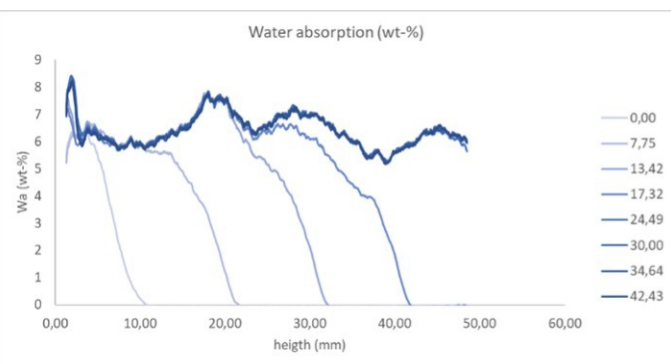
St. Margarethen_B_NC-12C_P_Sample 2



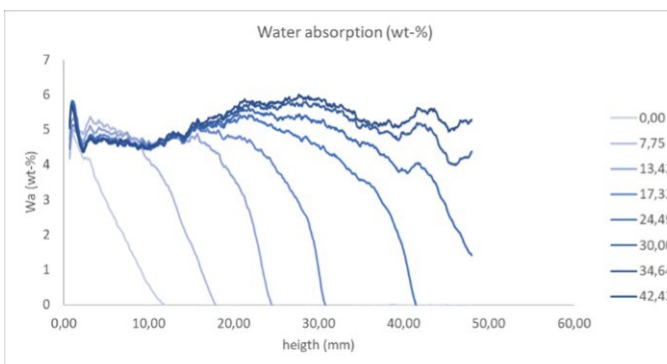
St. Margarethen_B_NC-12C_P_Sample 3



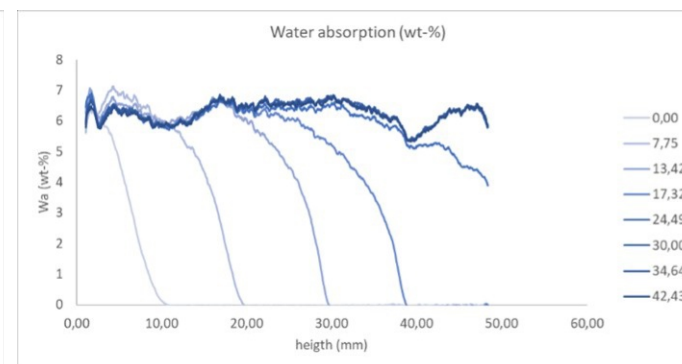
St. Margarethen_B_NC-12C_wP_Sample 1



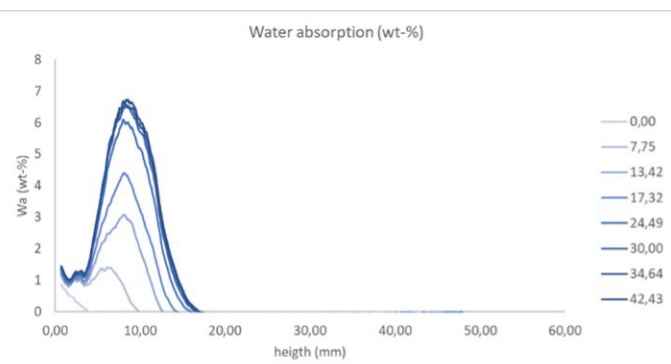
St. Margarethen_B_NC-12C_wP_Sample 2



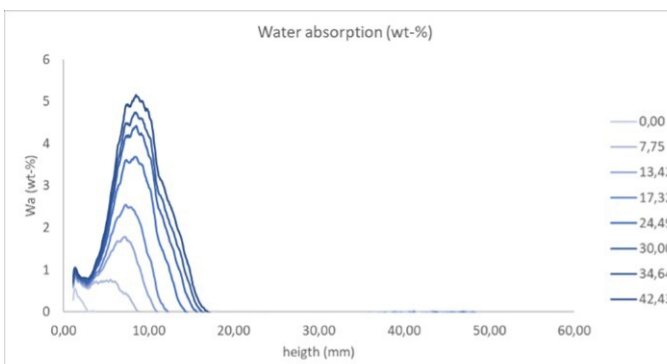
St. Margarethen_B_NC-12C_wP_Sample 3



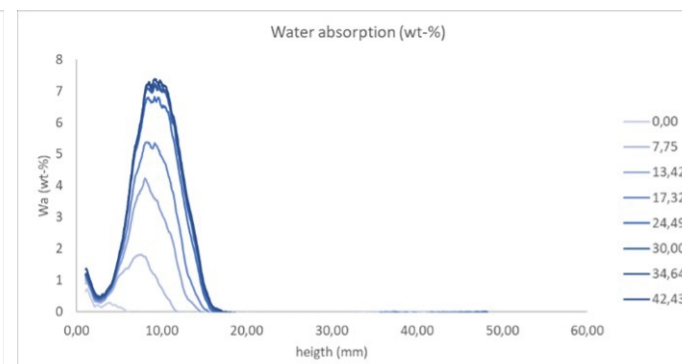
St. Margarethen_B_NC-25C_Sample 1



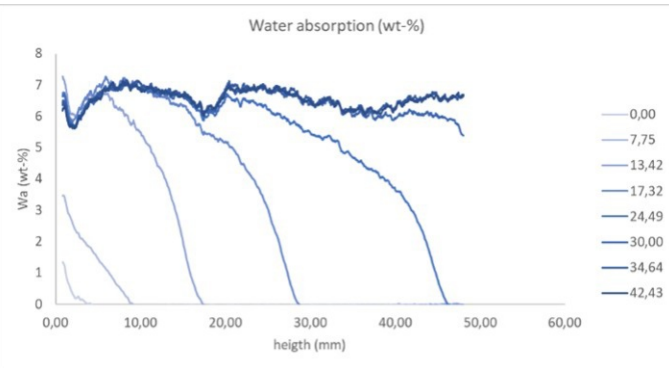
St. Margarethen_B_NC-25C_Sample 2



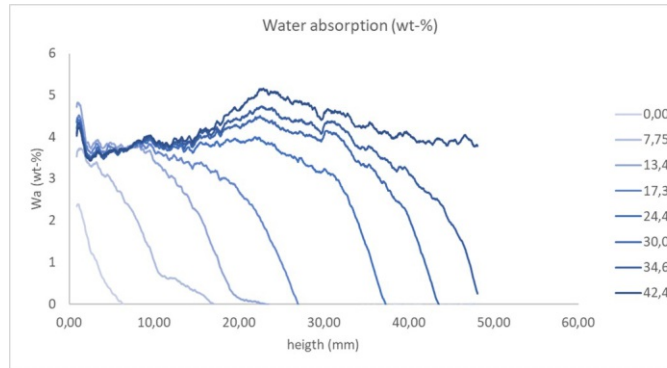
St. Margarethen_B_NC-25C_Sample 3



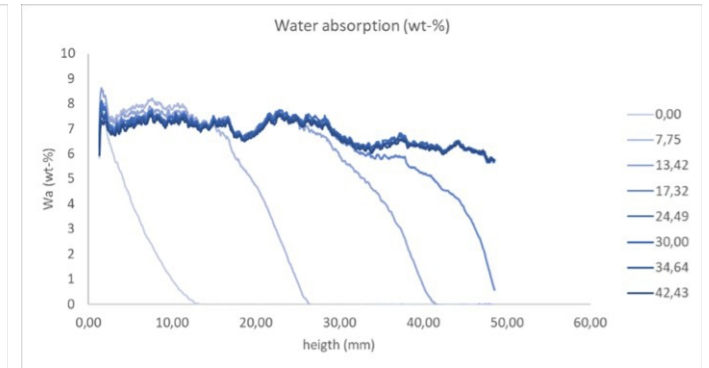
St. Margarethen_P_NC-12C_P_Sample 1



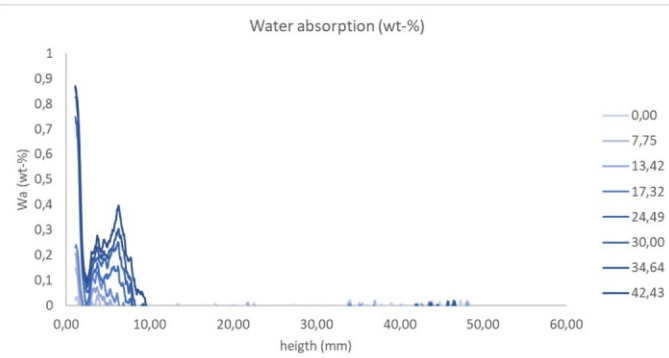
St. Margarethen_P_NC-12C_P_Sample 2



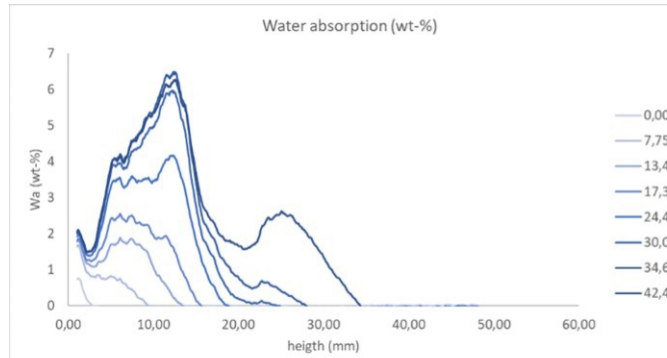
St. Margarethen_P_NC-12C_P_Sample 3



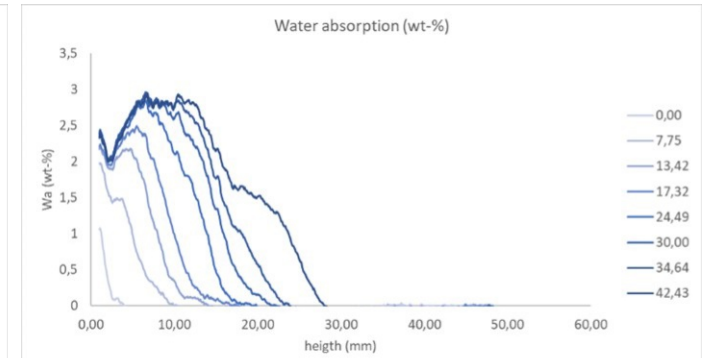
St. Margarethen_P_NC-25C_Sample 1



St. Margarethen_P_NC-25C_Sample 2

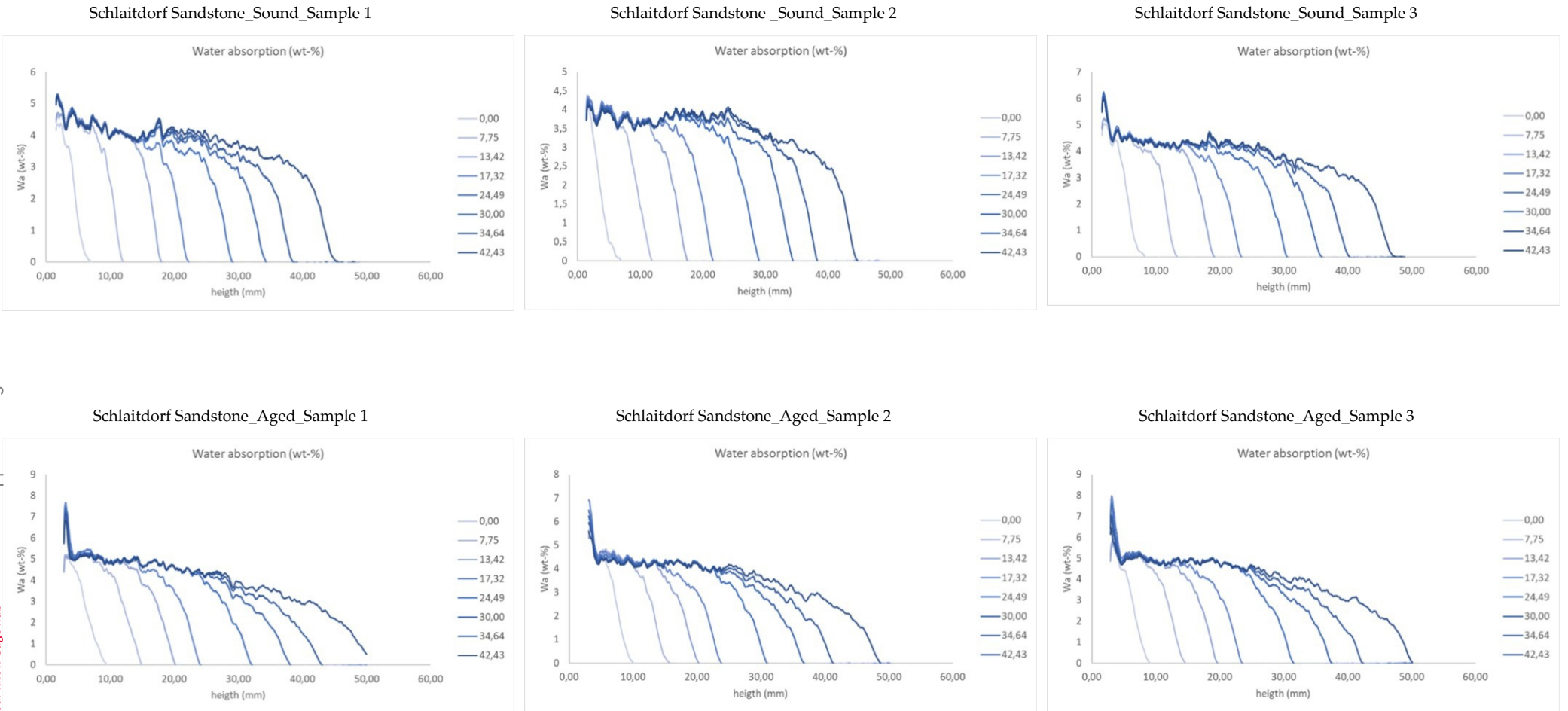


St. Margarethen_P_NC-25C_Sample 3

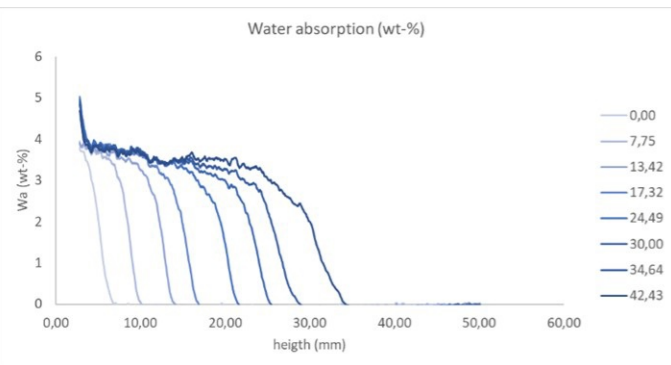


Schlaitdorf Sandstone

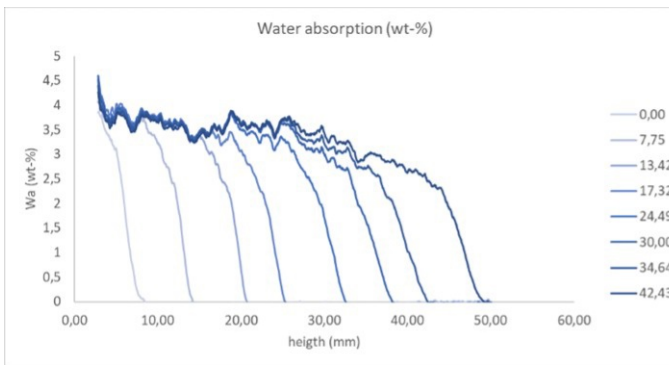
Figure S4. Water absorption (wt-%) extracted from neutron radiography scans on three specimens per lithotype and condition (sound, aged, consolidated).



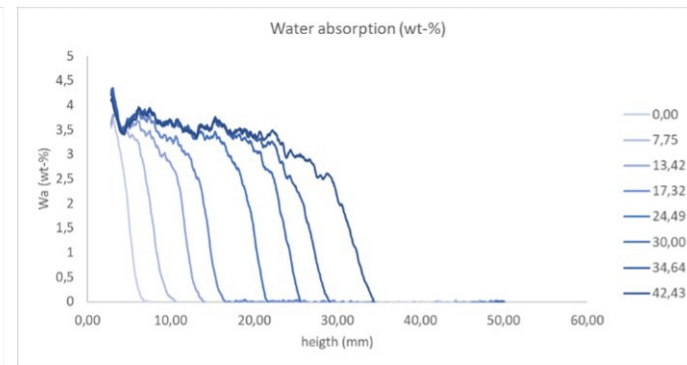
Schlaitdorf Sandstone_C_NC-12C_P_Sample 1



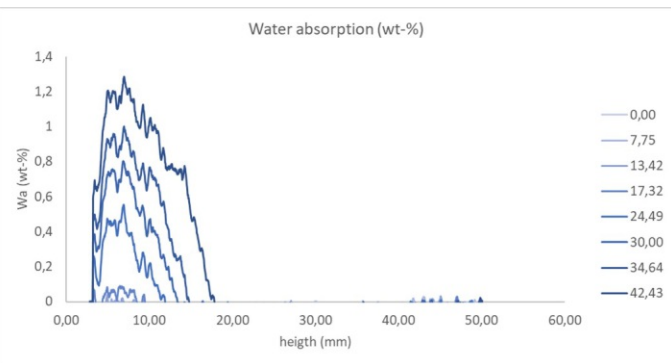
Schlaitdorf Sandstone_C_NC-12C_P_Sample 2



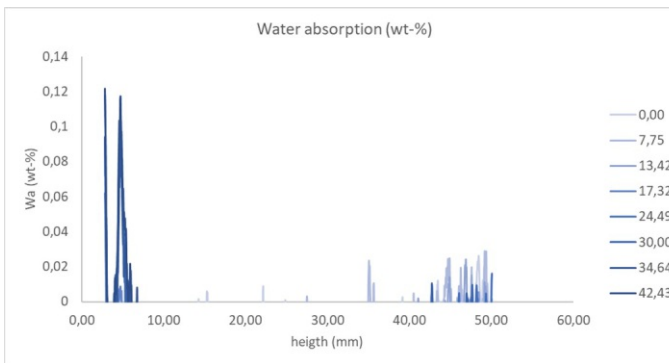
Schlaitdorf Sandstone_C_NC-12C_P_Sample 3



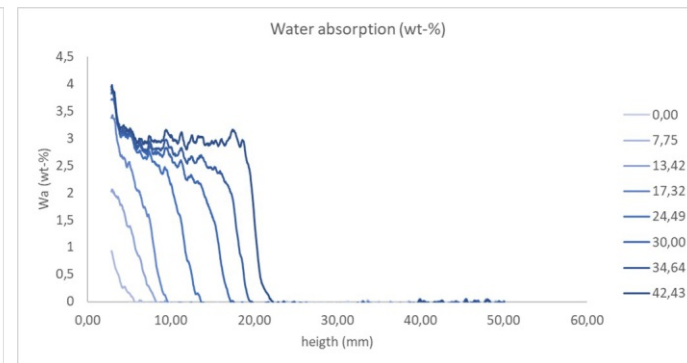
Schlaitdorf Sandstone_C_NC-25C_Sample 1



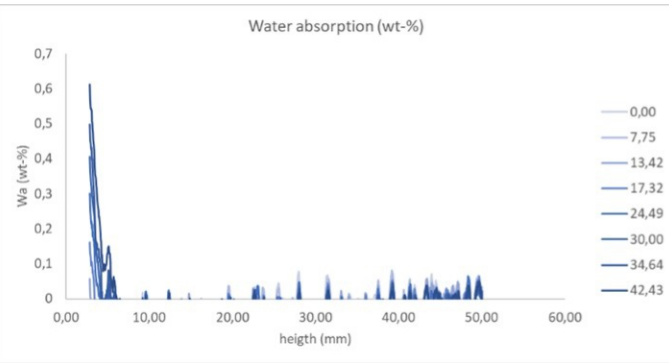
Schlaitdorf Sandstone_C_NC-25C_Sample 2



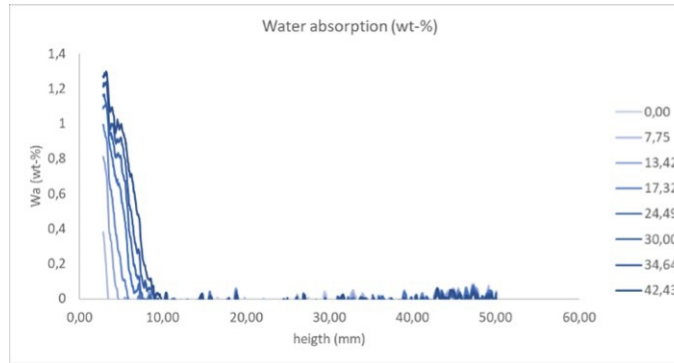
Schlaitdorf Sandstone_C_NC-25C_Sample 3



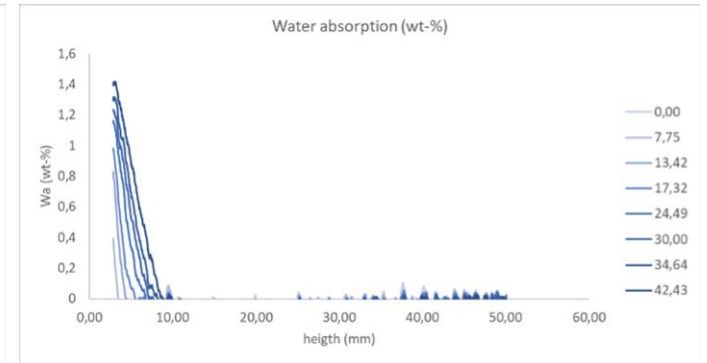
Schlaitdorf Sandstone_C_NC-25C_Oc_Sample 1



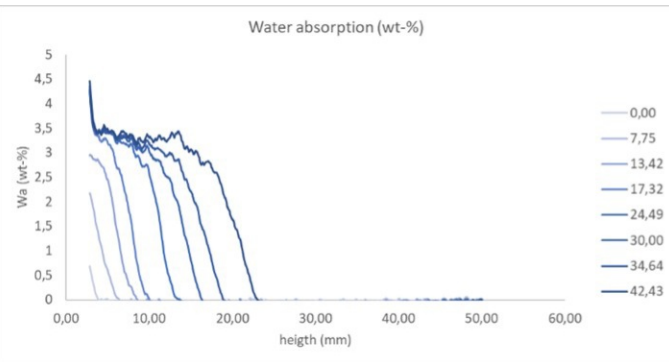
Schlaitdorf Sandstone_C_NC-25C_Oc_Sample 2



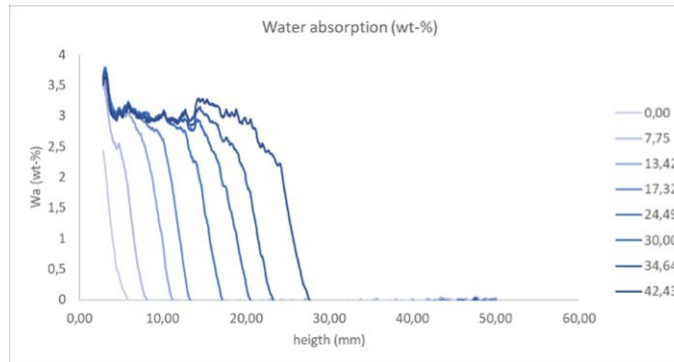
Schlaitdorf Sandstone_C_NC-25C_Oc_Sample 3



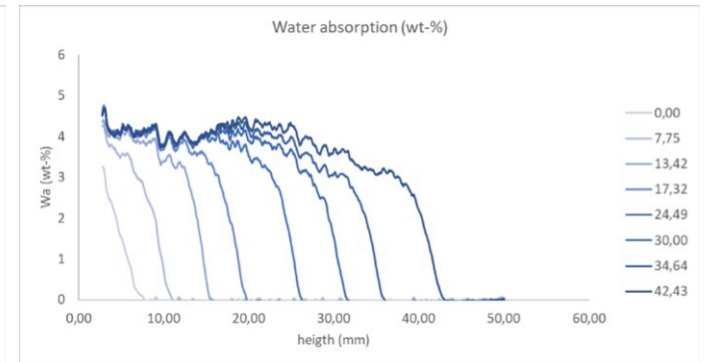
Schlaitdorf Sandstone_B_NC-12C_P_Sample 1



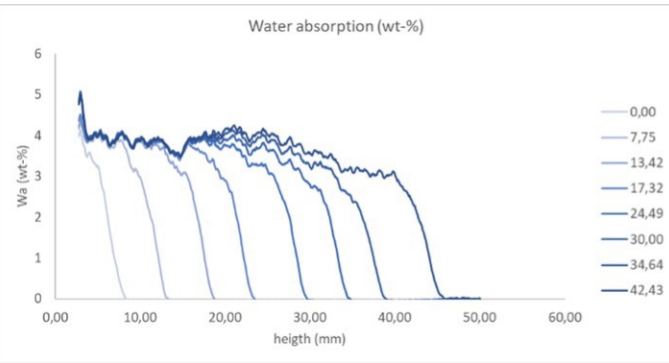
Schlaitdorf Sandstone_B_NC-12C_P_Sample 2



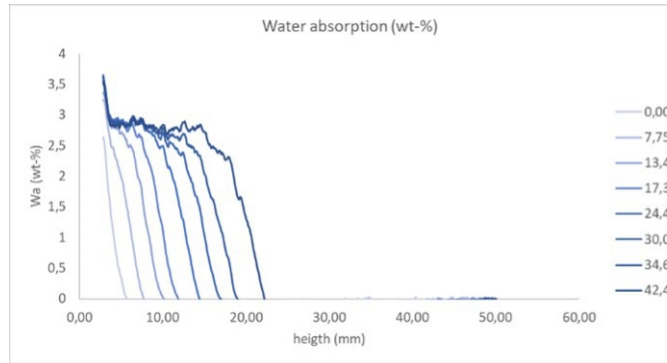
Schlaitdorf Sandstone_B_NC-12C_P_Sample 3



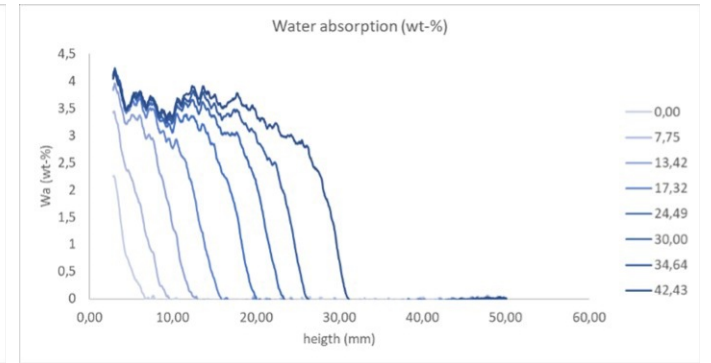
Schlaitdorf Sandstone_B_NC-12C_wP_Sample 1



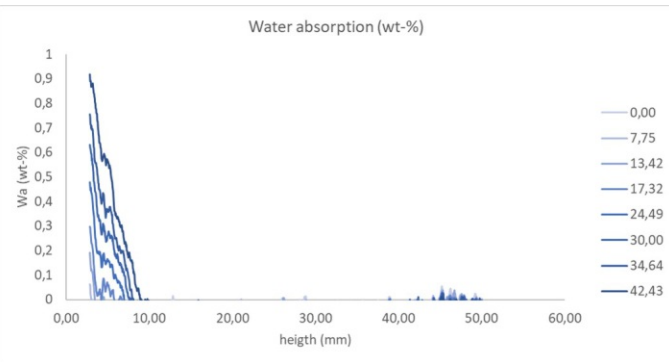
Schlaitdorf Sandstone_B_NC-12C_wP_Sample 2



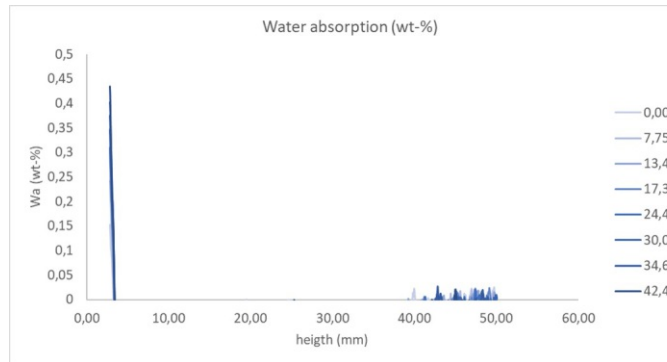
Schlaitdorf Sandstone_B_NC-12C_wP_Sample 3



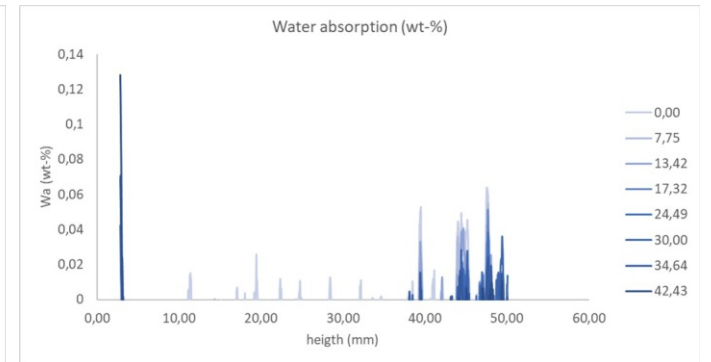
Schlaitdorf Sandstone_B_NC-25C_Sample 1



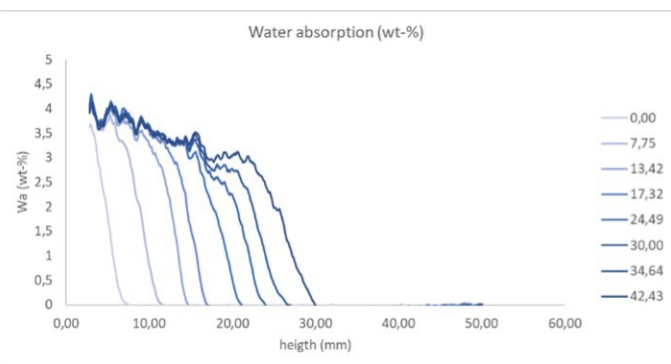
Schlaitdorf Sandstone_B_NC-25C_Sample 2



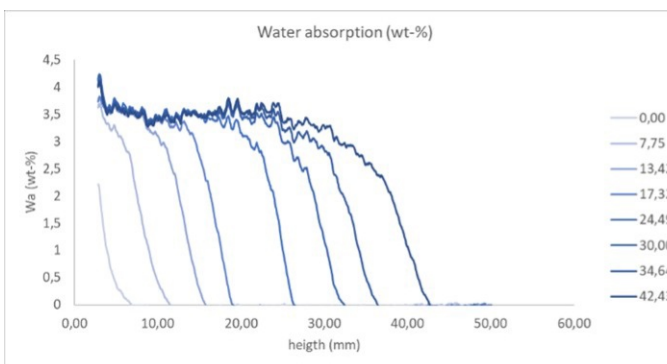
Schlaitdorf Sandstone_B_NC-25C_Sample 3



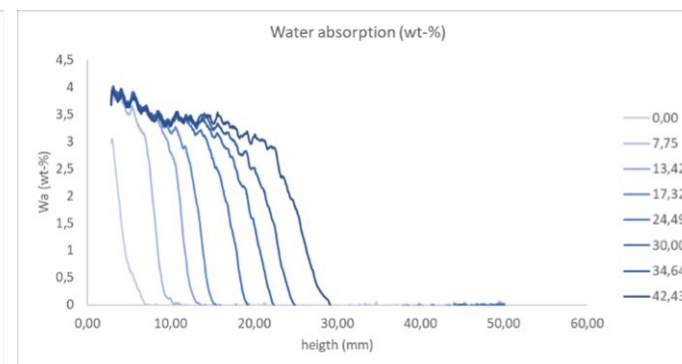
Schlaitdorf Sandstone_P_NC-12C_P_Sample 1



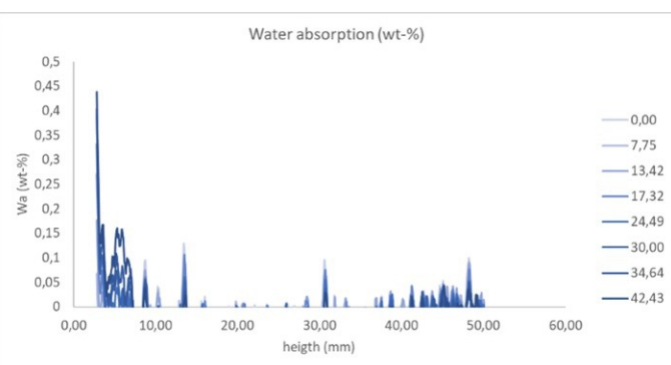
Schlaitdorf Sandstone_P_NC-12C_P_Sample 2



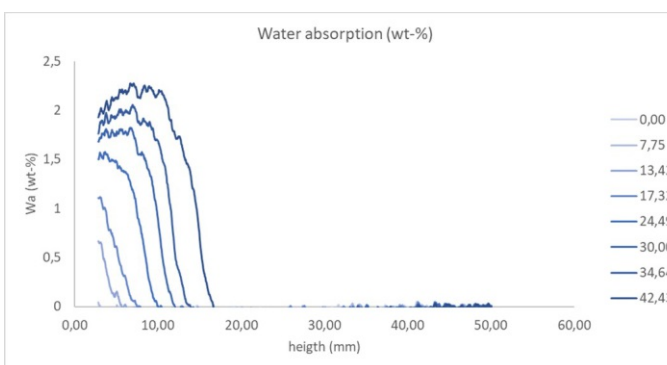
Schlaitdorf Sandstone_P_NC-12C_P_Sample 3



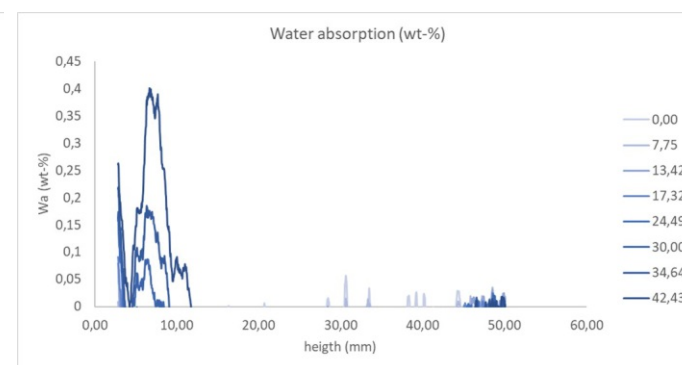
Schlaitdorf Sandstone_P_NC-25C_Sample 1



Schlaitdorf Sandstone_P_NC-25C_Sample 2



Schlaitdorf Sandstone_P_NC-25C_Sample 3



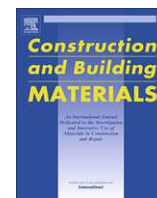
D

Distribution depth of stone consolidants applied on-site:
Analytical modelling with field and lab cross-validation.



Contents lists available at ScienceDirect

Construction and Building Materials

journal homepage: www.elsevier.com/locate/conbuildmat

Distribution depth of stone consolidants applied on-site: Analytical modelling with field and lab cross-validation

Matea Ban ^{a,*}, Laura Aliotta ^{b,2}, Vito Gigante ^{b,2}, Elisabeth Mascha ^c, Antonella Sola ^{d,1}, Andrea Lazzeri ^b

^a Institute of Geotechnics, Faculty of Civil Engineering, TU Wien, Austria

^b Department of Civil and Industrial Engineering, University of Pisa, Italy

^c Institute of Art and Technology, Conservation Science, University of Applied Arts Vienna, Austria

^d Department of Engineering 'Enzo Ferrari', University of Modena and Reggio Emilia, Italy

HIGHLIGHTS

- Modelling and evaluation of distribution depth of stone consolidants.
- Colloidal suspensions exhibit an exponential decline to varying degrees.
- Drilling resistance shows over-consolidation which agrees with the applied model.
- Deposition of consolidants inside the stone determines a treatment's performance.
- Mechanical tests confirm the treatments efficiency (i.e. mechanical strength gain).

ARTICLE INFO

Article history:

Received 1 February 2020

Received in revised form 22 July 2020

Accepted 24 July 2020

Available online 1 September 2020

Keywords:

Analytical modelling

Stone consolidation

Distribution of consolidants

Scanning electron microscopy

Drilling resistance

ABSTRACT

An analytical model was applied in order to understand the distribution depth of cured stone consolidants. The model is grounded on a case study of Vienna's St. Stephen's Cathedral and was verified against drilled cores examined by SEM and image analysis, on-site drilling resistance measurements and laboratory-based mechanical tests. The results reveal that the variation of the concentration gradient with penetration depth resembles an exponential decline. The deposition of the cured consolidant is governed by capillary forces upon drying within water-based nano-zirconia dispersions and water/alcohol-based colloidal silica. This effect is less pronounced within reactive consolidants, which undergo polycondensation reactions, as with alkoxysilanes.

© 2020 The Authors. Published by Elsevier Ltd. This is an open access article under the CC BY license (<http://creativecommons.org/licenses/by/4.0/>).

1. Introduction

Preservation of architectural surfaces is a common practice, and for such purposes, new materials are continuously being developed and modified. One of the most demanding tasks in built heritage preservation is the restoration of the physical characteristics and mechanical properties of a building's surface that has naturally aged. These surfaces usually exhibit a degradation pattern, more severe at the exposed surface and less so towards the inner struc-

ture of the building's wall material. To restore such complex patterns, various stone consolidants are frequently applied. These consolidants differ in chemical, physical and mechanical properties, and the choice and study of their interaction with a substrate is often grounded on a case-by-case basis, considering certain stones or architectural surfaces. Occasionally, a combination of consolidants is used to remedy problems regarding damages of varying sizes [1]. Moreover, efforts have been made to modify particle size and shape to overcome decay patterns of different magnitudes and to treat substrates of higher porosities [2]. Some consolidant modifications include the functionalisation of surfaces to retard further decay caused by e.g. biological colonization [3] or water penetration [4]. Some common consolidants include metal oxides and colloidal silica in various solvents as well as alkoxysilanes that form a silica gel that strengthens the substrate. Furthermore, synthetic organic polymers, calcium hydroxide, ammonium

* Corresponding author.

E-mail addresses: matea.ban@tuwien.ac.at (M. Ban), laura.aliotta@dice.unipi.it (L. Aliotta), vito.gigante@dice.unipi.it (V. Gigante), elisabeth.mascha@uni-ak.ac.at (E. Mascha), antonella.sola@unimore.it (A. Sola), andrea.lazzeri@unipi.it (A. Lazzeri).

¹ Present address: Commonwealth Scientific and Industrial Research Organisation, Manufacturing Business Unit, Metal Industries Program, Clayton, VIC, Australia; antonella.sola@csiro.au.

² These authors contributed equally to the work.

<https://doi.org/10.1016/j.conbuildmat.2020.120394>

0950-0618/© 2020 The Authors. Published by Elsevier Ltd.

This is an open access article under the CC BY license (<http://creativecommons.org/licenses/by/4.0/>).

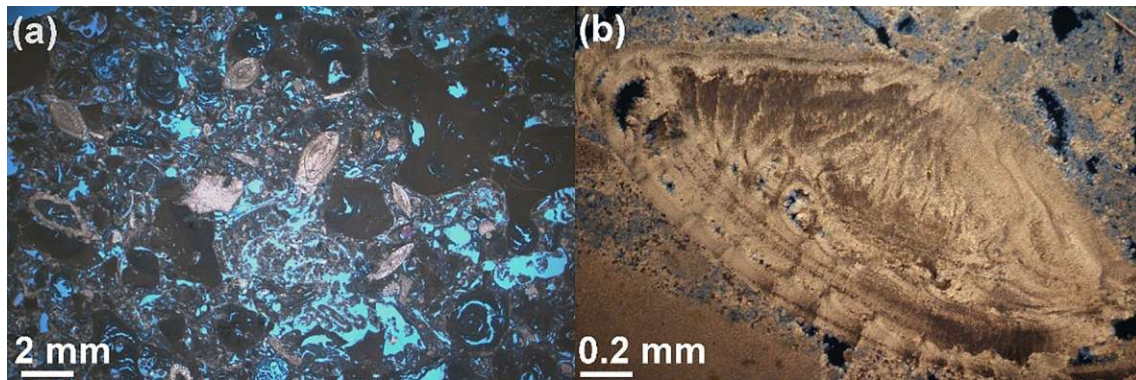


Fig. 1. a) Microstructure of freshly quarried *St. Margarethen* as observed in thin section under parallel-polarised light using a Nikon optical microscope. b) Detail of a foraminifera fragment surrounded with the binding medium, a fine crystalline calcite cement observed in cross-polarised mode. Blue and black space represents the resin used for embedment of the stone specimens. (For interpretation of the references to colour in this figure legend, the reader is referred to the web version of this article.)

century, and it exhibits extensive granular disintegration and the formation of black crusts (see Fig. 2). Granular disintegration is a generic term describing lost cohesion between the grains of a substrate, whereas the formation of black crusts is a form of mineral replacement reaction to the detriment of calcite that can be traced to the activity of sulphate agents and environmental pollutants [20]. For detailed information about the predominant decay patterns found on-site and a condition assessment, see Supporting Information.

The preparation of the surface involved sensitive mechanical and chemical cleaning, with micro chisels and poultice of ammonium bicarbonate, respectively. However, an accurate removal of the gypsum in depth was not possible due to the severely damaged surface. A careful steam cleaning was carried out before consolidants were applied. The application of the three consolidants, listed in Table 1, was done by the run-off method using pipettes until refusal of the consolidant was visible. This procedure was repeated the next day, having in total a treatment application of two cycles. The curing involved a loose 1 week coverage with foil to protect the treated surface from sun and rain exposure and to avoid a too fast evaporation.

The consolidants were developed during a recently finished Horizon 2020 project known as 'Nano-Cathedral', short for 'Nanomaterials for conservation of European architectural heritage developed by research on characteristic lithotypes' (Grant Agreement No. 646178). The exact routes of synthesis for these consolidants are therefore protected by non-disclosure agreements, as industrial partners were involved in product development. However, the project ensured a high technology readiness level (TRL) of these newly engineered materials. They have been validated in laboratory and relevant environment, including a development of technical and safety data for their use. For specialists on-site, industrial products are more relevant than consolidants developed by academic researchers as the latter often fail to be implemented on-site, also due to liability reasons. Most consolidants used in construction work are industry developed products.

The effectiveness of each consolidant, that is, its capability to increase mechanical strength after treatment, was assessed in a laboratory-based study using sound speed propagation and splitting tensile strength. For that work, freshly quarried *St. Margarethen* samples were artificially aged by heat treatment to induce micro-cracks in the substrate. The ageing procedure is described elsewhere [21] and involved preliminary studies concerning residence time, cycles and heating rates to achieve microstructural defects that reduce the soundness of the stone without macroscopic failure (i.e. large cracks traversing the specimen). Thermal stresses are commonly employed for ageing pur-

poses prior to stone consolidation studies [22]. In the present study, the stone samples were placed in an electrical furnace (model Heraeus K114 from Thermo Scientific) with a heating rate of $40\text{ }^{\circ}\text{C min}^{-1}$ until the target temperature of $600\text{ }^{\circ}\text{C}$ was reached and maintained for 1 h. A rapid cooling of approx. 15 min to room temperature followed. When the specimens reached room temperature, the procedure was repeated. A total of three heating cycles were completed. For more details on the effect of artificial ageing please refer to Supporting Information.

Consolidation in the laboratory was performed by capillary absorption for 1 h on the bottom side of each specimen (i.e. the lower side was left dipped in a vat of consolidant for 1 h while the lateral sides were sealed with a parafilm sealing tape) that was equilibrated under laboratory conditions ($22 \pm 3\text{ }^{\circ}\text{C}$, $\sim 50\%$ RH) beforehand. Thorough penetration of the specimens by the consolidant was ensured by visual inspection. In fact, as often happens with water, the movement of the wetting front of the consolidant progressively changed the colour of the stone (i.e., darkening) and this allowed to follow the penetration of the specimens with the naked eye. A total of two consolidant application cycles were completed, with 24 h between the two applications. Afterwards, the specimens were loosely covered with a polyethylene foil for 1 week, simulating on-site aftercare conditions. After treatment, the samples were weighed for 1 month once per day in order to determine when equilibrium was reached. Testing of the specimens was done 2 to 3 months after consolidation, to ensure that sufficient curing time for complete alkoxy silane polymerisation had passed. The latter point was particularly important as a polycondensation reaction might be ongoing for an indefinite period, as reported by other authors [23,24].

It is important to note that a direct comparison of specimens treated on-site and in the laboratory cannot be made, but rather the latter should serve as supporting information in evaluating on-site tests. Treatment application on-site and in laboratory is not comparable and might lead to varying treatment performances. Specifically, the applicability of the lab-based treatment method (i.e., capillary rise from one side) cannot be mimicked on-site and variable factors (e.g. gravity, pressure, precision, contact area, etc.) might influence a treatments outcome. Moreover, on-site conditions, including micro- and macro-climate, decay pattern variation and application amount, cannot be properly mimicked in the laboratory and require further efforts in research analysis. Nevertheless, laboratory-based methods are good indicators for a treatment's effectiveness [9] and a necessary step in evaluating newly engineered consolidants. Details regarding the amount of consolidants applied on-site and in laboratory can be seen in Supporting Information.

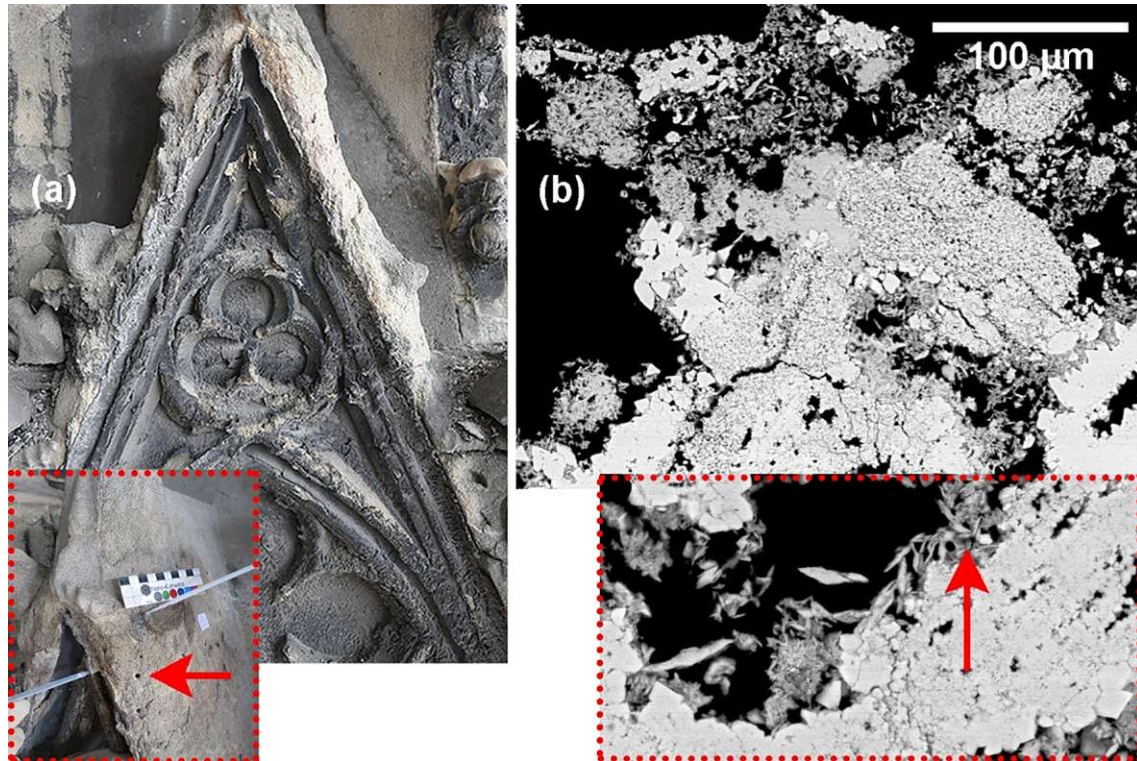


Fig. 2. **a)** Architectural element on the south façade of St. Stephen's Cathedral used as the testing area. Inset shows the surface during application of a consolidant and the drilling resistance holes made for the purpose of testing the condition prior to treatment (red arrow). **b)** Typical decay pattern, observed in back-scattered mode on polished thin sections, exhibiting damage more pronounced at the surface. Inset shows the presence of gypsum in the microstructure, visible in the form of needles (red arrow). (For interpretation of the references to colour in this figure legend, the reader is referred to the web version of this article.)

Table 1
Characteristics of the studied stone consolidants.

Project labelling	Commercial name (producer, country)	Materials chemistry	Dimension of Nanoparticles (nm)	Concentration in wt% (***)
NC-25C	HFES 70 (ChemSpec, IT)	Nano TiO ₂ (1%) mod. TEOS ^(*) in isopropanol	10–20 TiO ₂ (**)	47 ± 0.5
NC-12C	ZG12 (Colorobbia, IT)	SiO ₂ in water/ethanol	~70	23 ± 0.5
NC-29C	ZR110 (Tecnan, ES)	ZrO ₂ in water	~119	11 ± 0.5

^(*) Tetraethyl orthosilicate, also known under the general term alkoxyasilane and abbreviated as TEOS, with the chemical formula Si(OC₂H₅)₄. ^(**) Contains approx. 80% anatase and 20% rutile. ^(***) The solid content after curing was calculated on laboratory treated specimens by dividing the residue weight of the consolidant after curing, assessed approx. 2 months after application, by the applied weight of consolidant and multiplying by 100 to obtain percent; using 10 specimens with a dimension of 5 × 5 × 5 cm. Note that the mass of NC-25C might deviate with time due to ongoing polycondensation reactions. .

2.3. Characterisation

Characterisation of the naturally weathered and consolidated building stone included SEM examination on extracted drilled cores and subsequent image analysis. Moreover, to cross-validate the findings, drilling resistance was performed on-site in the vicinity of the holes that originated from extracted drilled cores used for image analysis. Additionally, sound speed propagation and splitting tensile strength were tested on laboratory specimens for the purpose of studying mechanical strength gain after consolidation.

The polished cross-sections were observed by SEM (Philips XL 30 ESEM), at 20 kV under low vacuum, using back-scattered electrons and employing energy-dispersive X-ray analysis. Detailed phenomena such as adhesion were studied at high magnification (normally 200x to 1500x, mostly 400 x), whereas SEM micrographs, taken at low magnification of 100x, were assembled using Photoshop® to observe the full depth of a sample and analyse the distribution depth of a given consolidant. Analysed depth was limited to approximately 10 to 15 mm. SEM studies were also done on laboratory-treated specimens to validate on-site observations.

The image analysis process was carried out using the software ImageJ [25] (v 1.51r, National Institutes of Health, Bethesda, MD, USA). In that analysis, each image was divided into vertical columns, and each column-like micrograph was again subdivided into horizontal bands 1 mm in height. The consolidant, within the structure of the stone, was mapped using false colours. For each band, the volume fraction occupied by the consolidant was calculated as the fraction of false-coloured pixels in the image. In this way, the concentration of solid content after curing was determined as a function of depth within the stone. An average concentration profile and corresponding standard deviation were calculated over two subdivisions of each micrograph prior to modelling. The assumption made in the SEM analysis was that all the consolidant (i.e. 100% of its solid content) applied at the specimen's surface was contained within the analysed specimens and, in particular, within the depth observed in the image.

Drilling resistance measurements were performed on-site with a DRMS cordless device developed by SINT Technology s.r.l. (Italy). Drilling resistance measures the resistance in Newton to a penetration force. It is calculated as a function of the speed of rotation, the

penetration speed, the drill bit diameter and the material tested. The rotation speed of 600 rpm and the penetration speed of 10 mm/min were kept constant. The penetration depth amounted to 15 mm, comparable with the image depth analysed by SEM. A custom-made 5 mm polycrystalline diamond bit was used for each treatment evaluation, which obviated the need for a correction for drill bit wear. The drilling resistance test was performed before treatment application and 1 year after application on-site.

Determination of the dynamic modulus of elasticity, by measuring the fundamental resonance frequency, was performed by longitudinal study on each of three prismatic specimens ($1 \times 1 \times 4$ cm) in their pristine, artificially aged (i.e. heat treated) and subsequently consolidated states according to EN 14146 [26]. The tested size ensured that the consolidants penetrated the entire body of each specimen. A Conosonic C2-GS ultrasonic pulse generator, a pair of UP-DW transducers and a notebook preinstalled with Light House Touch software, all developed by Geotron-Elektronik (Pirna, Germany), were used. The device used was equipped with a built-in algorithm that calculated the dynamic modulus of elasticity, Ed_L , in GPa, obtained from the measured longitudinal fundamental resonance frequency F_L as

$$Ed_L = 4 \times 10^{-6} \times l^2 \times F_L^2 \times \rho \times T \quad (1)$$

where l represents the length and ρ the density of the stone. The correction factor T can be assumed to equal 1, as the width of the specimens is four times its length, so Eq. (1) is simplified by the correction factor.

The test method for splitting tensile strength, investigated according to ASTM D3967 [27], was implemented with an Austro Test Hrdina GmbH MA-CO89 four-column hydraulic servo control loading device. The testing setup consisted of a flat bearing block at the bottom and a curved bearing block on the top of the stone specimen. Cardboard bearing strips of 0.6 mm thickness were used to reduce the contact stresses. An average was calculated from six specimens of diameter of 6 cm and thickness of 3 cm. The splitting tensile strength σ_t in MPa was determined as

$$\sigma_t = \frac{2P}{\pi LD} \quad (2)$$

where P represents the maximum load applied in Newtons as indicated by the testing machine, and L and D correspond respectively to the thickness and diameter of the specimen in mm.

An overview of the analysis carried out on *St. Margarethen* treated on-site and in laboratory as well as the methods used to investigate the treatments performance can be viewed in Table 2.

2.4. Analytical model to describe the distribution depth of the consolidant after curing

An analytical model was obtained to evaluate the quantity, as a function of depth, of consolidant present in the building stone, following an on-site treatment with three consolidants. The first approximation to model this phenomenon is to view the system (i.e. stone and consolidant) as a filtering system in which the stone acts as a filter against the consolidant that passes through it. In the literature, this approach is usually found in studies concerning oil recovery. The probabilistic sieve model describing microfiltration [28–30], used to analyse pore blocking processes, allows the determination of physicochemical parameters of nonstationary filtration phenomena of aqueous suspension.

In the present case study, the driving forces that carry the consolidant through the stone's fabric are capillary forces. In order to evaluate the concentration of consolidant c as a function of depth x , a mass balance is applied in the following form:

Table 2
Analysis carried out on *St. Margarethen* treated on-site and in laboratory.

Type of test (Standard)	On-site	Laboratory	Note
SEM-EDX (Not Stand.)	Yes ⁽¹⁾	Yes ⁽²⁾	⁽¹⁾ One drilled core, 2 cm in diameter, per test area (i.e., consolidant) extracted. ⁽²⁾ One specimen per consolidant.
PLM (Not Stand.)	Yes	No	Condition assessment and damage analysis in combination with SEM-EDX. Three specimens were extracted on-site for damage analysis.
Drilling resistance (Not Stand.)	Yes	No	Distance of bore holes before and after treatment application approx. 2 cm. Low-destructive test.
Drying behaviour (EN 16322)	No	Yes	Average of three samples ($5 \times 5 \times 5$ cm) per consolidant with daily monitoring for four weeks.
Dynamic elastic modulus (EN 14146)	No	Yes	Average of three samples ($1 \times 1 \times 4$ cm). Direct comparison of sound, artificially aged and consolidated conditions. Non-destructive test.
Splitting tensile strength (ASTM D 39967)	No	Yes	Average of 10 samples per condition (i.e., sound, artificially aged and consolidated). Destructive test.

(1) For modelling purposes, doing false colour mapping using Photoshop® and ImageJ. (2) Analysis of details regarding bridging capacity, cracking and adhesion to substrate.

$$V \frac{dc}{dx} = D \frac{d^2c}{dx^2} \quad (3)$$

where D is the diffusivity and V the filtration speed of the studied system. As equilibrium conditions are reached (i.e. the curing of the consolidant completes), time dependence becomes negligible. Therefore, the boundary conditions to solve Eq. (3) are

$$B.C. \begin{cases} c(x=0) = c_0 \\ c(x=L) = c_L \end{cases} \quad (4)$$

where C_0 is the solid content concentration found on the stone's surface at the end of the curing process and C_L is the solid content concentration at the maximum depth reached by the treatment within the analysed sample volume. As the system is described to be a filtration system, where the treated stone is the filter, the expression of velocity follows Darcy's law [31,32]. Therefore, the effective filtering speed V is connected to Darcy's speed V_D according to the following relation:

$$V = \varepsilon \cdot V_D = -\frac{k}{\mu} \frac{\Delta P}{L} \quad (5)$$

In Eq. (5), the negative sign of the term on the right-hand side provides for positive values of the velocity in the direction of the motion. The suspension viscosity is given by μ , whereas k is the permeability and $\Delta P L^{-1}$ the pressure drop over a given distance. ε represents the average porosity of the stone, evaluated using image analysis as described above. The permeability indicates the capability of a viscous fluid to penetrate a porous system and can be evaluated through experimental tests or, for well-known systems, found in the literature [33,34]. Otherwise, as a first approximation, the Blake-Kozeny relation (eq. (6)) can be used to calculate the stones permeability k in terms of the average pore diameter D_p and stone porosity ε as follows:

$$k = \frac{D_p^2 \cdot \varepsilon^3}{150 \cdot (1 - \varepsilon)^2} \quad (6)$$

As capillarity is the driving force of this system, it obeys the Young–Laplace equation:

$$\frac{\Delta P}{L} = \frac{2\sigma \cos\theta}{R_p^2} \quad (7)$$

where σ is the surface tension, θ the wettability (contact angle) and R_p the pore radii of the system. Inserting Eqs. (6) and (7) into Eq. (5), the final expression of filtering velocity is obtained. Solving Eq. (3), the degree of solid content concentration as a function of sample depth can be described as an analytical solution as follows:

$$\left[-\frac{2D_p\sigma\cos\theta}{75\mu DL} \cdot \frac{\varepsilon^3}{(1-\varepsilon)^2} \right] \frac{dc}{dx} = \frac{d^2c}{dx^2}. \quad (8)$$

In Eq. (8), it is possible to define the following parameters:

$$A = \frac{\varepsilon^3}{(1-\varepsilon)^2} \quad (9)$$

$$B = \frac{2D_p\sigma\cos\theta}{75\mu DL}, \quad (10)$$

where A is a function of the stone's effective porosity, evaluated by image analysis as the weighted average along the depth of the stone, and B is an empirical parameter obtained through mathematical iterations (using the Generalized Reduced Gradient (GRG) method until the convergence was obtained), encompassing the wettability, average porous dimensions, permeability and diffusivity of the macroscopic system. Substituting the starting boundary conditions (Eq. (4)) into Eq. (8), we obtain the following solution:

$$c(x) = \frac{e^{-ABx}(C_0 \cdot (e^{ABL} - e^{ABx}) + C_L \cdot e^{ABL}(e^{ABx} - 1))}{e^{ABL} - 1} \quad (11)$$

which can be rewritten in the following form:

$$c(x) = \frac{(C_L - C_0) \cdot e^{-ABx} - (C_L - C_0) + C_0 \cdot (e^{-ABL} - 1)}{e^{-ABL} - 1} \quad (12)$$

The solution given through Eq. 11 or 12 makes it evident that the distribution of the solid content after curing follows an exponential growth or decline. To estimate the adequacy with which the obtained equations describe the distribution depth of the consolidants, they have been verified in relation to the values obtained from image analysis. The mathematical rearrangement from Eq. (12) to Eq. (11) can be viewed in Appendix I.

3. Results and discussion

3.1. Image analysis and analytical solution for the distribution depth of consolidants

SEM analysis provided the basis for the development of the analytical model as well as the evaluation procedure. The image-analysed distribution depth for all three consolidants can be seen in Fig. 3.

Additional information obtained through SEM analysis regards the adhesion of the consolidants onto the grain surfaces and the bridging capacity between grains. The latter is correlated with cracking of the consolidating matrix. The SEM results are summarised in Table 3, with examples shown in Fig. 4a–d. SEM analysis shows that the nanoparticle-based consolidants exhibit better adhesion and bridging capacities than alkoxysilane. The poor adhesion and bridging of NC-25C can be attributed to drying stresses and thus its susceptibility to cracking.

The micrographs analysed and reported in Fig. 3 indicate that the solution of the differential equation based on the stone used as a filter represents a good methodology to model the complex

system. In fact, Eq. (12) fits very well with the experimental data for all the studied consolidants, as can be seen in Fig. 5. The experimentally assessed and thus modelled curves exhibit exponential decline to different extents.

The curves in Fig. 5 show that NC-12C and NC-29C deposit preferentially on the stone surface compared to NC-25C. NC-12C exhibits a more pronounced accumulation of solid content in the subsurface area, through the first 3 mm of sample depth. This slight difference from NC-29C might be related to the more volatile solvent, namely, a water/ethanol mixture. The fast solvent evaporation of the consolidated stone was further confirmed through gravimetric analysis for the determination of solid content reported in Table 1 and displayed in Fig. 6. It is evident that NC-12C and NC-29C exhibit an equilibrium mass after ~ 5 days of weighing, whereas treatment NC-25C requires approximately 4 weeks to establish equilibrium under laboratory conditions. Therefore, an accumulation of solid content after curing on the surface and in the subsurface zone can be related to a back-migration of particles, carried with the solvent during evaporation (see Fig. 6b). Specifically, the first drying phase is governed by capillary forces; only during later stages, the drying behaviour changes and can be attributed to diffusion velocities (i.e. vapor diffusion). Franzen and Mirwald already demonstrated such a process in natural stone using water [35]. The present study confirms that such behaviour is also present for colloidal water and water/ethanol systems.

Treatments NC-12C and NC-29C show comparable distribution depth behaviour after curing, which is distinguishable from that of treatment NC-25C. NC-25C shows the most promising depth distribution, possibly explained through its chemistry. Namely, the higher relative humidity and temperature on-site favour an immediate gelation of the consolidant. Moreover, the pore walls of an on-site object might contain more water, thereby catalysing polymerisation more effectively. An initiated gelation would hamper a back-migration of the consolidant and could have a positive effect on the distribution of the consolidant inside the stone.

The analytical model can be evaluated using two approaches. The first possibility is to describe the results through the two terms obtained from Eqs. (9) and (10). The first term A , in Eq. (9), corresponds to the image-analysed porosity after consolidation (i.e. concentration of solid content that remained inside the stone). In contrast, the term B , found in Eq. (10), is more difficult to analyse, as it describes a variety of physical parameters, which, if assessed experimentally one by one, could provide advanced insights (and not average, mathematically derived values) that possibly fit with more precision to the experimental data. Both terms are evaluated in Table 4.

It is evident that the stone structure exhibits a range of porosities, given by term A , even though the examined drilled cores belonged to the same architectural element. This explanation is intuitive, as the material under study is a highly heterogeneous stone, consisting of many fragments of various shapes and dimensions. The term B describes phenomena such as permeability and diffusivity, which are linked to structural changes. Moreover, wettability of crystalline material also depends on microtextural variations and chemical composition, evident in various samples of the stone. However, neither term can be explained solely through the substrate; the interaction of the consolidant with the substrate plays a role as well. Studies concerning the latter are lacking in published research. As an example, it is not known how different wettabilities influence a reaction between consolidant and substrate or how a colloidal suspension diffuses with respect to varying roughnesses or distributions of pore radii. Such processes would involve the study of capillary or interfacial forces, surface complexations and electrostatic interactions, to name few phenomena that would need to be considered when assessing the interaction of substrate and consolidant. Nonetheless, a second

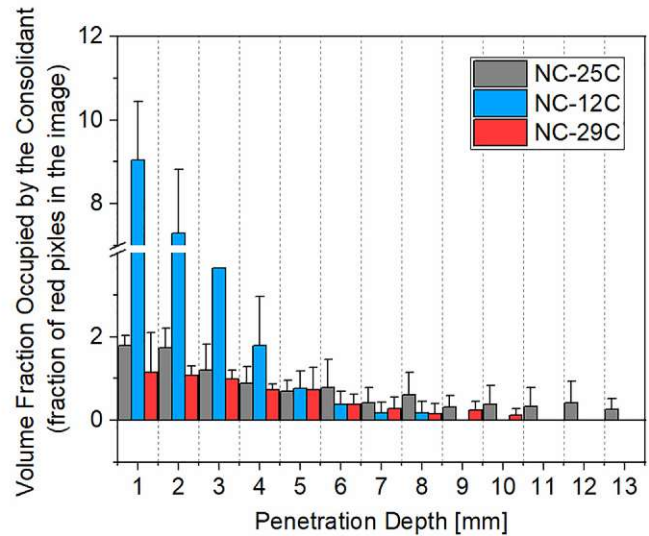
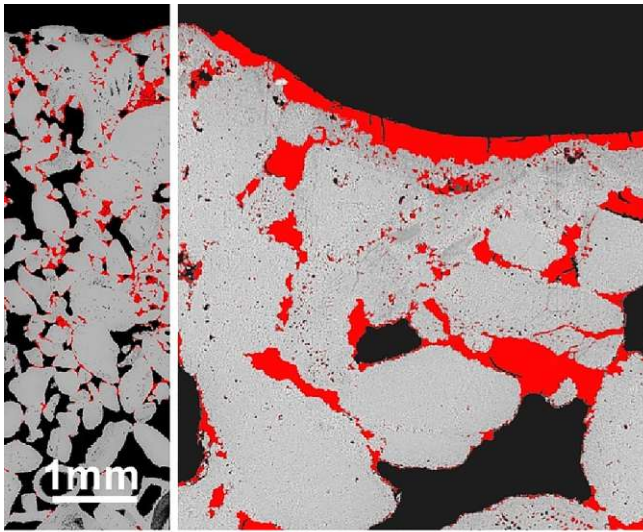


Fig. 3. Left: Example of distribution depths of a consolidant, assessed by image analysis and false-colour mapping. Right: A graph displaying the volume fraction occupied by the consolidant in the stone structure as a function of sample depth.

Table 3
Qualitative SEM analysis of polished cross-sections of the treated stone.

Treatment	Distribution depth ^(*)	Adhesion between stone and consolidant	Bridging between grains
NC-25C (HFES70)	~15 mm	+	average of ~ 50 μ m
NC-12C (ZG12)	~10 mm	+++	up to 100 μ m
NC-29C (ZR110)	~10 mm	+++	up to 100 μ m

^(*) The distribution depth is limited through the sample size analysed. Coding for the evaluation of adhesion: (+++) good and (+) poor.

possibility for evaluating the analytical model and giving predictive indicators of treatment performance lies in modifying the well-known exponential function $f(x) = e^x$, with the following constants added to the equation:

$$c(x) = C_1 + C_2 \cdot e^{(-C_3 \cdot x)} \quad (13)$$

The constants are obtained by a basic nonlinear exponential curve fitting using the software OriginPro[®]. Herein, constant C_1 describes the offset from the Y axis, constant C_2 describes the offset from the X axis and constant C_3 relates to the vertical exaggeration of the exponential curve. An evaluation based on Eq. (13) is often used in cases in which exponential phenomena play a role, as is the case with degradation patterns [36]. All constants found in Eq. (13) are also reported in Table 4 for each of the three consolidants.

Empirical meanings of these constants can be extrapolated from the real-world results. A higher C_1 value, in the present case the value that is closer to zero, indicates deeper distribution, corresponding to the concentration of consolidant at the maximum analysed depth in the specimen. This value does not correspond solely to the distribution depth of solid content of consolidant but also to the ratio of consolidant and to the stone porosity at a given depth. The term C_2 relates to the term C_1 as it describes the difference between the concentration present on the surface and that present at the maximum analysed depth in the sample. The C_2 value gives insights into the homogeneity of the distributed consolidant from the surface to the analysed depth. The lower the C_2 value, the more homogeneous the distribution is along the depth transect. As regards the exponential coefficient of the distribution depth curve given by C_3 , lower values indicate that the distribution is more homogeneous along

the depth transect. The higher the C_2 and C_3 values, the more solid content is placed in the near-surface zone. However, these interpretations are based on a mathematical treatment of the constants, in which the concentration of solid content is not considered. That is, if the same distribution of fitted points on the curve is present but with higher values, the constants yield the same values, underestimating the importance of the solid content concentration. Still, C_2 and C_3 are valuable indices for mechanical differentiation stresses that can come about if more consolidant is present at the very surface followed by an abrupt concentration change at shallow depth. Such distributions might cause an over-consolidation of the near-surface zone. It is important to note that consolidant distribution is itself an incomplete criterion, since more solid content might be needed in the vicinity of the surface, where a more pronounced decay is usually found. To deepen the above described mathematical evaluation regarding a treatment performance, the consolidants used must be further evaluated with mechanical tests.

Finally, the used approach to mathematically describe the distribution depth could be extrapolated for the entire monument. However, it should be noted that an extended diagnostic is necessary. As different micro and macro climatic conditions are found on-site, with varying exposures, different decay patterns will be present. This might have an influence on a treatment's performance and thus the distribution depth of applied consolidants. Nevertheless, the used approach can help identify various parameters that possibly influence a penetration depth (e.g. state of the substrate, application cycle, application method, curing conditions, type of consolidant, etc.). This methodology allows for an advanced description and a possible preparation of a model that takes more physical and chemical phenomena into account.

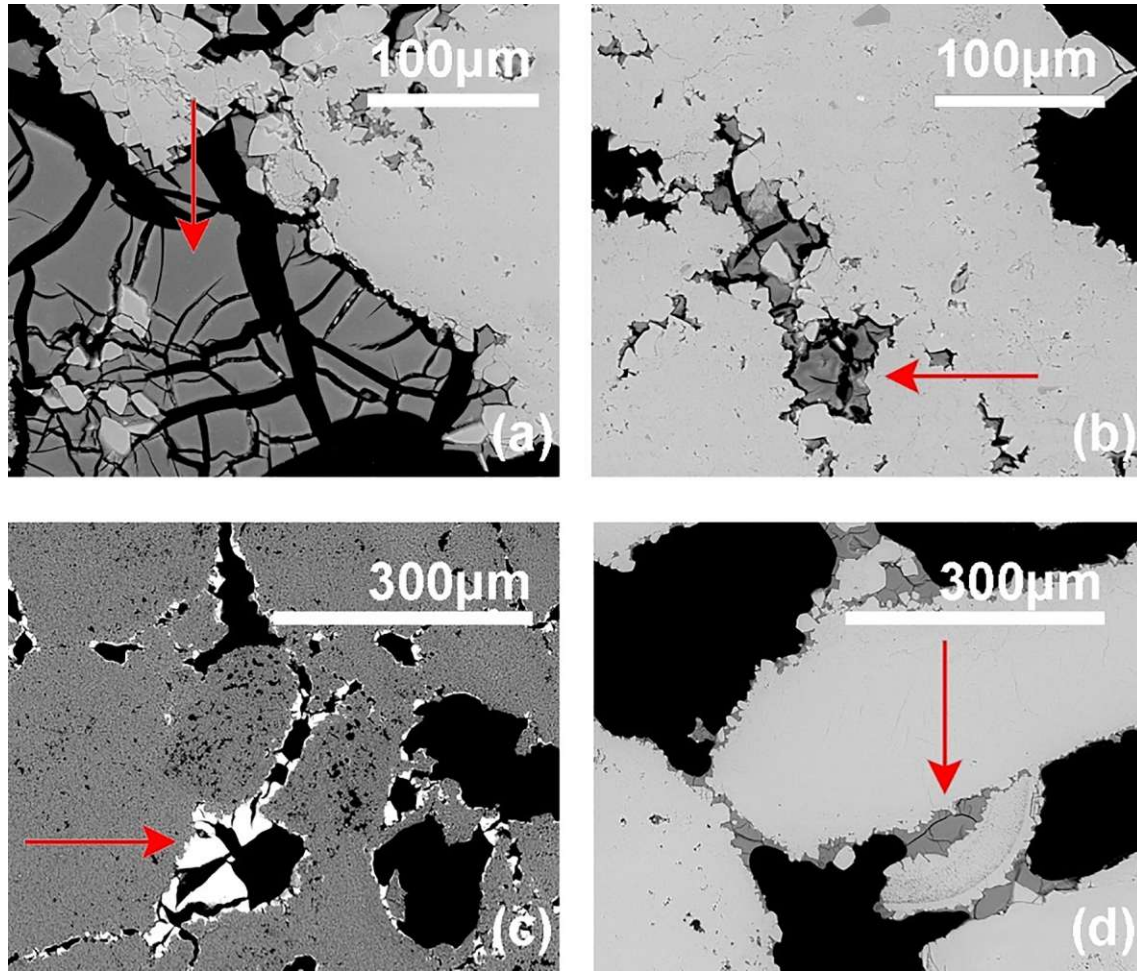


Fig. 4. Example micrographs of laboratory-treated stone showing consolidant properties. **a)** Cracking present in the silica gel matrix of consolidant NC-25C. **b)** Partially loose silica gel plates of NC-25C in the pore space. **c)** Good adhesion between *St. Margarethen* and nano-zirconia (NC-29C). **d)** Good adhesion between *St. Margarethen* and nano-silica (NC-12C).

3.2. Cross-validation with mechanical tests

Mechanical tests performed on-site after application of consolidants included drilling resistance measurements in the vicinity of the SEM analysed samples (approx. distance of 2–3 cm), whereas mechanical tests performed in the laboratory included sound speed propagation tests as well as splitting tensile strength tests on sound, artificially aged and treated samples. The results from drilling resistance measurements performed before and after the treatment can be seen in Fig. 7. The outcome clearly mirrors the results obtained through SEM image analysis. In particular, an exponential decline is also visible through drilling resistance measurements, for treatments NC-12C and NC-29C. Both of those consolidating materials exhibited an over-consolidation in the first two millimetres, where the surface became higher in strength than at higher penetration depths. However, consolidation treatment was necessary, as conveyed by all the drilling resistance values prior to treatment. That is, the very low values of drilling resistance prior to consolidation reveal that the weathered stone was initially of low mechanical strength and that the surface was disintegrated. After treatment, an increase in drilling resistance was observed for all three consolidants, implying some restoration of the strength of the material. It is important to note that the starting stone conditions are different for different samples even under a single consolidant's treatments, as observed in Fig. 7c within treatment NC-29C. In that case, a surface higher in drilling resistance was already pre-

sent before the consolidant was applied. Such situations are most probably caused by the presence of gypsum inside the stone structure, as observed by SEM (see Fig. 2b).

Such over-consolidation phenomena might pose a danger by setting up strong differences in mechanical and physical properties in the material and abrupt transitions (i.e. higher strength at the very surface, decreasing drastically as in the cases of NC-12C and NC-29C). Consequently, over-consolidation can result in spalling or pore clogging. However, more research concerning such phenomena is needed in order to assess the effectiveness and compatibility of a given consolidant that exhibits over-consolidation. Micromechanical and nanomechanical studies of various consolidants [37] should be performed in order to assess the cohesion of the consolidant. In addition, macroscopic mechanical tests should be performed with different stiffnesses present in the stone [38] in order to assess the cohesion of the consolidated stone. Furthermore, a possible way to overcome the accumulation of the consolidant near the surface, if caused by a back-migration, could be pretreatment of the surface (e.g. prewetting with alcohol) or a more controlled aftercare until curing completes. Likewise, cyclic treatments or different application techniques might help control the outcome of a treatment's depth distribution. A promising method might be the overlapping application of multiple consolidants to combine their advantages.

Further laboratory mechanical analysis included the determination of the dynamic modulus of elasticity and the splitting tensile

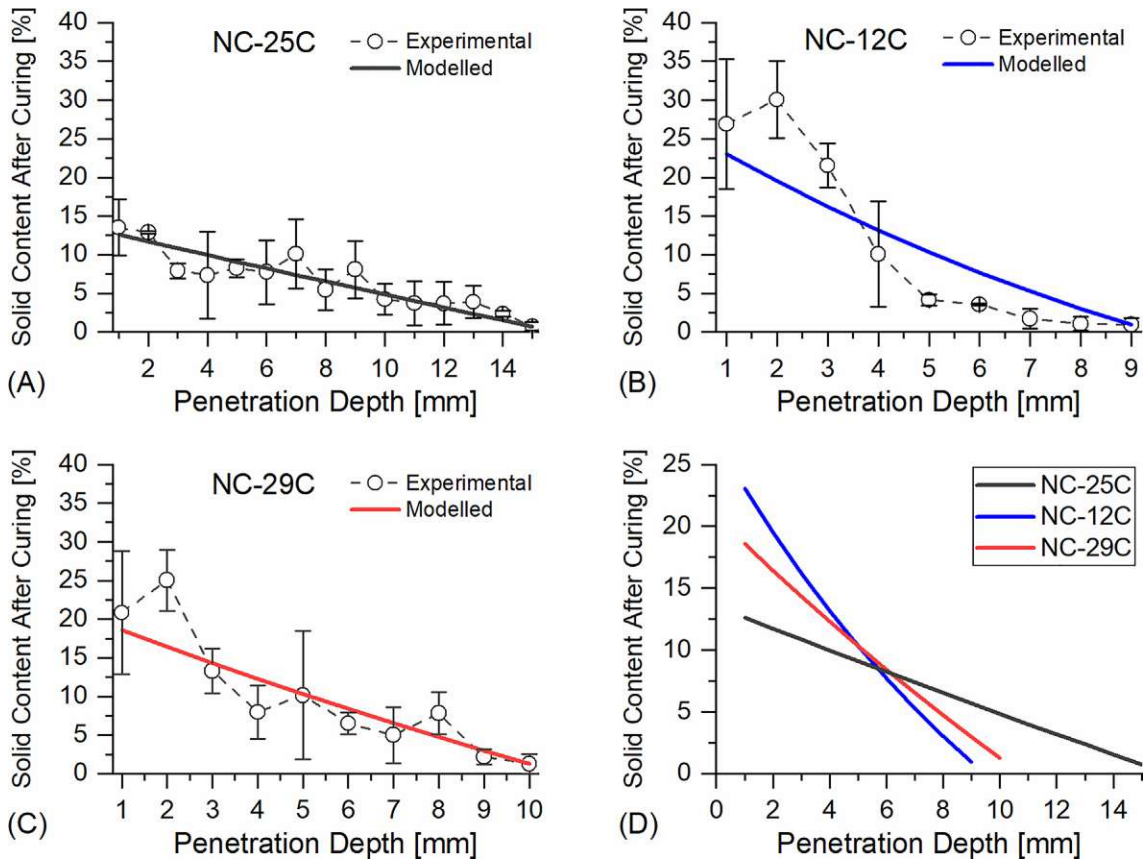


Fig. 5. Comparison of experimental (symbols) and modelled curves (lines) obtained from image analysis of the drilled cores and the analytical model, respectively, for **a)** NC-25C (titania-modified alkoxyxilane), **b)** NC-12C (nano-silica) and **c)** NC-29C (nano-zirconia). **d)** Overlap of all three treatments as obtained through the analytical model, to emphasise the differences in their depth distributions. The Y axis displays the percentage connected to solid content after curing as a function of the stone's effective porosity.

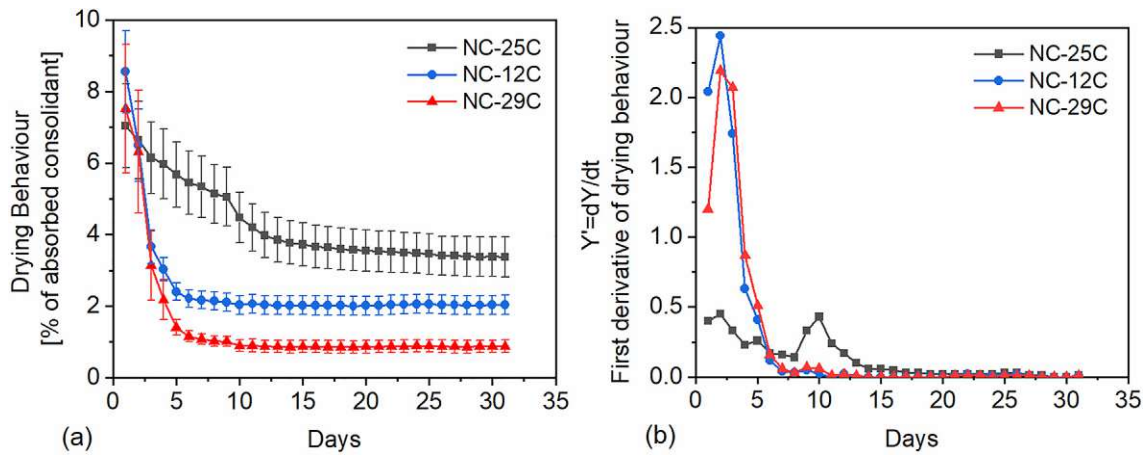


Fig. 6. **a)** Gravimetric monitoring of the mass loss recorded after consolidation, for a total of 30 days. The height at equilibrium corresponds to the amount of solid content residue in the stone structure, as determined for three specimens with dimensions $5 \times 5 \times 5$ cm under laboratory conditions ($\sim 50\%$ RH, $\sim 22^\circ\text{C}$). **b)** First derivative of the mass loss to indicate the importance of capillary forces during the first days of drying for treatments NC-12C and NC-29C.

Table 4

Constants A and B calculated from image analysis and iterated through the analytical model, respectively. And, constants C_1 to C_3 used to assess the treatments performance, as evaluated through the modified exponential function in Eq. (13).

Treatment	A	B	C_1	C_2	C_3
NC-25C (HFES70)	0.09	0.08	-28.042	41.555	0.024
NC-12C (ZG12)	0.09	0.85	-30.936	57.849	0.064
NC-29C (ZR110)	0.04	0.69	-53.270	74.096	0.031

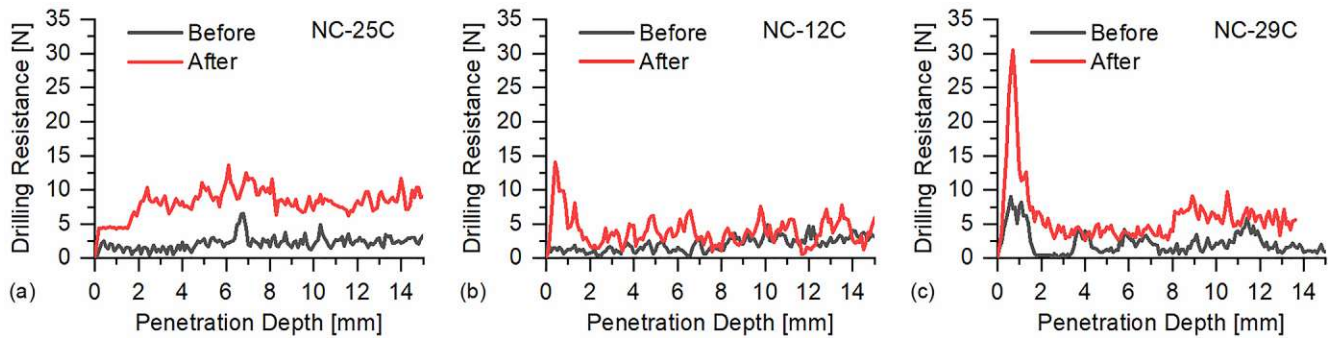


Fig. 7. Drilling resistance measurements performed on-site on St. Margarethen before and after treatment with a) NC-25C, b) NC-12C and c) NC-29C.

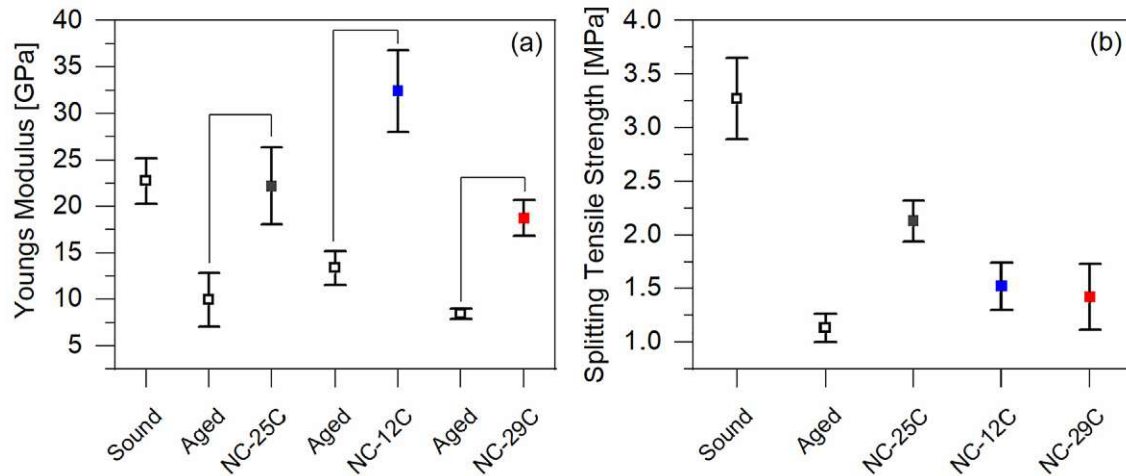


Fig. 8. a) Young's modulus and b) splitting tensile strength tested on sound (fresh), artificially aged (heat treated) as well as artificially aged and subsequently consolidated specimens treated in the laboratory. Please note that for the determination of the Young's modulus (Fig. 8a), the same specimens were tested in different conditions (non-destructive testing method), while the determination of splitting tensile strength (Fig. 8b), was carried out on different sets of samples (destructive testing method).

strength. These data supported the findings obtained on-site through drilling resistance measurements, as can be seen in Fig. 8.

The Young's modulus increased after the application of each of the three treatments and equalled or exceeded the values of the sound or fresh stone. Judged by these tests, treatment NC-12C shows the largest increase. However, these values can also depend on the deposition of the consolidant inside the structure. If the consolidant is well distributed in the sample volume and placed between the grain contacts, it can attain higher values. Nevertheless, those high values may not correspond with the macroscopic mechanical strength, as the cohesion of the consolidant itself might be poor. Therefore, splitting tensile strength tests have been done to confirm mechanical performance. In those tests, it was evident that the consolidant with the highest mechanical strength gain was NC-25C, followed by NC-12C, itself followed closely by NC-29C. The reason for this result lies most probably in the solid content after curing. Notably, the solid content after curing for NC-25C was two to four times higher than those of the other consolidants (see Table 1). If more consolidator solids remain in the stone matrix, it is likely that the strength will increase that much more. Earlier studies of a similar type, in which different alkoxy-silanes with varying gel deposition rates were tested, confirm this hypothesis [39]. The amount of consolidant deposited inside the structure is the governing aspect for the mechanical strength gain. Moreover, the same trend can be confirmed through the drilling resistance measurements in Fig. 7. In those measurements, NC-25C showed the highest value, followed by lower drilling resistance values observed for NC-29C and NC-12C.

All three treatments showed an essential gain with respect to mechanical strength in laboratory and on-site measurements. To determine the possibility of harmful over-consolidation effects, additional studies concerning the compatibility of the treatments (e.g. water vapour diffusion tests, durability tests, etc.) need to be done in the laboratory with comparable depth distributions of consolidants.

4. Conclusions

The aim of the present study was to analyse the distribution depth of stone consolidants applied on-site after curing and to mathematically model, with an analytical approach, the concentration of the consolidants' solid content as a function of depth within the stone. Three consolidants were applied on a historical façade of St. Stephen's Cathedral in Vienna, Austria. The drilled cores examined by SEM and image analysis showed that all consolidants exhibited an exponential decline of consolidant solid content with increasing depth into the stone, being highest on the surface and subsurface area and declining towards the inner part of the structure to different extents. The model based on a version of one-dimensional Fick's second law successfully describes the depth distribution, allowing improved interpretations and performance indicators for different stone consolidation treatments. We conclude that capillary forces, acting upon drying, are the governing factor for the distribution of the consolidants within water-based nano-zirconia and water-alcohol-based colloidal silica. For reactive alkoxy-silane, capillary forces acting upon drying are less pro-

nounced, which is why such consolidants exhibit a more homogeneous depth distribution. Furthermore, we determine that drilling resistance measurements performed on-site, in the vicinity of the bore holes where the drilled cores have been extracted, confirm the modelled and image-analysed findings. Young's modulus and splitting tensile strength tests on laboratory-treated specimens further confirm the mechanical strength gain assessed through drilling resistance measurements. Finally, we hope that the present study lays a foundation for systematic activities of modelling in the area of stone consolidation, which is lacking in published research and is urgently needed in order to address the complexity of a given treatment's outcome.

CRedit authorship contribution statement

Matea Ban: Conceptualization, Data curation, Formal analysis, Investigation, Methodology, Validation, Visualization, Writing - original draft. **Laura Aliotta:** Conceptualization, Data curation, Formal analysis, Investigation, Methodology, Validation, Writing - review & editing. **Vito Gigante:** Conceptualization, Data curation, Formal analysis, Investigation, Methodology, Validation, Writing - review & editing. **Elisabeth Mascha:** Investigation, Methodology, Writing - review & editing. **Antonella Sola:** Investigation, Methodology, Writing - review & editing. **Andrea Lazzeri:** Conceptualization, Funding acquisition, Project administration, Supervision, Writing - review & editing.

Funding Sources

The authors acknowledge TU Wien University Library for financial support through its Open Access Funding Programme. The consolidants studied in the present work have been developed through the supported by the 'Nano-Cathedral' project, funded by the European program Horizon 2020 Call NMP21-AC "Nanomaterials for conservation of European architectural heritage developed by research on characteristic lithotypes" (GA 646178).

Declaration of Competing Interest

The authors declare that they have no known competing financial interests or personal relationships that could have appeared to influence the work reported in this paper.

Acknowledgements

Cecilia Pesce and Lukas Achleitner are gratefully acknowledged for their support in the lab. We thank Peter Urbanek and Paul Sonnleitner for proofreading and generally supporting this work. Johannes Weber and Andreas Rohatsch are recognised for their help in discussing the data. The authors thank Colorobbia S.p.A (Italy) for the supplied consolidant NC-12C, Technologia Navarra de Nanoproductos, S.L. - Tecnan (Spain) for NC-29C and ChemSpec S.R.L. (Italy) for NC-25C.

Appendix I

Equation (11) is a computed solution, using WolframAlpha LLC (Software Mathematica), while equation (12) is analytically derived. In the following, the mathematical rearrangement from the analytical solution to the computed answer is shown:

$$c(x) = \frac{(C_L - C_0) \cdot e^{-ABx} - (C_L - C_0) + C_0 \cdot (e^{-ABL} - 1)}{e^{-ABL} - 1} \tag{A1}$$

$$c(x) = \frac{C_L \cdot e^{-ABx} - C_0 \cdot e^{-ABx} - C_L + C_0 + C_0 \cdot e^{-ABL} - C_0}{e^{-ABL} - 1} \cdot \frac{-e^{+ABL}}{-e^{+ABL}} \tag{A2}$$

$$c(x) = \frac{-C_L \cdot e^{-ABx} \cdot e^{+ABL} + C_0 \cdot e^{-ABx} \cdot e^{+ABL} + C_L \cdot e^{+ABL} - C_0 \cdot e^{-ABL} \cdot e^{+ABL}}{e^{+ABL} - 1} \tag{A3}$$

$$c(x) = \frac{C_0 \cdot (e^{-ABx} \cdot e^{+ABL} - 1) + C_L \cdot (e^{+ABL} - e^{-ABx} \cdot e^{+ABL})}{e^{+ABL} - 1} \tag{A4}$$

$$c(x) = \frac{C_0 \cdot (e^{-ABx} \cdot e^{+ABL} - e^{-ABx} \cdot e^{+ABx}) + C_L \cdot (e^{+ABL} \cdot e^{-ABx} \cdot e^{+ABx} - e^{-ABx} \cdot e^{+ABL})}{e^{+ABL} - 1} \tag{A5}$$

$$c(x) = \frac{e^{-ABx} \cdot [C_0 \cdot (e^{+ABL} - e^{+ABx}) + C_L \cdot e^{+ABL} \cdot (e^{+ABx} - 1)]}{e^{+ABL} - 1} \tag{A6}$$

Corresponding constants obtained though Eq. (11) and Eq. (12) as well as the modelled curves can be observed in Table A.1 and Fig. A.1.

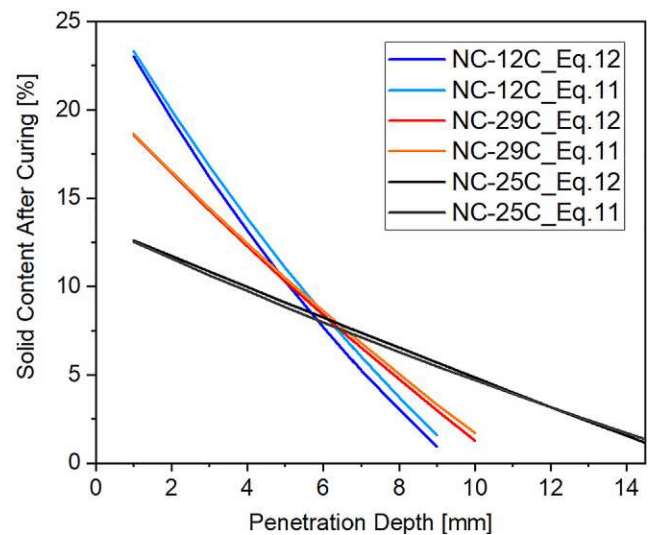


Fig. A1. Comparison between the modelled curves obtained through the computed solution (Eq. (11)) or the analytical model (Eq. (12)) for treatments NC-12C (nanosilica), NC-29C (nano-zirconia) and NC-25C (titania-modified alkoxy silane).

Table A1

Comparison between constants A, calculated from image analysis, and B, iterated through the computed solution (Eq. (11)) or the analytical model (Eq. (12)), respectively. Constants C₁ to C₃ assess a treatments performance, as evaluated through the modified exponential function using Eq. (13).

Treatment	A (Eq.11)	B (Eq.11)	A (Eq.12)	B (Eq.12)	C ₁ (Eq.13)	C ₂ (Eq.13)	C ₃ (Eq.13)
NC-25C (HFES70)	0.09	0.23	0.09	0.08	-28.042	41.555	0.024
NC-12C (ZG12)	0.09	0.63	0.09	0.85	-30.936	57.849	0.064
NC-29C (ZR110)	0.04	0.62	0.04	0.69	-53.270	74.096	0.031

References

- [1] J. Brus, P. Kotlík, Consolidation of stone by mixtures of alkoxysilane and acrylic polymer, *Stud. Conserv.* 41 (2) (1996) 109–119, <https://doi.org/10.1179/sic.1996.41.2.109>.
- [2] R. Ševčík, P. Šašek, A. Viani, Physical and nanomechanical properties of the synthetic anhydrous crystalline CaCO₃ polymorphs: vaterite, aragonite and calcite, *J. Mater. Sci.* 53 (6) (2017) 4022–4033, <https://doi.org/10.1007/s10853-017-1884-x>.
- [3] S.C. De la Rosa-García, A.F. Fuentes, S. Gómez-Cornelio, U. Zagada-Domínguez, P. Quintana, Structural characterization of antifungal CaZn₂(OH)₆·2H₂O nanoparticles obtained via mechanochemical processing, *J. Mater. Sci.* 53 (19) (2018) 13758–13768, <https://doi.org/10.1007/s10853-018-2327-z>.
- [4] D.S. Facio, J.A. Ordóñez, M.L.A. Gil, L.A.M. Carrascosa, M.J. Mosquera, New Consolidant-Hydrophobic Treatment by Combining SiO₂ Composite and Fluorinated Alkoxysilane: Application on Decayed Biocalcareous Stone from an 18th Century Cathedral, *Coatings* 8 (5) (2018), <https://doi.org/10.3390/coatings8050170>.
- [5] A.P. Ferreira Pinto, J. Delgado Rodrigues, Consolidation of carbonate stones: Influence of treatment procedures on the strengthening action of consolidants, *J. Cult. Heritage* 13 (2) (2012) 154–166.
- [6] A. Ferreira Pinto, J. Delgado Rodrigues, Stone consolidation: The role of treatment procedures, *J. Cult. Heritage* 9 (1) (2008) 38–53, <https://doi.org/10.1016/j.culher.2007.06.004>.
- [7] F. Braun, J. Orłowski, Effect of Different Silicic Acid Ester on the Properties of Sandstones with Varying Binders, *Restorat. Build. Monum.* 23 (1) (2018) 1–13, <https://doi.org/10.1515/rbm-2017-0003>.
- [8] G. Borsoi, B. Lubelli, R. van Hees, R. Veiga, A.S. Silva, L. Colla, L. Fedele, P. Tomasin, Effect of solvent on nanolime transport within limestone: How to improve in-depth deposition, *Colloids Surf., A* 497 (2016) 171–181, <https://doi.org/10.1016/j.colsurfa.2016.03.007>.
- [9] J. Delgado Rodrigues, A. Grossi, Indicators and ratings for the compatibility assessment of conservation actions, *J. Cult. Heritage* 8 (1) (2007) 32–43, <https://doi.org/10.1016/j.culher.2006.04.007>.
- [10] M. Ban T. De Kock F. Ott G. Barone A. Rohatsch S. Raneri Neutron Radiography Study of Laboratory Ageing and Treatment Applications with Stone Consolidants Nanomaterials (Basel) 9 4 2019 10.3390/nano9040635
- [11] G. Graziani, C. Colombo, C. Conti, E. Possenti, E. Perelli Cippo, M. Realini, E. Sassoni, Neutron radiography as a tool for assessing penetration depth and distribution of a phosphate consolidant for limestone, *Constr. Build. Mater.* 187 (2018) 238–247, <https://doi.org/10.1016/j.conbuildmat.2018.07.173>.
- [12] F. Hameed, B. Schillinger, A. Rohatsch, M. Zawisky, H. Rauch, Investigations of stone consolidants by neutron imaging, *Nucl. Instrum. Methods Phys. Res., Sect. A* 605 (1–2) (2009) 150–153, <https://doi.org/10.1016/j.nima.2009.01.139>.
- [13] C. Conti, C. Colombo, G. Festa, J. Hovind, E.P. Cippo, E. Possenti, M. Realini, Investigation of ammonium oxalate diffusion in carbonatic substrates by neutron tomography, *J. Cult. Heritage* 19 (2016) 463–466, <https://doi.org/10.1016/j.culher.2015.12.005>.
- [14] M. Slavíková, F. Krejčí, J. Žemlička, M. Pech, P. Kotlík, J. Jakúbek, X-ray radiography and tomography for monitoring the penetration depth of consolidants in Opuka – the building stone of Prague monuments, *J. Cult. Heritage* 13 (4) (2012) 357–364, <https://doi.org/10.1016/j.culher.2012.01.010>.
- [15] M. Lanzón, V.E. García-Vera, A.J. Tenza-Abril, V. De Stefano, Use of image analysis to evaluate surface dispersion and covering performance of nanolime coatings sprayed on heritage material substrates, *Appl. Surf. Sci.* 480 (2019) 962–968, <https://doi.org/10.1016/j.apsusc.2019.03.066>.
- [16] H. Pape, C. Clauser, J. Iffland, Permeability prediction based on fractal pore-space geometry, *Geophysics* 64 (5) (1999) 1447–1460, <https://doi.org/10.1190/1.1444649>.
- [17] B. Berkowitz, I. Dror, S.K. Hansen, H. Scher, Measurements and models of reactive transport in geological media, *Rev. Geophys.* 54 (4) (2016) 930–986, <https://doi.org/10.1002/2016rg000524>.
- [18] G.K. Darbha, C. Fischer, J. Luetzenkirchen, T. Schafer, Site-specific retention of colloids at rough rock surfaces, *Environ. Sci. Technol.* 46 (17) (2012) 9378–9387, <https://doi.org/10.1021/es301969m>.
- [19] A. Rohatsch (2005) Neogene Bau- und Dekorgesteine Niederösterreichs und des Burgenlandes. In: Schwaighofer, B., Eppensteiner, W. (Eds.), "Junge" Kalke, Sandsteine und Konglomerate – Neogen. Mitteilungen IAG BOKU, pp. 27–31.,
- [20] D. Benedetti, E. Bontempi, R. Pedrazzani, A. Zacco, L.E. Depero, Transformation in calcium carbonate stones: some examples, *Phase Transitions* 81 (2–3) (2008) 155–178, <https://doi.org/10.1080/01411590701514342>.
- [21] B.M. Baragona, A. Ghaffari, E. Weber, J. Rohatsch (2016) Artificial aging techniques on various lithotypes for testing of stone consolidants. Paper presented at the Science and Art: A Future for Stone: Proceedings of the 13th International Congress on the Deterioration and Conservation of Stone, Volume 1. Paisley: University of the West of Scotland; Hughes, J., & Howind, T. (Eds.); 2016,
- [22] E. Franzoni, E. Sassoni, G.W. Scherer, S. Naidu, Artificial weathering of stone by heating, *J. Cult. Heritage* 14 (3) (2013) E85–E93, <https://doi.org/10.1016/j.culher.2012.11.026>.
- [23] J. Lukaszewicz, D. Kwiatkowski, M. Klingspor, Consolidation of Gotland stone in monuments Methods of evaluating products for the conservation of porous building materials in monuments: preprints of the international colloquium, Rome, 19–21, 1995, 1995, 179–187.
- [24] L. Normand, S. Duchêne, V. Vergès-Belmin, C. Dandrel, D. Giovannacci, W. Nowik, Comparative in Situ Study of Nanolime, Ethyl Silicate and Acrylic Resin for Consolidation of Wall Paintings with High Water and Salt Contents at the Chapter Hall of Chartres Cathedral, *Int. J. Architect. Heritage* 1–14 (2020), <https://doi.org/10.1080/15583058.2020.1731628>.
- [25] F. Papadopoulos, M. Spinelli, S. Valente, L. Foroni, C. Orrico, F. Alviano, G. Pasquinielli, Common tasks in microscopic and ultrastructural image analysis using ImageJ, *Ultrastruct. Pathol.* 31 (6) (2007) 401–407, <https://doi.org/10.1080/01913120701719189>.
- [26] CEN (2004) Standard EN 14146, Determination of dynamic elastic modulus by measuring the fundamental resonant frequency.
- [27] ASTM International WC, USA (2008) ASTM D 3967–08, Standard test method for splitting tensile strength of intact rock core specimens.
- [28] Y.M. Volkovich, A.N. Filippov, V.S. Bagotsky, Structural properties of porous materials and powders used in different fields of science and technology, Springer (2014), <https://doi.org/10.1007/978-1-4471-6377-0>.
- [29] A. Filippov, V. Starov, D. Llyod, S. Chakravarti, S. Glaser, Sieve mechanism of microfiltration, *J. Membr. Sci.* 89 (3) (1994) 199–213, [https://doi.org/10.1016/0376-7388\(94\)80102-9](https://doi.org/10.1016/0376-7388(94)80102-9).
- [30] A.N. Filippov, R.K. Iksanov, Mathematical modeling of microfiltration of polydisperse suspension on heterogeneous membranes, *Pet. Chem.* 52 (7) (2012) 520–526, <https://doi.org/10.1134/s0965544112070043>.
- [31] J. Happel, H. Brenner, *Low Reynolds number hydrodynamics: with special applications to particulate media*, Springer Science & Business Media, 2012.
- [32] Barenblatt G.I., Entov V.M., Ryzhik V.M. (1989) Theory of fluid flows through natural rocks.
- [33] J. Šperl, J. Trčková, Permeability and porosity of rocks and their relationship based on laboratory testing, *Acta Geodyn. Geomater.* 5 (149) (2008) 41–47.
- [34] Brace W Permeability of crystalline and argillaceous rocks. In: International Journal of Rock Mechanics and Mining Sciences & Geomechanics Abstracts, 1980, vol 5. Elsevier, pp 241–251. doi:10.1016/0148-9062(80)90807-4
- [35] C. Franzen, P.W. Mirwald, Moisture content of natural stone: static and dynamic equilibrium with atmospheric humidity, *Environ. Geol.* 46 (3–4) (2004), <https://doi.org/10.1007/s00254-004-1040-1>.
- [36] M. Drdacky, J. Lesak, S. Rescic, Z. Slizkova, P. Tiano, J. Valach, Standardization of peeling tests for assessing the cohesion and consolidation characteristics of historic stone surfaces, *Mater. Struct.* 45 (4) (2012) 505–520, <https://doi.org/10.1617/s11527-011-9778-x>.
- [37] M. Remzova, R. Zouzelka, J. Lukes, J. Rathousky, Potential of Advanced Consolidants for the Application on Sandstone, *Applied Sciences* 9 (23) (2019), <https://doi.org/10.3390/app9235252>.
- [38] M. Drdáký, Testing Efficiency of Stone Conservation Treatments. In: Majid H, Ioannis K (eds) *Advanced Materials for the Conservation of Stone*. Springer, 2018. pp 175–184, ISBN 978-173-319-72259-72257.
- [39] M. Ban, E. Mascha, J. Weber, A. Rohatsch, J.D. Rodrigues, Efficiency and Compatibility of Selected Alkoxysilanes on Porous Carbonate and Silicate Stones, *Materials (Basel)* 12 (1) (2019), <https://doi.org/10.3390/ma12010156>.

D

Distribution depth of stone consolidants applied on-site:
Analytical modelling with field and lab cross-validation.

Supporting Data

Supporting Information for:

Distribution Depth of Stone Consolidants Applied On-Site: Analytical Modelling with Field and Lab Cross-Validation

Matea Ban ^{a,2,*}, Laura Aliotta ^{b,2}, Vito Gigante ^{b,2}, Elisabeth Mascha ^c, Antonella Sola ^{d,1} and Andrea Lazzeri ^b

^a Institute of Geotechnics, Faculty of Civil Engineering, TU Wien, Austria

^b Department of Civil and Industrial Engineering, University of Pisa, Italy; laura.aliotta@dici.unipi.it, vito.gigante@dici.unipi.it and andrea.lazzeri@unipi.it

^c Institute of Art and Technology, Conservation Science, University of Applied Arts Vienna, Austria; elisabeth.mascha@uni-ak.ac.at

^d Department of Engineering 'Enzo Ferrari', University of Modena and Reggio Emilia, Italy; antonella.sola@unimore.it

* Corresponding author: matea.ban@tuwien.ac.at

¹ Present address: Commonwealth Scientific and Industrial Research Organisation, Manufacturing Business Unit, Metal Industries Program, Clayton, VIC, Australia; antonella.sola@csiro.au

² These authors contributed equally to the work

CONTENTS

Table S1. Petrographic description St. Margarethen.	3
Figure S1. SEM-BSE micrographs of fresh quarried St. Margarethen.	4
Table S2. Porometric data from mercury intrusion tests	5
Determination of Frost Resistance after EN 12371	6
Table S8. Overview of stone decay patterns found on-site	11
Figure S4 to S8. SEM-BSE micrographs of naturally weathered St. Margarethen	12
Table S9. Comparison of water absorption tests on-site	16
Figure S9. Drilling resistance of weathered and fresh quarried St. Margarethen	16
Figure S10, Figure S11 Intermediate restoration state	17
Table S10. Effect of artificial ageing	19
Figure S12. Increase of water absorption and decrease of ultrasound pulse velocity	19
Figure S13. SEM-BSE, overview of artificially induced micro cracks	20
Table S11. Amount of consolidant applied on-site.	21
Table S12. Amount of consolidant applied in laboratory	21
Table S13. Splitting tensile strength and drilling resistance measurements	22
Table S14. Measures of variability for splitting tensile strength	23

Table S1. Petrographic description of the studied lithotype *St. Margarethen*.

General description		
Provenience	St. Margarethen (Burgenland, Leithagebirge, Austria). The so-called “Roman quarry” of St. Margarethen in Burgenland was an important Leithakalk quarry in eastern Austria with an exploitation history dating back to the roman times. The characteristic detritic limestone has been used since as dimension stone for buildings, monuments and their restoration. [1]	
Commercial name	<i>St. Margarethen</i> Leithakalk	
Petrographic Group	Sedimentary rock	
Petrographic Family	Biogeneous sedimentary rock	
Lithotype	Biosparite, grainstone, calcareous arenite	
Typical color	Yellowish-brown to light grey	
Geological age	Miocene/Langhian-Serravallian: Badenian	
Petrographic description		
Components	Composed mainly of small fragments of coralline algae and foraminifera. Additionally, echinoderms, fragments of serpulides and ostracods can be observed.	
Granulometry and texture	In thin sections it occurs very porous and is composed mainly of small fragments of coralline red algae and foraminifera.	
Grain contacts and binder minerals	Components are cemented with microsparitic calcite, a fine-grained calcite.	
Technical Data [2]		
Stone properties	Homogenous variety	Coarse-grained variety
Bulk density	2030 kg/m ³	2060 kg/m ³
Open porosity	15.2 Vol. %	11.2 Vol. %
Water absorption	7.5 M. %	5.4 M. %
Sound speed propagation	3.37-3.52 km/s	3.55 - 4.20 km/s
Compressive strength	25.4 (19.3 - 30.9) N/mm ²	---
Bending tensile strength	5.25 (3.03 - 8.08) N/mm ²	---

See **Figure S1** for details on components, granulometry and texture as well as the binder material.

The preparation of samples is done by vacuum-embedding of the specimen in a blue dyed epoxy resin (Araldite® 2020). Blue colored epoxy resin is used in order to improve the visualization of the open pore spaces. Petrographic thin sections of about 25 µm thickness as well as polished cross sections were produced perpendicular to the surface.

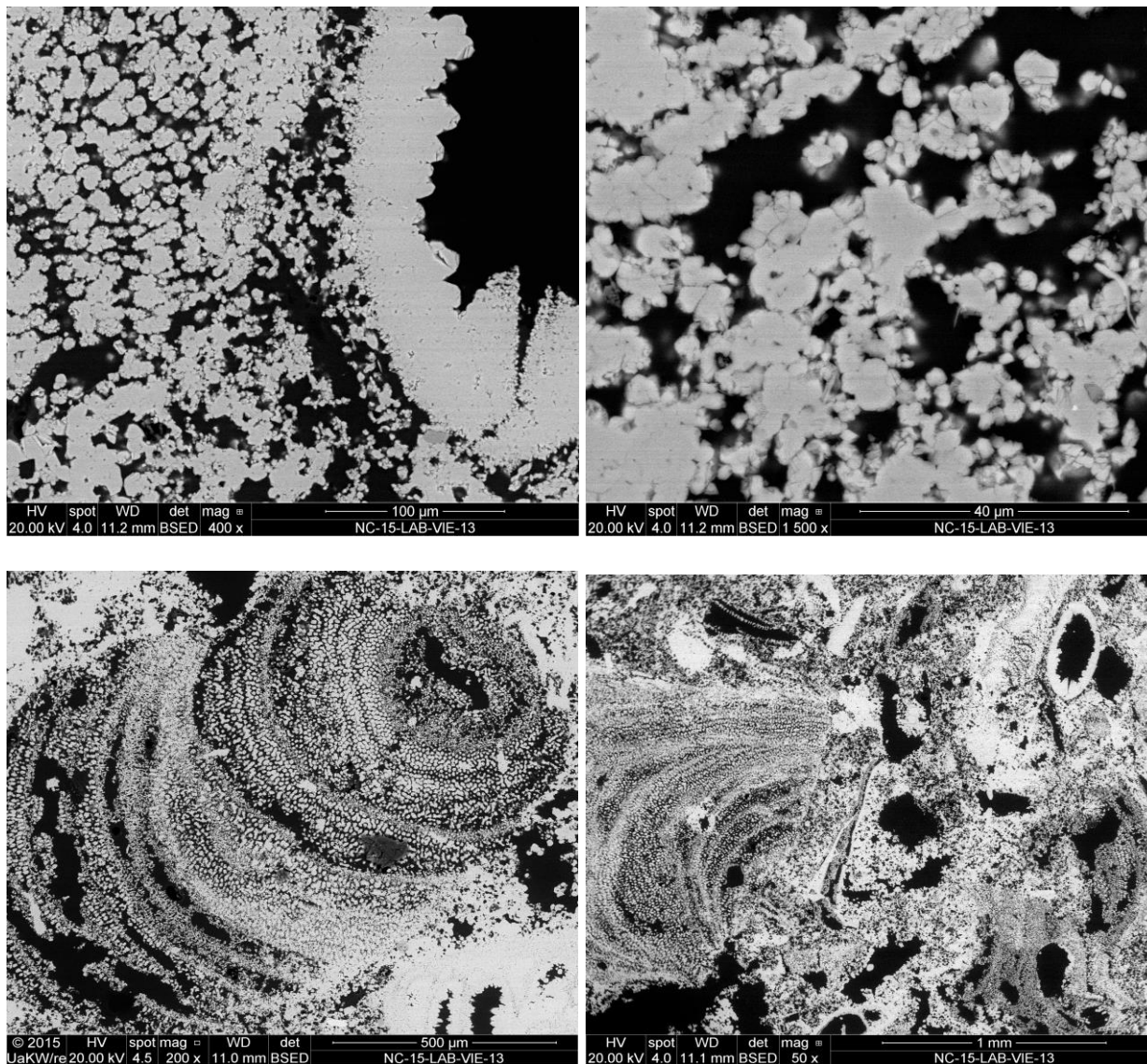


Figure S1. Details of the microstructure exhibiting the rich textural and structural diversity of *St. Margarethen*. Figures at the top show details of the cementation, with the fine-grained calcite, while the bottom figures exhibit fragments of foraminifera (*Heterostegina sp.*).

Table S2. Porometric data from mercury intrusion tests for *St. Margarethen* specimens in fresh conditions with corresponding total pore size.

Characteristics	Double determination		Pore diameter ranges [μm]	Porosity 1 st test [%]	Porosity 2 nd test [%]
	1 st test	2 nd test			
Number of tests	1 st test	2 nd test	150-125	0.000	0.000
Total pore surface [m^2/g]	0.82	3.08	125-100	1.373	2.920
Average pore diameter [μm]	0.48	0.14	100-50	7.184	7.621
Hg-total porosity [%]	20.65	22.54	50-20	4.070	3.925
			20-10	1.661	1.530
			10-5	1.209	1.106
			5-2	1.281	1.061
			2-1	0.865	0.748
			1-0.5	0.710	0.676
			0.5-0.2	0.656	0.546
			0.2-0.1	0.407	0.313
			0.1-0.05	0.386	0.507
			0.05-0.02	0.807	0.166
			0.02-0.01	0.037	0.750
			0.01-0.005	0.000	0.656
			0.005-0.002	0.000	0.000
0.002-0.001	0.000	0.000			

Note that the difference between the determined values (e.g. total pore surface) can be attributed to the intrinsic properties of this lithotype, that is, its textural and structural inhomogeneity. Moreover, mercury intrusion porosimetry tests use rather small specimens (1 cm^3), exaggerating the effect of aggregate size and are therefore prone to deliver less meaningful results for such lithotypes in fresh or weathered conditions.

Determination of Frost Resistance after EN 12371

The effect of freeze/thaw cycles on *St. Margarethen* was studied according to the Test B recommended in the EN 12371 standard. The test allows for estimating the mass loss after 168 freeze/thaw cycles; moreover, in order to quantify the effects of freeze/thaw cycles on the petro-physical properties of the stones, ultrasound velocity and Young's modulus have been measured before testing and after 14, 56, 84, 140 and 168 cycles.

The test has been carried out on six specimens. A total of 168 freeze/thaw cycles have been carried out. Each cycle consists of a 6 h freezing period in air (temperature variation from +20 °C to -12 °C within the 6h), followed by a 6 h thawing period (+5 °C < T < 20 °C) during which the specimens are immersed in water. At the end of the tests (168 cycles), specimens have been weighted to estimate the possible loss of weight; finally, ultrasound velocity and Young's modulus have been measured. Before the testing and after the 168 cycles the change in apparent volume according to EN 1936 was measured. Afterwards the specimens have been left under water for 48h.

For all testing's the specimens were dried at 70 °C until a constant mass was reached. For determination of ultrasound pulse velocity and the Young's modulus the device from *Geotron-Elektronik* was used (see the corresponding manuscript for the details on the device). The climatic chamber MA-C314 with a controller MA-C314ET acquired from Austro Test Hrdina GmbH came to use.

Table S3. Loss of weight [wt-%] after 168 freeze-thaw cycles.

SM ₀	SM ₁₆₈	[Δg]	[Δwt-%]
1378.30	1376.20	2.10	0.152
1754.91	1753.20	1.71	0.097
1425.98	1422.90	3.08	0.216

Table S4. Change of compressional wave velocities V_p [km/s] after 168 freeze-thaw cycles.

SM ₀	SM ₁₆₈	ΔV _p	ΔV _p [%]
3.57	3.22	0.34	9.67
5.22	4.93	0.29	5.50
3.86	3.69	0.17	4.44

Table S5. Change of Young's modulus [kN/mm²] after 168 freeze-thaw cycles.

SM ₀	SM ₁₆₈	ΔE _d	ΔE _d [%]
21.480	10.285	11.195	52
50.977	49.140	1.837	4
23.492	23.119	0.373	2

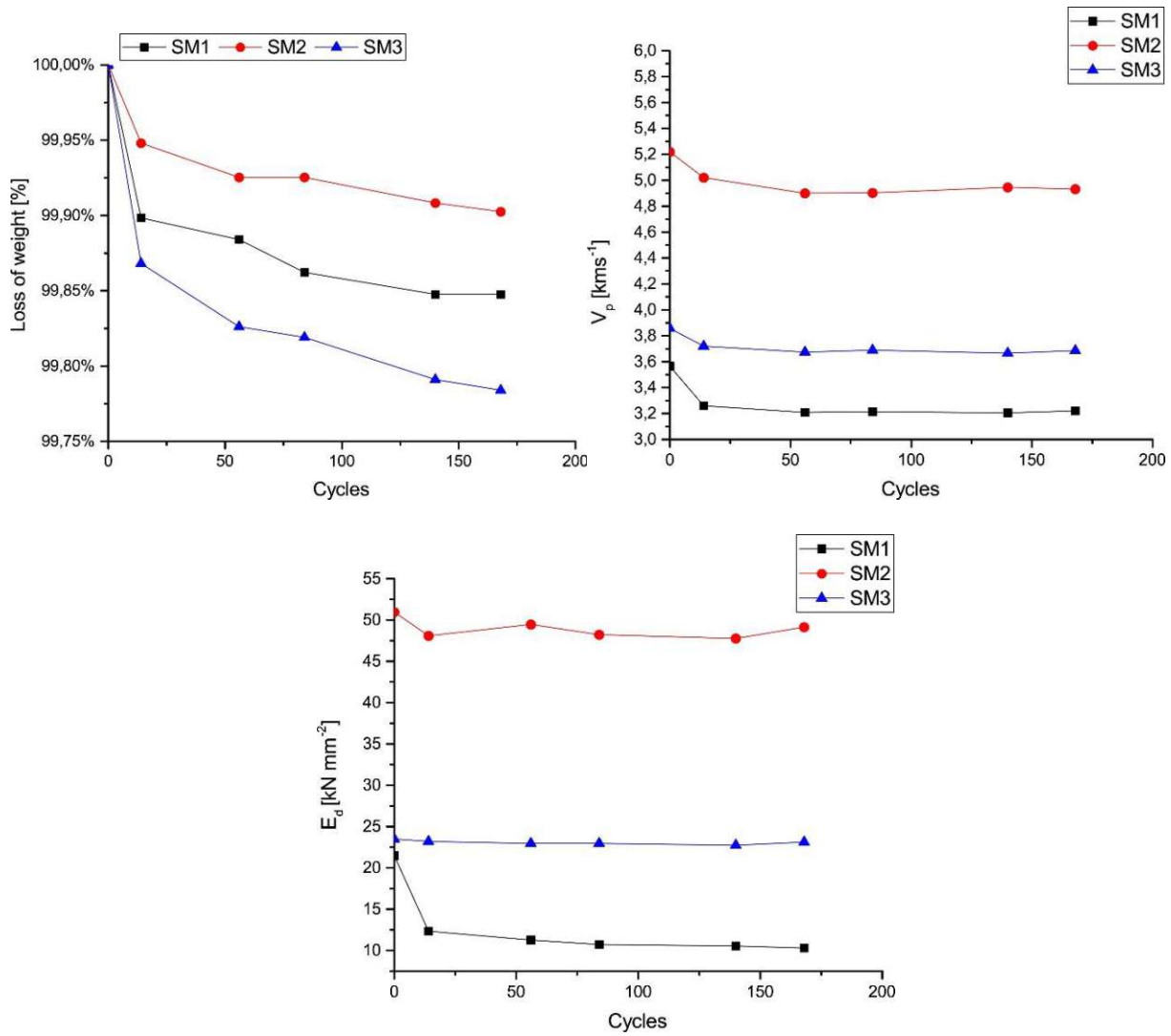


Figure S10. Corresponding visualization for Table S3 to S5

Table S6. Change in apparent volume

Sample	Apparent Vol. V_{b0} [ml] before and after 168 cycles	Note
SM1	730 to 725	
SM2	744 to 739	
SM3	732 to 723	
SM4	---	Specimens with major cracks and/or broken (e.g. Fig. S2)
SM5	---	
SM6	---	

Table S7. Visual inspection

Sample \ Cycles	14	56	84	140	168
SM1	4	---	---	---	---
SM2	0	0	0	1	1
SM3	0	4	---	---	---
SM4	4	---	---	---	---
SM5	0	0	4	---	---
SM6	0	0	0	1	1

After the freeze-thaw cycles, the specimens are examined on all faces and sides and their behaviour is scored using the following scale: **(0)** specimen intact. **(1)** very minor damage (minor rounding of corners and edges) which does not compromise the integrity of the specimen. **(2)** one or several minor cracks ($\leq 0,1$ mm width) or detachment of small fragments (≤ 30 mm² per fragment). **(3)** one or several cracks, holes or detachment of fragments larger than those defined for the '2' rating, or alteration of material in veins, or the specimen shows important signs of crumble or dissolution. And, **(4)** specimen with major cracks or broken in two or more or disintegrated. The number of cycles at which the score of the visual examination attains 3 is noted.



Figure S2. *St. Margarethen* after 56 cycles. Complete failure of the sample.

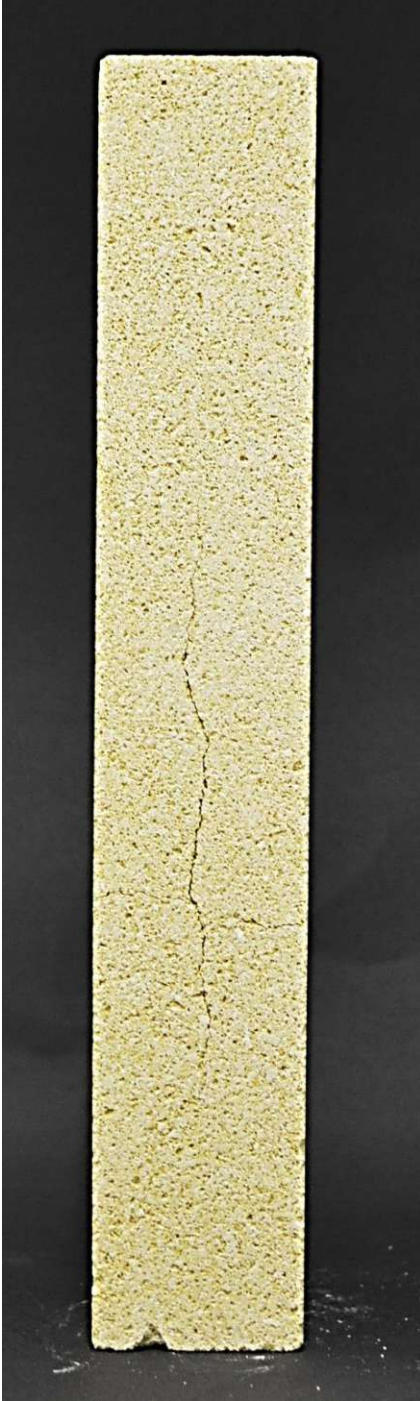


Figure S3. *St. Margarethen* after 14 cycles. Occurance of major cracks.

Interpretation and evaluation

Different intrinsic and extrinsic properties (*e.g.* porosity, temperature, presence of salt and humidity, etc.) influence the frost-thaw resistance of a building stone, which represents one of the major causes of decay in the built environment.

In the case of *St. Margarethen*, the frost-thaw induced star cracks in as few as 14 cycles (see **Figure S3**). However, it should be noted that the test consists in accelerate aging, accentuating the real exposure conditions and cycling rate. The observed decay phenomena cannot be found on-site in the same manner. We explain this behavior by the testing conditions, which exaggerate the water content in the stone during freezing and thawing and cause a premature failing of the specimens [3]. Moreover, to provide an in-depth analysis, more cycles would be necessary to account for the microstructural decay of the fabric [4]. Nevertheless, the results suggest a certain susceptibility towards intrinsic mechanical processes.

No significant changes in apparent volume can be observed within the tested specimens although other methods show more significant alterations. The comparative measurements of ultrasound velocity and Young's modulus before and after the artificial aging, show measurable changes for *St. Margarethen*. It can be concluded that there is a significant difference in deterioration phenomena caused by frost and thawing for this lithotype, also indicated through the three out of six samples that could be analyzed.

Table S8. Overview of stone decay patterns found on-site, on the studied architectural element. The damage analysis was done by means of visual inspection and sample extraction for scanning electron microscopy (coupled with energy dispersive X-Ray spectroscopy) and optical microscopy. Three samples of different size have been extracted and investigated in form of stone chips, thin section, and polished cross section in the frame of the condition assessment analysis.

<i>St. Margarethen</i> calcareous fossil arenite – biosparite grain stone				
Predominant decay phenomena			Secondary decay phenomena	
Decay pattern	Sulphation (gypsum crust formation)	Sulphation	Granular disintegration	Erosion
Key origin of microstructural defect	Mineral replacement reaction and pollutants incorporation	Mineral replacement reaction	Loss of microsparitic calcite binder, dissolution.	Selective loss of components due to chemical weathering (i.e., dissolution).
Depth of defect	On the surface of the rain-shadow areas	Up to 4 cm evidenced	Up to 2.5 cm in depth	Surface and subsurface zone
Width/thickness of defects	~5 mm thickness of black crust.	---	100 µm need to be bridged	---
Conservation requirements	Mechanical removal (e.g. micro chisels) and steam cleaning.	Pre-consolidation after chemically converting gypsum.	Consolidation: structural. Protection: coating can be considered.	Consolidation: structural. Protection: coating can be considered.

The predominant decay phenomenon is the calcite to gypsum transformation in varying depths and densities as well as the creation of black crusts on the surfaces of the studied lithotype. Secondary decay patterns observed on-site include granular disintegration and erosion. The consolidation focused on the former to restore the lost cohesion between the grains. Granular disintegration caused a weakened stone substrate and in severe cases, overlapping with additional decay patterns, a scaling and delamination. The granular disintegration was observed in form of micro cracks and a loss of the microsparitic calcite binder by means of microscopic techniques (see **Figures S4** to **Figure S8**). Furthermore, it was confirmed by means of drilling resistance measurements that the substrates soundness and mechanical strength were reduced (see **Figure S9**).

Beside these above-mentioned main decay phenomena, many other typical deterioration patterns have been documented according to the Icomos glossary on stone deterioration patterns [5]. The observed decay patterns included different types of biological colonization on the stone surfaces (e.g. mosses, lichens, fungus, algae, etc.), leaking joints, efflorescence, macroscopic cracks, the loss of stone substance and many more. It should be noted that an extensive restoration and conservation campaign including chemical and mechanical cleaning of black crusts and biological colonization was undertaken but is not presented in the frame of this work. Instead, the present work focused solely on the granular disintegration decay patterns that needed to be consolidated.



Figure S4. SEM-BSE, overview of the surface and subsurface zone exhibiting cracks parallel to the surface and between the fragments.

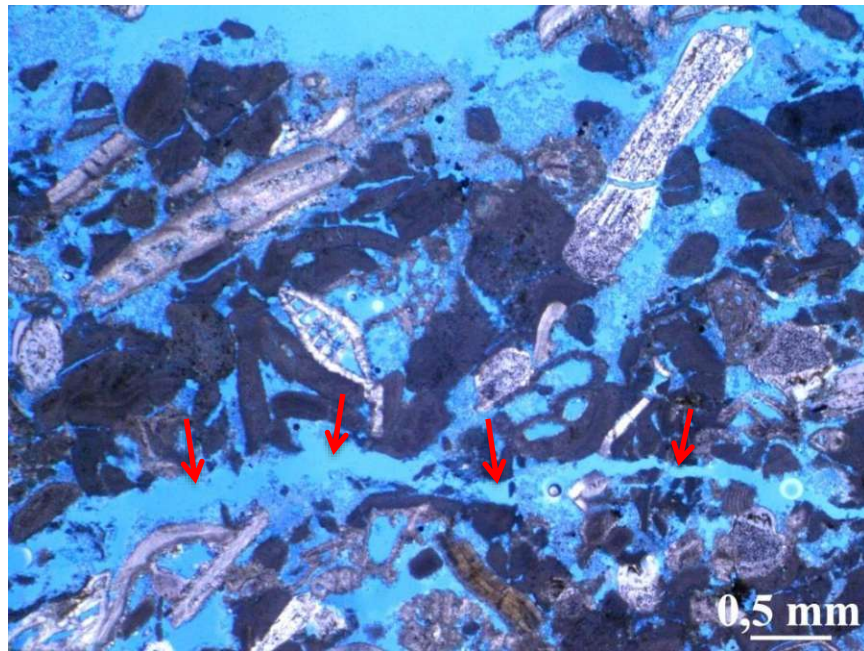


Figure S5. PLM micrograph, thin section, //N. View of a larger crack parallel to the surface.



Figure S6. SEM-BSE, stitched micrograph, overview of dissolution effects (upper part of the sample), granular disintegration with inter- and intragranular micro cracks and the porous microstructure.

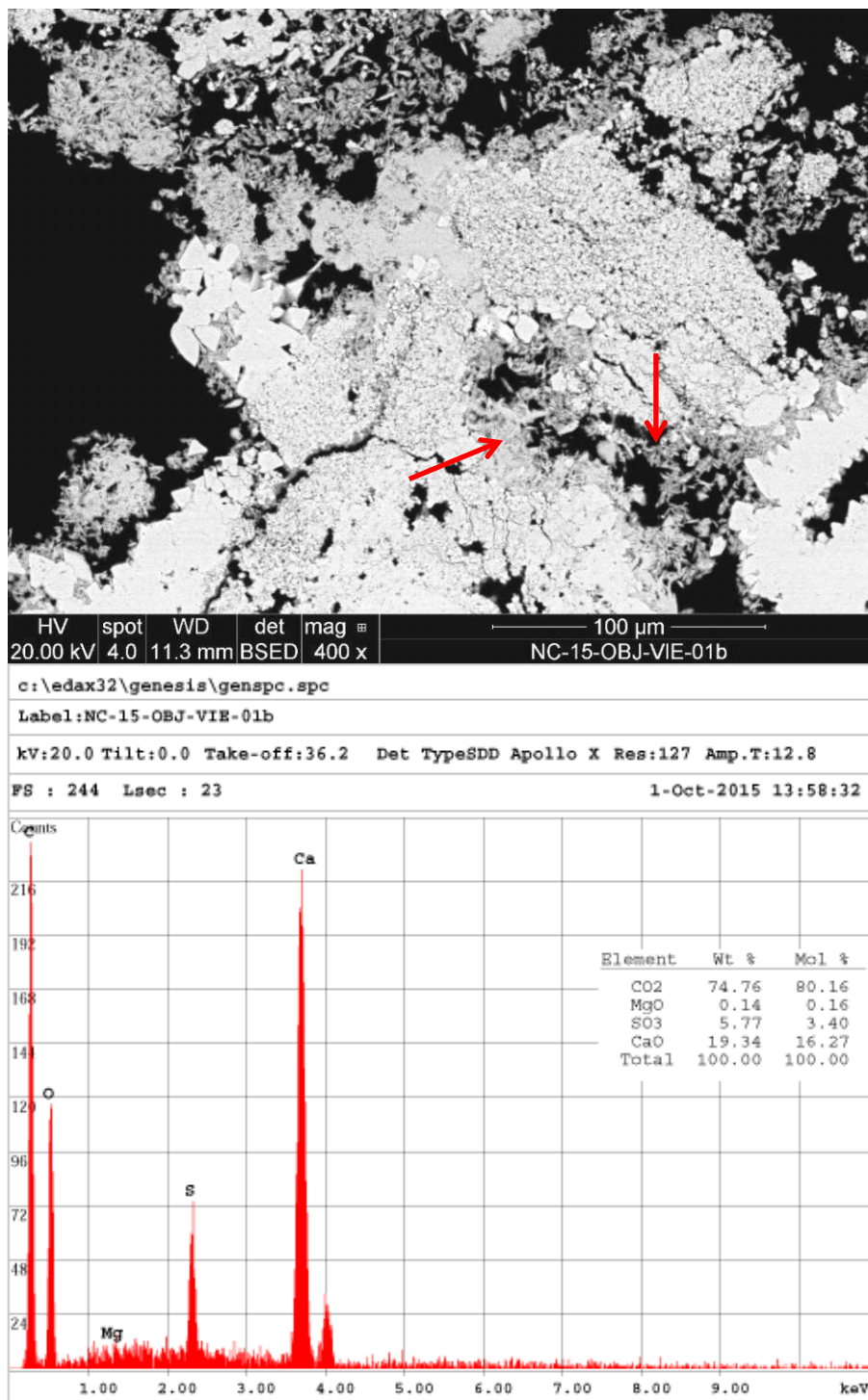


Figure S7. Upper figure: SEM-BSE, details of cracks and presence of gypsum (arrow-indicated). Lower graph: SEM-EDX analysis of the gypsum.

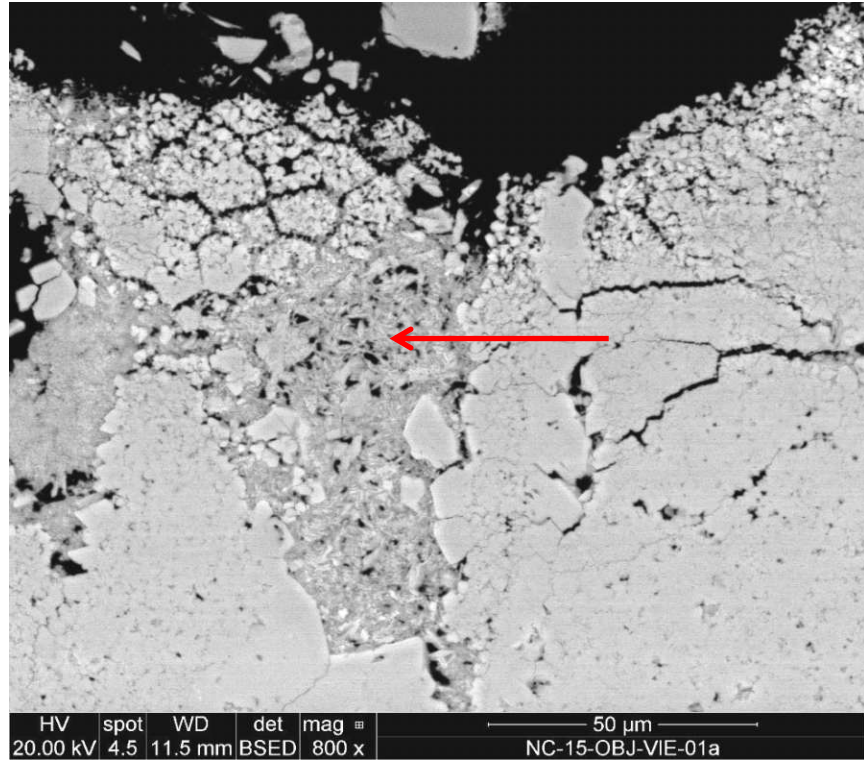


Figure S8. SEM-BSE, details of intragranular micro cracks and gypsum needles within the pores (arrow-indicated)

One of the main disadvantages of the studied on-site area was its variable morphology and thus varying porosity, as can be observed in **Table S9**, **Figures S10** and **Figure S11**.

Table S9. Comparison of water absorption tests on-site to determine the condition of the substrate. An average of four tests was performed with the *Contact Sponge* method, with a contact time of 90 s. In addition, three tests have been performed with *Karsten Tube* and nine tests with the *Mirowski Pipe* to determine the water absorption coefficient after one hour.

Contact time	Contact Sponge	Karsten Tube	Mirowski Pipe
90 s [$\text{g m}^{-2} \text{s}^{-1}$]	6±4	197±187	12±6
60 min [$\text{kg m}^{-2} \text{h}^{-0.5}$]	---	23±12	31±18

These water absorption tests are commonly used to assess the condition of architectural surfaces [6]. The results reveal how inhomogeneous the substrate is, even when it seems homogeneous by visual inspection. Moreover, the wide spread of values in the initial stage of adsorption (i.e., Contact Sponge) as well as after one hour (i.e., Karsten Tube and Mirowski Pipe) indicates that an averaging is not possible. Furthermore, not only the surface but also the profile of degradation exhibits a substrate which condition is in need of a consolidation treatment (see **Figure S9**).

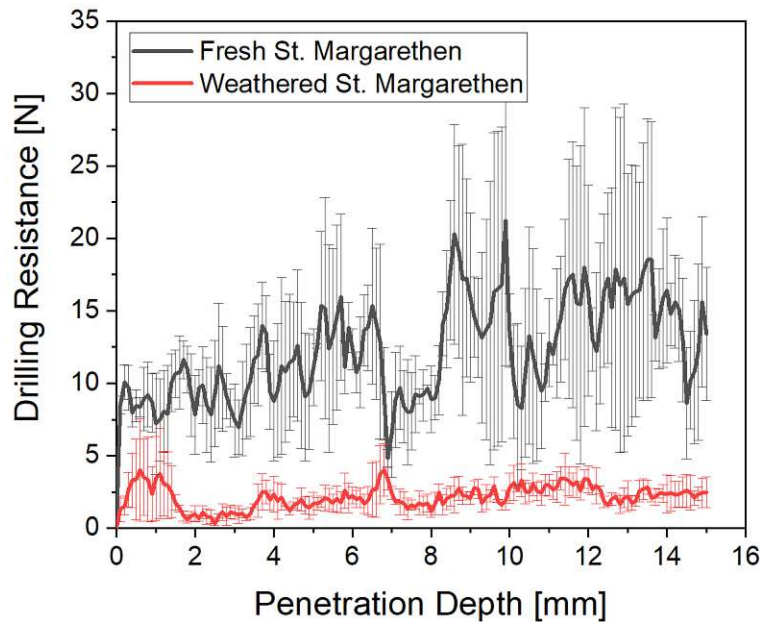


Figure S9. Drilling resistance measurement of weathered and fresh quarried *St. Margarethen*. The curve represents an average of three drilling holes for each condition. The weathered surfaces belong to the studied on-site areas where the consolidants were applied.



Figure S10. Intermediate restoration state, during the cleaning procedure and before treatment application. The rain exposed surfaces marked in red (top figure) have been used for consolidation purposes in the frame of this work. Bottom figures exhibit the differences in densities and decay patterns.



Figure S11. Intermediate restoration state, during the cleaning procedure and treatment application. The consolidants were applied by means of run-off methods with varying utensils.

Table S10. Effect of artificial ageing in respect to water absorption and ultrasound pulse velocity. The reported values were determined on six samples (5 x 5 x 5 cm) heat-treated from 500 °C to 600 °C.

Lithotype	Capillary absorption coefficient Initial value [kg/(m ² h ^{0.5})] Increase Δ WAC [%]			Ultrasound pulse velocity Initial value [km/s] Decrease Δ UPV [%]		
	Mean	Min	Max	Mean	Min	Max
St. Margarethen	7.98 +12.07	6.03 +5.27	8.98 +27.56	3.57 -55.06	3.36 -43.41	3.87 -65.93

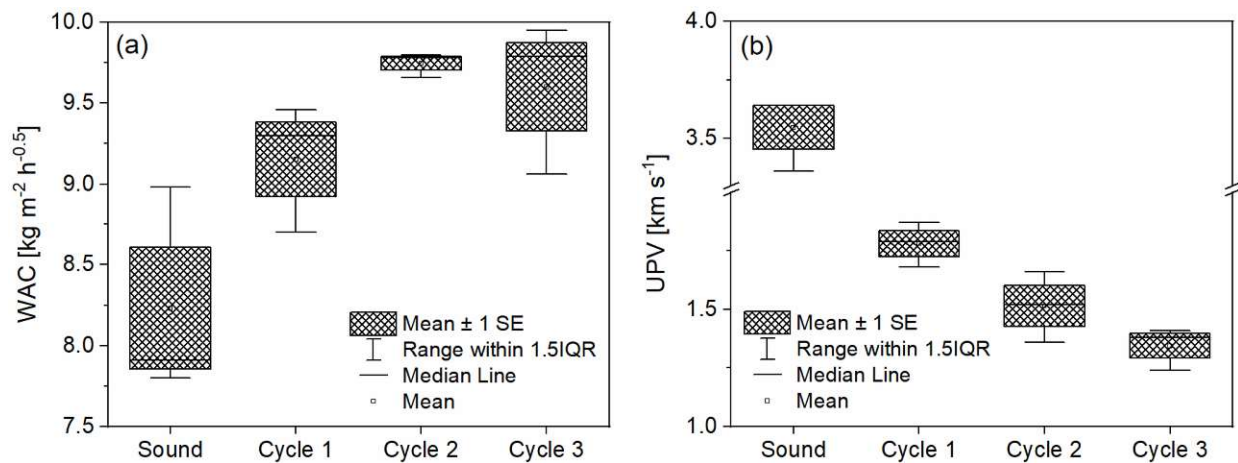


Figure S12. (a) Increase of water absorption coefficient [kg/(m²h^{0.5})] and (b) decrease of ultrasound pulse velocity (km/s) after each cycle of heat treatment at 600 °C. An average of three specimens, 5 x 5 x 5 cm in size, is reported.

The predominate methods for checking the efficacy of the artificial ageing was ultrasonic pulse velocity (apparatus Labek, oscillation frequency 40 kHz) and water absorption coefficient after one hour. One concrete, reproducible result that could be attained quickly with thermal aging was a reduction in ultrasound pulse velocity and an increase of water absorption capillarity, both of which correspond to a reduction in a stone sample's soundness by formation of new micro cracks and the opening of existing cracks (see **Table S10** and **Figure S12**). A general finding of this pre-screening was that heating the stone is by far the most time efficient way to deteriorate and to reach a reduction of soundness reflective of the degradation processes observed in-situ (compare **Figure S4** to **Figure S8** with **Figure S13**), that is, the formation of micro cracks.

The degree of degradation is of major importance when studying stone consolidants; thus, a systematic approach to age the substrate is required. Moreover, the decay level can be specifically tailored, and a systematic investigation of the efficacy is possible. Therefore, the large-scale production of samples on which to test consolidants was mainly achieved through thermal treatment. Nevertheless, it should be noted that the results may vary drastically if specimens with different size are subjected to the same conditions of thermal aging.

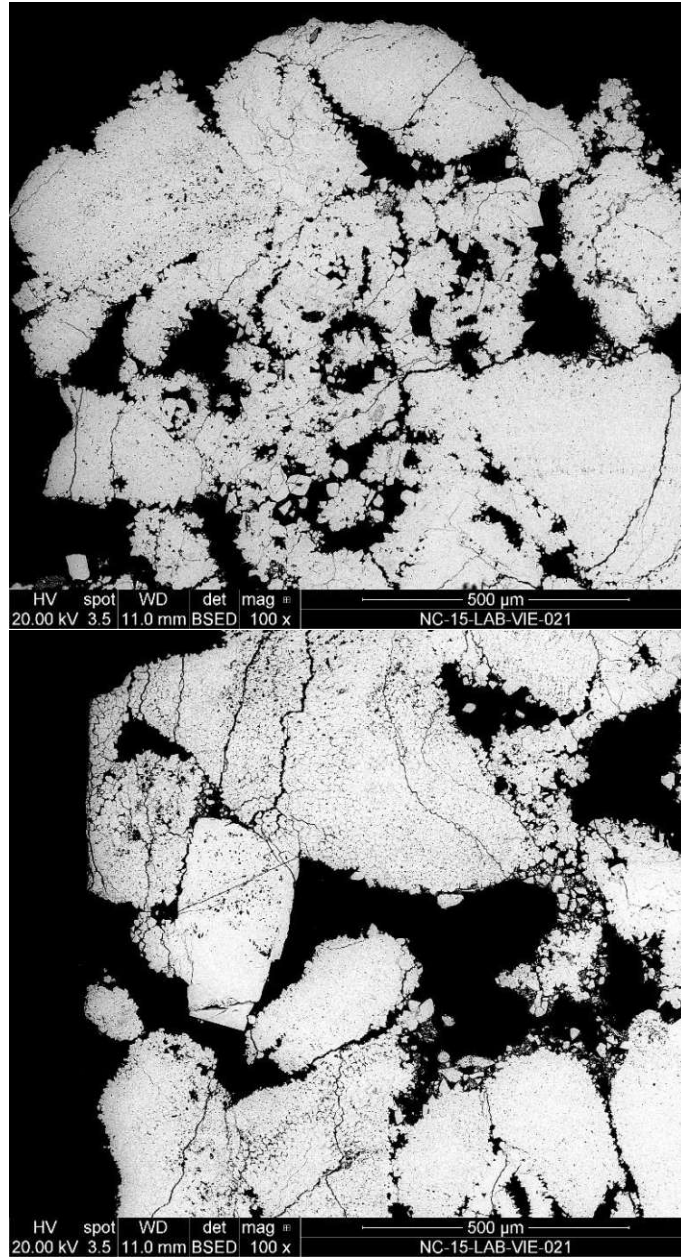


Figure S13. SEM-BSE, overview of artificially induced micro cracks by means of heat-treatment.

The artificially aged or heat-treated specimens allowed an inducement of micro cracks that can also be found on-site. However, their quantity and extent are not equivalent. The artificially aged specimens exhibit a more severe decay pattern when compared to the naturally weathered samples. Anyhow, the type, that is, the intergranular and intragranular micro cracks, can be observed on both, naturally and artificially aged specimens.

Table S11. Amount of consolidant applied on the test areas on-site. Two application cycles were performed by run-off, with an intermitted pause of 24 hours in between the cycles.

Consolidant	Area [cm ²]	1 st cycle [ml]	[ml·cm ⁻²]	2 nd cycle [ml]	[ml·cm ⁻²]	Total [L·m ⁻²]
NC-25C (HFES70)	400	80	0.200	75	0.187	387
NC-12C (ZG12)	400	90	0.225	70	0.175	400
NC-29C (ZR110)	187	30	0.160	100	0.535	695

Note that the second application cycle of the treatment NC-29C (ZR110) tripled in comparison to the first cycle. It was observed that the consolidant did not equally penetrate the test area, some regions were adsorbing more while others stayed dump during the entire application procedure. We explain this behavior by either an intrinsic property of the lithotype (e.g. big inclusions of shell fragments) or a different aging pattern (e.g. varying degrees of mineral replacement reaction and thus formation of gypsum) causing distinct porosities.

It is important to note that the volume of the architectural element is large when compared to the chosen test areas. Therefore, we cannot make confident statements of where the consolidant was distributed. In other words, the actual penetration depth is not known as the consolidants might penetrate in the depths of the architectural element or they might also be distributed along the subsurface zones, or a combination of both.

Table S12. Amount of consolidant applied in laboratory on artificially aged (i.e., heat-treated) specimens with a size of 5 x 5 x 5 cm. The values represent an average calculated on 10 specimens per consolidant. Two application cycles were performed by capillary absorption for one hour, with an intermitted pause of 24 hours in between the cycles.

Consolidant	Area [cm ²]	1 st cycle [ml]	[ml·cm ⁻²]	2 nd cycle [ml]	[ml·cm ⁻²]	Total [L·m ⁻²]
NC-25C (HFES70)	25	13.0 ±5.4	0.521	3.5 ±1.3	0.140	661
NC-12C (ZG12)	25	18.3 ±3.5	0.732	2.8 ±0.3	0.110	842
NC-29C (ZR110)	25	18.9 ±3.1	0.755	1.8 ±0.4	0.072	828

The absorbed amount changes with size and volume of the specimens as well as the conservation state of the substrate. It should be emphasized that a comparison between treatment applications performed in laboratory and on-site are not reliable. Effects like gravity, different treatment application (i.e., run-off and capillary absorption) and curing conditions (e.g. differing relative humidity, micro- and macroclimatic conditions, etc.) affect the outcome of the treatments performance and can therefore not be compared. It is particularly difficult to give meaningful specifications in the case of highly porous architectural elements, where the penetration depths and paths are unknown. In the case of laboratory treatment, for purposes of testing stone consolidants, capillary absorption is a preferred application method [7], as it assures a reproducible

way to apply a consolidant, making the interpretation of results easier. The total absorbed amount can therefore be described reliably only on laboratory treated specimens. In fact, not the total absorbed amount but the solid content after curing, is the governing factor and a direct function of the effectiveness of the consolidant [8]. As the solid content decreases in the following order NC-25C > NC-12C > NC-29C, it is easily accepted that the mechanical strength gain will follow the same trend, as can be confirmed by splitting tensile strength (performed in the laboratory) and drilling resistance measurements (performed on-site), see here for **Table S13**.

Table S13. Splitting tensile strength performed on laboratory specimens and average values (from 2 to 13 mm) of drilling resistance measurements performed on-site, before and after treatment application.

Test	NC-25C		NC-12C		NC-29C	
	Before	After	Before	After	Before	After
Splitting Tensile	1.13±0.1	2.13±0.2	1.13±0.1	1.52±0.2	1.13±0.1	1.42±0.3
Drilling Resistance	2.29±1	8.67±1.4	1.96±1	3.53±1.5	1.98±1.2	4.95±1.5

Note that the average values of drilling resistance measurements for the treatments NC-12C and NC-29C are not following the same trend regarding the above-mentioned solid content after curing when considering the mechanical strength gain. This deviation might be explained through the higher amount of consolidant applied on-site (see **Table S11**).

Table S14. Measures of variability for splitting tensile strength data.

Measures of Variability	Sound σ_t [N/mm ²]	Aged σ_t [N/mm ²]	NC-25C σ_t [N/mm ²]	NC-12C σ_t [N/mm ²]	NC-29C σ_t [N/mm ²]
Average	3.27	1.13	2.13	1.52	1.42
Standard deviation	0.41	0.14	0.19	0.24	0.34
Median	3.19	1.14	2.12	1.51	1.41
Minimum	2.79	0.88	1.89	1.23	0.89
Maximum	4.02	1.38	2.48	1.94	1.79

Table S14 reports on the measures of spread for the destructive test determining splitting tensile strength, as it is not possible to analyse a treatments performance on the same specimens before and after consolidation. Please note that the artificially aged specimens have been consolidated.

Acknowledgements

Lukas Achleitner, Anthony Baragona, Mario Blazevic, Anja Ziniel, Verena Hammerschmidt, Georg Heidfogel, Sofia Zamfirescu, Martin Pliessnig and Malkorzata Mozdyniewicz are gratefully acknowledged for their support in the lab and on-site. Johannes Weber and Andreas Rohatsch are recognised for their help in discussing the data and generally supporting this work.

Author Contributions

M.B. was the main responsible for the condition assessment on-site. E.M. performed the microscopy analysis. M.B. and E.M. evaluated and analysed the data jointly.

Reference

1. Moshammer B, Uhlir C, Rohatsch A, Unterwurzacher M (2015) Adnet ‘Marble’, Untersberg ‘Marble’ and Leitha Limestone—Best Examples Expressing Austria’s Physical Cultural Heritage. *Engineering Geology for Society and Territory* Volume 5:253-257
2. Rohatsch A (2005) Neogene Bau- und Dekorgesteine Niederösterreichs und des Burgenlandes. In: Schwaighofer, B., Eppensteiner, W. (Eds.), “Junge” Kalke, Sandsteine und Konglomerate — Neogen. *Mitteilungen IAG BOKU*, pp. 27-31.,
3. Deprez M, De Kock T, De Schutter G, Cnudde V (2020) A review on freeze-thaw action and weathering of rocks. *Earth-Science Reviews* 203. doi:10.1016/j.earscirev.2020.103143
4. Ruedrich J, Kirchner D, Siegesmund S (2011) Physical weathering of building stones induced by freeze-thaw action: a laboratory long-term study. *Environ Earth Sci* 63 (7-8):1573-1586. doi:10.1007/s12665-010-0826-6
5. Verges-Belmin V (2008) Illustrated glossary on stone deterioration patterns. ICOMOS-ISCS (International Scientific Committee for Stone),
6. Vandevorde D, Cnudde V, Dewanckele J, Brabant L, de Bouw M, Meynen V, Verhaeven E (2013) Validation of in situ applicable measuring techniques for analysis of the water adsorption by stone. *Procedia Chem* 8:317-327. doi:10.1016/j.proche.2013.03.039
7. Ferreira Pinto AP, Delgado Rodrigues J (2012) Consolidation of carbonate stones: Influence of treatment procedures on the strengthening action of consolidants. *Journal of Cultural Heritage* 13 (2):154-166
8. Ferreira Pinto A, Delgado Rodrigues J (2008) Stone consolidation: The role of treatment procedures. *Journal of Cultural Heritage* 9 (1):38-53. doi:10.1016/j.culher.2007.06.004

A.1

Artificial aging techniques on various lithotypes for testing of stone consolidants



myresearchspace.uws.ac.uk

Science and Art: A Future for Stone

Hughes, John; Howind, Torsten

Published: 01/01/2016

Document Version

Publisher's PDF, also known as Version of record

[Link to publication on MyResearchSpace UWS](#)

Citation for published version (APA):

Hughes, J., & Howind, T. (Eds.) (2016). Science and Art: A Future for Stone: Proceedings of the 13th International Congress on the Deterioration and Conservation of Stone, Volume 1. Paisley: University of the West of Scotland.

General rights

Copyright and moral rights for the publications made accessible in the public portal are retained by the authors and/or other copyright owners and it is a condition of accessing publications that users recognise and abide by the legal requirements associated with these rights.

- Users may download and print one copy of any publication from the public portal for the purpose of private study or research.
- You may not further distribute the material or use it for any profit-making activity or commercial gain
- You may freely distribute the URL identifying the publication in the public portal ?

Take down policy

If you believe that this document breaches copyright please contact us providing details, and we will remove access to the work immediately and investigate your claim.

Download date: 31 Aug 2016



Die approbierte gedruckte Originalversion dieser Dissertation ist an der TU Wien für die elektronische Version verfügbar.
The approved original version of this doctoral thesis is available in print at TU Wien Bibliothek.



SCIENCE and ART: A Future for Stone

**Proceedings of the 13th International Congress on the
Deterioration and Conservation of Stone – Volume I**

**Edited by
John Hughes & Torsten Howind**

SCIENCE AND ART: A FUTURE FOR STONE

PROCEEDINGS OF THE 13TH INTERNATIONAL CONGRESS ON THE DETERIORATION AND CONSERVATION OF STONE

6th to 10th September 2016, Paisley, Scotland

VOLUME I

Edited by
John J. Hughes and Torsten Howind



UNIVERSITY OF THE
WEST of SCOTLAND
UWS

© University of the West of Scotland, Paisley, 2016

Licensed under a Creative Commons Attribution 4.0 International License.



ISBN: 978-1-903978-57-3

ISBN: 978-1-903978-54-2 (eBook)

ISBN: 978-1-903978-59-7 (Set: Volume 1&2)

ISBN: 978-1-903978-56-6 (eBook-Set: Volume 1&2)

Hughes J.J. and Howind T. (Editors), “Science and Art: A Future for Stone. Proceedings of the 13th International Congress on the Deterioration and Conservation of Stone”, University of the West of Scotland, Paisley, September 6th to 10th, 2016.

Cover image: The front door of the Paisley Technical College building, now University of the West of Scotland. T.G. Abercrombie, architect 1898. Photograph and cover design by T. Howind.

ARTIFICIAL AGEING TECHNIQUES ON VARIOUS LITHOTYPES FOR TESTING OF STONE CONSOLIDANTS

M. Ban^{1*}, A.J. Baragona², E. Ghaffari², J. Weber² and A. Rohatsch¹

Abstract

This paper focuses on a series of ageing tests performed in the frame of a wider study on the use of innovative consolidants for various architectural stone types. The tested lithotypes can generally be broken down into two categories: silicate (quartz sandstone with a clayey matrix) and carbonate (porous detrital limestone and marble). The predominant deterioration phenomenon of all these stones on-site is loss of grain cohesion and the formation of micro cracks. Thus, the emphasis lies on reproducing this key-deterioration effect in every lithotype. An additional effect to be studied for porous limestone is the formation of a gradient of compactness within the specimen, mimicking a crust on loose substratum. The ageing progress was evaluated by the methods of determining changes in ultrasound velocity and water absorption coefficient by capillarity. At critical stages the micro defects created are analysed by polarizing light and scanning electron microscopy on petrographic thin sections and mercury intrusion porosimetry. The methodologies for artificial ageing are as following: 1.) The samples were treated thermally by temperatures up to 600°C to induce various types of decay; 2.) All samples were additionally subjected to acid attack, freeze-thaw cycles and salt crystallization alone or in combination with thermal treatment. The approach of matching the ageing procedure for each lithotype to its predominant sensitivity and methods used to assess the effect of the ageing treatments are discussed in terms of relevance to the natural decay phenomena found in exterior environments of buildings. Thermal treatment proves to be a cost and time efficient method for assessing artificial ageing for testing of stone consolidants.

Keywords: artificial ageing, deterioration phenomena, consolidants, material testing

1. Introduction

Using sound stone to test the efficacy of consolidants in laboratory programs is likely to produce unrealistic results, due to the fact that these differ in their key properties from the weathered material. Unless a poorer quality of the same lithotype can be employed (Pápay and Török 2007, Ahmed 2015), ageing of the specimens prior to treatment is a prerequisite for such studies, though it must be kept in mind that artificial ageing will hardly result in a perfect mimic of true weathering states. While surface defects which could eventually be produced through salt or frost cycles causing, e.g. scaling or sanding, could in principle reflect true states of weathering usually associated with in-depth gradients, they don't

¹ M. Ban* and A. Rohatsch

Research Centre of Engineering Geology, Vienna University of Technology, Austria
matea.ban@tuwien.ac.at

² A.J. Baragona, E. Ghaffari and J. Weber

Institute of Art and Technology, Conservation Science, University of Applied Arts Vienna, Austria

*corresponding author

match the needs of modern test standards, most of which base on the assumption of properties evenly distributed over the full diameter of the test body, e.g. a cube of 5×5×5 cm³. Lubelli *et al.* (2015) designed a method where the stones were ground and sieved to a grain size approximate to that of the fresh stone with the particles then re-aggregated on top of the fresh stone by the addition of air lime. While this method seems appropriate to study prerequisites of consolidants and promises to create different decay profiles going from granular disintegration to the sound fabric, it still needs further investigation in terms of physical and mechanical characteristics. The literature reveals some possibilities of ageing different lithotypes but most of them are time consuming, costly and bear negative side effects, e.g. salt contamination (Labus and Bochen 2012). Moreover most standards for determining the resistance of building materials by applying artificial ageing techniques (e.g. EN 12371:2010) focus on describing the failure of a material rather than achieving the level of degradation necessary to study consolidation products. It is generally accepted that salt as well as ice crystallisation causes major deterioration phenomena in building materials. Even though it is certain that damage will occur with Mg- and Na-sulphate solutions, it is first likely that decay processes induced by the action of salt are limited to the surface of the test body, and second it may be very difficult to desalinate the samples to the extent that a novel consolidants can be applied in order to study its fundamental principles. On the other hand, freeze-thaw weathering often causes premature damage in certain lithotypes while others remain unaffected. Systematic observation of fabric decay by frost action is not often considered after a material collapses or shows cracks going through samples. Ruedich *et al.* (2011) describes that in most cases at least 50 cycles need to be accomplished in order to investigate clear deterioration patterns. An important decay process induced by the action of water is described within clay-containing stones, which can be damaged through the swelling and shrinkage of clay by wetting and drying cycles (Jiménez-González *et al.* 2008). Generally, the observation of these deterioration mechanisms is rather slow and can be obtained only in long-term studies. Clay minerals can be treated with different acids, with the aim of partly dissolving them. Concentrated hydrochloric-, nitric- and sulphuric acid may dissolve clay minerals but due to their reactivity they preferentially dissolve carbonate binding materials by destroying their grain boundaries and consequently causing sanding and granular disintegration. Sulphuric acid and sulphur dioxide are used to form gypsum by reproducing a gradient of compactness within the specimen mimicking a crust on loose substratum (Janvier-Badosa *et al.* 2015). However, a negative side effect of using acids to age stone is the formation of salts, which hinders the ability to study innovative consolidants. Thermal ageing is a widely studied technique for fissure formation in compact stones. In particular, various marbles but also limestones have been studied in terms of their anisotropic behaviour and main factors that influence deterioration caused by thermal stresses (Siegesmund *et al.* 2000, Andriani *et al.* 2014). Researchers Sassoni and Franzoni (2014) have systematically studied weathering levels induced by heating prior to test consolidants. However, Franzoni *et al.* (2013) summarises that the process of heating may differ between the stones significantly and thus necessitating a development of suitable heating procedures for every lithotypes. Of these, the method that shows the best performance in terms of reproducing damage as found in-situ will be applied on a large number of specimens prior to test stone consolidants.

2. Lithotypes selected and their typical deterioration phenomena

Samplings of small specimens were taken to study typical decay phenomena occurring on three cathedrals, namely the Cologne Cathedral (Germany), the Cathedral in Pisa (Italy) and the Cathedral in Vienna (Austria). The tested lithotypes were two silicate based sandstones with a clayey matrix from Cologne and two carbonate based stones, a porous detrital limestone from Vienna and a marble from Pisa. Two basic types of defects can be observed and need to be reproduced: (1) granular disintegration is a characteristic feature of clastic sedimentary and some types of volcanic rocks as well as granular metamorphic rocks like marbles; and (2) fissuring of various kinds, characteristic of compact rocks such as dense limestones, siliceous metamorphic and plutonic rocks. In addition to the described defects, shales and crusts that tend to detach from the surface can be found in all lithotypes.

The main materials from the 19th century reconstruction used for the load bearing structure of Cologne Cathedral were quartz arenites named after the towns in which they were quarried: Obernkirchen and Schlaitdorf. Obernkirchen is a fine-grained quartz dominated sandstone. It is composed mainly of quartz and few lithic siliceous fragments with sutured grain contacts between quartz grains and with a slight authigenic growth of quartz. Additional occurrence of kaolinite and dolomite can be observed. Schlaitdorf quartz arenite is a coarse grained sandstone without a visible sedimentary layering. The main components are quartz and few lithic siliceous fragments. Furthermore dolomite (coarse grained spar cement and microcrystalline binder), kaolinite and illite are present. The Carrara marble from the Apuan Alps was used for the construction of the Cathedral of Pisa. It is a more or less non-foliated low metamorphic carbonatic rock mainly consisting of calcite and traces of dolomite. The last stone which was investigated is a fine- to coarse-grained, rhodolite bearing, neogene calcareous arenite from the quarry in St. Margarethen (Austria, Burgenland). In thin sections it appears very porous and is composed mainly of small fragments of coralline red algae and foraminifera. The components are cemented with fine-grained dog-tooth calcite cement.

3. Artificial ageing techniques and evaluation methods

General aim of all ageing tests was to widen existing pore spaces, loosen grain contacts, or create micro fissures to an extent that the stone fabric could still be classified compact enough to be handed for test reasons. A wide variety of techniques were employed either individually or in combination. The predominate methods for checking the efficacy of the ageing treatments was by determining the ultrasonic pulse velocity (apparatus Labek, oscillation frequency 40 kHz) and rate of water absorption by capillarity after one hour, which was tested after each heat cycle or acid attack. Ultrasound pulse velocity was measured after every 5th cycle of wetting and drying, freeze-thaw and/or salt crystallisation. Mercury intrusion porosimetry (Porosimeter Porotec Pascal 140/440) were measured on 3 samples when the desired state of degradation was achieved in comparison to the sound material. Polished thin sections were produced from the latter stone samples, which were then examined by polarizing light microscopy and scanning electron microscopy. For every ageing method three 5×5×2.5 cm samples were investigated.

The sandstones were heated up in a muffle oven to 600°C to form a sudden volume exchange through the conversion from α to β quartz, which occurs at ~573°C. Thermal expansion is known to form anisotropic deformation of calcite crystals, therefore temperatures from 300 to 400°C followed by “quenching” in water of 20±5°C were used

for marble. For the porous limestone higher temperatures were applied, from 400 to 600°C, to generate more stress and thus form micro cracks. The number of one-hour cycles used depended on whether the sample failed or had reached a “meta-stable” state; usually occurring between 3 and 5 cycles. The sandstones were additionally subjected to 80 wet/dry cycles (12 h water immersion by 20±5°C followed by 12 h drying at 75°C) as well as a 5% hydrochloride acid attack for partly dissolving the clayey matrix (12 h immersed and repeated 3 times). All lithotypes were aged by 25 cycles of freeze/thaw (12 h immersion in water by 20±5°C and 12 h freezing at -20°C). Another technique involved a two hour saturation of stones with a 14 % solutions of either magnesium or sodium sulphate, with a subsequent 16h drying out cycle at 75°C, which was repeated up to 25 times. With sodium sulphate, the specimens were dried at 100°C with addition of 350 ml water in the drying oven. Moreover the calcareous limestone was subjected to a 15 % sulphuric acid attack by a relative humidity of 50±5 %. The specimen was immersed edge-first into a 15 % sulphuric acid solution in order to draw the acid into its pore space till the top side is saturated. After ~24 hours of capillary absorption the side surfaces were sealed and the samples were put into water for one week so that a controlled evaporation only from the top side ensues. Nitric acid was additionally used for the limestone as it seems promising for stones with high porosity (Franzoni and Sassoni 2012). The samples were immersed in a 1.6 % solution for 24 h and afterwards washed for 3 days in an ultrasonic bath with constant change of the water. This ageing technique was repeated 3 times. A subsequent weathering effect was studied by immersing all samples into a 30 % hydrogen peroxide for the duration of 6 h and repeated 5 times. Finally the combination of heat treatment with freeze-thaw, hydrogen peroxide and acid attack was attempted, with the goal of forming susceptible damage.

4. Results and discussion

One concrete, reproducible result that could be attained quickly with thermal ageing was a reduction in ultrasound pulse velocity and an increase of water absorption capillarity, both of which correspond with a reduction in a stone sample’s soundness by formation of new micro cracks and the opening of existing cracks. A general finding was that heating the stone is by far the most time efficient way for any lithotype to deteriorate and to reach a reduction of strength (Tab. 1 and Fig. 1). A suitable temperature to cause the desired effects for Carrara marble is 400°C while other lithotypes show the highest decrease in soundness at 600°C. Care in heating and cooling the samples must be taken as macro-cracking can occur, such as in the case of Obernkirchen which can crack after the first heat cycle unrelated to its original texture. Thermal conductivity of stones and resulting stresses formed through rapid or slow cooling play a crucial role in the failure of samples. The overall results of thermal treatment may vary drastically if specimens with different size and shape are subjected to the same conditions of thermal ageing.

Tab. 1: Mean values of water absorption by capillarity after 5 cycles of heat treatment

Difference	Carrara	Obernkirch.	Schlaitd.	St. Marga.	Units
Sound	0.058	2.641	3.031	10.846	kg/(m ² h ^{0.5})
Aged	0.854	4.235	5.337	12.074	kg/(m ² h ^{0.5})
Increase	1364.29	60.37	76.08	11.33	%

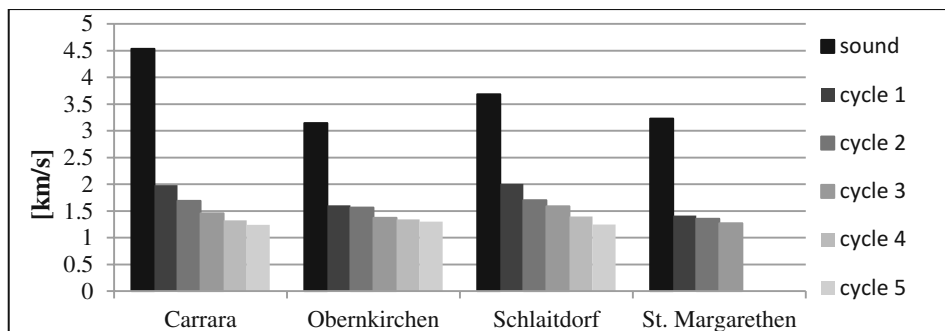


Fig. 1: Mean value of ultrasound pulse velocity after 5 cycles of heat treatment.

Following the measurement of water absorption by capillarity, the lowest increase can be seen in St. Margarethen limestone due to the high porosity of the stone that allows the calcite crystals more room for expansion without creating additional cracks. In this case, the rate of water uptake was constant after the 3rd cycle. As for the sandstones and the marble the relative increase of the capillary absorption is much higher due to the formation of inter- and intra-granular fractures, for example Obernkirchen shows an increase in water absorption after 3 cycles of approximately 25 % depending on its anisotropic orientation.

The evaluation of an aged stone's soundness by ultrasound pulse velocity shows the most significant drop after the first heat cycle but in the case of marble and the two silicates the velocity continues to decrease after additional cycles (Fig. 1). A stable state occurs after the 5th cycle. For St. Margarethen and very often also for Obernkirchen only 3 cycles are necessary to reach the lowest possible values. For the latter 3 cycles are likely to cause the failure of the sample. While some of the results may seem unrealistically low, for the testing of stone consolidants the lowest values should be taken even though in real life this condition indicates the danger of breakdown and the stones would either be replaced or put in a controlled environment (Siegesmund and Dürrast 2014). The highest possible deviation between sound and aged specimens make it possible to describe more accurately the difference of mechanical and physical properties of the stones and the performance of the consolidant.

The reasons for decay can be observed by scanning electron microscopy. The fissures created can be compared to the ones found in-situ (Fig. 2). The only difference is that the artificially induced cracks range through the whole specimens and are quite homogenous while the naturally developed occur only in exposed surfaces. While inter- and intra-granular fractures can be observed in the whole specimen, the natural decay phenomena show cracks parallel to the surface and thus contour scaling of different depths. Moreover the naturally decayed specimens show hollow spaces in a range of 10 μm up to 1 mm and the same effect can be achieved through thermal treatment. These effects are created due to the reduction of kaolin cement, some of which has been converted to meta-kaolin and re-deposited away from the grain boundaries and the formation of fissures within the silica grains (Fig. 2). On St. Margarethen calcareous arenite it is observable that the first heating results in the increase in porosity while re-heating the stone shows only minimal changes. This is due to the formation of micro-cracks that can accommodate more calcite crystals

deformation and therefore a less significant drop is observed after this cycle, a phenomenon observed also by Sassoni and Franzoni (2014). It was observed that stones with smaller crystals size tend to crack faster during thermal ageing and depending on the shape large cracks and complete failures can ensue.

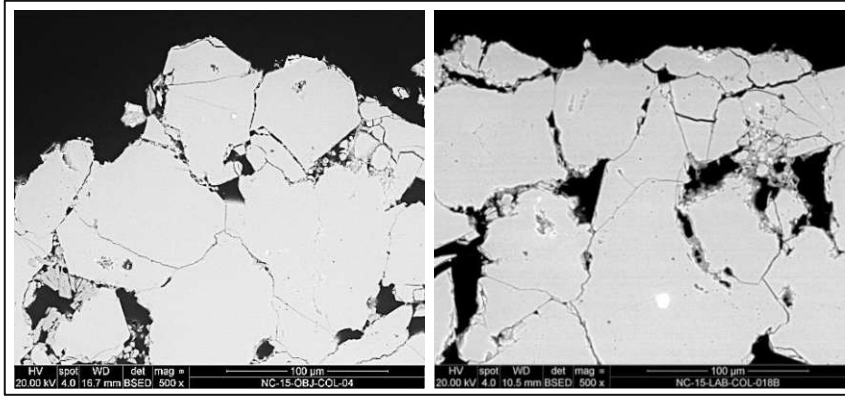


Fig. 2: Naturally (left) - compared to artificially aged (right) Obernkirchen Sandstone.

Tab. 2: Range of porometric parameters before and after thermal treatment.

	Carrara	Obernkirchen	Schlaitdorf	St. Margarethen
Total pore volume mm ³ /g	2.79-3.90	74.77-79.79	62.26-72.96	119.02-130.90
	11.96-19.97	95.57-102.13	64.25-77.18	143.03-144.46
Total porosity Vol. %	0.76-1.05	16.66-17.29	14.65-16.11	23.65-26.17
	3.25-5.23	20.09-22.09	14.41-17.70	27.69-28.16
Average pore diameter µm	0.07-0.37	0.69-1.10	0.82-0.83	0.37-0.44
	0.53-2.38	0.59-0.67	0.25-1.09	0.42-0.54
Median pore diameter µm	0.20-3.28	6.14-6.28	20.88-29.96	48.92-49.81
	3.96-6.75	6.14-6.65	15.20-27.94	45.24-46.55

The changes in the pore structure can be determined by mercury intrusion porosimetry for all lithotypes. All lithotypes, in particular Carrara and Obernkirchen, show an apparent increase in total porosity. In the case of Carrara and Schlaitdorf this is accompanied by a shift in pore diameter, which should be investigated further through microscopy. However, the MIP results for St. Margarethen are of limited utility due to the heterogeneity of this lithotype.

The non-thermal ageing procedures gave very mixed results, which pointed to their marginal usefulness for the purposes of this study. However if the goal is the creation of surface or gradated phenomena to be evaluated by non-normative methods such as microscopy, a number of the following procedures may produce interesting results.

Hydrochloric acid was found to have the effect of reducing the soundness of sandstones when used in combination with heat-treatment due to a partial dissolution of the clayey matrix. Due to the formation of salt and the efficacy of the thermal treatment as a solely ageing method, ageing by hydrochloric acid will be omitted from future testing. In response to sodium sulphate crystallization only Obernkirchen fine-grained sandstone produced granular disintegration, sanding and flaking, which occurred as soon as after the 5th cycle. A rougher surface and light sanding could be observed on Schlaitdorf as well, while other lithotypes showed no damage that could be observed macroscopically. Magnesium sulphate showed no visible damage to any of the sample lithotypes after 25 cycles. With both sulphate solutions the evaluation methods did not show any significant difference despite the desalination. This, coupled with the difficulty of removing the salts before consolidation has led to the decision that this procedure be excluded from the future test program, but is of interest for additional research. The freeze-thaw ageing caused total failure of St. Margarethen limestone after as few as 3 cycles while other lithotypes remained sound after 25 cycles. Due to the complete failure of St. Margarethen and the different life cycles of the stones this method was aborted. Drying and wetting didn't cause any measurable changes after 80 cycles except colour changes due to the iron-containing components. While a gypsum crust was formed on the St. Margarethen limestone following partial immersion in weak acid, it was found to have a consolidating rather than degrading effect, at least in the short term. Since naturally weathered samples of all lithotypes show the formation of gypsum inside the fabric, the consolidation efficiency on a gypsum-contaminated substrate will be topic for further investigation. No significant changes could be observed with the ageing with nitric acid after 3 cycles.

Combining the above methods did not show a significant change in the degradation process. Thus even with a wide variety of treatments it was determined that thermal ageing is by far the most time efficient technique with reliably reproducible results.

5. Conclusion and Outlook

The degree of degradation is of major importance when studying stone consolidants; thus a systematic approach to age the substrate is required. Heat treatment allows a cost and time efficient reduction of soundness reflective of the degradation processes observed in-situ. Moreover the decay level can be specifically tailored and a systematic investigation of the efficacy is possible for every lithotype. Therefore the large scale production of samples on which to test consolidants will be mainly achieved through thermal treatments. Nevertheless, the results may vary drastically if specimens with different size are subjected to the same conditions of thermal ageing. Laboratory observations alone cannot always provide insight into understanding these interacting phenomena, but used in combination with numerical modelling these phenomena can be understood with greater precision, with the caveat that even these data are only roughly comparable with what occurs naturally. The influences of gypsum, salt and biological colonisation will be studied separately in advanced stage of this project. The most important conclusion of our research is that a set of standards for the artificial ageing of stone by lithotype is desirable.

Acknowledgments

This research was conducted in the framework of the European program Horizon 2020 Call NMP21-AC 646178 “Nanomaterials for conservation of European architectural heritage developed by research on characteristic lithotypes (NANO-CATHEDRAL)”. The authors wish to express their gratitude towards Verena Hammerschmidt and Karin Fussenegger.

References

- Ahmed, H.T., 2015, Physical and Mechanical Characteristics of Helwan Limestone: For Conservation Treatment of Ancient Egyptian Limestone Monuments, *Journal of American Science*, 11 (2), 136-151.
- Andriani, F.G. and Germinario, L., 2014, Thermal decay of carbonate dimension stones: fabric, physical and mechanical changes, *Environ. Earth Sci.*, 72, 2523-2539
- Franzoni, E., Sassoni, E., Scherer, G.W. and Naidu S., 2013, Artificial weathering of stone by heating, *Journal of Cultural heritage*, 14S, 85-93.
- Franzoni, E. and Sassoni, E., 2012, Comparison between different methodologies for artificial deterioration of stone aimed at consolidants testing, in proceedings of the 12th International Congress on the Deterioration and Conservation of Stone, Columbia University, New York, ICOM-CC.
- Jiménez-González, I., Rodríguez-Navarro, C. and Scherer, G.W., 2008, Role of clay minerals in the physicommechanical deterioration of sandstone, *J. Geophys. Res.*, 113, F02021, 1-17.
- Janvier-Badosa, S., Beck, K., Brunetaud, X., Guirimand-Dufour, A. and Al-Mukhtar, M., 2015, Gypsum and spalling decay mechanism of tuffeau limestone, *Environl. Earth Sci.*, 74 (3), 2209-2223.
- Lubelli, B., Van Hees, R.P.J., Nijland, T.G. and Bolhuis, J., 2015, A new method for making artificially weathered stone specimens for testing of conservation treatments, *Journal of Cultural heritage*, 16, 698-704.
- Labus, M. and Bochen, J., 2012, Sandstone degradation: an experimental study of accelerated weathering, *Environ. Earth Sci.*, 67, 2027-2042.
- Pápay, Z. and Török, Á., 2007, Evaluation of the efficiency of consolidants on Hungarian porous limestone by non-destructive test methods, *Central European Geology*, 50 (4), 299-312.
- Ruedrich, J., Kirchner, D. and Siegesmund, S., 2011, Physical weathering of building stones induced by freeze-thaw action: a laboratory long-term study, *Environ. Earth Sci.*, 63, 1573-1586.
- Siegesmund, S., Ullemeyer, K., Weiss, T. and Tschegg, E.G., 2000, Physical weathering of marbles caused by anisotropic thermal expansion, *Int. J. Earth Sci.*, 89, 170-182.
- Sassoni, E. and Franzoni, E., 2014, Influence of porosity on artificial deterioration of marble and limestone by heating, *Applied Physics A*, 115, 809-816.
- Siegesmund, S. and Dürrast, H., 2014, Physical and Mechanical Properties of Rock, in *Stone in Architecture: Properties, Durability*, Siegesmund, S. and Snethlage, R. (eds.), Springer-Verlag Berlin Heidelberg, ISBN 978-3-642-45155-3, 97-225.

B.1

Silicates for the consolidation of stone: nano silica vs. ethyl silicate

Not published in open access

C.1

The potential of neutron imaging in stone conservation

Not published in open access

D.1

Forschung zu Nano-Materialien für die
Gesteinsrestaurierung. Auswirkung von
Festigungsmaßnahmen in Laborversuchen im Rahmen des
EU-Projektes Nano-Cathedral.

Not published in open access